Microbial transformations of sulfur: environmental and (paleo) ecological implications

Thesis by
Daniela Osorio Rodríguez

In Partial Fulfillment of the Requirements for the
Degree of
Doctor of Philosophy

CALIFORNIA INSTITUTE OF TECHNOLOGY
Pasadena, California

2023
Defended May 25th, 2023

Daniela Osorio Rodríguez
ORCID: 0000-0001-6676-4124

ACKNOWLEDGEMENTS

The very fact that I was able to pursue a PhD would not have been possible without having had the chance to attend very high quality schools and universities in Colombia, in which I found a variety of female role models. Unbeknown to me before I started hearing about these conversations at Caltech, many women doubt their capacities as academics or scientists having grown used to seeing themselves as a minority. This was never the case for me, since I had more than five science and math female professors in high school, and at least half of my college classes were taught by female professors as well. I want to thank in particular Silvia Restrepo, for her knowledge and support, and Adriana Bernal, my undergrad and MSc advisor, for being the person who probably first saw my potential. Adri, you were my first example and role model for pursuing a scientific career. I am so glad that I could learn from your strict and professional approach, your impeccable work ethic and your attention to detail, and that I can consider you my friend. Thanks to Adriana and Silvia, and other female scientist leaders at the Department of Biological Sciences at Universidad de los Andes, most of my former colleagues from this institution were able to successfully pursue PhDs in Colombia and elsewhere. I am incredibly thankful to Jairo Peña, Juan Santiago Vieco, Leonor García, and Miguel Gómez, who provided valuable support in my applications to PhD programs.

I am infinitely indebted to my PhD thesis advisors, Jess Adkins and John Grotzinger. They both gave me the chance to be part of their research groups, coming from a country and universities that were completely obscure to them, never having heard of my undergraduate and masters advisors. I had no previous experience in the type of research that they both specialize in, yet they welcomed me with open arms and always made me feel confident in my knowledge, skills and capabilities. Jess, I appreciate your commitment to making me a little bit of a chemical oceanographer. I am very grateful for the first year weekly paper discussions, the group meetings where I was always eager to learn more from you and the blind trust you deposited in me, to the point of allowing me to propose and develop my own ideas. You gave me the chance to travel to other institutions as part of my projects, and to participate in two research cruises that were some of the most unique and valuable experiences that I had during my PhD. John, it has been an incredible honor to interact and learn from one of the most respected sedimentologists and Mars researchers. Being in your group has made me become a more grounded geobiologist. Having the chance

of being in the field with you in places as varied as Death Valley and the Italian Apennines has been one of the most intensive and rich learning experiences that I have had as a geologist. I also admire your commitment to physical health and fitness and I hope to keep the motivation to work and workout as hard as you do for as long as you have done it.

I am also incredibly grateful to Victoria Orphan. Victoria, you are the Orphan, but curiously enough, you adopted me for all the fun microbe stuff that I did in my PhD. I felt very welcomed in your group and I value all your support and input, as well as the interactions with all the Orphan lab members. I also want to express appreciation towards my academic advisor and committee chair, Alex Sessions. Alex, you always had a genuine smile and were available whenever I wanted to stop by for a quick chat or needed some insight about anything isotope (or life) related. You also let me participate in the 2019 International Geobiology Course, which was a once in a lifetime experience. I consider myself very lucky for having had in practice four advisors with different expertises, which enriched my PhD experience and contributed to my academic growth way beyond my expectations.

I want to extend my thanks to other faculty members, in particular Woody Fischer and George Rossman. Woody, you have such a wide breadth of knowledge that it is just inspiring to be in the same building and exchange ideas with you. You are one of the best lecturers that I have had and I am very grateful for the class that I took and TA-ed for you and the Geobiology journal club that you so kindly hosted for students. George, I appreciate all your mineralogy and analytical knowledge, your stories, and the joy you transmit when you are helping people out. I want to thank Tom Hanson from the University of Delaware and Maya Gomes from Johns Hopkins university for briefly and very kindly hosting me in their labs, as well as Will Berelson (USC), Russell Shapiro (CSU Chico), and Paul Myrow (Colorado College) for the fruitful interactions, and exchanges of ideas and samples.

This thesis would not have been possible without technical help from many people. Special thanks to Stephanie Connon, Fenfang Wu, Chi Ma, and Yunbin Guan for analytical assistance, as well as Eliza Carter, and the crew and science parties of the *R/V Sally Ride* cruise SR2113 for help with sample collection, ideas, etc. I also appreciate all the help, support and interactions with my lab and office mates. I treasure so much all the exchanges I had with the Adkins, Sessions, Orphan and Grotzinger lab members, but I want to give special thanks to Ted Present, Frankie Pavia, Alex Phillips, Kelsey Moore, Kriti Sharma, Magdi Mayr, Kyle Metcalfe,

Reto Wijker, Daniel Utter, and Selva Marroquín. I also thank Julie Lee, Nora Oshima, Leilani Rivera, Jen Shechet, Julia Zuckerman, and Janice Grancich for administrative assistance, and Daniel Yoder and Laura Flower Kim from ISP.

I have to recognize the support of my Caltech friends, without whom surviving the intricacies of the PhD being far away from home and the COVID-19 pandemic would not have been possible. Many thanks to Elsy Buitrago (and Isa), Nico Pelaez, Phillip Hon, Camilla Urbaniak, Livia Morais, Alejandro Granados (and Orika), David Larios (and Brie), Juan David Hernández, Elvira Moreno, Adriana Piña, Porfirio Quintero, Ellen Yan, Josh Lieber, and Terry and Thomas and other members of the Tango club. I also have to acknowledge Kitty Cahalan from the Caltech Center for Teaching, Learning and Outreach (CTLO), and the members of Club Latino for helping me find a sense of community and purpose at Caltech. I have to give a special shout-out to my best friend for three years, collaborator, and impressive scientist, Manuel Razo Mejia, for all his support, patience, and teachings.

These acknowledgements wouldn't be complete without mentioning my family. I recognize that I had the incredible opportunity of making a PhD at Caltech from growing up in a middle-class privileged family in Colombia. Sin embargo, le debo toda la inspiración, el apoyo, el creer siempre en mí y el ejemplo de trabajadores incansables y perseverantes a mis padres, Ruth Nohora Rodriguez y Antonio Osorio. A ustedes doy gracias eternas porque todo lo que soy es gracias a ustedes, y toda la motivación que tengo para seguir adelante viene de ustedes. También quiero agradecer a mis hermanos, tíos y demás familiares, amigos del colegio y universidad, profesores, y otras personas que creyeron siempre en mí, me enseñaron, me ayudaron, y me acompañaron a celebrar los triunfos en cada etapa del camino. Finally, I want to thank my partner Buck. I have learned so much from the way you live your life to make mine better. I wake up every day feeling immensely grateful for you. I can't think of a better relationship than the one we have. You showered me with love since day one and the happiness that I derive from being with you makes me a better person and a better scientist.

ABSTRACT

This thesis is centered around the role that sulfur plays in the cycling of carbon and in microbial energetics. In the oceans, sulfate is the most important electron acceptor for the remineralization of organic matter after oxygen has been depleted, and sulfate reduction is particularly relevant in coastal environments and in marine and freshwater sediments. The opposite process, reduced sulfur oxidation, allows autotrophic microorganisms to fix carbon in environments where oxygen is scarce. Organic sulfur is also a relevant component of the sulfur cycle, since sulfur is the sixth most abundant element in biomass, it can protect organic matter from degradation, and it is composed of hundreds of molecules that are produced mainly by microorganisms, with potentially relevant ecological roles.

This work has been divided into two parts. In the first one, we attempt to expand our understanding on different aspects of the sulfur cycle. In Chapter 2, published in *Limnology and Oceanography*, we focus on dimethylsulfoniopropionate (DMSP), the most abundant organic sulfur compound in the oceans with roles of UV, cryo, and osmoprotection, and involved in the formation of sulfate aerosols. We propose a framework to differentiate between the microbial degradation pathways of DMSP based on the sulfur isotope fractionations imprinted by each one of them. In Chapter 3, we perform a survey of sulfate, sulfide, and reduced sulfur intermediates, as well as redox-sensitive elements, in porewaters of a 40 cm core from the San Clemente Basin (California) and three 1.2-2 m cores near Cocos Ridge (Costa Rica). We correlate these concentrations with the sediment microbial community composition to unveil the specifics of organic matter and sulfur cycling at these localities. In Chapter 4, we explore the utility of sulfur isotope fractionations to characterize different pathways involved in microbial sulfur oxidation (MSO), and examine the role of nutrient limitation and growth rates on the magnitude of the fractionation.

In the second part of this thesis, we aim at understanding biomineralization by consortia between anaerobic methanotrophic archaea (ANME) and sulfate-reducing bacteria (SRB), which comprise more than 90% of the microbial biomass in deep sea sediments around hydrocarbon seeps. In Chapter 5 (in review at *Proceedings of the National Academy of Sciences*) we establish that modern ANME-SRB aggregates precipitate amorphous silica in undersaturated solutions in sediments and carbonates, often in the form of rims, which pinpoints to a potentially new microbial biomineralization mechanism. In Chapter 6, we posit the use of this proxy, together with distinctive spectral and isotopic signals, to find potential microfossils of ANME-SRB aggregates in the rock record of the Earth and other planetary bodies where methane seepage has occurred throughout geologic time. This suite of tools is used in conjunction to identify ANME-SRB aggregates in the Tepee Buttes (Colorado, 75 Mya) seep carbonates.

PUBLISHED CONTENT AND CONTRIBUTIONS

Osorio-Rodriguez, D., Razo-Mejia, M., Dalleska, N. F., Sessions, A. L., Orphan, V. J., & Adkins, J. F. (2021). "Sulfur isotope fractionations constrain the biological cycling of dimethylsulfoniopropionate in the upper ocean". *Limnology and Oceanography* 66(10), pp.3607-3618. DOI: 10.1002/lno.11901.

> DOR designed the project (with JFA), performed experiments and analytical measurements (with help from NFD), analyzed data (with MRM), interpreted data (with input from all the authors), designed and tested the models (with MRM), and wrote the manuscript (with input from all the authors).

Osorio-Rodriguez, D.*, Metcalfe K.S.*, McGlynn, S.E., Yu, H., Dekas, A.E., Ellisman, M. H., Deerink, T. J., Grotzinger, J. P. & Orphan, V. J. "Silicate biomineralization by anaerobic methane-oxidizing consortia and implications for microbial fossil preservation". In review at *Proceedings of the National Academy of Sciences.*

> * These authors contributed equally to this work. DOR, KSM, JPG, and VJO designed the project. DOR, KSM, SEM, HY, and AED performed experiments and analytical measurements (with help from MHE and TJD), analyzed data, and interpreted data (with input from all the authors). KSM designed and tested the models. DOR and KSM wrote the manuscript (with input from all the authors).

TABLE OF CONTENTS

Chapter 1

INTRODUCTION AND SUMMARY

The wide diversity and flexibility of microbial metabolisms derives from the variety of environments where life forms can survive on Earth. These environments must offer a source of energy (from which electrons that power cells can be stripped off), an electron acceptor (which stores electrons after these have been utilized by cells), a source of carbon, and availability of macro (such as nitrogen, phosphorus, and sulfur) and micronutrients (trace elements and vitamins required for cells' vital functions) for microorganisms to be able to colonize and multiply in them. The discipline of geobiology arises from the curiosity to understand the feedback loops between environments and the organisms that inhabit them. In modern settings, we can study how different microbes thrive in the environments where they are found, how they interact with others and form communities which allow them to better survive on them, and how they modify the environments where they live. In turn, we can study rocks, sediments, ice, and other ancient records to identify how these microbe-environment interactions operated in the past, how they are different from present day ones, and how they contribute to the understanding of each other.

This thesis' unifying theme is one of the main branches of geobiology: the study of the sulfur cycle. Sulfur is abundant in Earth's mantle (Canfield, 2004) and it reaches the surface mostly through terrestrial (Stoiber et al., 1987) and subaqueous (Von Damm, 1990) volcanic activity. Early in Earth's history, anoxic conditions allowed sulfur to accumulate in pyrite and other reduced sulfur minerals on Earth's surface (Farquhar et al., 2000). Between 2.45 and 2.22 Gya (Bekker et al., 2004), at what is now known as the Great Oxygenation Event (GOE; Holland, 2002), an unprecedented raise in atmospheric oxygen levels took place, as evidenced in multiple rock

and mineral deposits (Olejarz et al., 2021). As a consequence, there was a massive oxidation of exposed pyrite to sulfate, which is today the main reservoir of sulfur in the oceans (e.g. Bottrell and Newton, 2006). An abundance of marine sulfate expanded the geologic record of sulfur containing minerals, leading to the formation of deposits of evaporitic sulfates (Blättler et al., 2018) after ~ 2 Gya (Grotzinger, 1989; Grotzinger and James, 2000). Before the Archaean, sulfate concentrations in the oceans were negligible ($< 200\mu M$; Crowe et al., 2014; Habicht et al., 2002) and sulfate evaporites were absent (Grotzinger, 1989; Grotzinger and Kasting, 1993), but this changed when oxygen started to be produced by cyanobacteria, and sulfate reached concentrations of 2.8 to 8.4 mM by 2.3 Gya (Luo et al., 2016).

Sulfur plays an essential role in all living organisms, mainly in the amino acids cysteine and methionine, but also as a component of oligopeptides, vitamins, and cofactors (e.g. Saito (2004)), and even as a constituent of secondary metabolites involved in ecological interactions (Levine, 2016). In addition to these assimilatory pathways, utilized for the consumption of organic (Moran and Durham, 2019) and inorganic (e.g. Patron et al. (2008)) sulfur, a variety of microorganisms have evolved dissimilatory pathways in which sulfur is utilized in energy-generating oxidation-reduction (redox) reactions. The high versatility of sulfur in redox reactions is given by the fact that sulfur can vary in valence from -2 (in sulfide) to +6 (in sulfate). The abiotic or biotic oxidation of sulfide leads to the formation of sulfur species with intermediate valence states like elemental sulfur (S_0), thiosulfate ($S_2O_3^{2-}$), tetrathionate ($S_4O_6^{2-}$), and sulfite (SO_3^{2-}) (Elsgaard and Jørgensen, 1992), which can serve as a source of energy (from oxidation), electron acceptors (from reduction; Jørgensen et al., 2019), or both, in a process known as disproportionation (Jørgensen, 1990; Thamdrup et al., 1993). Despite the fact that reduced sulfur can be oxidized by oxygen, nitrate, iron, and, manganese (e.g. Schippers and Jørgensen, 2001), the reduction of oxidized sulfur species in the absence of a catalyst is extremely

unfavorable. Additionally, the residence time of sulfate in the oceans is in the order of 10^7 years (Holland, 1973), whereas that of some organic sulfur molecules (e.g. DMSP) is as low as days or hours in the upper ocean (Zubkov et al., 2002). For these reasons, microorganisms have an enormous impact on the diversity and abundance of sulfur molecules that are found on Earth, and the rates of sulfur turnover between different reservoirs.

It is thought that sulfur became critical for microbial energetics once sulfate began to accumulate in the oceans in the Proterozoic, as previously abundant and more energetically favorable electron acceptors such as iron and manganese began to precipitate out of the oceans as oxides (e.g. Roy, 2006). Today, sulfate is thought to be responsible for the remineralization of half of the organic matter that reaches the sediments in coastal settings (Jørgensen, 1982), as it is the most abundant electron acceptor after oxygen, at a concentration of 28 mM (Morris and Riley, 1966). It is thought to play an even more critical role in the near future, as oxygen minimum zones are and will keep expanding globally as a consequence of climate change (e.g. Long et al., 2021). Cryptic sulfur cycles (i.e. with no obvious in situ geochemical expression), in which sulfate-reducing and sulfide-oxidizing bacteria live in close association and have high turnover rates of both substrates (Canfield et al., 2010), are also expected to strengthen (Crowe et al., 2018). The sulfur cycle is critical not only for organisms that depend on it as a source or outlet for electrons, but also for the cycling of other elements, of which the most notable are carbon and oxygen. The remineralization of organic matter through sulfate reduction tightly couples the sulfur and carbon cycles (e.g. Leavitt et al., 2013). Additionally, the long term burial of reduced (sulfate) vs. oxidized (sulfide) minerals in sediments regulates atmospheric oxygen levels (Berner and Raiswell, 1983; Garrels and Lerman, 1981), with implications for the long-term evolution of Earth's climate and redox state (Fike et al., 2015; Veizer et al., 1980).

This thesis has been divided into two parts. The first part focuses on constraining the microbial cycling of sulfur in the modern ocean with geochemical tools, mainly quantifications of sulfur (and sulfur-containing molecules) in porewaters and in microbial cultures, sulfur isotope compositions of multiple sulfur pools, and sulfur isotope fractionations by different metabolic pathways. The second part explores the syntrophy between anaerobic methanotrophic archaea (ANME) and sulfate-reducing bacteria (SRB) in modern settings to identify the characteristics that may enhance their preservation in the carbonate rock record. The main takeaway from the framework presented here is that the microbial transformations of organic and inorganic sulfur can be constrained by combining analytical, geochemical, and microbiological tools, and by studying modern systems as analogs of ancient environments and conditions.

PART I: SULFUR ISOTOPES ARE IMPORTANT PROXIES FOR THE MICROBIAL CYCLING OF ORGANIC AND INORGANIC SULFUR

Stable isotopes are an important tool for constraining biogeochemical cycles, because chemical and enzymatic reactions can have associated kinetic isotope effects, in which reaction rates are affected by the ratios of the masses and the vibrational energies of the isotopes (Kendall and Caldwell, 1998). These manifest as fractionations (redistribution of isotopes) between the reactant and the product (Kendall and Caldwell, 1998). Characterizing these fractionations thus allows to establish the trajectory that the atoms in a particular material have followed. Sulfur has 4 stable isotopes, $^{36}\mathrm{S}$, $^{34}\mathrm{S}$, $^{33}\mathrm{S}$, and $^{32}\mathrm{S}$, with natural abundances of 0.0136%, 4.22%, 0.76%, and 95.02% , respectively (Canfield, 2001). Because $^{34}\mathrm{S}$ and $^{32}\mathrm{S}$ are the most abundant ones, their ratios are the most frequently utilized to characterize sulfur-containing molecules. Sulfur isotope compositions are usually expressed as per mil (‰) differences relative to the Vienna Cañon Diablo Troillite standard, and

are presented in standard delta (δ) notation:

$$\delta^{34}\mathrm{S} = [(^{34}\mathrm{S}/^{32}\mathrm{S})_{\mathrm{sample}}/(^{34}\mathrm{S}/^{32}\mathrm{S})_{\mathrm{standard}} - 1] \cdot 1000. \tag{1.1}$$

Similarly, fractionations are expressed with units of ‰ in terms of (ε):

$$\varepsilon_{(\mathrm{A–B})} = 1000 \cdot (\alpha_{(\mathrm{A–B})} - 1), \tag{1.2}$$

where A is the reactant, B is the product, and $\alpha_{(\mathrm{A–B})}$ is defined as:

$$\alpha_{(\mathrm{A–B})} = \mathrm{R_A}/\mathrm{R_B}, \tag{1.3}$$

where R is the ratio between the heavy and light isotopes in the reactant (A) or the product (B).

The microbial cycling of sulfur in the modern ocean is a very broad area of study, mostly because sulfur is composed of organic and inorganic pools, which are utilized in different ways by microorganisms. Dissolved organic sulfur (DOS) is 10^9 less abundant in the modern oceans than the most abundant form of sulfur, sulfate, at a concentration of 28 mM (Ksionzek et al., 2016). However, it is fascinating from a microbial ecology perspective. On one hand, more than 800 DOS chemical formulas have been predicted based on mass spectrometry in the ocean, most of which are unique to the upper ocean (Ksionzek et al., 2016). Most of these molecules haven't been characterized yet, but those that have are known to be involved in interactions between organisms, such as chemotaxis (dimethylsulfoniopropionate-DMSP), quorum sensing (DMSP), and exchange of vitamin B12 for organic carbon between phototrophs and heterotrophs (dihydroxypropane-1-sulfonate-DHPS; Levine, 2016). Chapter 2 of this thesis focuses on dymethylsulfoniopropionate (DMSP), the most abundant organic sulfur molecule in the ocean, at a concentration of $\sim$ 2 nM in the upper ocean (Levine et al., 2012). It is produced by phytoplankton, mainly dinoflagellates and coccolithophores, diatoms, corals, green algae, plants, and even

Alphaproteobacteria, and consumed by *Alphaproteobacteria* (e.g. Bullock et al., 2017). It can also be degraded by multiple clades of marine bacteria to dimethylsulfide (DMS; e.g. Reisch et al., 2011). When incorporated, it can be utilized as carbon and sulfur sources by marine bacteria (e.g. Dixon et al., 2020), and it has also been hypothesized to have roles as osmoprotectant, cryoprotectant, and to be against oxidative stress (Kiene et al., 2000). Traditionally, the presence and expression of DMSP production and consumption related genes has been used to characterize the distribution of this compound in the ocean (Levine et al., 2012; Varaljay et al., 2015; Vorobev et al., 2020). Here, we use sulfur isotope fractionations, a geochemical proxy, to better constrain DMSP degradation in the ocean. We determine the in vitro sulfur isotope fractionations by enzymes involved in DMSP demethylation (consumption) or cleavage to DMS, finding that the residual DMSP from the demethylation pathway is 2.7‰ enriched in $^{34}\mathrm{S}$ relative to the initial DMSP, and that the fractionation factor ($^{34}\varepsilon$) of the cleavage pathways varies between -1 and -9‰. Despite these values being relatively small and overlapping between them, preventing a complete discrimination between enzymes or pathways based on this proxy alone, we incorporated these fractionation factors into mass balance calculations to model how the relative contributions of the different biological processes that act on DMSP could account for the $\delta^{34}\mathrm{S}$ values of DMSP in seawater. We conclude that the reported fractionation factors provide a way to establish the relevance of the demethylation and cleavage pathways of DMSP in natural environments which is complementary to gene abundance and expression data, and thus recommend the use of both approaches in studies that aim to constrain the cycling of elements in the environment.

In Chapter 3, we implement a combination of 16S rRNA sequencing and geochemical characterizations (concentrations and isotopes) to constrain the cycling of sulfur and other redox sensitive elements in deep ocean sediments from a $\sim 40\mathrm{cm}$ multi-

core collected at the San Clemente Basin, California, and 3 1.2-2 m gravity cores collected at separate stations near Cocos Ridge, Costa Rica. Unlike the second chapter of this thesis, which focuses on organic sulfur, Chapter 3 is centered around the dynamics of inorganic sulfur oxidation. Our study is the first one to generate high resolution (3-5 cm) porewater profiles of major ions, redox sensitive elements and sulfur intermediates through 1.2-2 m depth in the oligotrophic Pacific Ocean. It is also a pioneer in the generation of similar high resolution 16S rRNA data for the microbial community composition, which we utilized to explore which microorganisms are the main drivers of sulfur cycling at the study site. We found gradients of porewater nitrate, manganese, and iron that are consistent with their utilization as electron acceptors for organic matter remineralization in order of energetic yield ($NO_3^- > MnO_2 > Fe_2O_3$; Froelich et al., 1979), and which are similar to previous reports for the Eastern Equatorial Pacific (Emerson et al., 1980; Klinkhammer, 1980). We also identified a small decrease of $\sim 1\mathrm{mM}$ in sulfate between the top and the bottom of the sediment cores collected, and the analysis of sulfur and oxygen isotopes of sulfate at Cocos Ridge provided evidence for microbial sulfate reduction. We provide the first meter scale depth profiles of porewater sulfite, sulfide, and thiosulfate for the oligotrophic Equatorial Pacific. These sulfur intermediates were detected at nanomolar concentrations, which, as expected, are much lower than those measured in euxinic, high organic matter flux basins like the Black Sea (Zopfi et al., 2004) and stratified lakes (Findlay and Kamyshny, 2017). We did not find differences in the 16S rRNA identified microorganisms or their diversity between localities, although a general abundance of *Actinobacteria* and *Bacilli* was established at all sampling sites, as well as an increase in dominance of *Chloroflexi* and *Plactomycetes* with depth, which coincides with previous studies on Pacific abyssal sediment microbial communities (Durbin and Teske, 2011). At Cocos Ridge, we generally observed an increase in the relative abundance of the sulfur-oxidizers

Hyphomicrobiales (*Alphaproteobacteria*), *Thiomicrospirales* (*Gammaproteobacteria*), as well as *Bacteroidota*, and *Thermoplasmatota* with depth. However, we could not establish significant correlations between the relative abundance of specific microbial taxa and the porewater profiles of iron, manganese, sulfate or sulfur intermediates. Based on 16S rRNA data, we hypothesize that the metabolic flexibility of microorganisms, as opposed to organic matter fluxes or oxidant availability, could be the main driver of redox cycling in the pelagic Pacific ocean. This is consistent with enrichment experiments using methane seep sediments (Eitel et al., in prep), and environmental surveys in marine benthic habitats (Krämer and Cypionka, 1989; Lovley, 2006; Pjevac, 2014; Roden and Lovley, 1993) which indicate that microbial communities can adapt to utilize different forms of sulfur as electron donors as well as multiple electron acceptors.

Chapter 4 of this thesis focuses on sulfur isotope fractionations during the microbial oxidation of sulfur (MSO). Sulfide, which is mainly a product of microbial sulfate reduction in modern aquatic environments, and other reduced sulfur species, serve as electron donors for carbon dioxide fixation by autotrophic microorganisms (Brune, 1989; Friedrich et al., 2001). The sulfur isotope fractionations associated with this oxidation process have been studied since the 1960s, and have been found to be negligible, between -5 and 4‰ (compiled by Pellerin et al., 2019). Other microbial transformations of inorganic sulfur, such as sulfur disproportionation and sulfate reduction (MSR), have large associated sulfur isotope fractionations, down to ∼-70‰ (Canfield and Thamdrup, 1994) and -75‰ (Brunner and Bernasconi, 2005), respectively. During MSR, it has been established that pH, temperature (Hoek et al., 2006), and supplies of electron donor (Harrison and Thode, 1958; Kaplan and Rittenberg, 1964) and electron acceptor (Jones and Starkey, 1957) are responsible for the magnitude of the fractionations, mostly through their impact on growth rates and specific sulfate reduction rates (Chambers et al., 1975; Habicht and Canfield,

1997; Kaplan and Rittenberg, 1964) and reaction reversibility (Holler et al., 2011; Trudinger and Chambers, 1973; Wing and Halevy, 2014). We reviewed the reported sulfur isotope fractionations for MSO (compiled by Pellerin et al., 2019) and found that most of these culturing experiments were carried out under high nutrient concentrations, which are probably not representative of the natural conditions where these microorganisms live. We hypothesized that an excess of nutrients could minimize the size of sulfur isotope fractionations during MSO, by enhancing growth rates and sulfide oxidation rates —such that the rate-limiting step becomes diffusion of sulfide into the cell—. If that is the case, performing culturing experiments under oligotrophic nutrient concentrations might give more realistic sulfur isotope fractionations that could be utilized to refine models that seek to constrain the role of MSO throughout Earth's history and at different locations by examining the sulfur isotope compositions of S-bearing minerals. We assessed the impacts of nutrient limitation on the sulfur isotope fractionations by the *Deltaproteobacterium Desulfurivibrio alkaliphilus* and the *Chlorobia Chlorobaculum tepidum*. We found that large sulfur isotope fractionations during MSO are only found in *D. alkaliphilus*, consistent with a previous report (Pellerin et al., 2019), and that only in this organism nutrient availability has an impact in the magnitude of the fractionations. *D. alkaliphilus* grows only at alkaline pH and utilizes, at least partially, different metabolic pathways for the oxidation of sulfur than those used by all other microbial sulfur oxidizers (Thorup et al., 2017). For this reason, we conclude that, pending studying nutrient limitation impacts on sulfur isotope fractionations by other sulfur oxidizers, MSO probably does not produce large sulfur isotope fractionations that are relevant for the interpretation of sulfur isotopic compositions in most environmental samples.

PART II: INSIGHTS ON BIOMINERALIZATION AND MICROBIAL PRESERVATION IN ROCKS

Part II of this thesis explores the potential of microorganisms to fossilize in the

carbonate rock record, specifically in methane seep carbonates. Hydrocarbon seeps are located along plate boundaries, back-arc basins, and unstable sedimentary basins, where faulting, diapirism, sediment compaction, or undersea landslides favor the migration of methane-rich porewaters from the sediments to the water column (e.g. Campbell, 2006). The anaerobic oxidation of methane (AOM) by anaerobic methanotrophic archaea (ANME) is a common energy yielding metabolism in these environments (Hinrichs et al., 1999; Wegener et al., 2008). It is syntrophically coupled to sulfate reduction (SR) by sulfate-reducing bacteria (SRB; Hoehler et al., 1994; Michaelis et al., 2002), and is given by the following reaction:

$$\mathrm{CH_4(g) + SO_4^{2-}(aq) \longrightarrow HS^-(aq) + HCO_3^-(aq) + H_2O(l)} \tag{1.4}$$

More than 90% of the methane produced in the oceans is consumed by AOM-SR (Hinrichs and Boetius, 2013; Reeburgh, 2007), thus controlling most of the atmospheric methane efflux from the ocean ($< 2\%$ of the global flux; Reeburgh, 2007). AOM-SR occurs at the so-called sulfate-methane transition zone, a region within marine sediments where sulfate-rich descending waters coexist with ascending methane, and oxidants stronger than sulfate, such as oxygen and nitrate, have been depleted (Barnes and Goldberg, 1976; Martens and Berner, 1974). The production of one mole of bicarbonate ($\mathrm{HCO^{3-}}$) and hydrogen sulfide ($\mathrm{HS^-}$) each by the coupling of AOM and SR increases by two total units the alkalinity of the surrounding waters (e.g. Knittel and Boetius, 2009). The sulfides combine with reduced iron to form newly precipitated iron sulfide minerals (e.g. Berner, 1984). In turn, the alkalinity increase enhances the precipitation of carbonate minerals, as exemplified here by calcium carbonate:

$$\mathrm{Ca^{2+}(aq) + 2HCO_3^-(aq) \longrightarrow CaCO_3(s) + CO_2(g) + H_2O(l)} \tag{1.5}$$

Methane-derived authigenic carbonates have been observed at seafloor cold seeps (e.g. Aloisi et al., 2002; Bohrmann et al., 1998; Ritger et al., 1987) and their

precipitation is thought to be favored by a combination of the increased carbonate alkalinity and decreased solubility from a pressure decrease when porewater escapes fractures (Ritger et al., 1987). Seep carbonates have distinctive negative carbon isotope signatures, which allow for easily fingerprinting them both in modern and ancient settings (Naehr et al., 2007; Peckmann et al., 2002). Here, and in Chapter 6, we express carbon isotope compositions as per mil (‰) differences relative to the Vienna Pee Dee Belemnite standard, and present them in standard delta (δ) notation:

$$\delta^{13}\mathrm{C} = [(^{13}\mathrm{C}/^{12}\mathrm{C})_{\mathrm{sample}}/(^{13}\mathrm{C}/^{12}\mathrm{C})_{\mathrm{standard}} - 1] \cdot 1000 \tag{1.6}$$

Methane has a wide range of $\delta^{13}\mathrm{C}$ values, between -110 and -20‰ (Whiticar, 1999). When methane is a major source of the carbon in carbonates, they typically have $\delta^{13}\mathrm{C}$ values below -20‰ (Aloisi et al., 2002), although methane seep carbonates have been found to span a $\delta^{13}\mathrm{C}$ range of -69‰ (Campbell et al., 2002) to 8‰ in ancient carbonates, and 25‰ in modern carbonates (Loyd et al., 2016). ANME-SRB also have strong depletions in $^{13}\mathrm{C}$ in their biomass, since ANME utilize methane as a carbon source, and both incorporate carbon from bicarbonate into their biomass (Wegener et al., 2008). Typical archaeal isoprenoid biomarkers like crocetane and pentamethylicosane are highly depleted in $^{13}\mathrm{C}$ ($\delta^{13}\mathrm{C}$ = -124‰; Elvert et al., 1999), and archaeol and sn-2-hydroxyarchaeol are similarly depleted in $^{13}\mathrm{C}$ (-114‰ and -133‰, respectively; Hinrichs et al., 1999). Iso- and anteiso-C15 fatty acids, which are abundant in SRB, also have light carbon isotopic compositions (-63‰ and -75‰, respectively; Orphan et al., 2001). For reference, *Thaumarchaeota*, abundant in marine sediments, with auto and mixotrophic metabolisms (Pearson et al., 2016), and heterotrophic bacteria (e.g. Taipale et al., 2015), have lipid biomarkers with carbon isotopic compositions between ~ -22 and -19‰.

In the 1970s, methane oxidation with sulfate was predicted to be thermodynamically favorable ($\Delta\mathrm{G} = -25\mathrm{kJ\,mol^{-1}}$; Martens and Berner, 1977; Reeburgh, 2007). How-

ever, it was not until 1994 that a syntrophic association between methanogens and sulfate-reducing bacteria was predicted in methane-rich coastal sediments (Hoehler et al., 1994). In 1999, the first 16S rRNA and lipid biomarker signatures of anaerobic methanotrophic archaea were recognized in methane-oxidizing and sulfate-reducing consortia (Hinrichs et al., 1999) were found to be the methane-oxidizing microbes in such consortia. Soon after, it was found that two distinct archaeal lineages (ANME-1 and ANME-2), related to the order *Methanosarcinales*, are consistently associated with methane seep marine sediments, and that ANME-2 forms aggregates with *Desulfobacterota* (former *Deltaproteobacteria*) SRB (Orphan et al., 2001). In seep sediments, these aggregates range from $1\,\mathrm{to}11\,\mu\mathrm{m}$ in diameter with an average of $3.2 \pm 1.5\,\mu\mathrm{m}$, and may reach abundances of $10^7\,\mathrm{cm}^{-3}$ (Boetius et al., 2000). Our observations, as well as other reports (Marlow et al., 2021), show that they can be much larger in carbonate rocks, reaching sizes up to $\sim 100\,\mu\mathrm{m}$. These studies were able to identify the specific archaea and sulfate-reducing bacteria in the consortia thanks to fluorescence in situ hybridization (FISH), a technique that utilizes fluorescently-labelled oligonucleotide probes based on partial 16S rRNA sequences to target specific microbes (Amann et al., 1990).

Despite accelerated research on ANME-SRB over the last two and a half decades since their discovery in methane seep sediments, very little research has focused on AOM-related microbe-mineral interactions and the potential for the preservation of their biomass in authigenic carbonates. Chen et al. (2014) noted that ANME-2-SRB aggregates in sediments, identified with FISH, are often surrounded with a thick organic matrix, and are associated with silica-rich phases cements and clay minerals. Marlow et al. (2021) was the first study to visualize FISH-confirmed ANME-2-SRB aggregates in situ in seep carbonates. Himmler et al. (2022) reported putative microfossils of AOM-SR mediating microbes in modern seep carbonates, based uniquely on morphology and isotopic compositions of carbonate. Many reported

microbial fossils have been identified in chert, which is composed entirely of primary silica (e.g. Dodd et al., 2017; Schopf et al., 2017; Walsh and Lowe, 1985), and is thought to be key for the adequate structural and chemical preservation of the fossils (Alleon et al., 2016). Recent studies have tried to identify the potential of microbes to induce the precipitation of silica and what is the mechanism behind it (Moore et al., 2021; Moore et al., 2020). However, the potential of ANME-SRB and specifically, of ANME-2-SRB aggregates, to actively induce silica biomineralizations has not been adequately investigated. Chapters 5 and 6 of this thesis focus on exploring whether ANME-2-SRB aggregates actively precipitate amorphous silica, and whether this could enhance their preservation as microfossils in seep carbonates, thus allowing their identification in ancient seep carbonates.

In Chapter 5, we assess the composition of the mineral phases that associate with ANME-2-SRB aggregates incubated with and without sediments, in media undersaturated with respect to silica. We found that ANME-2-SRB aggregates are consistently associated with silica, and that the treatments without sediment had lower Si:Al and Si:Al+Mg than treatments with sediment. Further observation of this silica phase allowed to establish that it often manifests as rims surrounding the microbial aggregates, and that it is much more depleted in cations like aluminum, iron, and magnesium compared to typical clay mineral compositions. A similar association with silica was identified in modern methane seep carbonates, in which ANME-2-SRB aggregates were confirmed with FISH. We thus provide the first evidence for the production of an amorphous silica precipitate that surrounds ANME-2-SRB consortia both in AOM enrichments and carbonate rocks. The fact that this phase 1) forms in the presence of ANME-2-SRB aggregates in media undersaturated with respect to silica, 2) is strongly depleted in cations, and 3) no genes previously attributed to silica precipitation were found in ANME and SRB genomes, suggests a different silica precipitation mechanism.

In Chapter 6, we use the silica proxy in combination with analytical techniques, such as electron microscopy, energy-dispersive X-ray spectroscopy (EDS), Raman spectroscopy, and carbon isotope compositions to better characterize ANME-2-SRB aggregates in modern carbonates and to identify them in ancient seep carbonates. We utilize Cretaceous seep carbonates from Colorado (Tepee Buttes; Campanian-Lower Maastrichtian - ~ 76 Mya-) and California (Panoche Hills; Danian - ~ 65 Mya-) and Bear Creek (Valanginian- ~ 135 Mya-) as search materials for potential fossilized ANME-SRB aggregates. We found some candidate ANME-SRB aggregates in the Tepee Buttes seep carbonates, that seem to be entombed in the carbonate matrix and are associated with silica, have low $\delta^{13}\mathrm{C}$ values, and have similar Raman and EDS spectra to modern ANME-2-SRB aggregates confirmed with FISH. To our knowledge, this constitutes the first report of potential microfossils in carbonates, in which early silica entombment may have favored morphological and organic preservation. We recommend the use of comparative approaches between modern and ancient materials, as well as a combination of the microscopy and analytical techniques that we utilized here, to find microfossils of ANME-SRB aggregates in the carbonate rock record, as well as in extraterrestrial bodies where methane emissions may have occurred.

References

Alleon, J., Bernard, S., Le Guillou, C., Daval, D., Skouri-Panet, F., Pont, S., Delbes, L., & Robert, F. (2016). Early entombment within silica minimizes the molecular degradation of microorganisms during advanced diagenesis. *Chemical Geology*, *437*, 98–108. https://doi.org/10.1016/j.chemgeo.2016.05.034

Aloisi, G., Bouloubassi, I., Heijs, S. K., Pancost, R. D., Pierre, C., Sinninghe Damsté, J. S., Gottschal, J. C., Forney, L. J., & Rouchy, J.-M. (2002). CH4-consuming microorganisms and the formation of carbonate crusts at cold seeps. *Earth and Planetary Science Letters*, *203*(1), 195–203. https://doi.org/10.1016/S0012-821X(02)00878-6

Amann, R. I., Krumholz, L., & Stahl, D. A. (1990). Fluorescent-oligonucleotide probing of whole cells for determinative, phylogenetic, and environmental studies in microbiology. *Journal of bacteriology*, *172*(2), 762–770.

Barnes, R. O., & Goldberg, E. D. (1976). Methane production and consumption in anoxic marine sediments. *Geology*, *4*(5), 297–300. https://doi.org/10.1130/0091-7613(1976)4<297:MPACIA>2.0.CO;2

Bekker, A., Holland, H. D., Wang, P. L., Rumble, D., Stein, H. J., Hannah, J. L., Coetzee, L. L., & Beukes, N. J. (2004). Dating the rise of atmospheric oxygen. *Nature*, *427*(6970), 117–120. https://doi.org/10.1038/nature02260

Berner, R. A. (1984). Sedimentary pyrite formation: An update. *Geochimica et Cosmochimica Acta*, *48*(4), 605–615. https://doi.org/10.1016/0016-7037(84)90089-9

Berner, R. A., & Raiswell, R. (1983). Burial of organic carbon and pyrite sulfur in sediments over phanerozoic time: a new theory. *Geochimica et Cosmochimica Acta*, *47*(5), 855–862. https://doi.org/10.1016/0016-7037(83)90151-5

Blättler, C. L., Claire, M. W., Prave, A. R., Kirsimäe, K., Higgins, J. A., Medvedev, P. V., Romashkin, A. E., Rychanchik, D. V., Zerkle, A. L., & Paiste, K. (2018). Two-billion-year-old evaporites capture Earth's great oxidation. *Science*, *360*(6386), 320–323.

Boetius, A., Ravenschlag, K., Schubert, C. J., Rickert, D., Widdel, F., Gieseke, A., Amann, R., Jørgensen, B. B., Witte, U., & Pfannkuche, O. (2000). A marine microbial consortium apparently mediating anaerobic oxidation of methane. *Nature*, *407*, 623.

Bohrmann, G., Greinert, J., Suess, E., & Torres, M. (1998). Authigenic carbonates from the Cascadia subduction zone and their relation to gas hydrate stability. *Geology*, *26*(7), 647–650. https://doi.org/10.1130/0091-7613(1998)026<0647:ACFTCS>2.3.CO;2

Bottrell, S. H., & Newton, R. J. (2006). Reconstruction of changes in global sulfur cycling from marine sulfate isotopes. *Earth-Science Reviews*, *75*(1-4), 59–83. https://doi.org/10.1016/j.earscirev.2005.10.004

Brune, D. C. (1989). Sulfur oxidation by phototrophic bacteria. *BBA - Bioenergetics*, *975*(2), 189–221. https://doi.org/10.1016/S0005-2728(89)80251-8

Brunner, B., & Bernasconi, S. M. (2005). A revised isotope fractionation model for dissimilatory sulfate reduction in sulfate reducing bacteria. *Geochimica et Cosmochimica Acta*, *69*(20), 4759–4771. https://doi.org/10.1016/j.gca.2005.04.015

Bullock, H. A., Luo, H., & Whitman, W. B. (2017). Evolution of dimethylsulfoniopropionate metabolism in marine phytoplankton and bacteria. *Frontiers in microbiology*, *8*, 637.

Campbell, K. A., Farmer, J. D., & Des Marais, D. (2002). Ancient hydrocarbon seeps from the Mesozoic convergent margin of California.pdf. *Geofluids*, *2*, 63–94.

Campbell, K. A. (2006). Hydrocarbon seep and hydrothermal vent paleoenvironments and paleontology: Past developments and future research directions. *Palaeogeography, Palaeoclimatology, Palaeoecology*, *232*(2-4), 362–407. https://doi.org/10.1016/J.PALAEO.2005.06.018

Canfield, D. E. (2001). Biogeochemistry of sulfur isotopes. *Reviews in Mineralogy and Geochemistry*, *43*(1), 607–636.

Canfield, D. E., & Thamdrup, B. (1994). The production of 34S-depleted sulfide during bacterial disproportionation of elemental sulfur. *Science*, *266*, 1973–1975. https://doi.org/10.1126/science.11540246

Canfield, D. E., Stewart, F. J., Thamdrup, B., De Brabandere, L., Dalsgaard, T., Delong, E. F., Revsbech, N. P., & Ulloa, O. (2010). A cryptic sulfur cycle in oxygen-minimum-zone waters off the Chilean coast. *Science*, *330*(6009), 1375–1378. https://doi.org/10.1126/science.1196889

Canfield, D. E. (2004). The evolution of the Earth surface sulfur reservoir. *American Journal of Science*, *304*(10), 839–861.

Chambers, L. A., Trudinger, P. A., Smith, J. W., & Burns, M. S. (1975). Fractionation of sulfur isotopes by continuous cultures of Desulfovibrio desulfuricans. *Canadian Journal of Microbiology*, *21*(10), 1602–1607.

Chen, Y., Li, Y. L., Zhou, G. T., Li, H., Lin, Y. T., Xiao, X., & Wang, F. P. (2014). Biomineralization mediated by anaerobic methane-consuming cell consortia. *Scientific Reports*, *4*, 1–9. https://doi.org/10.1038/srep05696

Crowe, S. A., Cox, R. P., Jones, C. A., Fowle, D. A., Santibañez-Bustos, J. F., Ulloa, O., & Canfield, D. E. (2018). Decrypting the sulfur cycle in oceanic oxygen minimum zones. *ISME Journal*, *12*(9), 2322–2329. https://doi.org/10.1038/s41396-018-0149-2

Crowe, S. A., Paris, G., Katsev, S., Jones, C. A., Kim, S. T., Zerkle, A. L., Nomosatryo, S., Fowle, D. A., Adkins, J. F., Sessions, A. L., Farquhar, J., & Canfield, D. E. (2014). Sulfate was a trace constituent of Archean seawater. *Science*, *346*(6210), 735–739. https://doi.org/10.1126/science.1258966

Dixon, J. L., Hopkins, F. E., Stephens, J. A., & Schäfer, H. (2020). Seasonal changes in microbial dissolved organic sulfur transformations in coastal waters. *Microorganisms*, *8*(3), 1–20. https://doi.org/10.3390/microorganisms8030337

Dodd, M. S., Papineau, D., Grenne, T., Slack, J. F., Rittner, M., Pirajno, F., O'Neil, J., & Little, C. T. (2017). Evidence for early life in Earth's oldest hydrothermal vent precipitates. *Nature*, *543*(7643), 60–64. https://doi.org/10.1038/nature21377

Durbin, A. M., & Teske, A. (2011). Microbial diversity and stratification of South Pacific abyssal marine sediments. *Environmental Microbiology*, *13*(12), 3219–3234. https://doi.org/10.1111/j.1462-2920.2011.02544.x

Elsgaard, L., & Jørgensen, B. B. (1992). Anoxic transformations of radiolabeled hydrogen sulfide in marine and freshwater sediments. *Geochimica et Cosmochimica Acta*, *56*(6), 2425–2435.

Elvert, M., Suess, E., & Whiticar, M. J. (1999). Anaerobic methane oxidation associated with marine gas hydrates: superlight C-isotopes from saturated and unsaturated C20 and C25 irregular isoprenoids. *Naturwissenschaften*, *86*(6), 295–300.

Emerson, S., Jahnke, R., Bender, M., Froelich, P., Klinkhammer, G., Bowser, C., & Setlock, G. (1980). Early diagenesis in sediments from the eastern equatorial Pacific, I. Pore water nutrient and carbonate results. *Earth and Planetary Science Letters*, *49*(1), 57–80. https://doi.org/10.1016/0012-821X(80)90150-8

Farquhar, J., Bao, H., & Thiemens, M. (2000). Atmospheric Influence of Earth's Earliest Sulfur Cycle. *Science*, *289*(5480), 756–758. https://doi.org/10.1126/science.289.5480.756

Fike, D. A., Bradley, A. S., & Rose, C. V. (2015). Rethinking the ancient sulfur cycle. *Annual Review of Earth and Planetary Sciences*, *43*, 593–622.

Findlay, A. J., & Kamyshny, A. (2017). Turnover rates of intermediate sulfur species (Sx2-, S0, S2O32-, S4O62-, SO32-) in anoxic freshwater and sediments. *Frontiers in Microbiology*, *8*, 2551. https://doi.org/10.3389/fmicb.2017.02551

Friedrich, C. G., Rother, D., Bardischewsky, F., Quentmeier, A., & Fischer, J. (2001). Oxidation of Reduced Inorganic Sulfur Compounds by Bacteria.pdf. *Applied and Environmental Microbiology*, *67*(7), 2873–2882. https://doi.org/10.1128/AEM.67.7.2873

Froelich, P. N., Klinkhammer, G. P., Bender, M. L., Luedtke, N. A., Heath, G. R., Cullen, D., Dauphin, P., Hammond, D., Hartman, B., & Maynard, V. (1979). Early oxidation of organic matter in pelagic sediments of the eastern equatorial Atlantic: suboxic diagenesis. *Geochimica et Cosmochimica Acta*, *43*(7), 1075–1090. https://doi.org/10.1016/0016-7037(79)90095-4

Garrels, R. M., & Lerman, A. (1981). Phanerozoic cycles of sedimentary carbon and sulfur. *Proceedings of the National Academy of Sciences*, *78*(8), 4652–4656. https://doi.org/10.1073/pnas.78.8.4652

Grotzinger, J. P. (1989). Facies and Evolution of Precambrian Carbonate Depositional Systems: Emergence of the Modern Platform Archetype. In P. D. Crevello, J. L. Wilson, J. F. Sarg, & J. F. Read (Eds.), *Sepm special publication n. 41: Controls on carbonate platforms and basin development*.

Grotzinger, J. P., & James, N. P. (2000). Precambrian Carbonates: Evolution of Understanding. In J. P. Grotzinger & N. P. James (Eds.), *Sepm special publication: Carbonate sedimentation and diagenesis in the evolving precambrian world*.

Grotzinger, J. P., & Kasting, J. F. (1993). New constraints on Precambrian ocean composition. *The Journal of Geology*, *101*(2), 235–243.

Habicht, K. S., & Canfield, D. E. (1997). Sulfur isotope fractionation during bacterial sulfate reduction in organic-rich sediments. *Geochimica et Cosmochimica Acta*, *61*(24), 5351–5361. https://doi.org/10.1016/S0016-7037(97)00311-6

Habicht, K. S., Gade, M., Thamdrup, B., Berg, P., & Canfield, D. E. (2002). Calibration of sulfate levels in the Archean ocean. *Science*, *298*(5602), 2372–2374. https://doi.org/10.1126/science.1078265

Harrison, A. G., & Thode, H. G. (1958). Mechanism of the bacterial reduction of sulphate from isotope fractionation studies. *Transactions of the Faraday Society*, *54*, 84–92.

Himmler, T., Crémière, A., Birgel, D., Wirth, R., Orphan, V. J., Kirsimäe, K., Knies, J., Peckmann, J., & Lepland, A. (2022). Putative fossils of chemotrophic microbes preserved in seep carbonates from Vestnesa Ridge, off northwest Svalbard, Norway. *Geology*, *50*(2), 169–173. https://doi.org/10.1130/g49620.1

Hinrichs, K.-U., Hayes, J. M., Sylva, S. P., Brewer, P. W., & Delong, E. (1999). Methane-consuming archaebacteria in marine sediments. *Nature*, *398*, 802–805.

Hinrichs, K.-U., & Boetius, A. (2013). The Anaerobic Oxidation of Methane: New Insights in Microbial Ecology and Biogeochemistry. *Ocean Margin Systems*, 457–477. https://doi.org/10.1007/978-3-662-05127-6_28

Hoehler, T. M., Alperin, M. J., Albert, D. B., & Martens, C. S. (1994). Field and laboratory, evidence for a methane-sulfate reducer consortium.pdf. *Global Biogeochemical Cycles*, *8*(4), 451–463.

Hoek, J., Reysenbach, A.-L., Habicht, K. S., & Canfield, D. E. (2006). Effect of hydrogen limitation and temperature on the fractionation of sulfur isotopes by a deep-sea hydrothermal vent sulfate-reducing bacterium. *Geochimica et Cosmochimica Acta*, *70*(23), 5831–5841. https://doi.org/10.1016/j.gca.2006.07.031

Holland, H. D. (1973). Systematics of the isotopic composition of sulfur in the oceans during the Phanerozoic and its implications for atmospheric oxygen. *Geochimica et Cosmochimica Acta*, *37*(12), 2605–2616. https://doi.org/10.1016/0016-7037(73)90268-8

Holland, H. D. (2002). Volcanic gases, black smokers, and the Great Oxidation Event. *Geochimica et Cosmochimica acta*, *66*(21), 3811–3826.

Holler, T., Wegener, G., Niemann, H., Deusner, C., Ferdelman, T. G., Boetius, A., Brunner, B., & Widdel, F. (2011). Carbon and sulfur back flux during anaerobic microbial oxidation of methane and coupled sulfate reduction. *Proceedings of the National Academy of Sciences*, *108*(52), E1484–E1490.

Jones, G. E., & Starkey, R. L. (1957). Fractionation of stable isotopes of sulfur by microorganisms and their role in deposition of native sulfur. *Applied microbiology*, *5*(2), 111–118.

Jørgensen, B. B. (1990). A thiosulfate shunt in the sulfur cycle of marine sediments. *Science*, *249*(4965), 152–154. https://doi.org/10.1126/science.249.4965.152

Jørgensen, B. B. (1982). Mineralization of organic matter in the sea bed - the role of sulphate reduction. *Nature*, *296*(5858), 643–645.

Jørgensen, B. B., Findlay, A. J., & Pellerin, A. (2019). The Biogeochemical Sulfur Cycle of Marine Sediments. *Frontiers in Microbiology*, *10*(April), 1–27. https://doi.org/10.3389/fmicb.2019.00849

Kaplan, I. R., & Rittenberg, S. C. (1964). Microbiological Fractionation of Sulphur Isotopes. *Journal of General Microbiology*, *34*(2), 195–212. https://doi.org/10.1099/00221287-34-2-195

Kendall, C., & Caldwell, E. A. (1998). Fundamentals of Isotope Geochemistry. In C. Kendall & J. McDonnell (Eds.), *Isotope tracers in catchment hydrology* (pp. 51–86). Elsevier. https://doi.org/10.1016/B978-0-444-81546-0.50009-4

Kiene, R. P., Linn, L. J., & Bruton, J. A. (2000). New and important roles for DMSP in marine microbial communities. *Journal of Sea Research*, *43*(3-4), 209–224. https://doi.org/10.1016/S1385-1101(00)00023-X

Klinkhammer, G. P. (1980). Early diagenesis in sediments from the eastern equatorial Pacific, II. Pore water metal results. *Earth and Planetary Science Letters*, *49*(1), 81–101. https://doi.org/10.1016/0012-821X(80)90151-X

Knittel, K., & Boetius, A. (2009). Anaerobic Oxidation of Methane: Progress with an Unknown Process. *Annual Review of Microbiology*, *63*(1), 311–334. https://doi.org/10.1146/annurev.micro.61.080706.093130

Krämer, M., & Cypionka, H. (1989). Sulfate formation via ATP sulfurylase in thiosulfate-and sulfite-disproportionating bacteria. *Archives of microbiology*, *151*, 232–237.

Ksionzek, K. B., Lechtenfeld, O. J., McCallister, S. L., Schmitt-Kopplin, P., Geuer, J. K., Geibert, W., & Koch, B. P. (2016). Dissolved organic sulfur in the ocean: Biogeochemistry of a petagram inventory. *Science*, *354*(6311), 456–459.

Leavitt, W. D., Halevy, I., Bradley, A. S., & Johnston, D. T. (2013). Influence of sulfate reduction rates on the Phanerozoic sulfur isotope record. *Proceedings of the National Academy of Sciences*, *110*(28), 11244–11249.

Levine, N. M. (2016). Putting the spotlight on organic sulfur. *Science*, *354*(6311), 418–419. https://doi.org/10.1126/science.aai8650

Levine, N. M., Varaljay, V. A., Toole, D. A., Dacey, J. W. H., Doney, S. C., & Moran, M. A. (2012). Environmental, biochemical and genetic drivers of DMSP degradation and DMS production in the Sargasso Sea. *Environmental microbiology*, *14*(5), 1210–1223.

Long, A. M., Jurgensen, S. K., Petchel, A. R., Savoie, E. R., & Brum, J. R. (2021). Microbial Ecology of Oxygen Minimum Zones Amidst Ocean Deoxygenation. *Frontiers in Microbiology*, *12*(October), 1–18. https://doi.org/10.3389/fmicb.2021.748961

Lovley, D. (2006). Dissimilatory Fe(III)- and Mn(IV)-reducing prokaryotes. In M. Dworkin, S. Falkow, E. Rosenberg, K.-H. Schleifer, & E. Stackebrandt (Eds.), *Prokaryotes 2* (pp. 635–658).

Loyd, S. J., Sample, J., Tripati, R. E., Defliese, W. F., Brooks, K., Hovland, M., Torres, M., Marlow, J., Hancock, L. G., Martin, R., Lyons, T., & Tripati, A. E. (2016). Methane seep carbonates yield clumped isotope signatures out of equilibrium with formation temperatures. *Nature Communications*, *7*, 1–12. https://doi.org/10.1038/ncomms12274

Luo, G., Ono, S., Beukes, N. J., Wang, D. T., Xie, S., & Summons, R. E. (2016). Rapid oxygenation of Earth's atmosphere 2.33 billion years ago. *Science Advances*, *2*(5), 1–10. https://doi.org/10.1126/sciadv.1600134

Marlow, J. J., Hoer, D., Jungbluth, S. P., Reynard, L. M., Gartman, A., Chavez, M. S., El-Naggar, M. Y., Tuross, N., Orphan, V. J., & Girguis, P. R. (2021). Carbonate-hosted microbial communities are prolific and pervasive methane oxidizers at geologically diverse marine methane seep sites. *Proceedings of the National Academy of Sciences*, *118*(25), e2006857118.

Martens, C. S., & Berner, R. A. (1974). Methane production in the interstitial waters of sulfate-depleted marine sediments. *Science*, *185*(4157), 1167–1169.

Martens, C. S., & Berner, R. A. (1977). Interstitial water chemistry of anoxic Long Island Sound sediments. 1. Dissolved gases 1. *Limnology and Oceanography*, *22*(1), 10–25.

Michaelis, W., Seifert, R., Nauhaus, K., Treude, T., Thiel, V., Blumenberg, M., Knittel, K., Gieseke, A., Peterknecht, K., Pape, T., Boetius, A., Amann, R., Jørgensen, B. B., Widdel, F., Peckmann, J., Pimenov, N. V., & Gulin, M. B. (2002). Microbial Reefs in the Black Sea Fueled by Anaerobic Oxidation of Methane. *Science*, *297*(5583), 1013 LP –1015. https://doi.org/10.1126/science.1072502

Moore, K. R., Gong, J., Pajusalu, M., Skoog, E. J., Xu, M., Feliz Soto, T., Sojo, V., Matreux, T., Baldes, M. J., Braun, D., Williford, K., & Bosak, T. (2021). A new model for silicification of cyanobacteria in Proterozoic tidal flats. *Geobiology*, *19*(5), 438–449. https://doi.org/10.1111/gbi.12447

Moore, K. R., Pajusalu, M., Gong, J., Sojo, V., Matreux, T., Braun, D., & Bosak, T. (2020). Biologically mediated silicification of marine cyanobacteria and implications for the Proterozoic fossil record. *Geology*, *48*(9), 862–866. https://doi.org/10.1130/G47394.1

Moran, M. A., & Durham, B. P. (2019). Sulfur metabolites in the pelagic ocean. *Nature Reviews Microbiology*, *17*(11), 665–678. https://doi.org/10.1038/s41579-019-0250-1

Morris, A. W., & Riley, J. P. (1966). The bromide / chlorinity and sulphate / chlorinity ratio in sea water. *Deep Sea Research*, *13*, 699–705.

Naehr, T. H., Eichhubl, P., Orphan, V. J., Hovland, M., Paull, C. K., Ussler, W., Lorenson, T. D., & Greene, H. G. (2007). Authigenic carbonate formation at hydrocarbon seeps in continental margin sediments : A comparative study. *Deep Sea Research Part II: Topical Studies in Oceanography*, *54*, 1268–1291. https://doi.org/10.1016/j.dsr2.2007.04.010

Olejarz, J., Iwasa, Y., Knoll, A. H., & Nowak, M. A. (2021). The Great Oxygenation Event as a consequence of ecological dynamics modulated by planetary change. *Nature Communications*, *12*(1), 3985. https://doi.org/10.1038/s41467-021-23286-7

Orphan, V. J., Hinrichs, K.-U., Ussler, W., Paull, C. K., Taylor, L. T., Sylva, S. P., Hayes, J. M., & DeLong, E. F. (2001). Comparative analysis of methane-oxidizing archaea and sulfate-reducing bacteria in anoxic marine sediments. *Applied and Environmental Microbiology*, *67*(4), 1922–1934.

Patron, N. J., Durnford, D. G., & Kopriva, S. (2008). Sulfate assimilation in eukaryotes: Fusions, relocations and lateral transfers. *BMC Evolutionary Biology*, *8*(1), 1–14. https://doi.org/10.1186/1471-2148-8-39

Pearson, A., Hurley, S. J., Walter, S. R. S., Kusch, S., Lichtin, S., & Zhang, Y. G. (2016). Stable carbon isotope ratios of intact GDGTs indicate heterogeneous sources to marine sediments. *Geochimica et Cosmochimica Acta*, *181*, 18–35. https://doi.org/10.1016/j.gca.2016.02.034

Peckmann, J., Goedert, J. L., Thiel, V., Michaelis, W., & Reitner, J. (2002). A comprehensive approach to the study of methane-seep deposits from the Lincoln Creek Formation, western Washington State, USA. *Sedimentology*, *49*(4), 855–873. https://doi.org/10.1046/j.1365-3091.2002.00474.x

Pellerin, A., Antler, G., Holm, S. A., Findlay, A. J., Crockford, P. W., Turchyn, A. V., Jørgensen, B. B., & Finster, K. (2019). Large sulfur isotope fractionation by bacterial sulfide oxidation. *Science Advances*, *5*, eaaw1480.

Pjevac, P. (2014). *Co-existence and niche differentiation of sulfur oxidizing bacteria in marine environments* (Doctoral dissertation). University of Bremen, Bremen, Germany.

Reeburgh, W. S. (2007). Oceanic Methane Biogeochemistry. *Chemical Reviews*, *107*(2), 486–513. https://doi.org/10.1021/cr050362v

Reisch, C. R., Moran, M. A., & Whitman, W. B. (2011). Bacterial catabolism of dimethylsulfoniopropionate (DMSP). *Frontiers in microbiology*, *2*, 172.

Ritger, S., Carson, B., & Suess, E. (1987). Methane-derived authigenic carbonates formed by subduction-induced pore-water expulsion along the Oregon/Washington margin. *GSA Bulletin*, *98*(2), 147–156.

Roden, E. E., & Lovley, D. R. (1993). Dissimilatory Fe (III) reduction by the marine microorganism Desulfuromonas acetoxidans. *Applied and Environmental Microbiology*, *59*(3), 734–742.

Roy, S. (2006). Sedimentary manganese metallogenesis in response to the evolution of the Earth system. *Earth-Science Reviews*, *77*(4), 273–305. https://doi.org/10.1016/j.earscirev.2006.03.004

Saito, K. (2004). Sulfur assimilatory metabolism. The long and smelling road. *Plant Physiology*, *136*(1), 2443–2450. https://doi.org/10.1104/pp.104.046755

Schippers, A., & Jørgensen, B. B. (2001). Oxidation of pyrite and iron sulfide by manganese dioxide in marine sediments. *Geochimica et Cosmochimica Acta*, *65*(6), 915–922.

Schopf, J. W., Kitajima, K., Spicuzza, M. J., Kudryavtsev, A. B., & Valley, J. W. (2017). SIMS analyses of the oldest known assemblage of microfossils document their taxon-correlated carbon isotope compositions. *Proceedings of the National Academy of Sciences*, *115*(1), 53–58. https://doi.org/10.1073/pnas.1718063115

Stoiber, R. E., Williams, S. N., & Huebert, B. (1987). Annual contribution of sulfur dioxide to the atmosphere by volcanoes. *Journal of Volcanology and Geothermal Research*, *33*(1-3), 1–8.

Taipale, S. J., Peltomaa, E., Hiltunen, M., Jones, R. I., Hahn, M. W., Biasi, C., & Brett, M. T. (2015). Inferring Phytoplankton, Terrestrial Plant and Bacteria Bulk $\delta^{13}C$ Values from Compound Specific Analyses of Lipids and Fatty Acids. *PLOS ONE*, *10*(7), e0133974.

Thamdrup, B. O., Finster, K., Hansen, J. W., & Bak, F. (1993). Bacterial disproportionation of elemental sulfur coupled to chemical reduction of iron or manganese. *Applied and environmental microbiology*, *59*(1), 101–108.

Thorup, C., Schramm, A., Findlay, A. J., Finster, K. W., & Schreiber, L. (2017). Disguised as a sulfate reducer: Growth of the deltaproteobacterium Desulfurivibrio alkaliphilus by Sulfide Oxidation with Nitrate. *mBio*, *8*(4), 1–9. https://doi.org/10.1128/mBio.00671-17

Trudinger, P. A., & Chambers, L. A. (1973). Reversibility of bacterial sulfate reduction and its relevance to isotope fractionation. *Geochimica et Cosmochimica Acta*, *37*(7), 1775–1778. https://doi.org/10.1016/0016-7037(73)90162-2

Varaljay, V. A., Robidart, J., Preston, C. M., Gifford, S. M., Durham, B. P., Burns, A. S., Ryan, J. P., Marin, R., Kiene, R. P., Zehr, J. P., Scholin, C. A., Moran, M. A., Marin III, R., Kiene, R. P., & Zehr, J. P. (2015). Single-taxon field measurements of bacterial gene regulation controlling DMSP fate. *ISME Journal*, *9*(7), 1677–1686. https://doi.org/10.1038/ismej.2015.23

Veizer, J., Holser, W. T., & Wilgus, C. K. (1980). Correlation of 13C12C and 34S32S secular variations. *Geochimica et Cosmochimica Acta*, *44*(4), 579–587.

Von Damm, K. L. (1990). Seafloor hydrothermal activity: black smoker chemistry and chimneys. *Annual Review of Earth and Planetary Sciences*, *18*(1), 173–204.

Vorobev, A., Dupouy, M., Carradec, Q., Delmont, T., Annamale, A., Wincker, P., & Pelletier, E. (2020). Transcriptome reconstruction and functional analysis of eukaryotic marine plankton communities via high-throughput metagenomics and metatranscriptomics. *Genome Research*, *30*(4), 647–659. https://doi.org/10.1101/gr.253070.119

Walsh, M. M., & Lowe, D. R. (1985). Filamentous microfossils from the 3,500-Myr-old Onverwacht Group, Barberton Mountain Land, South Africa. *Nature*, *314*, 530–532.

Wegener, G., Niemann, H., Elvert, M., Hinrichs, K. U., & Boetius, A. (2008). Assimilation of methane and inorganic carbon by microbial communities mediating the anaerobic oxidation of methane. *Environmental Microbiology*, *10*(9), 2287–2298. https://doi.org/10.1111/j.1462-2920.2008.01653.x

Whiticar, M. J. (1999). Carbon and hydrogen isotope systematics of bacterial formation and oxidation of methane. *Chemical Geology*, *161*(1), 291–314. https://doi.org/10.1016/S0009-2541(99)00092-3

Wing, B. A., & Halevy, I. (2014). Intracellular metabolite levels shape sulfur isotope fractionation during microbial sulfate respiration. *Proceedings of the National Academy of Sciences*, *111*(51), 18116–18125. https://doi.org/10.1073/pnas.1407502111

Zopfi, J., Ferdelman, T. G., & Fossing, H. (2004). Distribution and fate of sulfur intermediates - Sulfite, tetrathionate, thiosulfate, and elemental sulfur - In marine sediments. *Special Paper of the Geological Society of America*, *379*, 97–116. https://doi.org/10.1130/0-8137-2379-5.97

Zubkov, M. V., Fuchs, B. M., Archer, S. D., Kiene, R. P., Amann, R., & Burkill, P. H. (2002). Rapid turnover of dissolved DMS and DMSP by defined bacterioplankton communities in the stratified euphotic zone of the North Sea. *Deep-Sea Research Part II: Topical Studies in Oceanography*, *49*(15), 3017–3038. https://doi.org/10.1016/S0967-0645(02)00069-3

Part I: Sulfur isotopes are important proxies for the microbial cycling of organic and inorganic sulfur

Chapter 2

SULFUR ISOTOPE FRACTIONATIONS CONSTRAIN THE BIOLOGICAL CYCLING OF DIMETHYLSULFONIOPROPIONATE (DMSP) IN THE UPPER OCEAN

Daniela Osorio-Rodriguez[1], Manuel Razo-Mejia[2], Nathan F. Dalleska[1], Alex L. Sessions[1], Victoria J. Orphan[1], Jess F. Adkins[1]

[1]Division of Geological and Planetary Sciences, California Institute of Technology, Pasadena, CA, 91125
[2]Division of Biology and Biological Engineering, California Institute of Technology, Pasadena, CA 91125, USA

Osorio-Rodriguez, D., Razo-Mejia, M., Dalleska, N. F., Sessions, A. L., Orphan, V. J., Adkins, J. F. (2021). "Sulfur isotope fractionations constrain the biological cycling of dimethylsulfoniopropionate in the upper ocean". *Limnology and Oceanography* 66(10), pp.3607-3618. DOI: 10.1002/lno.11901.

Abstract

The rapid turnover of dimethylsulfoniopropionate (DMSP), the most abundant dissolved organic sulfur (DOS) compound in the ocean, makes it pivotal to understand the cycling of organic sulfur. DMSP is mostly synthesized by phytoplankton and it can be utilized as a carbon and sulfur source by marine bacteria or cleaved by bacteria or algae to produce the volatile compound dimethylsulfide (DMS), involved in the formation of sulfate aerosols. The fluxes between the consumption (i.e. demethylation) and cleavage pathways are thought to depend on community interactions and the sulfur demand. However, a quantitative assessment on the sulfur partitioning between each of these pathways is still missing. Here, we report for the first time the sulfur isotope fractionations by enzymes involved in DMSP degradation with different catalytic mechanisms. We show that the residual DMSP from the demethy-

lation pathway is 2.7‰ enriched in δ^{34}S relative to the initial DMSP, and that the fractionation factor ($^{34}\varepsilon$) of the cleavage pathways varies between -1 and –9‰. The incorporation of these fractionation factors into mass balance calculations constrains the biological fates of DMSP in seawater, supports the notion that demethylation dominates over cleavage in marine environments, and could be used as a proxy for the switch from demethylation to cleavage in marine microbial communities.

1. INTRODUCTION

Dissolved organic sulfur (DOS) is comprised of 432 identified compounds (Tang, 2020), and up to 800 compounds predicted by mass and structure (Ksionzek et al., 2016). Dimethylsulfoniopropionate (DMSP) is the most abundant of these DOS species, contributing 2.3 % of the minimum estimated marine DOS (Ksionzek et al., 2016) at an average concentration of 16.9 ± 22.2 nM, with a median of 9.8 nM (Kettle et al., 1999). DMSP is mainly produced by marine phytoplankton, has a turnover of hours to days (Levine, 2016; Zubkov et al., 2002), and has been hypothesized to be involved in different physiological functions, including protection from cold (Karsten et al., 1996; Kirst et al., 1991), osmotic (Dickson and Kirst, 1987), and oxidative stresses (Sunda et al., 2002). One of the biological degradation products of DMSP, dimethylsulfide (DMS), gathered atmospheric chemistry research attention on volatile DOS more than 30 years ago, when its potential to influence global climate by means of aerosol formation was first pointed out (Charlson et al., 1987). The so-called CLAW hypothesis predicted a negative climate feedback where Earth's temperature would be regulated by the interaction between sulfur emissions from phytoplankton and cloud formation. Although DMS emissions might actually not be significant for global climate regulation under a warming scenario (i.e. Quinn and Bates, 2011), they are expected to alter the regional formation of sulfate aerosols (Sanchez et al., 2018), with potential impacts on the weather at high latitudes (S.

Wang et al., 2018).

Beyond DMS, DOS is usually disregarded by sulfur biogeochemists because its abundance in seawater is exceeded by six orders of magnitude by that of sulfate (Ksionzek et al., 2016), which has a concentration of 28 mM (Morris and Riley, 1966). The fact that sulfate is an important electron acceptor, responsible for the remineralization of up to half of the organic matter in coastal sediments (Jørgensen, 1982), and that it leaves a fingerprint in the rock record as sulfate or sulfide (its reduction product) minerals, has made it central in the study of the geologic sulfur cycle (Garrels and Lerman, 1981). Nonetheless, the slow turnover of sulfate, which has a residence time of $\sim 10^7$ years in the ocean (Holland, 1973), highlights the relevance of addressing the dynamics of highly labile DOS, such as DMSP and DMS, toward a comprehensive understanding of the short scale processes that may affect the sulfur cycle. Reduced sulfur, and in particular DOS, might also be fundamental to understand the sulfur cycle during the Archaean, where oxygen and sulfate concentrations were negligible (Fakhraee and Katsev, 2019).

Recently, microbial ecologists have rekindled interest in DMSP as the role of DOS in ecosystem dynamics has been highlighted (Levine, 2016). DMSP and DMS have been demonstrated to be strong chemoattractants for marine bacteria and zooplankton (i.e. Seymour et al., 2010). Furthermore, DMSP induces the production of quorum sensing molecules (Johnson et al., 2016), is a mediator of bacterial virulence towards DMSP-producing algae (Barak-Gavish et al., 2018), and its cleavage to DMS may generate acrylate as a byproduct, considered to be a potential predator deterrent (e.g. Wolfe et al., 1997). DMSP has also been proven to satisfy up to 13% of the carbon (Levine, 2016), and 100% of the sulfur demand of marine heterotrophic bacteria (Kiene et al., 2000). In fact, the most abundant marine bacteria (SAR11 clade) are not able to assimilate sulfate and rely exclusively on DMSP and other reduced sulfur compounds to satisfy their sulfur requirements (Tripp et al.,

2008). Getting to know the relative routing of DMSP between the demethylation (i.e. consumption) pathway vs. the cleavage (DMS generating) pathways (Figure 1) is then critical to understand the importance of DMSP and DMS in the marine trophic webs, both as nutrient sources and as ecologically relevant molecules.

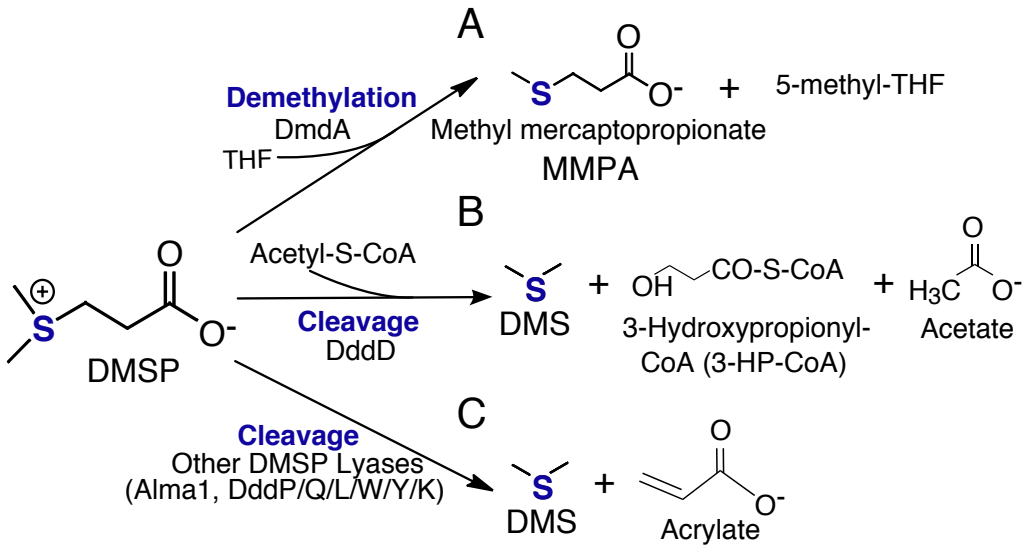

Figure 1: Biological fates of DMSP (modified from Lei, Alcolombri, et al., 2018). (A) Demethylation pathway. The first step (shown here) is catalyzed by DmdA, which uses tetrahydrofolate (THF) as a cofactor (Reisch et al., 2008). This pathway is utilized for the consumption of DMSP as a carbon and sulfur source by marine bacteria. (B) Cleavage pathway with production of 3-Hydroxypropionyl CoA, catalyzed by DddD. This pathway requires acetyl-CoA as cofactor (Alcolombri, Elias, et al., 2014). (C) Cleavage pathway with production of acrylate, catalyzed by DMSP lyases other than DddD. Both (B) and (C) produce DMS, a volatile S species that is usually released to the water column.

Insight into the relative contributions that each of the demethylation and cleavage genes/pathways may have to the fate of DMSP in seawater has been gained from studies with ^{35}S-labeled DMSP (Kiene et al., 2000), stable sulfur isotopes, and ocean expeditions data. The Global Ocean (GOS; Rusch et al., 2007) and Tara Oceans (Pesant et al., 2015) expeditions have collected both chemical (concentrations and sulfur isotopic compositions) and biological (genomic, transcriptomic, and proteomic) information relevant to the dynamics of DMSP and DMS. Sulfur

isotopes are deemed the most direct and precise geochemical proxies to trace the transformations of sulfur as it moves through different reservoirs (reviewed by Fike et al., 2015). Sulfur isotope measurements of DMSP and DMS in marine surface waters (Amrani et al., 2013; Carnat et al., 2018), as well as the fractionation in the DMS produced from DMSP in marine algae (Oduro et al., 2012) were the first attempts to identify a S isotopic signature during DMSP transformations. Although these fractionation factors constitute a proxy for the eukaryotic cleavage pathway, specific δ^{34}S signatures for the demethylation pathway and the bacterial cleavage pathways have not been determined.

Here, we constrained for the first time the S isotope fractionations of individual enzymes involved in the cleavage (DMSP lyases) and demethylation (DMSP demethylase) pathways of DMSP. We performed mass balance calculations to model how the relative contributions of the different biological processes that act on DMSP account for the δ^{34}S values of DMSP in seawater. Our data suggest that the fractionation imparted by the DMSP degrading enzymes is small, but nonetheless useful as a proxy for the main biological degradation pathways of DMSP in natural samples. Thus, the fractionation factors reported here provide a way to establish the relevance of the demethylation and cleavage pathways of DMSP in natural environments.

2. MATERIALS AND METHODS

Cultures and extraction of cell lysates

We obtained cell lysates from *Escherichia coli* BL21 cells independently transformed with DmdA, the only DMSP demethylase described to date (kindly provided by Will Whitman from the University of Georgia, Athens), and different DMSP lyases (kindly provided by Dan Tawfik from the Weizmann Institute of Science, Israel), under control of the lac operator inducer. These clones are listed in Table 1, and the natural taxonomic distributions of each enzyme are reviewed by Lei, Alcolombri,

et al. (2018).

Table 1: List of *E. coli* BL21 clones expressing different genes involved in DMSP degrading pathways utilized in this study.

Gene	Pathway	Cloned in *E. coli* from	Reference
dmdA	Demethylation	*Ruegeria pomeroyi* DSS-3 (Roseobacter; α-Proteobacteria)	Reisch et al. (2008)
alma1	Cleavage (DMS+acrylate)	*Emiliania huxleyi* (Coccolithophore)	Alcolombri et al. (2015)
dddP	Cleavage (DMS+acrylate)	*Ruegeria pomeroyi* DSS-3 (Roseobacter; α-Proteobacteria)	Todd et al. (2011)
dddY	Cleavage (DMS+acrylate)	*Desulfovibrio acrylicus* (δ-Proteobacteria)	Lei, Cherukuri, et al. (2018)
dddK	Cleavage (DMS+acrylate)	*Pelagibacter ubique* (SAR11; α-Proteobacteria)	Lei, Cherukuri, et al. (2018)
dddQ	Cleavage (DMS+acrylate)	*Ruegeria pomeroyi* DSS-3 (Roseobacter; α-Proteobacteria)	Todd et al. (2011)
dddD	Cleavage (DMS+3-HP-CoA)	*Marinomonas* MWYL1 (γ-Proteobacteria)	Alcolombri, Elias, et al. (2014)

Each of the *E. coli* transformants was separately grown in Luria-Bertani (LB) agar plates incubated overnight at 37°C. Individual colonies retrieved from the solid media were used to inoculate 5 mL liquid LB medium for overnight incubations at 37°C, and 1 mL of these cultures was added to flasks with 1 liter of sterile liquid LB media, that were kept at 37°C until they reached an OD_{600} of 0.6-0.8 (late exponential phase). Solid and liquid culture media were supplemented with the corresponding antibiotic (50 μg/mL ampicillin or kanamycin). The enzyme induction and the extraction of cell lysates were performed following a modification of a previously described protocol (Lei, Cherukuri, et al., 2018). Briefly, the growth temperature was reduced to 16°C, and enzyme expression was induced overnight with 0.1 mM of the lac operator inducer isopropyl β-d-1-thiogalactopyranoside (IPTG). The cells were harvested by centrifugation at 4°C and resuspended in lysis buffer (5 mM Tris-HCl pH 8.0, 0.2 g/l lysozyme), followed by sonication (10s on, 10s off for 4 min) and subsequent centrifugation at 10 000 g for 1 hour. Total protein concentration in the crude extracts was determined using the Bio-Rad Bradford

reagent with bovine serum albumin as the standard. The approximate concentration of each heterologous enzyme was calculated following So et al. (2011).

DMSP biodegradation experiments

DMSP degradation by cell lysates with each one of the enzymes in Table 1 was individually assayed in a similar way as previously described (Lei et al., 2018b). DMSP stock solution was prepared by mixing solid DMSP (Sigma-Aldrich) with reaction buffer (5 mM Tris-HCl pH 8.0), utilized to provide a suitable pH buffering for the enzymatic reactions. Reaction assays were set up by mixing crude cell extracts, DMSP stock and reaction buffer in plastic vials with a total volume between 1 and 5 mL at 28°C. The cell lysates were added at a total protein concentration of 5.6 mg/mL for DmdA, 1 $\mu g/mL$ for Alma1, 8.2 mg/mL for DddP, 14 $\mu g/mL$ for DddY, 0.9 mg/mL for DddK, 3 mg/mL for DddQ, and 0.6 mg/mL for DddD. The reaction mixture for the DddD assay was supplemented with 10 μM acetyl-CoA, which takes the methyl group removed from DMSP, and that for the DmdA assay was set up in anaerobic conditions with 0.685 mM tetrahydrofolate (THF), required as cofactor. At definite time intervals, the reaction was quenched by filtering through Amicon Ultra-4 or Ultra-15 30K (Millipore Sigma) with centrifugation at 5000 g for 10 min and 4°C for DMSP quantification and S isotope measurements.

DMSP quantification

For DMSP separation and quantification, an Acquity^{TM} ultra-performance liquid chromatograph (Waters, Milford, MA, USA) coupled to a Xevo G2-S electrospray ionization quadrupole time-of-flight mass spectrometer (Waters Micromass, Manchester, England) operated in positive ion mode [UPLC/(+) ESI-Q-TOF-MS] was used. Samples were prepared by diluting the stopped DMSP reactions 1:100 in acetonitrile to fall into the linear detection range of 1.5- 30 μM. The UPLC separation was

carried out with an Aquity UPLC^{TM} BEH HILIC column (1.7μm, 2.1mm x 100mm) kept at 27 °C, with water (solvent A) and acetonitrile (solvent B) following the same gradient used by Spielmeyer and Pohnert (2010). The separation started with 10% A at a flow rate of 0.25 mL/min for 0.4 min. The gradient was linearly increased to 60% A until 1.7 min. At 1.9 min, the flow rate was increased to 0.6 mL/min. At 2.7 min, the flow rate and gradient were set back to 0.25 mL/min and 10% A. Finally, the column was equilibrated for 1.3 min, resulting in a total analysis time of 4 min. Acetonitrile containing 5% v/v water was used as the working fluid in the autosampler syringe in order to maintain the low water content of the sample solution and initial mobile phase concentration that is critical for successful HILIC chromatography. The mass range from 50 to 300 *m/z* using a scan rate of 0.3 s was recorded. The injection volume was 1 μL and the sample was kept at 4 °C. The optimized ESI parameters used were: 3 kV capillary voltage, 40 V sampling cone, 80 V source offset, 120°C source temperature, 450°C desolvation temperature, and 6 V collision energy.

MS-MS mode data was also acquired to eliminate the possibility of isobaric interferences. For this measurement the quadrupole was set to pass a range of ±1 m/z around the mass of the parent ion (134 m/z). Collision energy was increased to 30 V and signal between 50 and 300 m/z was recorded at high resolution in the time-of-flight analyzer. The product ion at 73 m/z was used for quantitation. Instrumental stability (i.e., chromatographic and mass spectral reproducibility) was verified within 5% using a standard solution of DMSP (Sigma-Aldrich) run periodically (one standard every ten samples) during routine analysis. Data were acquired and processed using MassLynx v4.1 software. The enzymatic rates of DMSP consumption over time were fitted to Michaelis-Menten kinetics using the previously reported Michaelis-Menten constant (K_M) for each heterologously expressed enzyme (same references as those in Table 1 except for DddP (Kirkwood et al., 2010), DddK (Peng et al.,

2019), and DddQ (Burkhardt et al., 2017)).

Sulfur isotope analysis

To determine the isotopic composition of DMSP over the course of the enzyme assays, a volume of supernatant from the quenched reactions containing 3-5 μg of S was freeze dried, resuspended in distilled water, and allowed to evaporate in tin capsules heated at 60°C to concentrate DMSP and remove volatile sulfur. Sulfur was measured as SO_2 by EA-IRMS (Carlo Erba NC 2500 Elemental Analyzer connected to a Delta+ XL, ThermoQuest, via the Thermo Conflo III interface). We report sulfur isotope ratios using the conventional delta notation relative to the international standard Vienna-Canyon Diablo Troilite (VCDT):

$$\delta^{34}\mathrm{S} = ({}^{34}\mathrm{R}_{\mathrm{sample}}/{}^{34}\mathrm{R}_{\mathrm{VCTD}}) - 1, \tag{2.1}$$

where ${}^{34}\mathrm{R}$ refers to the ^{34}S/^{32}S ratio. The $\delta^{34}\mathrm{S}$ values of each sample were corrected by subtracting the blank and using a linear interpolation between two in house working standards (sulfanilamide and seawater), with an analytical repeatability better than 0.26 ‰.

The sulfur isotope fractionation factors for each enzyme (${}^{34}\varepsilon_{\mathrm{enz}}$) were calculated from the slope of the linear regression analysis of the most accurate approximate solution to the Rayleigh distillation equation (Mariotti et al., 1981; Scott et al., 2004):

$$\ln(1 + \delta^{34}\mathrm{S}_{\mathrm{DMSP}}) = \ln(1 + \delta^{34}\mathrm{S}_{\mathrm{DMSP},0}) - {}^{34}\varepsilon_{\mathrm{enz}} \cdot \ln(\mathrm{f_R}), \tag{2.2}$$

where enz can be replaced by any of the enzymes studied, $\mathrm{f_R}$ is the fraction of remaining DMSP in the assay vials, and $\delta^{34}\mathrm{S}_{\mathrm{DMSP},0}$ and $\delta^{34}\mathrm{S}_{\mathrm{DMSP}}$ are the sulfur isotopic compositions of the initial and remaining DMSP at the time of the measurement, respectively. The details of the corrections performed are included in the Supplementary Methods.

Data analysis

For the analysis of the data —both the substrate degradation kinetics and the inference of the fractionation factor— we took a Bayesian analysis approach. A full description of how this analysis was performed, including both the theoretical background and the assumptions behind the statistical analysis, can be found in the Supplementary Materials.

Data and code availability

All data and custom scripts were collected and stored using Git version control. Code for raw data processing, analysis, modelling, and figure generation is available in the GitHub repository (https://github.com/daniosro/DMSP).

3. RESULTS

The DMSP concentration in the reaction vials at different timepoints in the enzyme assays with DmdA (DMSP demethylase) or various DMSP lyases are shown in Figure 2. Their fits to Michaelis-Menten reaction kinetics were good for DmdA, Alma1, and DddK, and satisfactory for DddD and DddY (Supp. Figure 1). However, we noticed that in the case of DddP and DddQ the curves seem to flatten out before the reactions were completed. This was not surprising, since a low catalytic activity for both enzymes has been recognized (Alcolombri, Laurino, et al., 2014; P. Wang et al., 2015). To investigate if a deviation from Michaelis-Menten kinetics in these enzymes could be explained by a loss of their activity during the course of the reactions, we repeated the Michaelis-Menten fit incorporating a first order decay rate for the enzymes. If an enzyme loses activity over the course of the reaction, its concentration in the assay vial (E), is assumed to decrease following a first order rate (k):

$$\frac{\mathrm{dE}}{\mathrm{dt}} = -\mathrm{k}\ \mathrm{E}. \tag{2.3}$$

In turn, the change in the concentration of DMSP over time will be affected by the decrease in the amount of enzyme:

$$\frac{\mathrm{dDMSP}}{\mathrm{dt}} = \frac{-\mathrm{v_{max}\ E\ DMSP}}{\mathrm{K_M + DMSP}}, \tag{2.4}$$

where $\mathrm{K_M}$ is the previously reported Michaelis-Menten constant (see the Methods section) and $\mathrm{v_{max}}$ is the fitted maximum velocity per enzyme (units of nM substrate/min), such that $\mathrm{V_{max}}$, the maximum catalytic activity when the enzyme is saturated, is equal to $\mathrm{v_{max}E}$. The results of this modelling show very good agreement with the data (Figure 2). We performed additional enzyme assays for Alma1, the enzyme with the highest activity, in order to get experimental support for this hypothesis (Supplementary Methods). When the enzyme is in a very low concentration, the reaction stalls early and when most of the DMSP is still remaining in the reaction. Adding higher concentrations of enzyme proportionally increases the fraction of DMSP degraded. Similarly, when additional DMSP is added to reaction vials where most of it was already consumed, the added DMSP was degraded very slowly (Supp. Figure 2). Thus, the experimental results validate the modelled prediction of a loss of enzymatic activity over the course of the DMSP degradation assays.

Despite reacting DMSP with large concentrations of DddP and DddQ, the enzymes that seem to exhibit the larger loss of activity, we still could not detect complete degradation of DMSP by these enzymes. To establish if this could affect the fractionation factors calculated below from the isotopic compositions of DMSP over the course of the enzymatic degradation experiments, we performed modelling for DddP. We integrated Eqs. 2.3 and 2.4 for $^{34}\mathrm{DMSP}$ and $^{32}\mathrm{DMSP}$ (more details are provided in the Supplementary Methods), and used their values to compute the $\delta^{34}\mathrm{S}$ of DMSP for k = 0 and k = 0.08. We determined the theoretic fractionation factors ($^{34}\varepsilon$) from the slope of the regression of ln ($\delta^{34}\mathrm{S_{DMSP}}$ +1) vs. ln f (fraction

of DMSP remaining) in both cases, as described in the Methods section. We found that the apparent loss of enzyme activity should not affect the enrichment factors by more than 0.01 ‰ (Supp. Figure 3 A and B). If the enzyme activity was kept constant, the $\delta^{34}S$ values of DMSP that we measured would be larger, because they would be driven to a greater extent of reaction (more DMSP degradation) than under a loss of enzyme activity. In the two cases, there would be a substantial difference in the ln ($\delta^{34}S_{DMSP}$ +1) as a function of time, but not as a function of ln f (Supp. Figure 3 C).

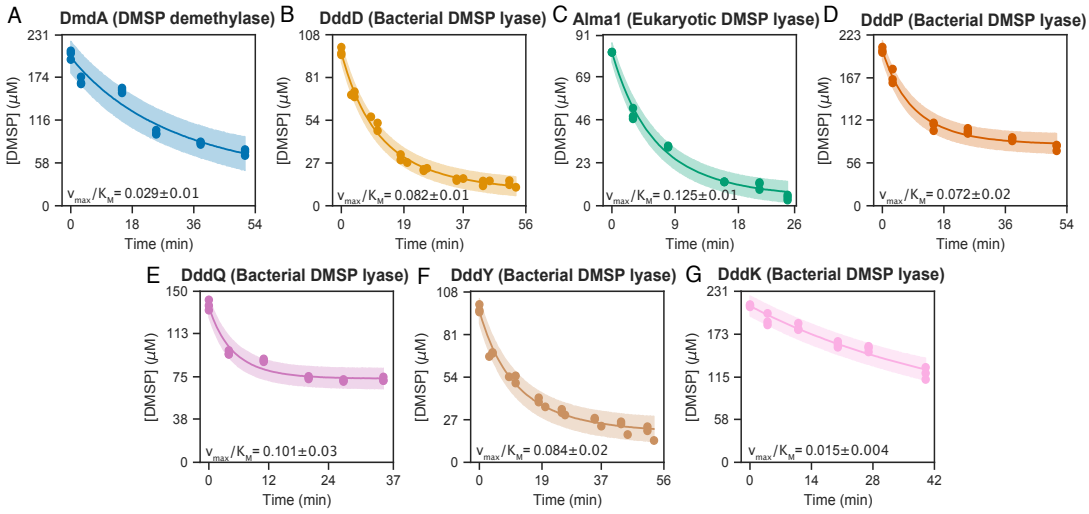

Figure 2: Degradation of DMSP by the enzymes depicted in Figure **??**: (A) DmdA, which catalyzes the demethylation pathway; (B) DddD, which catalyzes the cleavage pathway with the production of 3-HP-CoA; (C) Alma1, which is the only eukaryotic DMSP lyase described; (D) DddP, the most abundant and expressed bacterial DMSP lyase; and (E) DddQ, (F) DddY, and (G)DddK, other DMSP lyases. The points are combined data from triplicate measurements for each enzyme and the lines represent a fit of the reaction rate based on the Michaelis-Menten kinetics, assuming that the enzymes lose activity over time with a first order degradation rate. v_{max}/K_M is the effective catalytic rate of each enzyme, in min^{-1}. Shaded regions represent the 95% credible intervals from the Bayesian inference of Michaelis-Menten kinetics with enzyme degradation.

Since there is no way to discern if the isotope effects of the DMSP degrading enzymes impact V_{max} only, K_M only or both, the previous model had to make assumptions about them for both ^{34}S and ^{32}S, as well as about the rate of loss of

enzyme activity. To guarantee the reliability of the fractionation factors that we determined, we performed sensitivity tests to determine how much the fractionation factors at steady-state would change for different enzyme degradation rates, $^{32}\mathrm{V}_{\mathrm{max}}$ and $^{32}\mathrm{V}_{\mathrm{max}}/^{32}\mathrm{K}_{\mathrm{M}}$. We found that changing $^{32}\mathrm{V}_{\mathrm{max}}$ (or $^{34}\mathrm{V}_{\mathrm{max}}$) would have a neglibible impact on the fractionation factor, whereas changing $^{32}\mathrm{V}_{\mathrm{max}}/^{32}\mathrm{K}_{\mathrm{M}}$ (or $^{34}\mathrm{V}_{\mathrm{max}}/^{34}\mathrm{K}_{\mathrm{M}}$) would only change it by 0.02 ‰ (Supp. Figure 4). These analyses are fully described in the Supplementary Methods and allowed us to further confirm that the fractionation factors determined from the $\delta^{34}\mathrm{S}$ values of DMSP that we measured are reliable.

Having established that a loss of enzyme activity should not affect the measured δ^{34}S values, we used them together with the fractions of DMSP remaining in each enzymatic reaction at each data point to calculate the fractionation factors ($^{34}\varepsilon$, Figure 3). All of the enzymes evaluated were found to have normal kinetic isotope effects (i.e. negative fractionation factors), that range between -1.2 and -9.1‰.

4. DISCUSSION

The fractionation factors ($^{34}\varepsilon$) determined here are negative (normal isotope effects), span a range of $\sim 8‰$, and are not correlated with the effective catalytic rate ($\mathrm{v}_{\mathrm{max}}/\mathrm{K}_{\mathrm{M}}$) or the Michaelis-Menten constant (K_{M}) of each enzyme. These $^{34}\varepsilon$ values are small compared to those of other biological sulfur transformations such as sulfate reduction (Sim et al., 2011) and sulfur disproportionation (Canfield and Thamdrup, 1994). The most plausible reason is that the cleavage of the C-S bond is not the rate-limiting step in the reaction, and therefore, there is little sensitivity to sulfur isotopes once this step takes place (i.e. Goldstein, 1966). Specifically, in the case of the DMSP lyases that cleave DMSP to DMS and acrylate, the sulfur cleavage reaction happens near the end of a cascade that is initiated by removing the hydrogen from the alpha carbon position (Supp. Figure 5). The larger the

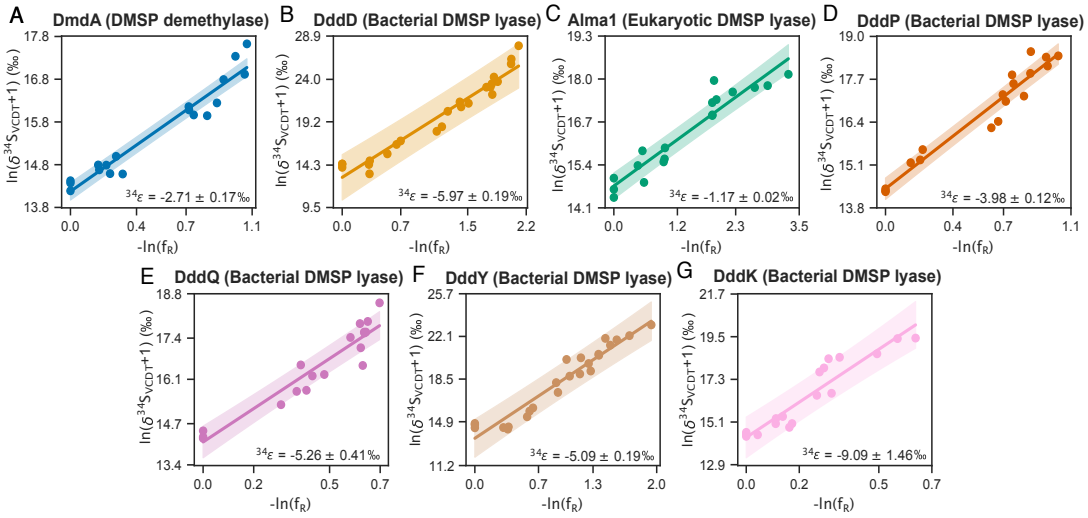

Figure 3: Evolution of the $\delta^{34}S$ values of DMSP as it is degraded by (A) DmdA, which catalyzes the demethylation pathway; (B) DddD, which catalyzes the cleavage pathway with the production of 3-HP-CoA; (C) Alma1, which is the only eukaryotic DMSP lyase described; (D) DddP, the most abundant and expressed bacterial DMSP lyase, and (E) DddQ, (F) DddY, and (G)DddK, other DMSP lyases. Measurements were made at the same points as the concentrations depicted in Figure 2. The points are combined data from triplicate measurements for each enzyme. Values of ln ($\delta^{34}S_{DMSP}$ +1) are plotted against the negative ln of the fraction of DMSP remaining (f_R). The lines represent a linear fit of the Rayleigh distillation equation, where the slope was taken as a measurement of the fractionation factor, $^{34}\varepsilon$. Shaded regions represent the 95% credible intervals from the Bayesian inference of the linear regression.

reversibility of this H abstraction step, the larger the size of the kinetic isotope on the S isotopes of the residual DMSP (Kaplan and Rittenberg, 1964). This expected trend matches our observations, since the magnitude of the fractionation factors (Alma1<DddP<DddY~DddQ<DddK) is correlated with the reversibility of the reactions. Alma1 uses cysteine as a nucleophile (Alcolombri et al., 2015), whereas DddP uses aspartate and coordination to an Fe atom (P. Wang et al., 2015), DddY and DddQ have DMSP coordinated to a Zn (sometimes Fe) atom and use tyrosine as nucleophile (Li et al., 2014), and DddK uses tyrosine as well but coordinates DMSP to a Mn or Ni atom (Peng et al., 2019; Schnicker et al., 2017, Supp. Figure 5). Thus, the DMSP cleavage reactions with acrylate as a byproduct in which a

stronger nucleophile is involved (i.e. cysteine) are less reversible than those where a weaker nucleophile is involved (i.e. tyrosine), and consequently have smaller isotope effects.

Despite the diversity of DMSP degrading enzymes, the Tara Oceans expedition found that more than 90% of the expressed bacterial DMSP lyases (fraction <3 μm) are DddP homologs (Curson et al., 2018; Supp. Figure 6). Thus, we modelled the expected $\delta^{34}S$ values of seawater DMSP assuming that DMSP is either demethylated or cleaved by only Alma1 (eukaryotic DMSP lyase) or DddP, incorporating our fractionation factors in the calculations. The model is described in detail in the Supplementary Methods, and the results for different activities of each enzyme are shown in Figure 4. We considered the ocean as a single box with a constant inward flux of DMSP from a single process (biosynthesis) and two possible outward fluxes, cleavage, and demethylation. The mixing ratio between the three possible consumption pathways for DMSP that our model considers — demethylation, bacterial cleavage by DddP, and eukaryotic cleavage by Alma1 — will determine the $\delta^{34}S$ of seawater DMSP. If the production of DMSP is balanced by consumption (a reasonable assumption in the ocean due to the rapid turnover of DMSP), mass balance constrains the isotopic composition of DMSP to be different from the input by the isotope effect (Hayes, 2001). In other words, the isotopic composition inherited by DMSP from its biosynthetic pathway is subsequently altered by consumption, and the enzyme with a higher concentration (due to differences in community composition and/or gene expression) or activity (faster reaction rates) will drive the $\delta^{34}S$ of DMSP towards its fractionation value. As a consequence, when eukaryotic cleavage is the dominant process (Alma1; $^{34}\varepsilon \sim -1‰$), DMSP will have the lowest $\delta^{34}S$, when demethylation dominates (DmdA; $^{34}\varepsilon =\sim -3‰$), DMSP will have an intermediate $\delta^{34}S$ value, and when bacterial cleavage dominates, DMSP will be able to reach the heaviest possible $\delta^{34}S$ values, assuming that the input of DMSP to the

ocean has an approximately constant $\delta^{34}S$ value.

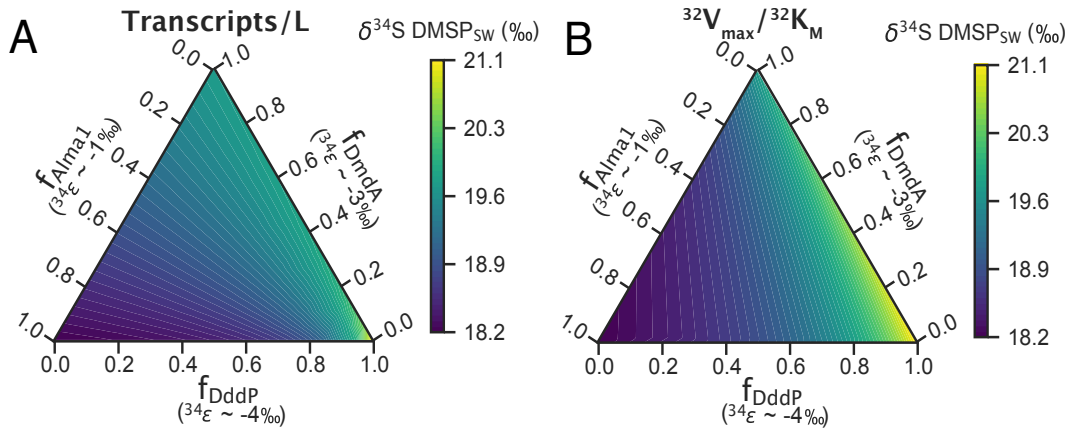

Figure 4: Prediction of the $\delta^{34}S$ values of DMSP in seawater (SW, colorbars), assuming that DMSP is degraded only by Alma1 (eukaryotic DMSP lyase), DddP (most abundant bacterial DMSP lyase), and DmdA (DMSP demethylase). The isotopic mass balance calculation assumed a $\delta^{34}S$ of 17 ‰ for the incoming flux of DMSP. The ternary plots show the expected S isotopic composition of DMSP when Alma1, DddP, and DmdA fractionally contribute to DMSP degradation amounting to a total of 1 (or 100%), when that contribution is considered in terms of (A) the enzyme concentrations in transcripts per liter or (B) the enzyme catalytic rate for the light and most abundant isotope of sulfur (^{32}S, $^{32}V_{max}/^{32}K_M$) of each enzyme.

The value of -1.18 ± 0.06‰ for the $^{34}\varepsilon$ of Alma1 agrees with an $^{34}\varepsilon$ of -1 to -1.5 ‰ reported for DMSP cleavage in culturing experiments with the macroalgae *Ulva lactuca* and *Ulva linza* (Oduro et al., 2012). To our knowledge, no other absolute fractionation factors for DMSP degrading enzymes had been reported before. Our modelling approach demonstrates their usefulness to infer the DMSP degradation process that dominates over a sample with a particular $\delta^{34}S_{DMSP}$. We predict values of environmental $\delta^{34}S$ of DMSP that range from 18.2 to 21.1‰. These values fall within the range of $\delta^{34}S$ of DMSP measured in seawater to date during normal (non-bloom) conditions (Amrani et al., 2013; Carnat et al., 2018), spanning 17.8 to 20.5‰ at depths up to 140 m, and 18.9 to 20.3‰ in surface waters (0 to 5 m). The model assumed an isotopic composition of 17‰ for newly synthesized DMSP (before it is affected by any degradation process) in order to capture the entire

range of non-bloom seawater $\delta^{34}S_{DMSP}$ measurements. This value is lower than the data of intracellular $\delta^{34}S_{DMSP}$ reported by Oduro et al. (2012) in macroalgae ($18.2 \pm 0.6‰$) and phytoplankton ($19.6 \pm 0.3‰$), and by Gutierrez-Rodriguez et al. (2017) in *Phaeocystis* and foraminifera ($\sim 20‰$). This indicates that there must be a normal isotope effect in the synthesis of DMSP from marine sulfate ($21‰$), and that the intracellular $\delta^{34}S_{DMSP}$ measured by Oduro et al. (2012) and Gutierrez-Rodriguez et al. (2017) might already have been affected by cleavage by Alma1, which would leave the residual DMSP enriched in ^{34}S.

On the other hand, the values measured by Amrani et al. (2013) for the $\delta^{34}S$ of DMS in seawater were found to be consistently higher relative to the $\delta^{34}S$ of DMSP in the same samples by an average of $0.6‰$ throughout the water column. The same study found a $-0.5‰$ fractionation factor associated to the volatilization of DMS. The fractionation factors for DMSP cleavage reported here and the fractionation factor for DMS volatilization reported by Amrani et al. (2013) alone would not be able to explain the seawater $\delta^{34}S_{DMS}$ under normal conditions. However, under non steady-state conditions, such as at the end of a bloom, fast recycling of organic sulfur compounds might increase the $\delta^{34}S_{DMS}$ values. The only other processes that could cause a fractionation of S isotopes in DMS are consumption by organisms and photooxidation. If photooxidation was responsible for the enrichment of ^{34}S in DMS relative to DMSP, Gutierrez-Rodriguez et al. (2017) should have found $^{34}\varepsilon$ values different than those reported by Oduro et al. (2012), since these studies performed incubations under light and dark conditions, respectively. Therefore, we propose that there must be a normal isotope effect of about -2.5 to -7.5 ‰ associated with microbial DMS consumption, which drives the residual DMS back to a $\delta^{34}S$ close to that of seawater sulfate (Fig. 5). This was previously hypothesized by Amrani et al. (2013) and it is consistent with the observations from Gutierrez-Rodriguez et al. (2017) in seawater incubations. Alternatively, the inputs of DMSP to the

ocean might have different $\delta^{34}S$ values, which would increase the range of possible $\delta^{34}S_{DMS}$ in seawater samples.

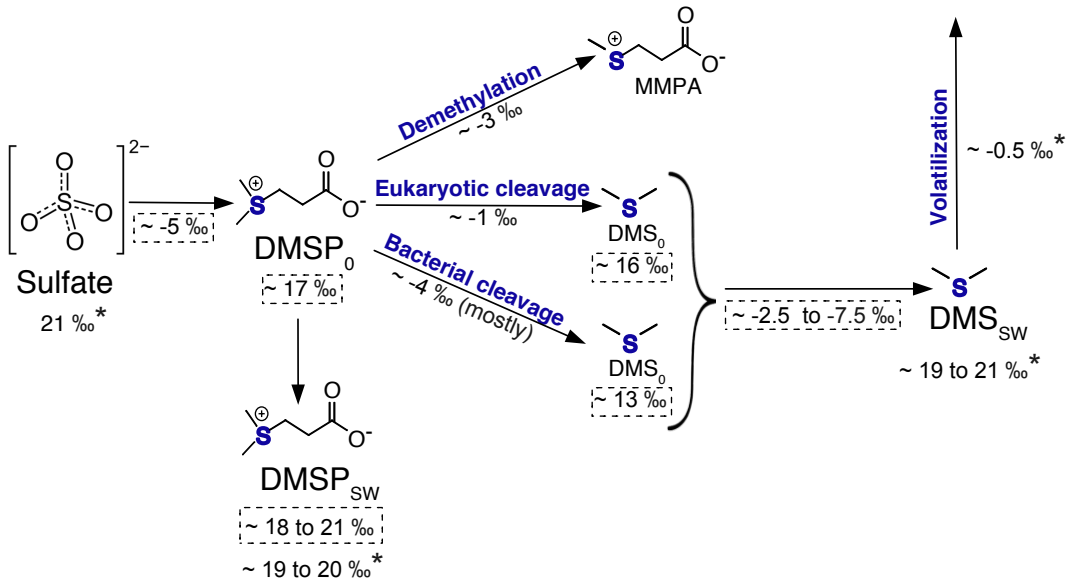

Figure 5: Schematic representation of the predicted and determined isotope fractionations associated with DMSP and DMS synthesis and degradation. The values with * were reported by Amrani et al. (2013) and the values surrounded by a dashed box are predicted based on the fractionation factors found in this study. The subscripts 0 refer to just synthesized DMSP or DMS, and the subscripts SW refer to the range of values of DMSP or DMS in seawater.

The presence of DMSP lyases in marine bacterial genomes is variable. In particular, DddK is much more abundant in southern high latitudes (Landa et al., 2019). On the other hand, it has been established that DMSP and DMS productivity is high in coastal and marine sediments, and that bacteria are important DMSP producers in these environments (Williams et al., 2019). DMSP lyases that do not have a high representation in the global ocean metatranscriptomes, such as DddD and DddY (Supp. Figure 6), have been isolated from coastal and intertidal settings (Curson et al., 2011; De Souza and Yoch, 1995; Todd et al., 2007), in association with plant roots and microaerobic environments. These differences could be responsible for local variability in the $\delta^{34}S$ of environmental DMSP. Studies based on the tracing of ^{35}S-labelled DMSP (Kiene et al., 2000) and the quantification of sulfur

species (Bates, 1994) determined that usually less than 30% of DMSP is cleaved in natural waters. This would imply that demethylation is the dominant DMSP-degrading process over most of the ocean, and is consistent with the presence of DmdA in 19% of the Tara Oceans' surveyed bacterial genomes, versus that of all of the bacterial DMSP lyases combined in only 9% of them (Landa et al., 2019). The average value of seawater $\delta^{34}S_{DMSP}$ from Amrani et al. (2013) (19.6‰) and values of environmental $\delta^{34}S_{DMSP}$ of ~ 19 to 20 ‰ predicted by our model are reasonable if demethylation is the dominant DMSP degradation process. It has also been established that the transcripts of DmdA are about one order of magnitude more abundant than those of DddP in the open ocean (Levine et al., 2012; Varaljay et al., 2015), and that both increase during algal blooms (Varaljay et al., 2015). Transcriptomic data for Alma1, the eukaryotic DMSP lyase (Vorobev et al., 2020, Supp. Figure 6), also indicate higher expression levels of this enzyme in the Southern Ocean and the North Atlantic Ocean, where high DMSP producers like *Phaeocystis*, coccolithophores and diatoms thrive (Yoch, 2002). However, no Alma1 transcripts were found in most of the stations sampled by the Tara Oceans expedition. This suggests that the expression of Alma1 is mostly limited to localized spots in the ocean, possibly associated with blooms. If that was the case, and its expression dominated over that of bacterial DMSP lyases during blooms, the $\delta^{34}S_{DMSP}$ would be driven closer to that of the source, because of its small normal isotope effect. Slightly higher values of $\delta^{34}S_{DMSP}$ were measured by Amrani et al. (2013) in a Greenland bloom in samples kept at 25 °C (19.5 to 22.1 ‰) relative to nonbloom conditions. These values might reflect a dominant activity of bacterial DMSP lyases during that bloom, or an enrichment in the ^{34}S enhanced by rapid recycling of organic sulfur. In the same study, the values of $\delta^{34}S_{DMSP}$ of a Mediterranean Sea bloom were not different from those of non-bloom conditions, which highlights the need of more studies on ecosystem changes during blooms to address these differences.

5. CONCLUSIONS

The fractionation factors reported here provide an indication of the biological fates of DMSP in the ocean. For most of the ocean, the $\delta^{34}S_{DMSP}$ values will be the result of a mixed contribution from demethylation, bacterial cleavage and eukaryotic cleavage. Our data can be useful to address whether bacterial or eukaryotic DMSP degrading processes dominate at a local scale. Since the bacterial DMSP lyases have higher fractionation factors (approx. -4 to -9 ‰), samples with heavier-than-average $\delta^{34}S_{DMSP}$ measurements might provide key clues to address why the switch from demethylation to cleavage happens in bacteria (Simó, 2001). More measurements of seawater $\delta^{34}S_{DMSP}$, tied to microbial metagenomics and metatranscriptomics, are needed to fully understand how seawater $\delta^{34}S_{DMSP}$ values are affected by ecological dynamics, and could also be key to understanding the role and evolution of the DMSP degrading enzymes. Additionally, identifying the S isotope fractionations imparted by DMSP biosynthesis and biological DMS consumption will be critical to improve our understanding of relative importance of bacteria and algae in the cycling of DOS and the implications of these processes for marine microbial communities.

6. ACKNOWLEDGEMENTS

We thank Dan Tawfik and Lei Lei (Weizmann Institute of Science), and William Whitman and Joe Wirth (University of Georgia, Athens), who kindly provided us the recombinant *E. coli* strains with DMSP lyases and DmdA, respectively. Guillem Salazar helped with the arrangement of the transcriptomic data. We also thank Reto Wijker, Elliot Mueller, and Thomas Hanson for useful discussions, as well as John Crounse, Fenfang Wu and Alex Phillips for both input and technical assistance. UPLC/Q-TOF-MS was performed in the Caltech Environmental Analysis Center, which is supported by the Caltech Environmental Science and Engineering program and the Beckman Institute at Caltech. This work was supported by the Caltech

Center for Environmental Microbial Interactions (CEMI) Training Grant to DOR and the National Science Foundation Grant 53994-ND2 to all authors.

7. SUPPLEMENTARY METHODS

Bayesian data analysis

In this section we specify the procedure to analyze both the non-linear substrate kinetics and the linear regression performed to infer the fractionation factor for the enzymes.

In general, Bayesian analysis is the natural language to quantify the plausibility of a particular parameterization of models given available data. For example, assume we have a function f that depends on parameters $\vartheta = \{\vartheta_1, \vartheta_2, \ldots, \vartheta_\mathrm{m}\}$. This function describes the process that generates some experimental measurements we got to observe. This data $\mathrm{D} = \{\mathrm{d}_1, \mathrm{d}_2, \ldots, \mathrm{d}_\mathrm{N}\}$ constrains the values that our parameters ϑ can take. But, given the intrinsic limitations of our measurements and the variability in experiments, we can never determine any particular parameter value with 100% accuracy. Instead, in the Bayesian framework we assign a probability distribution for the values that these parameters can take. Such probability $\mathrm{P}(\vartheta \mid \mathrm{D})$ —read as probability of parameter values ϑ given the data D— can be computed via Bayes' theorem as

$$\mathrm{P}(\vartheta \mid \mathrm{D}) = \frac{\mathrm{P}(\mathrm{D} \mid \vartheta)\mathrm{P}(\vartheta)}{\mathrm{P}(\mathrm{D})}. \tag{2.5}$$

Our objective is then to compute the so-called posterior distribution $\mathrm{P}(\vartheta \mid \mathrm{D})$, which is the product of the likelihood $\mathrm{P}(\mathrm{D} \mid \vartheta)$, i.e., the probability of having observed the experimental data given some parameterization ϑ of our model, the prior $\mathrm{P}(\vartheta)$, i.e., the information we have about the value of the parameters before we perform any measurements, and the so-called marginalized likelihood $\mathrm{P}(\mathrm{D})$ that, since it does not depend on the parameter values we care about, serves as a normalization constant that we will ignore.

The objective of any Bayesian inference problem is to select the functional form of each of these terms and populate them with our domain expertise. In other words, as with any statistical analysis, we make *explicit* assumptions about the features of the data, and choose certain probability functions for each of the terms previously mentioned.

Here we will apply this general framework to analyze our data and quantify the uncertainty on relevant parameters such as the enzymes' fractionation factors.

Inference of fractionation factors via Bayesian linear regression. As mentioned before, in Bayesian parameter inference we are concerned with learning the probability distribution over the quantities that parameterize our models. For the particular case of the linear regression needed to infer the fractionation factor (see Section 2.4 in Methods) let us define $\mathrm{x} \equiv \log(\mathrm{f_R})$ and $\mathrm{y} \equiv \ln(1 + \delta^{34}\mathrm{S_{DMSP}})$. Our simple linear regression model then takes the form of

$$\mathrm{y_i} = \mathrm{mx_i} + \mathrm{b} + \varepsilon_\mathrm{i}, \tag{2.6}$$

where m is the slope we are interested in, since it is the enzyme fractionation factor, b is the y–axis intercept, and ε_i is a random error associated with the intrinsic experimental errors. We take these errors to be random, i.e., we can only describe them probabilistically. As it is commonly done, we will assume that these errors are normally distributed, i.e.,

$$\varepsilon_\mathrm{i} = \mathrm{y_i} - (\mathrm{mx_i} + \mathrm{b}) \sim \mathcal{N}(0, \sigma^2), \tag{2.7}$$

where the symbol $\sim$ is read as "distributed as", and $\mathcal{N}$ represents the normal (Gaussian distribution), in this case with mean 0 and variance σ^2. From this equation, we would expect the random errors to have a mean of zero (positive and negative errors are equally likely, canceling each other), and they are characterized by an unknown variance σ^2.

The objective of this Bayesian regression is to compute the so-called posterior probability distribution $\mathrm{P}(\mathrm{m}, \mathrm{b}, \sigma^2 \mid \mathrm{D})$, where $\mathrm{D} \equiv \{\mathrm{y}_1, \mathrm{y}_2, \ldots, \mathrm{y}_\mathrm{N}\}$ is the experimental data. To compute this posterior distribution we can then write Bayes theorem as

$$\mathrm{P}(\mathrm{m}, \mathrm{b}, \sigma^2 \mid \mathrm{D}) = \frac{\mathrm{P}(\mathrm{D} \mid \mathrm{m}, \mathrm{b}, \sigma^2)\mathrm{P}(\mathrm{m}, \mathrm{b}, \sigma^2)}{\mathrm{P}(\mathrm{D})} \propto \mathrm{P}(\mathrm{D} \mid \mathrm{m}, \mathrm{b}, \sigma^2)\mathrm{P}(\mathrm{m}, \mathrm{b}, \sigma^2).$$

For the second equality we ignore the denominator $\mathrm{P}(\mathrm{D})$ since it does not depend on the parameter values, and therefore only serves as a normalization constant. Let's now analyze the two relevant terms.

The likelihood $\mathrm{P}(\mathrm{D} \mid \mathrm{m}, \mathrm{b}, \sigma^2)$**.** The likelihood term is called like this because it reflects how likely it is to observe the data D given a particular choice of parameter values m, b, and σ^2. This term captures the imprecision of our experimental measurements. Since we cannot measure things perfectly, we must model the random deviations from our expectation probabilistically.

The first thing we will assume is that all of our measurements are independent of each other. This is written mathematically as

$$\mathrm{P}(\mathrm{D} \mid \mathrm{m}, \mathrm{b}, \sigma^2) = \prod_{\mathrm{i}=1}^{\mathrm{N}} \mathrm{P}(\mathrm{y}_\mathrm{i} \mid \mathrm{m}, \mathrm{b}, \sigma^2), \tag{2.8}$$

i.e., the multiplication of the individual likelihoods. We already established what this term $\mathrm{P}(\mathrm{y}_\mathrm{i} \mid \mathrm{m}, \mathrm{b}, \sigma^2)$ looks like when we defined that the random errors ε_i have a normal distribution. What this implies is that we have a likelihood of the form

$$\mathrm{P}(\mathrm{D} \mid \mathrm{m}, \mathrm{b}, \sigma^2) = \prod_{\mathrm{i}=1}^{\mathrm{N}} \frac{1}{\sqrt{2\pi\sigma^2}} \exp\left[\frac{(\mathrm{y}_\mathrm{i} - \hat{\mathrm{y}}_\mathrm{i})^2}{2\sigma^2}\right], \tag{2.9}$$

where $\hat{\mathrm{y}}_\mathrm{i} = \mathrm{m}\mathrm{x}_\mathrm{i} + \mathrm{b}$ is the expected value given the linear model.

The prior $\mathrm{P}(\mathrm{m}, \mathrm{b}, \sigma^2)$**.** The prior, as the name suggests, captures all information we have prior to performing any measurement. It is through the prior that we

can include all of our domain expertise by establishing what is known about the parameters beforehand.

For our simple linear model we will use the so-called *non-informative priors*. Although in modern statistical literature there are many reasons to not use such priors, for such a simple linear model they will allow us to make a lot of progress analytically. The first thing we will assume is that each of the parameters' priors are independent. This is

$$\mathrm{P}(\mathrm{m}, \mathrm{b}, \sigma^2) = \mathrm{P}(\mathrm{m})\mathrm{P}(\mathrm{b})\mathrm{P}(\sigma^2). \tag{2.10}$$

For both the slope m and the intercept b we will assume *uniform priors*, i.e. every value within a range is equally likely. Mathematically, this is expressed as

$$\mathrm{P}(\mathrm{m}) = \frac{1}{\mathrm{m}_{\mathrm{max}} - \mathrm{m}_{\mathrm{min}}}, \tag{2.11}$$

where $\mathrm{m}_{\mathrm{max}}$ and $\mathrm{m}_{\mathrm{min}}$ are the maximum and minimum ranges that the slope could take. An equivalent distribution can be written for the intercept. Finally, for the observation error σ^2 we will assign the so-called Jeffreys' prior. This is the maximally non-informative prior for scale parameters such as σ^2. The prior takes the form

$$\mathrm{P}(\sigma^2) \propto \frac{1}{\sigma^2}. \tag{2.12}$$

The posterior distribution $\mathrm{P}(\mathrm{m}, \mathrm{b}, \sigma^2 \mid \mathrm{D})$**.** Having established the likelihood and the prior, we can write down the posterior distribution. We will ignore all constant terms -for example both priors for m and b- since they can be absorbed by the proportionality constant. After some algebra, this results in

$$\mathrm{P}(\mathrm{m}, \mathrm{b}, \sigma^2 \mid \mathrm{D}) \propto \frac{1}{\left(\sigma^2\right)^{\frac{\mathrm{N}+2}{2}}} \exp\left[\frac{-1}{2\sigma^2} \sum_{\mathrm{i}=1}^{\mathrm{N}} \left(\mathrm{y}_\mathrm{i} - (\mathrm{b} + \mathrm{m}\mathrm{x}_\mathrm{i})\right)^2\right]. \tag{2.13}$$

With this equation in hand we can now focus on integrating away the nuance parameters we don't care about.

Marginal probability distribution of slope $\mathrm{P(m \mid D)}$. In practice we do not care about the joint distribution of all parameters; what we care about is the probability distribution of individual parameters. Specifically, we want to compute the probability of the slope m given the data $\mathrm{P(m \mid D)}$ to obtain the fractionation factor. In order to compute this we need to integrate (marginalize) the other two parameters. This is mathematically expressed as

$$\mathrm{P\left(m \mid D\right) = \int db \int d\sigma^2 \, P\left(m, b, \sigma^2 \mid D\right)}. \tag{2.14}$$

For the most part such integrals do not have analytical solutions and one has to make use of numerical integration as we will do in the next section. But for the particular choice of priors and likelihood we have there is a closed-form solution. One can show that the result of this integral is a student-t distribution. More specifically we have that

$$\mathrm{m \mid y_1, \cdots, y_N \sim t\left(N-2, \hat{m}, \frac{\hat{\sigma}^2}{S_{xx}}\right)}, \tag{2.15}$$

where t is a student-t distribution with $\mathrm{N-2}$ degrees of freedom, $\hat{\mathrm{m}}$ is the most likely parameter value for the slope,

$$\mathrm{\hat{\sigma}^2 \equiv \sum_{i=1}^{N} \left(y_i - (\hat{m}x_i + \hat{b})\right)^2}, \tag{2.16}$$

again having $\hat{\mathrm{b}}$ being the most likely parameter value for the intercept, and

$$\mathrm{S_{xx} \equiv \sum_{i=1}^{N} \left(x_i - \bar{x}\right)^2}, \ \mathrm{\bar{x} \equiv \frac{1}{N} \sum_{i=1}^{N} x_i}. \tag{2.17}$$

In accordance with this result, we performed a linear regression of $\ln(\mathrm{f_R})$ vs. $\ln(1 + \delta^{34}\mathrm{S_{DMSP}})$ in order to compute $\hat{\mathrm{m}} \equiv {}^{34}\hat{\varepsilon}_{\mathrm{enz}}$ and $\hat{\mathrm{b}} \equiv \ln(1 + \delta^{34}\hat{\mathrm{S}}_{\mathrm{DMSP,0}})$. We then used these numerical parameter values to compute the full distribution of the fractionation factor, including the uncertainty on the estimates (Figure 3).

Non-linear regression of substrate kinetics. We were interested in the concentrations of DMSP as it was degraded by each enzyme in order to utilize the fraction

of DMSP remaining at each timepoint, together with its $\delta^{34}S$, in the calculation of the fractionation factors. The first version of this analysis consisted on simple irreversible kinetics based on Michaelis-Menten. The assumption here is that the rate at which the DMSP is degraded is given by the rate of product production. This is given by

$$\frac{\mathrm{dDMSP}}{\mathrm{dt}} = -\frac{\mathrm{V_{max\ DMSP}}}{\mathrm{K_M + DMSP}},$$

where DMSP is the concentration of DMSP, t is time, $\mathrm{V_{max}}$ is the maximum catalytic activity when the enzyme is saturated, and $\mathrm{K_M}$ is the Michaelis-Menten constant. The purpose of the Bayesian approach here is to infer the value of both parameters, $\mathrm{V_{max}}$ and $\mathrm{K_M}$.

To have a more general inference we will include the initial substrate concentration $\mathrm{DMSP_0}$ as a parameter to be determined. This is because there is uncertainty associated with both the experiment and the initial measurement of this quantity. In terms of Bayes theorem, this is written as

$$\mathrm{P(V_{max}, K_M, DMSP_0 \mid D) \propto P(D \mid V_{max}, K_M, DMSP_0) P(V_{max}, K_M, DMSP_0)},$$

where D is the time point at which the substrate concentration was measured. Let's look into each of the terms.

Likelihood $\mathrm{P(D \mid V_{max,K_M,DMSP_0)}}$**.** The first thing we need to distinguish is our theoretical expectation of the concentration of DMSP, and the actual experimental measurement that we will define as $\mathrm{\tilde{DMSP}}$. The differential equation we wrote before for the substrate concentration is a **deterministic** model. That means that for any given input DMSP it can only compute one output. Our likelihood function should then account for the expected deviations that our measurements $\mathrm{\tilde{DMSP}}$ will have with respect to the theoretical expectations DMSP. As is commonly done in practice, we will define the likelihood to be a Gaussian distribution with mean

around the theoretical expectation, and standard deviation σ^2. This is written as

$$\tilde{\mathrm{DMSP}}(\mathrm{t}) \sim \mathcal{N}(\mathrm{DMSP}(\mathrm{t}), \sigma^2),$$

where $\mathrm{DMSP}(\mathrm{t})$ is given by

$$\mathrm{DMSP}(\mathrm{t}) = \int_0^{\mathrm{t}} \mathrm{dt}\ \frac{\mathrm{dDMSP}}{\mathrm{dt}} = -\int_0^{\mathrm{t}} \mathrm{dt}\ \frac{\mathrm{V}_{\mathrm{max}\,\mathrm{DMSP}}}{\mathrm{K_M} + \mathrm{DMSP}}.$$

In other words, we assume that our experimental measurement of the substrate concentration at time t, $\tilde{\mathrm{DMSP}}(\mathrm{t})$, will depart from the expected theoretical prediction $\mathrm{DMSP}(\mathrm{t})$ with a characteristic distance σ^2. This theoretical prediction at time t is then computed by integrating the differential equation from time zero to the indicated time. Given that we do not have a closed-form solution for this integral, we will then use numerical integration to compute this expected quantity.

Furthermore, we will assume that each of the measurements in our dataset $\mathrm{D} = \{\tilde{\mathrm{DMSP}}_0, \tilde{\mathrm{DMSP}}_1, \ldots, \tilde{\mathrm{DMSP}}_\mathrm{N}\}$ are independent. This means that our likelihood then takes the explicit form

$$\begin{aligned}\mathrm{P}(\mathrm{D} \mid \mathrm{V_{max}}, \mathrm{K_M}, \mathrm{DMSP}_0, \sigma^2) &= \prod_{\mathrm{i}=1}^{\mathrm{N}} \mathrm{P}(\tilde{\mathrm{DMSP}}_\mathrm{i} \mid \mathrm{V_{max}}, \mathrm{K_M}, \mathrm{DMSP}_0, \sigma^2) \\ &= \prod_{\mathrm{i}=1}^{\mathrm{N}} \frac{1}{\sqrt{2\pi\sigma^2}} \exp\left[-\frac{(\tilde{\mathrm{DMSP}}_\mathrm{i} - \mathrm{DMSP}_\mathrm{i})^2}{2\sigma^2}\right], \quad (2.18)\end{aligned}$$

where we added the term σ^2 to the likelihood since this nuance parameter needs to be included in the inference.

Prior $\mathrm{P}(\mathrm{V_{max}}, \mathrm{K_M}, \sigma^2)$**.** For our prior, we will first assume that all parameters are independent of each other, i.e.

$$\mathrm{P}(\mathrm{V_{max}}, \mathrm{K_M}, \mathrm{DMSP}_0, \sigma^2) = \mathrm{P}(\mathrm{V_{max}})\mathrm{P}(\mathrm{K_M})\mathrm{P}(\mathrm{DMSP}_0), \mathrm{P}(\sigma^2).$$

For the maximum catalytic rate $\mathrm{V_{max}}$ we do not have a specific prior information of what this value could be since it depends both on the enzyme properties, and the amount of enzyme in the cell lysate, which we don't know. We could then use a maximally uniform prior as we did for the previous section. But for this case our posterior distribution, even if we were to use a non-informative prior, will not have an analytical solution. So, the benefits of using such priors are lost because of how computationally problematic such priors are. We will then assign a weakly informative prior. These are the kind of priors that help our computation take place without the numerical problems that non-informative priors can have. More specifically, we will use a broad Half-normal distribution

$$\mathrm{V\,max} \sim \text{Half-}\mathcal{N}(0, \sigma^2_{\mathrm{V_{max}}}),$$

where we will choose $\sigma^2_{\mathrm{V_{max}}}$ to be broad enough such that the prior has no influence on the outcome. In other words, we are constraining $\mathrm{V_{max}}$ to be positive (that's why it follows a half-Normal distribution centered at zero), but we are not putting a strict upper bound on which values this parameter could take.

For the Michaelis-Menten constant we have more prior information. Several papers have characterized this parameter for the enzymes. We will then use an informative prior for $\mathrm{K_M}$. More specifically, we will assume that $\mathrm{K_M}$ has a Gaussian prior of the form

$$\mathrm{K_M} \sim \mathcal{N}(\mu_{\mathrm{K_M}}, \sigma^2_{\mathrm{K_M}}),$$

where $\mu_{\mathrm{K_M}}$ and $\sigma^2_{\mathrm{K_M}}$ are the values of the mean and variance reported in the references, respectively. **Note**: Not all enzymes have a reported variance. For those we will use a rule of thumb assuming $\approx 10\%$ error in the measurements.

In practice, the reported Michaelis-Menten constants for all enzymes are orders of magnitude higher than the experimental substrate concentrations used in this work.

This means that we could approximate our original dynamics as

$$\frac{\mathrm{dDMSP}}{\mathrm{dt}} \approx \frac{\mathrm{V_{max}}}{\mathrm{K_M}}\mathrm{DMSP}, \quad \text{for } \mathrm{K_M} \gg \mathrm{DMSP}.$$

Therefore, the only value we should trust is the ratio of $\mathrm{V_{max}}/\mathrm{K_M}$, since the particular value of $\mathrm{V_{max}}$ for the experiment will depend on both the amount of initial enzyme in the lysate, and the $\mathrm{K_M}$ values reported in the literature.

For the initial concentration DMSP_0 we will also assume a Gaussian prior. For simplicity we will take it to be

$$\mathrm{DMSP}_0 \sim \mathcal{N}(\bar{\mathrm{DMSP}}_0, \sigma^2_{\mathrm{DMSP}_0}),$$

where $\bar{\mathrm{DMSP}}_0$ is the mean initial concentration measured, and $\sigma^2_{\mathrm{DMSP}_0}$ is the experimental variance in this number.

Finally, for the observation error σ^2 we will assume a half-Normal prior. This prior has the advantage compared to the Jeffreys' prior used in the previous section that it helps our sampler work properly. We chose a half-Normal distribution to allow the error to be arbitrarily close to zero without going into the forbidden negative values.

The (untractable) posterior distribution $\mathrm{P}(\mathrm{V_{max}}, \mathrm{K_M}, \mathrm{DMSP}_0, \sigma^2 \mid \mathrm{D})$**.** Putting all terms together gives a quite complicated posterior distribution. As mentioned before, this distribution cannot be marginalized to obtain the individual parameter distributions, so we have to make use of numerical methods.

More specifically, we used state-of-the-art Markov Chain Monte Carlo (MCMC) in order to sample out of this posterior distribution. The advantage of using MCMC is that, by generating a biased random walk in the 4D parameter space of this particular inference problem, the amount of time that a particular region in this parameter is visited by the walker is proportional to the probability of those parameters.

As seen in Supp. Fig. 1, the credible region of the inferences is very large for several of the enzymes. This suggests that the simple model with irreversible kinetics is not

sufficient to describe the phenomenology, and the uncertainty of the parameters is extremely large. For this reason, we performed the experiments to test the loss of the enzyme activities described in the Supplementary Methods, and we also performed a new fit to Michaelis-Menten kinetics assuming loss of enzymatic activity (described in the Results section).

Irreversible enzyme kinetics with enzyme degradation. The Bayesian inference from before still applies, and we just need to add an extra parameter k (rate of loss of enzyme activity) to the inference. Just as for the original $\mathrm{V_{max}}$, we will assign a half-Normal prior to both $\mathrm{v_{max}}$, the maximum catalytic rate per enzyme, and k. The results of this fit with the corresponding $\mathrm{v_{max}/K_M}$ are shown in Fig. 2. This extended model, in which the enzyme degradation is taken into account, has a much more satisfactory agreement with the data, and the values of $\mathrm{v_{max}/K_M}$ seem all reasonable. Since Alma1 was already properly fit with the original simpler model with just irreversible enzyme kinetics and no enzyme degradation, we took this enzyme to be properly modeled as the simple irreversible kinetics without enzyme degradation.

8. SUPPLEMENTARY FIGURES

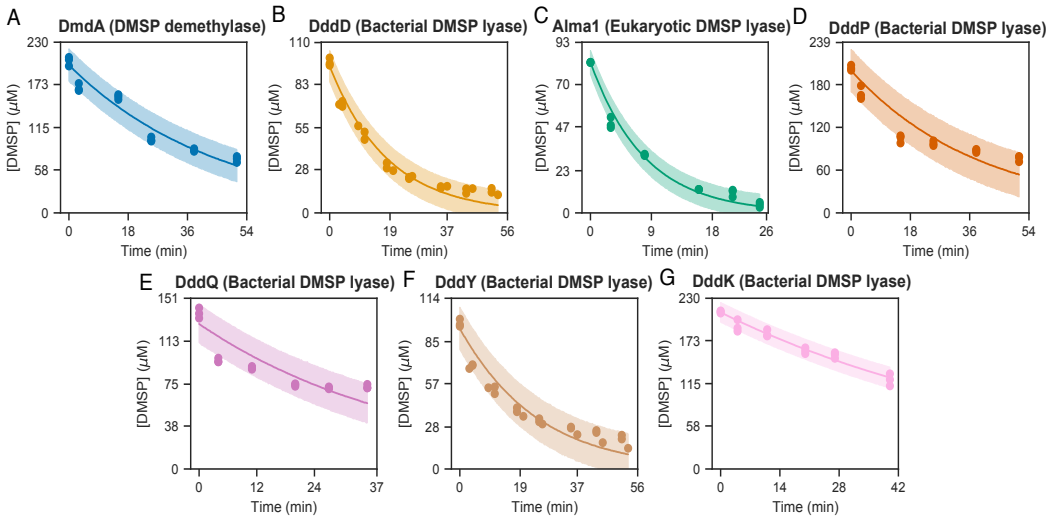

Supp. Fig. 1: Degradation of DMSP by the enzymes depicted in Fig. 1: (A) DmdA, which catalyzes the demethylation pathway; (B) DddD, which catalyzes the cleavage pathway with the production of 3-HP-CoA; (C) Alma1, which is the only eukaryotic DMSP lyase described; (D) DddP, the most abundant and expressed bacterial DMSP lyase; and (E) DddQ, (F) DddY, and (G)DddK, other DMSP lyases. The dots are combined data from triplicate measurements for each enzyme and the lines represent a fit of the reaction rate based on the Michaelis-Menten kinetics. Shades represent the 95% credible regions from the Bayesian inference of Michaelis-Menten kinetics.

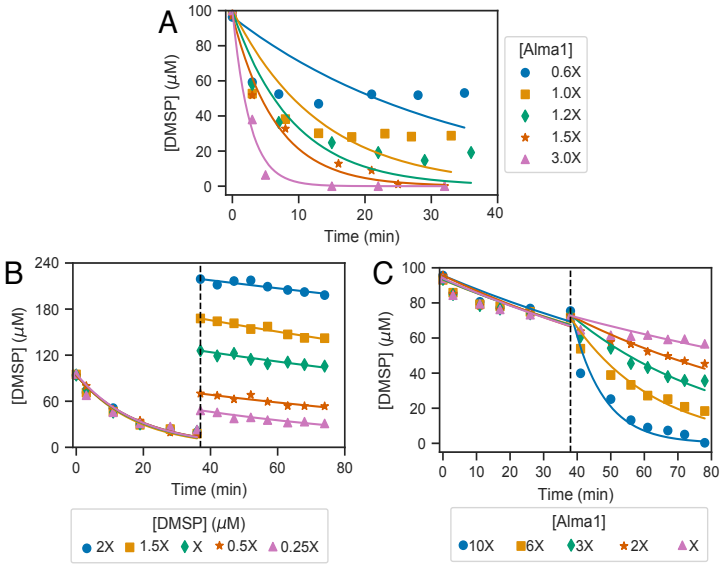

Supp. Fig. 2: DMSP degrading enzymes lose activity over time, as exemplified here by Alma1, the eukaryotic DMSP lyase. The plots show DMSP degradation over time at varying conditions. Enzyme assays were set up at an initial concentration of ~100 μM DMSP. (A) Degradation of DMSP by different concentrations of Alma1. (B) Degradation of DMSP by Alma1 at a concentration of 1.5X. 5 replicates were set up at t=0, and at t=38 min (dashed vertical line) further DMSP at different concentrations was added. (C) Degradation of DMSP by Alma1 at a concentration of 0.25X. 5 replicates were set up at t=0, and at t=38 min (dashed vertical line) further Alma1 at different concentrations was added.

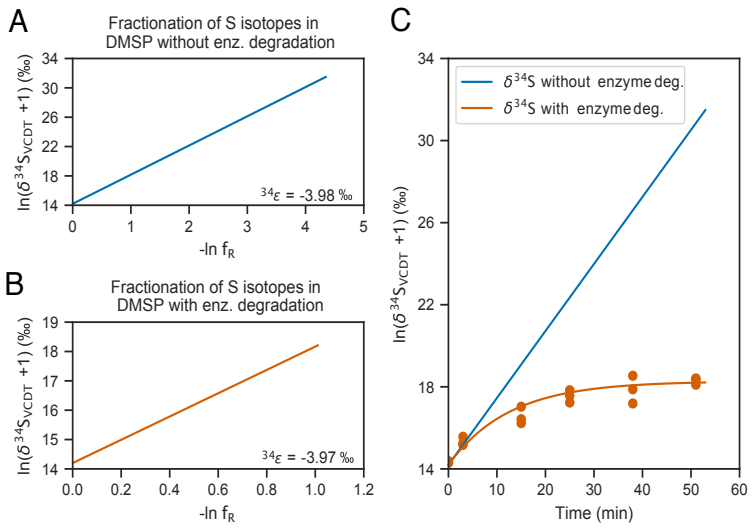

Supp. Fig. 3: The measured $\delta^{34}S$ values of DMSP (and the $^{34}\varepsilon$ calculated from them) are not greatly affected by loss of enzymatic activity. The plots correspond to modelling results for DddP. (A) Expected Rayleigh plot of ln ($\delta^{34}S$+1) values of remaining DMSP vs. negative ln of the fraction of DMSP remaining in the reaction, under a scenario where the enzymatic activity is constant (the degradation rate k is 0). (B) Expected Rayleigh plot of ln ($\delta^{34}S$+1) values of remaining DMSP vs. negative natural log. of the fraction of DMSP remaining in the reaction, under a scenario of loss of enzymatic activity throughout the course of the enzyme assay (k=0.08). (C) Measured ln ($\delta^{34}S$+1) values of remaining DMSP vs. time for 3 replicates of the enzyme assay (same as in Figure 3). The model predictions when there is loss (red curve) and no loss (blue line) of enzymatic activity are plotted on top.

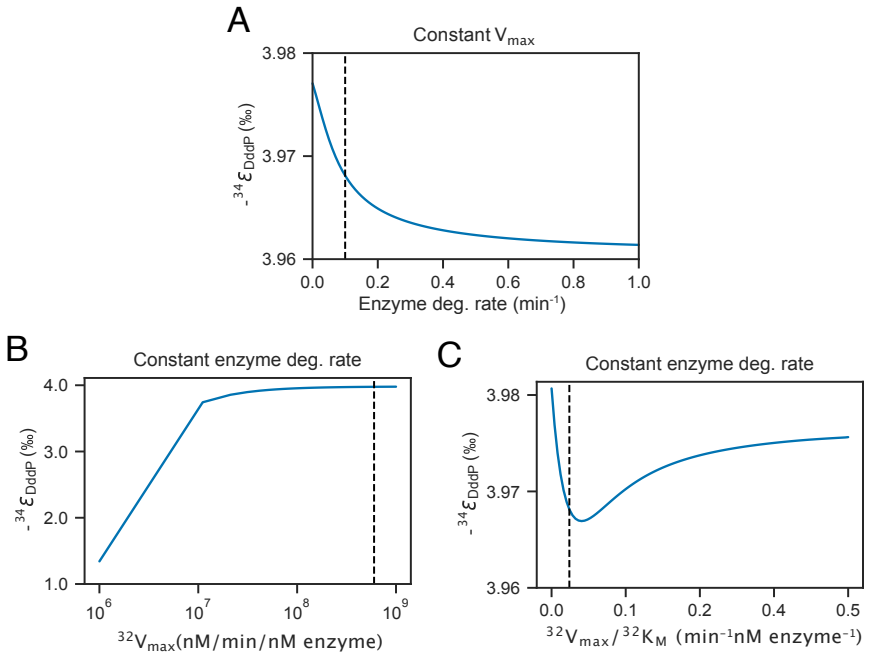

Supp. Fig. 4: Sensitivity of the measured $\delta^{34}S$ values of DMSP (and the $^{34}\varepsilon$ calculated from them) to variations of different parameters under a scenario of loss of enzymatic activity over the course of the enzyme degradation experiment. The plots correspond to modelling results for DddP. (A) Expected values of $^{34}\varepsilon$ of DMSP for different enzyme degradation rates. Values below the dashed lined are the ones where we estimate that the studied enzymes fall. (B) Expected values of $^{34}\varepsilon$ of DMSP at a constant enzyme degradation rate for different $^{32}V_{max}$ values. Values above the dashed lined are the ones where we estimate that the studied enzymes fall. (C) Expected values of $^{34}\varepsilon$ of DMSP at a constant enzyme degradation rate for different $^{32}V_{max}/^{32}K_M$ values. Values below the dashed lined are the ones where we estimate that the studied enzymes fall.

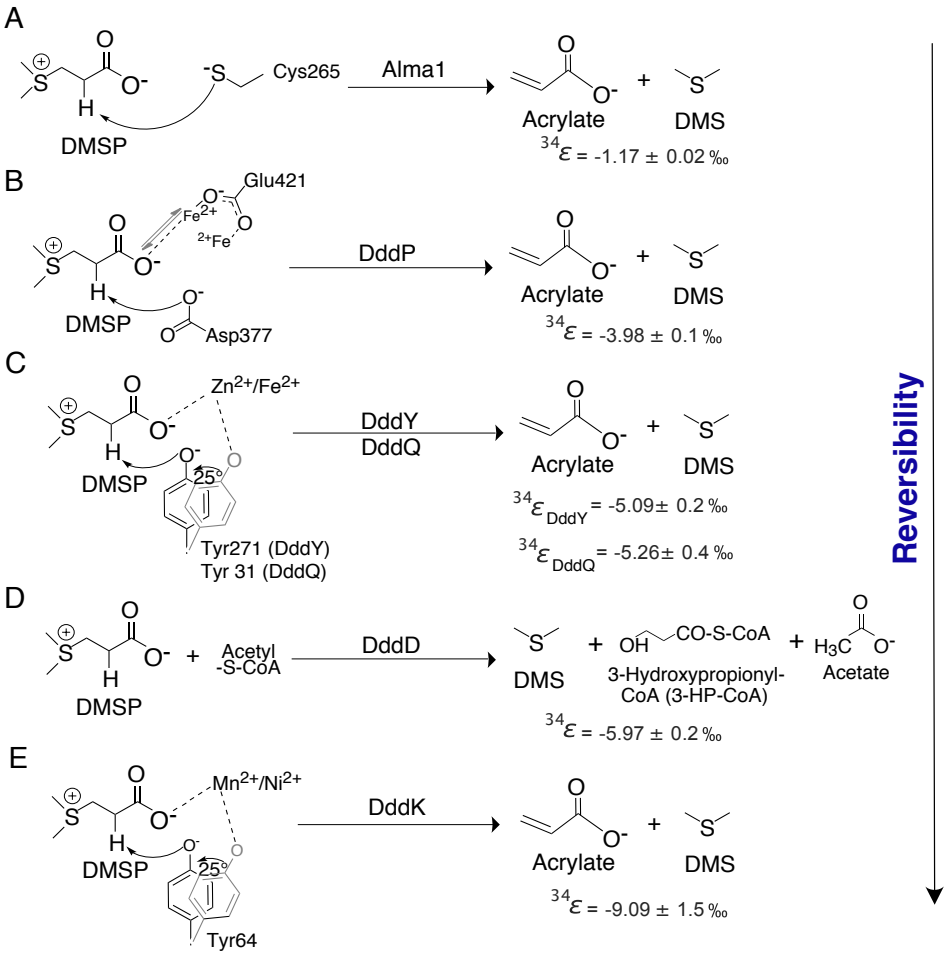

Supp. Fig. 5: DMSP lyases catalyze DMSP cleavage by different biochemical mechanisms. In each panel, the nomenclature of three letters plus a number corresponds to the catalytic residue from the enzyme that interacts with DMSP. The stronger the interaction between DMSP and the metal cofactor/nucleophile, the less reversible the reaction and the smaller the isotope effect. (A) DMSP cleavage by Alma1 (eukaryotic DMSP lyase) does not require a metal cofactor, and Cys265 is the catalytic base (Alcolombri et al., 2015). (B) The DddP catalytic mechanism differs from that of other acrylate-producing DMSP lyases in that it involves an ion shift (of Fe^{2+}) as opposed to a carboxylate shift. In a carboxylate shift, a carboxylate group in the active site of the enzyme changes its coordination form to the metal cofactor (Sousa et al., 2014), whereas an ion shift implies that the metal ion (Fe (II) here) moves inside the active side of the molecule to stabilize DMSP (P. Wang et al., 2015). This ion shift is mediated by Glu421 and the catalytic residue is Asp377 (P. Wang et al., 2015). (C) A coordination bond forms between DMSP and $\mathrm{Zn}^{2+}/\mathrm{Fe}^{2+}$, and Tyr271 (DddY; Li et al., 2017) or Tyr131 (DddQ; Li et al., 2014) acts as the catalytic base. (D) DddD has a dual activity as an acyl-CoA transferase and a DMSP lyase. The catalytic residue is Asp602 (not shown;Alcolombri, Elias, et al., 2014). (E) A coordination bond forms between DMSP and $\mathrm{Mn}^{2+}/\mathrm{Ni}^{2+}$, and Tyr64 from DddK acts as the catalytic base (Peng et al., 2019; P. Wang et al., 2015).

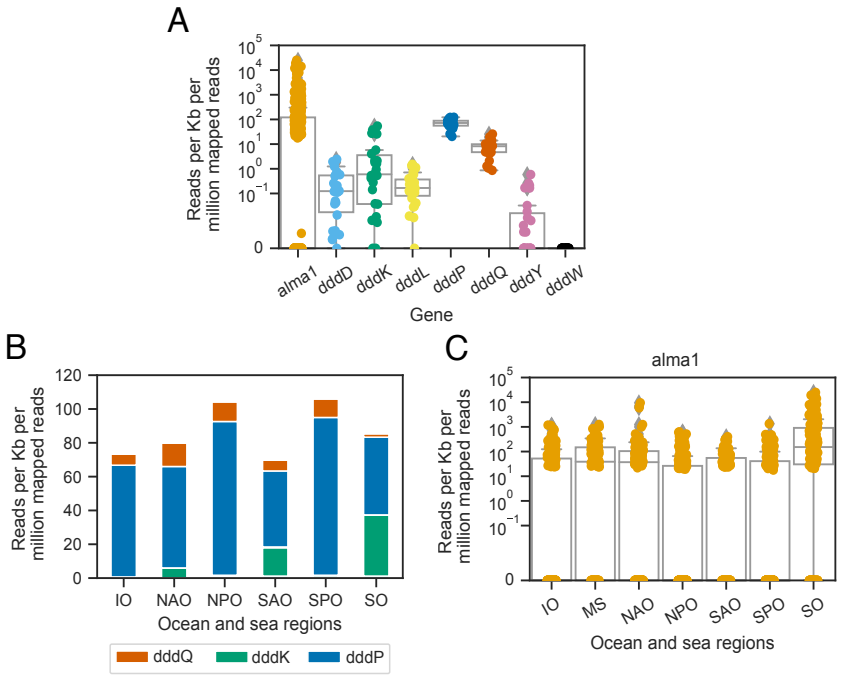

Supp. Fig. 6: Transcriptomic data for the expression of DMSP lyases from the Tara Oceans expedition (Pesant et al., 2015), in reads per kilobase per million mapped reads. The data belongs to the filter fraction $< 3\mu M$ and was compiled by Curson et al., 2018 and Vorobev et al., 2020. (A) Expression of DMSP lyase (cleavage pathway) genes. The y-axis is in linear scale from 0 to 10^{-1} and in log scale from 10^{-1} on. Note that the median for alma1 and dddY is 0. (B) Expression of bacterial DMSP lyase (cleavage pathway) genes across ocean and sea regions. The genes that are not shown have too low numbers to be visible in the plot. (C) Expression of Alma1 (eukaryotic DMSP lyase) across ocean and sea regions. Note that the medians are different from 0 only in the Mediterranean Sea, the North Atlantic and the Southern Ocean. Conventions for B and C: IO: Indian Ocean, MS: Mediterranean Sea, NAO: North Atlantic Ocean, NPO: North Pacific Ocean, SAO: South Atlantic Ocean, SPO: South Pacific Ocean SO: Southern Ocean.

References

Alcolombri, U., Ben-Dor, S., Feldmesser, E., Levin, Y., Tawfik, D. S., & Vardi, A. (2015). Identification of the algal dimethyl sulfide-releasing enzyme: A missing link in the marine sulfur cycle. *Science*, *348*(6242), 1466–1469.

Alcolombri, U., Elias, M., Vardi, A., & Tawfik, D. S. (2014). Ambiguous evidence for assigning DddQ as a dimethylsulfoniopropionate lyase and oceanic dimethylsulfide producer. *Proceedings of the National Academy of Sciences*, *111*(20), 2078–2079. https://doi.org/10.1073/pnas.1401685111

Alcolombri, U., Laurino, P., Lara-Astiaso, P., Vardi, A., & Tawfik, D. S. (2014). DddD is a CoA-transferase/lyase producing dimethyl sulfide in the ma-

rine environment. *Biochemistry*, *53*, 5473–5475. https://doi.org/10.1021/bi500853s

Amrani, A., Said-Ahmad, W., Shaked, Y., & Kiene, R. P. (2013). Sulfur isotope homogeneity of oceanic DMSP and DMS. *Proceedings of the National Academy of Sciences*, *110*(46), 18413–18418.

Barak-Gavish, N., Frada, M. J., Ku, C., Lee, P. A., DiTullio, G. R., Malitsky, S., Aharoni, A., Green, S. J., Rotkopf, R., Kartvelishvily, E., Sheyn, U., Schatz, D., & Vardi, A. (2018). Bacterial virulence against an oceanic bloom-forming phytoplankter is mediated by algal DMSP. *Science Advances*, *4*(10), eaau5716. https://doi.org/10.1126/sciadv.aau5716

Bates, T. S. (1994). The cycling of sulfur in surface seawater of the northeast Pacific. *Journal of Geophysical Research*, *99*(C4), 7835–7843. https://doi.org/10.1029/93JC02782

Burkhardt, I., Lauterbach, L., Brock, N. L., & Dickschat, J. S. (2017). Chemical differentiation of three DMSP lyases from the marine: Roseobacter group. *Organic and Biomolecular Chemistry*, *15*(20), 4432–4439. https://doi.org/10.1039/c7ob00913e

Canfield, D. E., & Thamdrup, B. (1994). The Production of 34S-Depleted Sulfide During Bacterial Disproportionation of Elemental Sulfur. *Science*, *266*(5193), 1973–1975. https://doi.org/10.1126/science.11540246

Carnat, G., Said-ahmad, W., Fripiat, F., Wittek, B., Tison, J.-l., Uhlig, C., & Amrani, A. (2018). Variability in sulfur isotope composition suggests unique dimethylsulfoniopropionate cycling and microalgae metabolism in Antarctic sea ice. *Communications Biology*, *1*(212). https://doi.org/10.1038/s42003-018-0228-y

Charlson, R., Lovelock, J., Andreae, M., & Warren, S. (1987). Ocean phytoplankton, atmospheric sulfur, cloud albedo, and climate. *Nature*, *326*, 655–661.

Curson, A. R. J., Williams, B. T., Pinchbeck, B. J., Sims, L. P., Martínez, A. B., Rivera, P. P. L., Kumaresan, D., Mercadé, E., Spurgin, L. G., Carrión, O., Moxon, S., Cattolico, R. A., Kuzhiumparambil, U., Guagliardo, P., Clode, P. L., Raina, J.-b., & Todd, J. D. (2018). DSYB catalyses the key step of dimethylsulfoniopropionate biosynthesis in many phytoplankton. *Nature Microbiology*, *3*, 430–439. https://doi.org/10.1038/s41564-018-0119-5

Curson, A. R., Sullivan, M. J., Todd, J. D., & Johnston, A. W. (2011). DddY, a periplasmic dimethylsulfoniopropionate lyase found in taxonomically diverse species of Proteobacteria. *ISME Journal*, *5*(7), 1191–1200. https://doi.org/10.1038/ismej.2010.203

De Souza, M. P., & Yoch, D. C. (1995). Purification and characterization of dimethylsulfoniopropionate lyase from an Alcaligenes-like dimethyl sulfide-producing marine isolate. *Applied and Environmental Microbiology*, *61*(1), 21–26. https://doi.org/10.1128/aem.61.1.21-26.1995

Dickson, D. M. J., & Kirst, G. O. (1987). Osmotic adjustment in marine eukaryotic algae: the role of inorganic ions, quaternary ammonium, tertiary sulphonium and carbohydrate solutes: I. Diatoms and a rhodophyte. *New Phytologist*, *106*(4), 645–655.

Fakhraee, M., & Katsev, S. (2019). Organic sulfur was integral to the Archean sulfur cycle. *Nature Communications*, *10*(1), 4556. https://doi.org/10.1038/s41467-019-12396-y

Fike, D. A., Bradley, A. S., & Rose, C. V. (2015). Rethinking the ancient sulfur cycle. *Annual Review of Earth and Planetary Sciences*, *43*, 593–622.

Garrels, R. M., & Lerman, A. (1981). Phanerozoic cycles of sedimentary carbon and sulfur. *Proceedings of the National Academy of Sciences*, *78*(8), 4652–4656. https://doi.org/10.1073/pnas.78.8.4652

Goldstein, M. J. (1966). Kinetic isotope effects and organic reaction mechanisms. *Nature*, *154*(3757), 1616–1621.

Gutierrez-Rodriguez, A., Pillet, L., Biard, T., Said-Ahmad, W., Amrani, A., Simó, R., & Not, F. (2017). Dimethylated sulfur compounds in symbiotic protists: A potentially significant source for marine DMS(P). *Limnology and Oceanography*, *62*(3), 1139–1154. https://doi.org/10.1002/lno.10491

Hayes, J. M. (2001). Fractionation of carbon and hydrogen isotopes in biosynthetic processes. *Reviews in Mineralogy and Geochemistry*, *43*(1), 225–277.

Holland, H. D. (1973). Systematics of the isotopic composition of sulfur in the oceans during the Phanerozoic and its implications for atmospheric oxygen. *Geochimica et Cosmochimica Acta*, *37*(12), 2605–2616. https://doi.org/10.1016/0016-7037(73)90268-8

Johnson, W. M., Kido Soule, M. C., & Kujawinski, E. B. (2016). Evidence for quorum sensing and differential metabolite production by a marine bacterium in response to DMSP. *The ISME Journal*, *10*(9), 2304–2316. https://doi.org/10.1038/ismej.2016.6

Jørgensen, B. B. (1982). Mineralization of organic matter in the sea bed - the role of sulphate reduction. *Nature*, *296*(5858), 643–645.

Kaplan, I. R., & Rittenberg, S. C. (1964). Microbiological Fractionation of Sulphur Isotopes. *Journal of General Microbiology*, *34*(2), 195–212. https://doi.org/10.1099/00221287-34-2-195

Karsten, U., Kück, K., Vogt, C., & Kirst, G. O. (1996). Dimethylsulfoniopropionate Production in Phototrophic Organisms and its Physiological Functions as a Cryoprotectant. In R. P. Kiene, P. T. Visscher, M. D. Keller, & G. O. Kirst (Eds.), *Biological and environmental chemistry of dmsp and related sulfonium compounds* (pp. 143–153). Springer US. https://doi.org/10.1007/978-1-4613-0377-0_13

Kettle, A. J., Andreae, M. O., Amouroux, D., Andreae, T. W., Bates, T. S., Berresheim, H., Bingemer, H., Boniforti, R., Curran, M. A., DiTullio, G. R., Helas, G., Jones, G. B., Keller, M. D., Kiene, R. P., Leek, C., Levasseur, M., Malin, G., Maspero, M., Matrai, P., . . . Uher, G. (1999). A global database of sea surface dimethylsulfide (DMS) measurements and a procedure to predict sea surface DMS as a function of latitude, longitude, and month. *Global Biogeochemical Cycles*, *13*(2), 399–444. https://doi.org/10.1029/1999GB900004

Kiene, R. P., Linn, L. J., & Bruton, J. A. (2000). New and important roles for DMSP in marine microbial communities. *Journal of Sea Research*, *43*(3-4), 209–224. https://doi.org/10.1016/S1385-1101(00)00023-X

Kirkwood, M., Le Brun, N. E., Todd, J. D., & Johnston, A. W. (2010). The dddP gene of Roseovarius nubinhibens encodes a novel lyase that cleaves dimethylsulfoniopropionate into acrylate plus dimethyl sulfide. *Microbiology*, *156*(6), 1900–1906. https://doi.org/10.1099/mic.0.038927-0

Kirst, G. O., Thiel, C., Wolff, H., Nothnagel, J., Wanzek, M., & Ulmke, R. (1991). Dimethylsulfoniopropionate (DMSP) in icealgae and its possible biological role. *Marine Chemistry*, *35*(1-4), 381–388.

Ksionzek, K. B., Lechtenfeld, O. J., McCallister, S. L., Schmitt-Kopplin, P., Geuer, J. K., Geibert, W., & Koch, B. P. (2016). Dissolved organic sulfur in the ocean: Biogeochemistry of a petagram inventory. *Science*, *354*(6311), 456–459.

Landa, M., Burns, A. S., Durham, B. P., Esson, K., Nowinski, B., Sharma, S., Vorobev, A., Nielsen, T., Kiene, R. P., Moran, M. A., & Moran, M. A. (2019). Sulfur metabolites that facilitate oceanic phytoplankton – bacteria carbon flux. *The ISME journal*, *13*, 2536–2550. https://doi.org/10.1038/s41396-019-0455-3

Lei, L., Alcolombri, U., & Tawfik, D. S. (2018). Biochemical Profiling of DMSP Lyases. *Methods in enzymology* (pp. 269–289). Elsevier.

Lei, L., Cherukuri, K. P., Alcolombri, U., Meltzer, D., & Tawfik, D. S. (2018). The Dimethylsulfoniopropionate (DMSP) Lyase and Lyase-Like Cupin Family Consists of Bona Fide DMSP lyases as Well as Other Enzymes with Unknown Function. *Biochemistry*, *57*, 3364–3377.

Levine, N. M. (2016). Putting the spotlight on organic sulfur. *Science*, *354*(6311), 418–419. https://doi.org/10.1126/science.aai8650

Levine, N. M., Varaljay, V. A., Toole, D. A., Dacey, J. W. H., Doney, S. C., & Moran, M. A. (2012). Environmental, biochemical and genetic drivers of DMSP degradation and DMS production in the Sargasso Sea. *Environmental microbiology*, *14*(5), 1210–1223.

Li, C.-y., Wei, T.-d., Zhang, S.-h., Chen, X.-l., Gao, X., Wang, P., & Xie, B.-b. (2014). Molecular insight into bacterial cleavage of oceanic dimethylsulfoniopropionate into dimethyl sulfide. *Proceedings of the National Academy of Sciences*, *111*(3), 1026–1031. https://doi.org/10.1073/pnas.1312354111

Li, C.-y., Zhang, D., Chen, X.-L., Wang, P., Shi, W.-L., Li, P.-Y., Zhang, X.-y., Qin, Q.-L., Todd, J. D., & Zhang, Y.-Z. (2017). Mechanistic Insights into Dimethylsulfoniopropionate Lyase DddY , a New Member of the Cupin Superfamily. *Journal of Molecular Biology*, *429*(24), 3850–3862. https://doi.org/10.1016/j.jmb.2017.10.022

Mariotti, A., Germon, J. C., Hubert, P., Kaiser, P., Letolle, R., Tardieux, A., & Tardieux, P. (1981). Experimental determination of nitrogen kinetic isotope fractionation: Some principles; illustration for the denitrification and nitrification processes. *Plant and Soil*, *62*(3), 413–430. https://doi.org/10.1007/BF02374138

Morris, A. W., & Riley, J. P. (1966). The bromide / chlorinity and sulphate / chlorinity ratio in sea water. *Deep Sea Research*, *13*, 699–705.

Oduro, H., Van Alstyne, K. L., & Farquhar, J. (2012). Sulfur isotope variability of oceanic DMSP generation and its contributions to marine biogenic sulfur emissions. *Proceedings of the National Academy of Sciences*, *109*(23), 9012–9016.

Peng, M., Chen, X.-l., Zhang, D., Wang, X.-j., Wang, N., Wang, P., & Todd, J. D. (2019). Structure-Function Analysis Indicates that an Active-Site Water Molecule Participates in Dimethylsulfoniopropionate Cleavage by DddK. *Applied and Environmental Microbiology*, *85*(8), 1–11.

Pesant, S., Not, F., Picheral, M., & Kandels-lewis, S. (2015). Open science resources for the discovery and analysis of Tara Oceans data. *Scientific Data*, *2*, 1–16. https://doi.org/10.1038/sdata.2015.23

Quinn, P. K., & Bates, T. S. (2011). The case against climate regulation via oceanic phytoplankton sulphur emissions. *Nature*, *480*(7375), 51–56. https://doi.org/10.1038/nature10580

Reisch, C. R., Moran, M. A., & Whitman, W. B. (2008). Dimethylsulfoniopropionate-dependent demethylase (DmdA) from Pelagibacter ubique and Silicibacter pomeroyi. *Journal of bacteriology*, *190*(24), 8018–8024.

Rusch, D. B., Halpern, A. L., Sutton, G., Heidelberg, K. B., Williamson, S., Yooseph, S., Wu, D., Eisen, J. A., Hoffman, J. M., Remington, K., Beeson, K., Tran, B., Smith, H., Baden-Tillson, H., Stewart, C., Tho, J., & Venter, C. (2007). The Sorcerer II Global Ocean Sampling expedition: Northwest Atlantic through Eastern Tropical Pacific. *PLoS Biology*, *5*(3), e77.

Sanchez, K. J., Chen, C. L., Russell, L. M., Betha, R., Liu, J., Price, D. J., Massoli, P., Ziemba, L. D., Crosbie, E. C., Moore, R. H., Müller, M., Schiller, S. A., Wisthaler, A., Lee, A. K., Quinn, P. K., Bates, T. S., Porter, J., Bell, T. G., Saltzman, E. S., . . . Behrenfeld, M. J. (2018). Substantial Seasonal Contribution of Observed Biogenic Sulfate Particles to Cloud Condensation Nuclei. *Scientific Reports*, *8*(1), 1–14. https://doi.org/10.1038/s41598-018-21590-9

Schnicker, N. J., De Silva, S. M., Todd, J. D., & Dey, M. (2017). Structural and Biochemical Insights into Dimethylsulfoniopropionate Cleavage by Cofactor-Bound DddK from the Prolific Marine Bacterium Pelagibacter. *Biochemistry*, *56*(23), 2873–2885. https://doi.org/10.1021/acs.biochem.7b00099

Scott, K. M., Lu, X., Cavanaugh, C. M., & Liu, J. S. (2004). Optimal methods for estimating kinetic isotope effects from different forms of the Rayleigh distillation equation. *Geochimica et Cosmochimica Acta*, *68*(3), 433–442. https://doi.org/10.1016/S0016-7037(03)00459-9

Seymour, J. R., Simó, R., Ahmed, T., & Stocker, R. (2010). Chemoattraction to dimethylsulfoniopropionate throughout the marine microbial food web. *Science*, *329*(5989), 342–345.

Sim, M. S., Bosak, T., & Ono, S. (2011). Large Sulfur Isotope Fractionation Does Not Require Disproportionation. *Science*, *333*, 74–77. https://doi.org/10.1089/jmf.2016.3871

Simó, R. (2001). Production of atmospheric sulfur by oceanic plankton: Biogeochemical, ecological and evolutionary links. *Trends in Ecology and Evolution*, *16*(6), 287–294. https://doi.org/10.1016/S0169-5347(01)02152-8

So, L. H., Ghosh, A., Zong, C., Sepúlveda, L. A., Segev, R., & Golding, I. (2011). General properties of transcriptional time series in Escherichia coli. *Nature Genetics*, *43*(6), 554–560. https://doi.org/10.1038/ng.821

Sousa, S. F., Cerqueira, N. M., Brás, N. F., Fernandes, P. A., & Ramos, M. J. (2014). Enzymatic "tricks": Carboxylate shift and sulfur shift. *International Journal of Quantum Chemistry*, *114*(19), 1253–1256. https://doi.org/10.1002/qua.24689

Spielmeyer, A., & Pohnert, G. (2010). Direct quantification of dimethylsulfoniopropionate (DMSP) with hydrophilic interaction liquid chromatography/mass spectrometry. *Journal of Chromatography B: Analytical Technologies in the Biomedical and Life Sciences*, *878*(31), 3238–3242. https://doi.org/10.1016/j.jchromb.2010.09.031

Sunda, W., Kieber, D. J., Kiene, R. P., & Huntsman, S. (2002). An antioxidant function for DMSP and DMS in marine algae. *Nature*, *418*, 317–320.

Tang, K. (2020). Chemical Diversity and Biochemical Transformation of Biogenic Organic Sulfur in the Ocean. *Frontiers in Marine Science*, *7*, 1–15. https://doi.org/10.3389/fmars.2020.00068

Todd, J. D., Curson, A. R., Kirkwood, M., Sullivan, M. J., Green, R. T., & Johnston, A. W. (2011). DddQ, a novel, cupin-containing, dimethylsulfoniopropionate lyase in marine roseobacters and in uncultured marine bacteria. *Environmental Microbiology*, *13*(2), 427–438. https://doi.org/10.1111/j.1462-2920.2010.02348.x

Todd, J. D., Rogers, R., Guo Li, Y., Wexler, M., Bond, P. L., Sun, L., Curson, A. R., Malin, G., Steinke, M., & Johnston, A. W. (2007). Structural and Regulatory Genes Required to Make the Gas Dimethyl Sulfide in Bacteria. *Science*, *315*, 666–669.

Tripp, H. J., Kitner, J. B., Schwalbach, M. S., Dacey, J. W., Wilhelm, L. J., & Giovannoni, S. J. (2008). SAR11 marine bacteria require exogenous reduced sulphur for growth. *Nature*, *452*(7188), 741–744. https://doi.org/10.1038/nature06776

Varaljay, V. A., Robidart, J., Preston, C. M., Gifford, S. M., Durham, B. P., Burns, A. S., Ryan, J. P., Marin, R., Kiene, R. P., Zehr, J. P., Scholin, C. A., Moran, M. A., Marin III, R., Kiene, R. P., & Zehr, J. P. (2015). Single-taxon field measurements of bacterial gene regulation controlling DMSP fate. *ISME Journal*, *9*(7), 1677–1686. https://doi.org/10.1038/ismej.2015.23

Vorobev, A., Dupouy, M., Carradec, Q., Delmont, T., Annamale, A., Wincker, P., & Pelletier, E. (2020). Transcriptome reconstruction and functional analysis of eukaryotic marine plankton communities via high-throughput metagenomics and metatranscriptomics. *Genome Research*, *30*(4), 647–659. https://doi.org/10.1101/gr.253070.119

Wang, P., Chen, X.-l., Li, C.-y., Gao, X., Zhu, D.-y., Xie, B.-b., Qin, Q.-l., Zhang, X.-y., Su, H.-n., & Zhang, Y.-z. (2015). Structural and molecular basis for the novel catalytic mechanism and evolution of DddP , an abundant peptidase-like bacterial Dimethylsulfoniopropionate lyase : a new enzyme from an old fold. *Molecular Microbiology*, *98*(2), 289–301. https://doi.org/10.1111/mmi.13119

Wang, S., Maltrud, M. E., Burrows, S. M., Elliott, S. M., & Cameron-Smith, P. (2018). Impacts of Shifts in Phytoplankton Community on Clouds and Climate via the Sulfur Cycle. *Global Biogeochemical Cycles*, *32*(6), 1005–1026. https://doi.org/10.1029/2017GB005862

Williams, B. T., Cowles, K., Bermejo Martínez, A., Curson, A. R., Zheng, Y., Liu, J., Newton-Payne, S., Hind, A. J., Li, C. Y., Rivera, P. P. L., Carrión, O., Liu, J., Spurgin, L. G., Brearley, C. A., Mackenzie, B. W., Pinchbeck, B. J., Peng, M., Pratscher, J., Zhang, X. H., . . . Todd, J. D. (2019). Bacteria are important dimethylsulfoniopropionate producers in coastal sediments. *Nature Microbiology*, *4*(11), 1815–1825. https://doi.org/10.1038/s41564-019-0527-1

Wolfe, G. V., Steinke, M., & Kirst, G. O. (1997). Grazing-activated chemical defence in a unicellular marine alga. *Nature*, *387*(6636), 894–897. https://doi.org/10.1038/43168

Yoch, D. C. (2002). Dimethylsulfoniopropionate: Its Sources, Role in the Marine Food Web, and Biological Degradation to Dimethylsulfid. *Applied and Environmental Microbiology*, *68*(12), 5804–5815. https://doi.org/10.1128/AEM.68.12.5804

Zubkov, M. V., Fuchs, B. M., Archer, S. D., Kiene, R. P., Amann, R., & Burkill, P. H. (2002). Rapid turnover of dissolved DMS and DMSP by defined bacterioplankton communities in the stratified euphotic zone of the North Sea. *Deep-Sea Research Part II: Topical Studies in Oceanography*, *49*(15), 3017–3038. https://doi.org/10.1016/S0967-0645(02)00069-3

Chapter 3

MICROBIAL CYCLING OF SULFUR AND OTHER REDOX-SENSITIVE ELEMENTS IN POREWATERS AND SEDIMENTS OF COCOS RIDGE, COSTA RICA

Daniela Osorio-Rodriguez[1], Frank J. Pavia[1], Selva M. Marroquín[1], Daniel R. Utter[1], Kameko Landry[2], Maya Gomes[3], Nathan D. Dalleska[1], Victoria J. Orphan[1], William M. Berelson[4], Jess F. Adkins[1]

[1]Division of Geological and Planetary Sciences, California Institute of Technology, Pasadena, CA, 91125
[2]Department of Earth and Environmental Sciences, Boston College, MA, 02467, USA
[3]Department of Earth and Planetary Sciences, University of John's Hopkins, MD, 21210, USA
[4]Department of Earth Sciences, University of Southern California, Los Angeles, CA, 90089, USA

Abstract

The microbial recycling of organic matter in marine sediments depends upon electron acceptors that are utilized based on availability and energetic yield. Since sulfate is the most abundant oxidant once oxygen has been depleted, the sulfide produced after sulfate reduction becomes an important electron donor for autotrophic microbes. The ability of sulfide to be re-oxidized through multiple metabolic pathways and intermediates with variable oxidation states prompts investigation into which species are preferentially utilized and what are the factors that determine the fate of reduced sulfur species. Quantifying these sulfur intermediates in porewaters is a critical first step towards achieving a more complete understanding of the oxidative sulfur cycle, yet this has been reported in fewer than 30 studies, none of which include oligotrophic sedimentary environments in the open ocean. Here we provide the first profiles of porewater sulfur intermediates from a multicore in the

San Clemente Basin (SCB), California, and three gravity cores collected at different depths near Cocos Ridge (CR), Costa Rica. We complement this information with depth profiles of major ions, sulfate isotope compositions, and redox-sensitive metals, and integrate these datasets with 16S rRNA microbial community composition data and solid-phase sulfur concentrations. We did not find significant correlations between S species or trace metals and specific S-cycling taxa at SCB or CR, which suggests that sediment microorganisms in pelagic, and oxic sediments may be generalists utilizing flexible metabolisms to oxidize organic matter with different electron acceptors.

1. INTRODUCTION

In deep sea sediment porewaters, electron acceptors are utilized for the remineralization of organic matter depending on their energetic yields and thermodynamic constraints in the following order: O_2, NO_3^-, MnO_2, Fe_2O_3, and SO_4^{2-} (Bender and Heggie, 1984; Froelich et al., 1979; Jørgensen, 1982; Stumm and Morgan, 1970). Typically, respiration processes for one of these electron acceptors should not begin until the previous one has been exhausted (Canfield and Thamdrup, 2009), but overlaps in natural environments are common, for instance, between the oxygen and nitrate (Jensen et al., 2008; Robertson et al., 1995), and the iron and sulfate (Canfield, Thamdrup, et al., 1993; Canfield, Jørgensen, et al., 1993) reduction zones. Half of the organic matter in coastal sediments gets remineralized through sulfate reduction (Canfield, 1989; Jørgensen, 1982), because of two main reasons: 1) the high abundance of marine sulfate (28 mM; Stumm and Morgan, 1970), enhanced by the solubility of sulfate salts, which makes it far more abundant that oxygen (~0.4 mM; Garcia et al., 2019), and 2) the high fluxes of labile organic carbon that characterize these settings (Berner, 1978; Goldhaber and Kaplan, 1975; Toth and Lerman, 1977), which lead to the rapid consumption of more energetically favorable elec-

tron acceptors like oxygen and nitrate, leaving sulfate as a major electron acceptor. Because of this, sulfate reduction dynamics have received considerable attention, particularly in coastal sediments (Berner, 1964; Kaplan et al., 1963; Raven et al., 2016; Thamdrup et al., 1994; Troelsen and Jørgensen, 1982). Global estimates suggest that 29% of the marine organic carbon flux gets remineralized through sulfate reduction on the seafloor, generating 11.3 teramoles of sulfide every year (Bowles et al., 2014). More than 90% of sulfide produced from sulfate reduction in marine sediments gets reoxidized to sulfate by biotic or abiotic means (Jørgensen, 1982) via the production of sulfur species with intermediate valence states, such as thiosulfate ($S_2O_3^{2-}$; Jørgensen, 1990), sulfite (SO_3^{2-}; Thamdrup et al., 1994), and elemental sulfur (S_0; Canfield, 2001; Troelsen and Jørgensen, 1982). These reduced sulfur intermediates may be utilized as a source of energy through oxidation (Troelsen and Jørgensen, 1982) or disproportionation (Bak and Pfennig, 1987; Bak and Cypionka, 1987) by marine microorganisms, in some cases leading to so-called cryptic sulfur cycles, in which sulfide is not detectable despite observations of active sulfate reduction, in particular at oxygen minimum zones and sulfate-methane transition zones (Holmkvist, Ferdelman, et al., 2011; Holmkvist, Kamyshny Jr, et al., 2011).

Sulfur isotopes have been used to characterize the microbial transformations of sulfur since S isotope fractionation during bacterial sulfate reduction (BSR) was first reported in 1951 (Thode et al., 1951). When sulfate is used as the electron acceptor for the oxidation of organic matter (dissimilatory BSR), sulfur isotope fractionation factors can range from slightly positive down to -66‰ (Detmers et al., 2001). Decades of research on the biological fractionation of sulfur isotopes (Canfield, 2001; Chambers and Trudinger, 1979) have led us to understand that the fractionation during dissimilatory BSR is negatively correlated with the availability of electron donor (Harrison and Thode, 1958; Kaplan and Rittenberg, 1964) and the specific rate of sulfate reduction (Habicht and Canfield, 1997), and often positively correlated

with sulfate concentrations (Habicht and Canfield, 1997; Jones and Starkey, 1957). Oxygen isotopes of sulfate are also an important tool to constrain the cycling of sulfur, because sulfate does not easily exchange oxygen atoms with water (Lloyd, 1968) but sulfur intermediates such as such as adenosine phosphosulfate (APS; Kemp and Thode, 1968; Mizutani and Rafter, 1973) and sulfite (Fritz et al., 1989) potentially do. As a result, the presence of non-marine $\delta^{18}O$ of SO_4 in porewater species implies that sulfate has originated from the microbial oxidation of reduced sulfur species.

Enclosed basins with low oxygen, high sulfide, and high organic matter content (Findlay et al., 2015; Hayes et al., 2006; Raven et al., 2015), such as the Black Sea (Zopfi et al., 2004) and the Santa Barbara Basin (Raven et al., 2016), have received the most attention regarding the oxidative sulfur cycle. In contrast, there has been a paucity of studies regarding the potential of oxic or hypoxic pelagic sediments to harbor intermediate sulfur species, which might be relevant for sustaining microbial communities, in particular where the availability of organic matter as an oxidant is low. The observation that sulfate in pelagic sediments shows little change in concentration with depth and has low reduction rates (Canfield and Des Marais, 1991) due to the absence of strong anoxic conditions (Froelich et al., 1979) might have led to the assumption that reduced sulfur species are negligible in these environments. However, sulfate reduction is reported in oxygenated environments (Canfield, 1991; Jorgensen and Bak, 1991), and also at micromolar concentrations in the deep ocean (Holmkvist, Ferdelman, et al., 2011; Holmkvist, Kamyshny Jr, et al., 2011), which suggests that an oxidative sulfur cycle could be active and relevant even under a low abundance of reduced sulfur species.

Here, we present the first profiles of porewater sulfur intermediates for pelagic sediments near Cocos Ridge (CR) in the Eastern Equatorial Pacific, as well as a 40 cm core from the San Clemente Basin (SCB). We complement them with

concentration, oxygen, and sulfur isotope profiles for sulfate, as well as concentration profiles of major ions, iron, and manganese. Most of these are sampled at 3 to 5 cm resolution across a depth of 1.2 to 2 meters, aiming at characterizing the extent of electron acceptor reaction zones within the sediments. We also provide 16S rRNA data for the sediment microbial community composition, as well as solid-phase organic carbon and elemental sulfur concentrations. We demonstrate that nM concentrations of thiosulfate, sulfite and sulfide are indeed present in pelagic, mostly oxygenated sediments, and can be detected with the bromobimane derivatization method using a combination of mass spectrometry and fluorescent detectors in a liquid chromatograph. We find that the diversity and type of 16S rRNA sequence variants are slightly correlated with depth, but not with locality or abundance of sulfur, manganese, and iron, which highlights the flexibility of microbial metabolism and the importance of integrating more comprehensive genomic and geochemical data towards a better understanding of global biogeochemical cycles.

2. MATERIALS AND METHODS

Site background and sample collection

The sediment cores analyzed in this study were collected in November and December 2021 as part of the *R/V Sally Ride* cruise SR2113. A 40 cm multi-core was taken from a depth of 1965 m at the San Clemente Basin (SCB) with a bottom water oxygen concentration of ~53 μM (Supp. Fig. 1). SCB is a semi-enclosed basin with one of the lowest sedimentation rates (~15 $\mathrm{mg/cm^2/yr}$) in the California Borderland (Schwalbach and Gorsline, 1985), and up to 2% TOC (Bender et al., 1989). Three 1.2-2 m gravity cores were collected at different stations, CR 02 (2633 m depth, ~100 μM bottom water O_2), CR 03 (1614 m depth, ~75 μM bottom water O_2), and CR 04 (1857 m depth, ~75 μM bottom water O_2) near Cocos Ridge in the Eastern Equatorial Pacific (Fig. 1) with sedimentation rates below 2 $\mathrm{mg/cm^2/yr}$ (Dong et

al., in prep; Supp. Fig. 1).

Immediately after collection, the cores were cut in ~70 cm fragments, drilled every 3 or 5 cm for < 0.4 mm diameter holes, and placed in an anaerobic bag filled with N_2 in a 4°C cold room. Rhizons (Rhizosphere Research Products) were inserted in the previously drilled holes for porewater collection. 2 ml of porewater were aliquoted into acid-washed vials for trace metal quantification, 2 ml were aliquoted into a vial for silica and major ion quantification, 1 ml was aliquoted in a vial with 1 ml of 1M $BaCl_2$ for precipitation of sulfate as $BaSO_4$, and 500 µl were aliquoted in a vial with 1 M zinc acetate for the precipitation of sulfide as ZnS. Vials were kept at 4°C until analysis. For preservation of reduced sulfur species, 150 µl of porewater were aliquoted in an amber vial with 150 µl of monobromobimane reagent (50 mM bromobimane in acetonitrile) and 225 µl of buffer (50 mM HEPES and 5 mM EDTA, pH 8). The reactions were quenched after 1h with the addition of 600 µl of 65 mM methanesulfonic acid, and the vials were kept at -20°C until analysis. We utilized derivatization with bromobimane to rapidly fix labile sulfur species and prevent their reactions with oxygen, and to enable non-destructive fluorescent detection (Smith et al., 2017). For sediment sampling, core fragments were taken outside the anaerobic bag and 1 cm diameter holes were drilled over the previously drilled holes. ~5 g of sediment was collected from each hole into a combusted and UV sterilized glass vial. The sediments were kept frozen at -80°C until analysis.

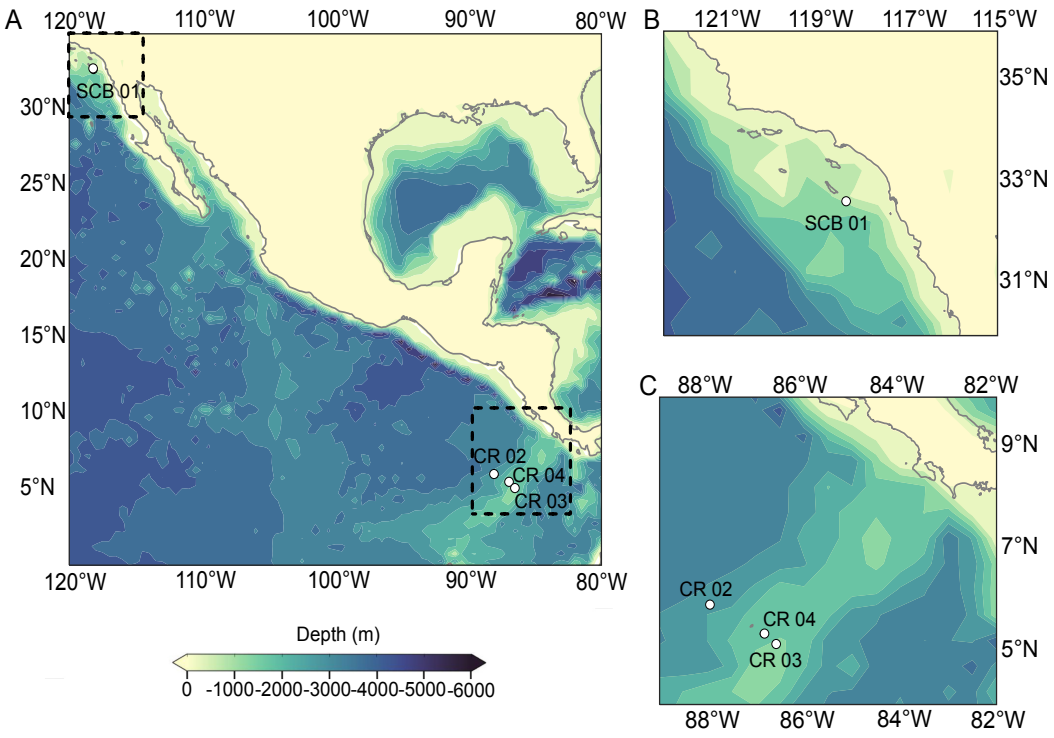

Figure 1: A) Map of the stations sampled for porewaters and sediments in this study. B) and C) show insets for the San Clemente Basin and Cocos Ridge stations, respectively, which correspond to the dashed squares in A).

Geochemical measurements

Porewaters

Major ions: Major ions were measured with parallel ion chromatography (IC) systems operated simultaneously (Thermo Integrion). Porewater samples from the San Clemente Basin multicore and the Cocos Ridge gravity cores were diluted 1:50 (for calcium, magnesium and sulfate) or 1:10 (for nitrate and strontium) with milli-Q water to a final volume of 5 ml, including an IAPSO salinity standard and an internal standard as quality controls every 5 samples, and a full standard curve at the beginning and the end of the run. 50 mM NaCl was used in the standards for matrix matching. Standard measurements were fitted to a line, and their ranges were ~2-600 μM. The detection limits were 10 µM and the relative standard deviations

were below 3%. The concentrations were normalized by sodium for potential evaporation. A single autosampler (Thermo AS-DV) loaded both the cation and anion systems' sample loops serially. The 5-microliter sample loop on the cation IC system was loaded first, followed by a 5-microliter sample loop on the anion IC system. Columns were maintained at 30°C, suppressors at 25°C, and detection was at 35°C. Anionic components in the sample were resolved using a AS-19 separator (2x250mm) column protected by an AG-19 guard (2x50mm). A hydroxide gradient was produced using a potassium hydroxide eluent generator cartridge and pumped at 0.25 mL per minute. The gradient began with a 10 mM hold for 5 minutes, increased linearly to 48.5 mM at 27 minutes and then to 50 mM until the end of data acquisition at 40 minutes. 10 minutes were allowed between analyses to return the column to initial conditions. Anions were detected at neutral pH using an ASRS-300 2mm suppressor (Thermo) operated in eluent recycle mode with an applied current of 30 mA and conductivity detection cell maintained at 35°C. Cations were resolved using a CS-16A separator column (2x250mm) protected by a CG-16A guard column (2x50). A methylsulfonic acid gradient was produced using a methylsulfonic acid-based eluent generated cartridge and pumped at 0.16 mL per minute. The initial concentration was 10 mM until 5 minutes, then increased to 20 mM at 20 minutes with a concave up profile (Chromeleon curve 7) and finally to 40 mM at 40 minutes with a convex down profile (Chromeleon curve 1). The column and detector systems were allowed to stabilize at the initial condition for 10 minutes in between runs. Suppressed conductivity detection using a Dionex CERS-500 2mm suppressor operated in eluent recycle mode with an applied current of 15 mA. Data was processed using ThermoFisher Scientific Chromeleon software, version 7.2.

Dissolved silica measurements were performed via a molybdenum blue spectrophotometric method (Parsons et al., 1984), and were used to correct the depths of the gravity cores by aligning them to multicores to account for loss of the sediment

at the sediment-water interface. The analytical precision of the measurements was 1.3%. We determined that the core collected at CR02 had an overpenetration of 3.5 cm and those collected at CR 03 and CR 04 had an overpenetration of 6 cm. The depths in the geochemical profiles we present have already incorporated this correction.

Trace metals: Iron and manganese concentrations were determined by Inductively Coupled Plasma - Mass Spectrometry (ICP-MS) using an Agilent 8800 QQQ-ICP-MS. The sample introduction system consisted of a micromist nebulizer, scott type spray chamber and fixed injector quartz torch. A guard electrode was used, and the plasma was operated at 1500 W. Measurements were made in no-gas single-quad mode or MS/MS mode with helium in the collision/reaction cell. External standards were prepared from mixed trace metal ICP-MS degree standards in 5% nitric acid from Inorganic Ventures/ I.V. Labs, Inc. (Lakewood, NJ, USA) in NaCl (to match the matrix of the samples) to a final concentration of ~1-50 ppb and 50 mM NaCl. Samples and standards were both analyzed at a dilution ratio of 20:1 5% nitric acid to sample. Detection limits for iron and manganese were 0.01 and 0.014 μM, and the relative standard deviation was 0.033 and 0.084%, respectively.

Reduced sulfur species: We attempted to measure sulfide through Cline assay (Cline, 1969), which has a detection limit of about 20 μM, but could not detect any. For this reason, we quantified sulfide, as well as sulfite and thiosulfate in porewater samples derivatized with monobromobimane in an AcquityTM ultra-performance liquid chromatograph (Waters, Milford, MA, USA) coupled to an ACQUITY fluorescence (FLR) and a Xevo G2-S electrospray ionization quadrupole time-of-flight (TOF) mass spectrometer (Waters Micromass, Manchester, England) [UPLC/ESI-Q-TOF-MS]. Mixed standards were prepared with serial dilutions of sodium thiosulfate, sodium sulfide and sodium sulfite (Sigma-Aldrich) in acetoni-

trile. Samples were prepared by diluting the samples 1:100 in acetonitrile to fall into the linear detection range of 0.005- 10 μM. The UPLC separation was carried out with an ACQUITY UPLC® BEH C18 column (2.1 mm × 50 mm, 1.7 μM, 130 A) maintained at 45°C using an injection volume of 1 μl. The elution profile contained a mobile phase comprised of 0.1% formic acid (solvent A) and 100%ACN (solvent B). Separation followed a modification of a previously described procedure(Smith et al., 2017). The program started with 95% A at a flow rate of 0.4 mL/min for 2.5 min, followed by 81% A until 4.2 min, 78% A until 4.25 min, 2% A until 5.1 min, and finally, the column was equilibrated for 0.4 min, resulting in a total analysis time of 5.5 min. The program started with effluent from the UPLC system was directed sequentially through an ACQUITY fluorescence (FLR) detector and a Xevo G2-S TOF mass spectrometer (both Waters).

The FLR detector was operated at an excitation wavelength of 380 nm and an emission wavelength of 480 nm. Mass spectrometry (MS) data was acquired with the TOF MS in negative resolution mode, with similar parameters as those used previously (Smith et al., 2017): source temperature 120°C, desolvation temperature 550°C, desolvation gas flow 800 L/h, capillary voltage 2.0 kV, cone voltage 40 V, cone gas flow 40 L/h, and flight tube 9.0 kV. Collision energy was 6.0 eV. Acquisition mass range was 50–1200 Da and the calibration mass range was 91.183– 1993.753 Da. A lock mass of 556.2771 Da was used to verify mass accuracy of ±3 mDa. The scan time was 0.2 s. Data was collected in centroid format. Sulfur species were quantified using the molecular ion.

We took several precautions to guarantee the quality of the data. FLR and MS measurements were consistently compared between each data point to assure the identity of the detected compound. Two seawater blanks which were derivatized and treated in the same way as samples were measured, and none of the reduced sulfur compounds was detected. Replicate analyses were performed on 3 depths

of each core (from which 3 separate samples were collected), and their standard deviations were 3.2, 5.4, and 4.1 for thiosulfate, sulfide, and sulfite, respectively. Instrumental stability (i.e., chromatographic and mass spectral reproducibility) was verified within 5% using a mixed standard solution run periodically (one standard every ten samples) during routine analysis. The detection limit was 5 nM for thiosulfate, and 10 nM for sulfide and sulfite. The relative standard deviation was below 5.1%, 3.4%, and 2.8% for the standard solutions of thiosulfate, sulfide, and sulfite, respectively. The integrated mass spectral peak area and integrated fluorescence peak area were recorded for each standard and sample using MassLynx® and QuanLynx® v4.1 software, which produced linear regressions of integrated peak area vs. concentration with average R^2 values ≥ 0.99.

δ^{34}S and δ^{18}O of sulfate: For sulfur isotope measurements, 0.03-0.05 mg of $\mathrm{BaSO_4}$ (plus 1 mg vanadium pentoxide) were weighed in tin capsules and measured as $\mathrm{SO_2}$ by EA-IRMS (flash combustion elemental analyzer coupled to a Delta V Plus IRMS via a Conflo IV universal interface) at Caltech. We report sulfur isotope ratios using the conventional delta notation relative to the international standard Vienna-Canyon Diablo Troilite (VCDT):

$$\delta^{34}\mathrm{S} = ({}^{34}\mathrm{R}_{\mathrm{sample}}/{}^{34}\mathrm{R}_{\mathrm{VCTD}}) - 1 \cdot 1000, \tag{3.1}$$

where ${}^{34}\mathrm{R}$ refers to the ${}^{34}\mathrm{S}/{}^{32}\mathrm{S}$ ratio. The values of each sample were corrected by subtracting the blank and using a linear interpolation between two in house working standards (sulfanilamide and seawater), with an analytical repeatability better than 0.12‰. For oxygen isotope measurements, 0.35–0.45 mg samples of $\mathrm{BaSO_4}$ were weighed out into silver boats. Analyses were performed on a Thermo Scientific Delta V Plus continuous-flow isotope ratio mass spectrometer via pyrolysis of $\mathrm{BaSO_4}$ to CO in a graphite crucible in a Temperature Conversion Element Analyzer (TC/EA) at Johns Hopkins University. We report oxygen isotope ratios using the conventional

delta notation relative to the international standard Vienna Standard Mean Ocean water (VSMOW):

$$\delta^{18}\mathrm{O} = ({}^{18}\mathrm{R}_{\mathrm{sample}}/{}^{18}\mathrm{R}_{\mathrm{VSMOW}}) - 1 \cdot 1000, \tag{3.2}$$

where ${}^{18}\mathrm{R}$ refers to the ${}^{18}\mathrm{R}/{}^{16}\mathrm{R}$ ratio. O isotope measurements were reproducible within 0.39‰ based on repeat analysis of international standards (IAEA SO-5, IAEA SO-6, and NBS 127).

Solid phase

Total organic carbon (TOC) concentration and δ^{13}C: About 1 mg of sediment from 20 depths of the CR 02 and CR 03 gravity cores each were decarbonized with the addition of 3 ml 1% hydrochloric acid in previously combusted glass vials. The reaction was left to proceed overnight, after which the sediments were centrifuged and washed two times with MilliQ water. Sediments were frozen at -80°C, freeze dried, and ~1 mg sample was weighted in tin capsules for carbon measurements. Carbon was measured as CO_2 by EA-IRMS (flash combustion elemental analyzer coupled to a Delta V Plus IRMS via a Conflo IV universal interface). We report carbon isotope ratios using the conventional delta notation relative to the international standard Vienna PeeDee Belemnite (VPDB)

$$\delta^{13}\mathrm{C} = ({}^{13}\mathrm{R}_{\mathrm{sample}}/{}^{13}\mathrm{R}_{\mathrm{VPDB}}) - 1 \cdot 1000, \tag{3.3}$$

where ${}^{13}\mathrm{R}$ refers to the ${}^{13}\mathrm{C}/{}^{12}\mathrm{C}$ ratio. The values of each sample were corrected by subtracting the blank and using a linear interpolation between two in-house working standards (methionine and glucose), with an analytical repeatability better than 0.09‰.

Elemental sulfur: Elemental sulfur was extracted by adding 10 ml of N_2-sparged methanol to 0.8-1.5 mg of sediment. After overnight incubation in a rotary

table, methanol was dried to a ~1ml volume, and the elemental sulfur in it was detected by reverse phase-HPLC and UV absorption at 263 nm. We utilized an Agilent 1100 with an Eclipse XDB-C18 (5 μm, 3x250 mm) column and an isocratic solvent of 95:5 methanol-water. Flow rate was 0.5 ml/min. The column was maintained at 35°C, and injection volume was 100 μl. A calibration curve was made by plotting integrated peak area against sulfur concentrations in a range of 0-100 μm. The standards were prepared by serial dilutions of a stock prepared by diluting 6 mg elemental sulfur in acetone with sonication and shaking, which was diluted in methanol to a concentration of 200 μm. The retention time for S_0 under these conditions was 8 min.

Microbiology

DNA extraction: DNA was extracted from subsamples taken from the San Clemente Basin multicore and the Cocos Ridge gravity cores sediments at 3 or 5 cm intervals. Briefly, 250 mg of sediment kept at -80°C was processed with the DNeasy PowerSoil Pro Kit (Qiagen, Valencia, CA, USA) according to the manufacturer's recommended protocol, including one extraction blank per 50 samples. Extracted DNA was quantified with Qubit (ThermoFisher Scientific, USA).

Microbial community composition analysis via 16S rRNA gene amplicon sequencing: PCR reactions to amplify the V4-V5 region of the 16S rRNA gene were set with ~10 ng DNA and the general archaeal/bacterial primers (Parada et al., 2016) with Illumina (San Diego, CA, USA) overhang (Illumina, 2013) for a 2-step amplification as in a previously described protocol (Aronson et al., 2022) with modifications. The first PCR mix was set up in two duplicate 15-ul reactions for each sample with Q5 Hot Start high-fidelity 2× master mix (New England Biolabs, Ipswich, MA, USA) in a 15-μl reaction volume according to the manufacturer's

directions, with annealing conditions of 54°C for 30 cycles. Duplicate PCR samples were then pooled and barcoded with Illumina Nextera XT index 2 primers that include unique 8-bp barcodes (P5 and P7). This second PCR step was identical to the first except with 2.5 μl of template in 25 μl of total reaction volume and run for 10 cycles annealed at 66°C. Barcoded samples were run on an agarose gel, and based on band intensity, were combined in approximately equimolar amounts into a single pool and purified by gel extraction using the Wizard SV Gel and PCR Clean-Up System A9281 (Promega, USA). The library pool was sequenced by Laragen (Culver City, CA) with 2x300 bp paired end on an Illumina MiSeq with the addition of 15-20% PhiX.

16S rRNA sequence processing and analysis: Forward and reverse primers were trimmed from the 5-end of sequences using cutadapt v 3.4 (Martin, 2011). The R code used for 16S rRNA sequence processing and analysis can be found in the reproducible workflow (https://github.com/daniosro/S_cycling_SCB_CR/code/analysis/DNA). DADA2 R package v 1.22.0 (Callahan et al., 2016) was used for the remaining sequence processing with default parameters (unless otherwise specified in the file '16S_rRNA_initial_processing.R'. Taxonomic assignments for ASVs were made using the DECIPHER package v 2.22.0 (Wright, 2016) with the SILVA (v 138) database (Quast et al., 2012; Yilmaz et al., 2014) combined with unpublished in-house full-length 16S sequences from various seep sites. Specifically, DECIPHER's IdTaxa function was implemented with a 40% confidence threshold. The data was saved as a taxonomy table ('decipher-tax-obj.RData' in the GitHub repository) where the counts for each taxonomy level were assigned to the corresponding categories. Sequences with a representation of less than 5% for each sample, as well as those assigned to mitochondria and chloroplasts, were categorized as "Other". Unassigned sequences at any taxonomy level were categorized as "Unclassified".

Downstream analyses and visualization were done using the R package phyloseq v 1.36.0 (McMurdie and Holmes, 2013). Statistical analyses, including diversity indices, and non-metric multidimensional scaling and correlation analyses, were conducted, and plots were produced in R using the packages vegan and ggplot2 (Oksanen et al., 2019; R Core Team, 2019; Wickham and Chang, 2016). ASV abundances were normalized to each sample's total reads and are reported as percent (relative) abundance. NMDS was performed on the phylum-level normalized counts data, generated through a variance stabilizing transformation to normalize across samples using the DESeq2 package. Alpha diversity was estimated using the Shannon index (Shannon, 1948). Depths with less than 600 reads were filtered out from the statistical analyses to minimize biases.

To investigate the sulfur-related community more closely, we determined the proportions of taxa that include sulfur transforming microorganisms at both locations. To eliminate potential noise, we excluded the samples from which less than 600 ASVs were retrieved, and we made bar charts by depth bins to normalize for local variations that could bias general trends in our high-resolution sampling (Fig. 5). We included phyla in which sulfur utilization genes or capabilities have been reported. Sulfur oxidation genes have been detected in *Bacteroidota*, *Alphaproteobacteria*, *Deltaproteobacteria*, *Actinobacteria*, *Marinimicrobia*, *Verrucomicrobia*, *Planctomycetes*, and *Chloroflexi* from lake sediments (Vigneron et al., 2021). Aditionally, *Beta-* and *Epsilonproteobacteria* (Pjevac, 2014), as well as *Spirochaetes* (Meyer et al., 2007), *Bacillus* (Xia et al., 2017), and *Thermoplasmatota* (Zheng et al., 2022), are known to possess genes involved in sulfur oxidation. The phylum *Nitrospirota* also includes sulfate-reducing bacteria and bacteria capable of disproportionating thiosulfate and elemental sulfur (Umezawa et al., 2020). The archaeal groups *Halobacterota* and *Crenarchaeota* from wetland (Mo et al., 2020; Sorokin et al., 2018) and marine ecosystems (Anderson et al., 2009) possess sulfate reduction

genes. However, since we did not detect any of the Crenarchaeota orders reported to have sulfur reduction or oxidation capabilities (Liu et al., 2012), we did not include this group. Other microbial groups where thiosulfate, sulfite, or sulfate reduction genes have been detected are *Actinobacteria* (Anantharaman et al., 2018), *Planctomycetes*, *Chloroflexi*, *Zixibacteria* (Vigneron et al., 2021), and *Acidobacteria* (Hausmann et al., 2018). Since the class *Deltaproteobacteria* was recently split into four phyla, including the *Desulfobacterota*, which comprises many organisms capable of reducing sulfur compounds via the DsrAB-dissimilatory sulfite reduction pathway (Waite et al., 2020), we included this phylum, as well as the phylum *Dadabacteria*, which has been proposed to get incorporated as part of the *Desulfobacterota* (Waite et al., 2020).

To further characterize the microbial communities identified, we utilized the Shannon diversity index as a measure of species richness and evenness of the community structure (Haegeman et al., 2013). We also performed non-metric multidimensional scaling (NMDS) analysis to identify similarities between the 16S rRNA sequences across samples and establish if any of the geochemical parameters we measured could be driving them. In order to further explore the association between the porewater geochemical parameters and the microbial community composition, we tested them for potential monotonic correlations through the Kendall rank correlation coefficient, adjusting the p-values for multiple environment comparison after Benjamini and Hochberg (1995).

Data and code availability

All data and custom scripts were collected and stored using Git version control. Code for raw data processing, analysis, and figure generation is available in the GitHub repository (https://github.com/daniosro/S_cycling_SCB_CR).

3. RESULTS

Porewater elemental concentrations

The profiles of redox-sensitive elements for San Clemente Basin multicore and Cocos Ridge, determined via IC (nitrate and sulfate) and ICP-MS (iron and manganese) are shown in Fig. 2. The profiles of calcium, magnesium and strontium, ions related to carbonate chemistry, were determined by IC and are shown in Supp. Fig. 2. We present all our geochemical profiles with a Savitzky-Golay filter, which smooths potential noise based on local least-squares polynomial approximation (Savitzky and Golay, 1964). At the San Clemente Basin (SCB), nitrate shows a rapid decrease from nearly 45 μM at the surface to 0 at about 10 cm depth. Dissolved iron starts to reach detectable levels below 6 cm depth to a concentration of up to 16 μM at 16 cm depth. Dissolved manganese increases rapidly in the top 4 cm of the multicore and is steady at about 110 μM until 20 cm depth, after which it decreases to 40 μM at 36 cm depth. A slight decrease of 1 mM in sulfate from seawater concentration (28 mM) is observed by depth 36 cm.

At Cocos Ridge, nitrate becomes exhausted at deeper depths than at SCB. At stations 3 and 4, the shallower sites at ~1600-1800m depth, nitrate, which is about ~ 45 μM at the sediment surface, was undetectable at 40 cm depth, and manganese stays close to 5 μM throughout the ~2 m sediment column. In contrast, at station 2 (~2600 m depth), nitrate disappears deeper, at 60 cm depth, and manganese increases with depth, reaching about 32 μM at 1.3 m depth. A similar behavior was observed for magnesium (Supp. Fig. 2), which decreases from ~53 to ~48 μM with depth for stations 3 and 4 and increases up to ~55 μM with depth for station 2. Dissolved iron starts increasing after 40 cm depth up to 4 μM at 1 m depth for station 3 and 12-14 μM at 1.2-1.4 m depth for stations 2 and 4, respectively. Sulfate stays above 27 mM throughout the 1.2 – 2 m porewater profiles at all the stations. Altogether,

porewater reveals subtle but active redox activity even in the low-sedimentation sites near Cocos Ridge.

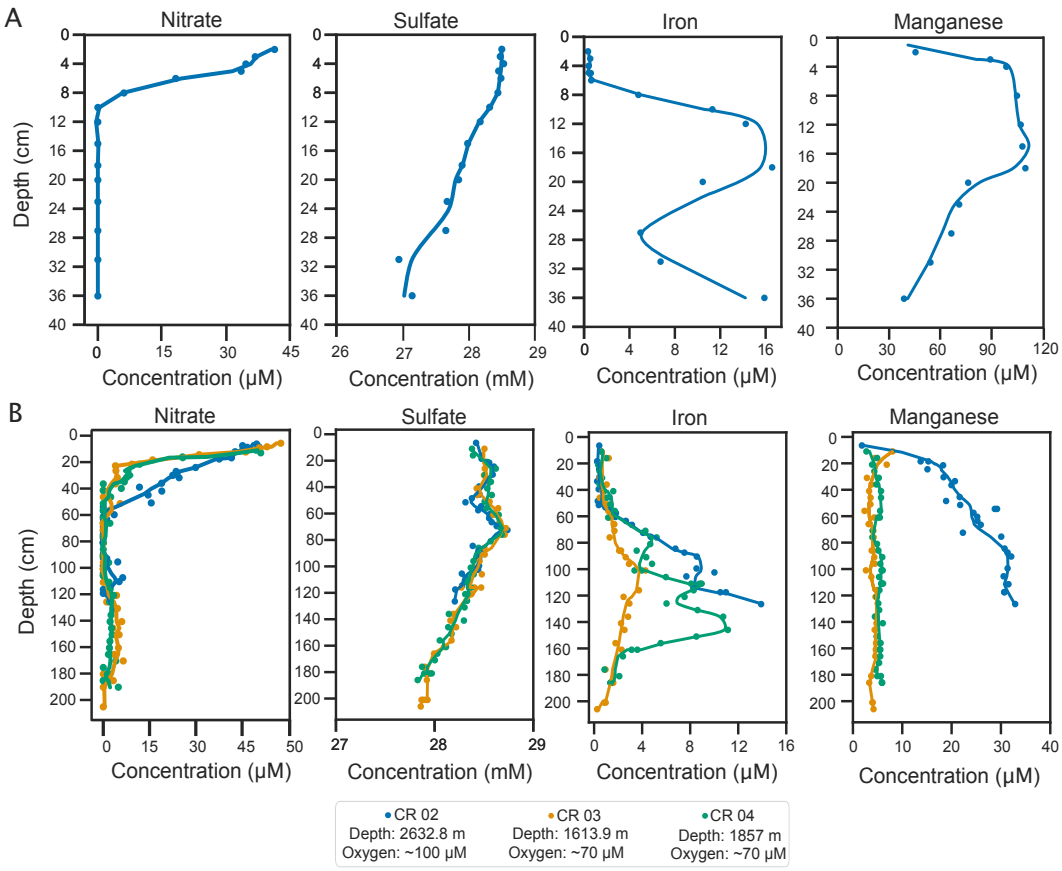

Figure 2: A) Porewater profiles of nitrate, sulfate, iron and manganese for (A) San Clemente Basin and (B) Cocos Ridge. The dots represent measured data, and the lines represent a Savitzky-Golay filter with a third-degree polynomial approximation to smoothening the data).

Sulfate isotope ratios and sulfur intermediate concentrations

In order to better understand the dynamics of sulfur cycling at Cocos Ridge, we determined the sulfur and oxygen isotopic compositions of porewater sulfate at stations CR02 and CR03 (Fig. 3). These are critical to understand the involvement of microorganisms in dissimilatory sulfur transformations, as will be explained in detail in the Discussion. We observed increases in the sulfur and oxygen isotopic compositions of sulfate with depth, and the rate of change varied over depth. We

further quantified reduced sulfur species from derivatized porewater samples for both San Clemente Basin and Cocos Ridge, and elemental sulfur in the solid phase for Cocos Ridge (Fig. 4). At San Clemente Basin, we measured concentrations below 20 nM for thiosulfate and sulfide, and below 125 nM for sulfite, for the 36 cm depth profile. At Cocos Ridge, sulfide was below 120 nM, sulfite was below 180 nM, and thiosulfate was below 100 nM. Peaks in the concentrations of sulfide and sulfite were observed both at the top and the bottom of the cores, whereas the highest thiosulfate concentrations were observed towards the bottom of the cores.

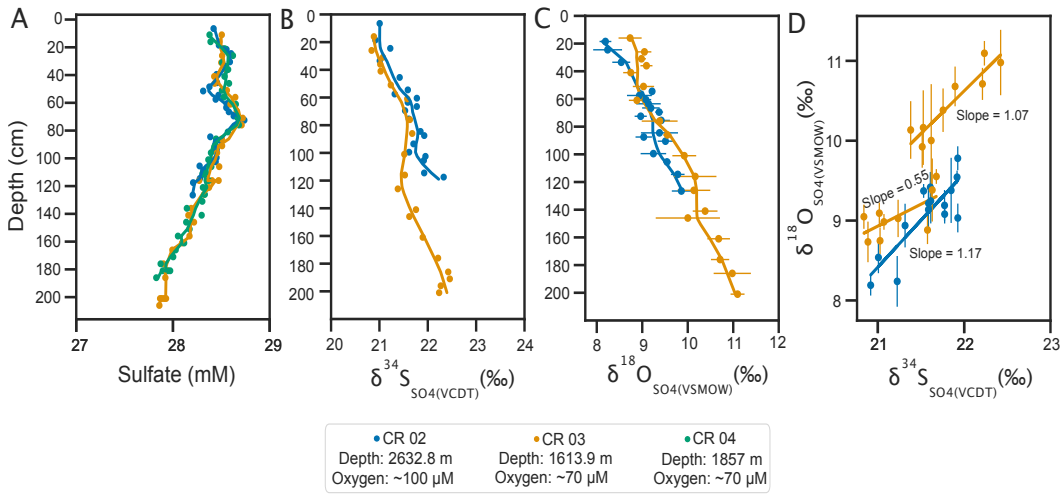

Figure 3: Porewater profiles of (A) sulfate (same as in Fig. 2), (B) sulfate $\delta^{34}S$, (C) sulfate $\delta^{18}O$, and (D) a crossplot between sulfate $\delta^{34}S$ and $\delta^{18}O$ for two of the Cocos Ridge gravity cores. The dots represent measured data, and the lines represent a Savitzky-Golay filter with a third-degree polynomial approximation to smoothening the data. Horizontal lines in (C) and vertical lines in (D) represent the error of triplicate measurements for oxygen isotope measurements. Lines in (D) represent a linear fit to the sulfate $\delta^{34}S$ vs. $\delta^{18}O$ data, with their corresponding slope of the apparent linear phase (SALP) values.

iTag 16S rRNA analysis of microbial diversity

To investigate associations between the microbial community composition and the sediment and porewater geochemistry at San Clemente Basin and Cocos Ridge, we performed 16S rRNA sequencing of sediment-extracted DNA at the same depths as

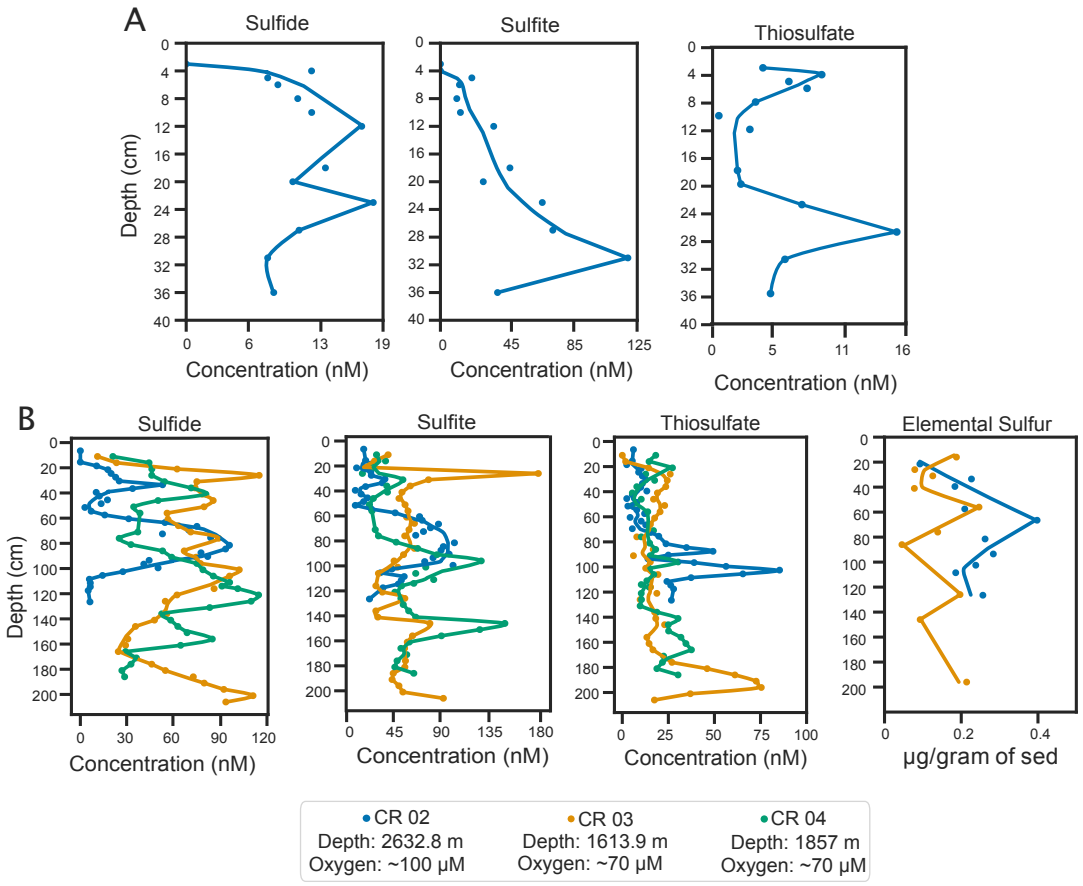

Figure 4: Porewater profiles of sulfide, sulfite, and thiosulfate for (A) San Clemente Basin and (B) Cocos Ridge. Solid-phase elemental sulfur profiles for CR 02 and CR 03 are shown in (B). The dots represent measured data, and the lines represent a Savitzky-Golay filter with a third-degree polynomial approximation to smoothening the data.

those sampled for geochemical measurements (Supp. Fig. 3). Sediments hosted diverse communities even at the phylum level, with 12 different phyla reaching abundances of at least 10%. From this preliminary visualization, no clear trends in the microbial community composition with depth or location were readily apparent. When focusing on sulfur cycling taxa, *Actinobacteria* (which include known sulfur oxidizer/reducers) were abundant throughout, accounting for 10-25% of the total ASVs recovered. *Bacilli* (putative sulfur-oxidizers) also represented up to 25% of the total ASVs, with higher relative abundance towards the top of the cores (Fig. 5). *Burkholderiales* (*Betaproteobacteria*) were more abundant within the

first 20 cm, as well as *Crenarchaeota* at the San Clemente basin and CR 04. As for potential sulfur reducers, we observe that the deeper communities tend to be dominated by *Chloroflexi* and *Acidobacteria*, which together account for 5-20% of the ASVs identified at any particular depth bin in all the cores. However, these groups are also heterotrophs, not necessarily limited to sulfur metabolism. The canonical sulfate-reducing group *Desulfobacterota* is present at most depths with relative abundance below 5%, and does not seem to exhibit trends with depth. At CR 02, where there is an increase in the concentrations of porewater sulfide and sulfite from ~55 to 85 cm depth and solid-phase elemental sulfur from ~20 to 65 cm depth, we observe a concomitant increase in the abundance of *Hyphomicrobiales* and other *Alphaproteobacteria*, as well as a higher diversity of sulfur-oxidizing *Hyphomicrobiales* (*Proteobacteria*), and higher abundances of *Bacteroidota* compared to shallower depths where sulfide and sulfite had lower concentrations.

We also tested for correlations between the diversity of the microbial community and geochemical parameters. The Shannon index (metric of alpha diversity) did not vary between depths and the medians were above 4 for all cores except for that from station CR 04 (Supp. Fig. 10). Although not statistically significant (Supp. Table 1), the NMDS analysis indicated that nitrate, sulfate, sulfide, and $\delta^{13}C_{Org}$ were the geochemical variables that could best explain sample clustering. The stress value of the analysis was 0.16, which indicates that the fit between the original and projected distances in the ordination diagram is acceptable (Clarke, 1993; Supp. Fig. 11). The correlation analysis at the phylum level between microorganisms and geochemical parameters (Supp. Fig. 12), although not significant (all p-values are above 0.05), identified positive associations between *Acidobacteriota* and porewater iron and manganese at CR02. At SCB, we identified positive correlations between nitrate and sulfate, and *Halobacterota*, *Crenarchaeota*, and *Plantomycetota*. At SCB, most groups showed negative correlations with sulfide and manganese, and

Proteobacteria and *Chloroflexi*, and *Thermoplasmatota*, were negatively and positively correlated with thiosulfate, respectively. Specific groups of microorganisms were not strongly correlated with reduced sulfur species for the CR stations.

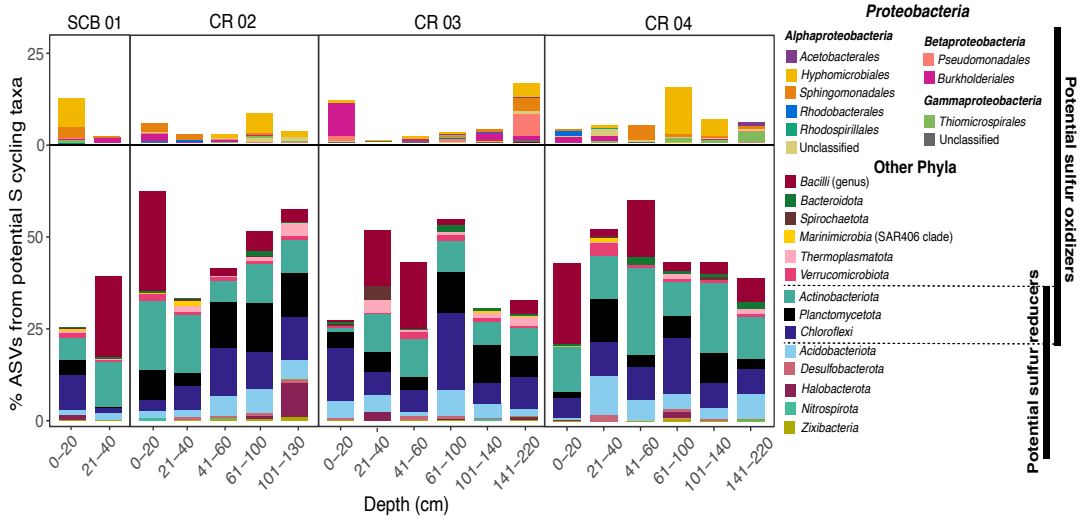

Figure 5: Relative proportions of amplicon sequence variants (ASVs) detected through 16S rRNA for classes for *Proteobacteria* (top) and phyla for all the others (bottom) that include sulfur transforming (oxidation, reduction and disproportionation) microorganisms. Each column corresponds to a different core and each bar corresponds to the designated depth bin, where the %ASVs were averaged across multiple depth horizons.

To complement the porewater measurements, we determined the content and the isotopic composition of organic carbon of the sediments at the same depths at which porewaters were retrieved for two of the Cocos Ridge Stations (Fig. 6).

4. DISCUSSION

This study focused on investigating microbial sulfur cycling in oxic, low-sedimentation basins of the oligotrophic Eastern Equatorial Pacific. We detected nanomolar concentrations of reduced sulfur species through a combination of bimane derivatization and HPLC. Oxygen and sulfur isotopes of sulfate confirmed the importance of bacterial sulfate reduction at Cocos Ridge, which provides the substrates to sustain an active sulfur cycle. Our quantifications of porewater nitrate, iron, manganese,

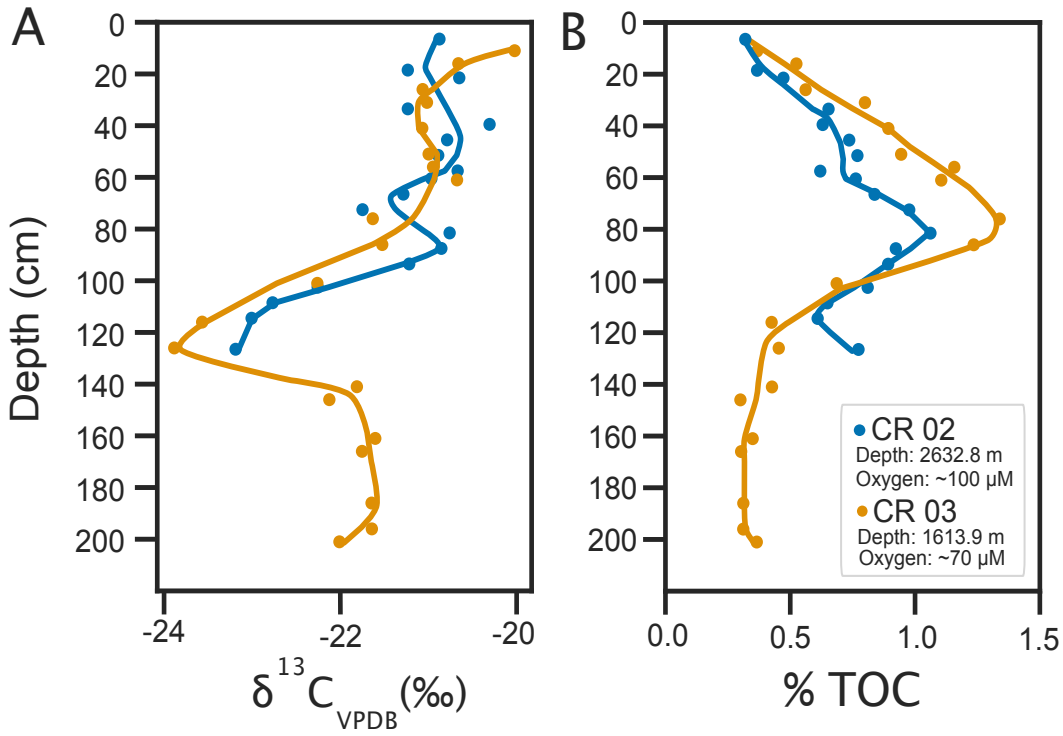

Figure 6: Sediment profiles of organic matter $\delta^{13}C$ (A) and total organic carbon percentage (B) Cocos Ridge. The dots represent measured data, and the lines represent a Savitzky-Golay filter with a third-degree polynomial approximation to smoothening the data.

and sulfate, the main electron acceptors used for organic matter oxidation, provided fine-grained resolution into the extent of the redox ladder both at San Clemente Basin and Cocos Ridge. At SCB, porewater nitrate was exhausted about 10 cm from the sediment-water interface. This is somewhat deeper than previous reports of 3-4 cm for the depth of depletion of nitrate at this locality (Bender et al., 1989; Shaw et al., 1990). Porewater iron and manganese were detected at tens and a few hundred of micromolar concentrations, respectively. Similar concentrations of iron were reported before peaking at 6 cm depth (Shaw et al., 1990), which is shallower than the peak we detected at 16 cm depth. Concentrations of porewater manganese up to about 80 μM have been reported previously for the San Clemente Basin peaking at ~10 cm depth, with a similar steady concentration profile as the one we found here starting at 4 cm depth (Bender et al., 1989; Shaw et al., 1990). An overlap between

the nitrate and manganese reduction zones at the San Clemente Basin had also been previously identified, and it was established that the profiles of these redox sensitive elements look more condensed than those from other ocean regions, due to the low bottom water oxygen and high organic carbon fluxes at the semi-enclosed basins of the California Borderland (Bender et al., 1989; Supp. Fig. 1). The nitrate, iron and manganese profiles that we determined seem to have deepened compared to those reported more than 30 years ago (Shaw et al., 1990), which could be explained by a decrease in the organic carbon flux at the San Clemente Basin, or bioirrigation. Sulfate does not show significant depletions, which is consistent with previous findings (Shaw et al., 1990) and with the sequential utilization of manganese oxides, iron oxides, and sulfate as electron acceptors for organic matter oxidation (Stumm and Morgan, 1970).

At Cocos Ridge, similar concentrations of porewater nitrate as those from SCB are detected at the shallowest part of the sediment, but it becomes exhausted at deeper depths than at SCB. This is consistent with lower organic fluxes at CR compared to SCB. An increase in dissolved manganese with depth in the sediments is observed at station 2 only, and it is consistent with manganese reduction, in particular after 60 cm, where nitrate is exhausted. An overlap between the nitrate and manganese oxide reduction zones has been previously reported for the Panama basin (Aller, 1990). One possibility for the lack of a similar trend for stations 3 and 4 is that at these stations manganese could be mostly concentrated in carbonates or other mineral phases in which it is protected from microbial utilization, whereas station 2 could be in closer proximity to ferromanganese crusts (Zawadzki et al., 2022). Solid-phase manganese enrichment is widespread in surface sediments of the Panama basin and derives from an upward flux of Mn^{2+} from hydrothermal sources and its subsequent reoxidation (Aller, 1990). It has been proposed that bioturbation alters oxic-suboxic reaction balances and promotes intense recycling of manganese,

such that manganese reduction is capable of accounting for the oxidation of the entire estimated annual flux of carbon at the Panama basin (Aller, 1990). We observed a ~1.5 mM increase in magnesium with depth at station 2 only, and a slight decrease (5 mM) at stations 3 and 4 (Supp. Fig. 2). The decrease is consistent with an alteration of basaltic basement beneath the sediments, and coincides with previously reported profiles for nearby locations (ODP sites 677 and 678; Mottl, 1989). Since calcium profiles do not show significant changes in concentration with depth, the most feasible sink for magnesium at CR 03 and CR 04 is the low-temperature precipitation of Mg-clay minerals (e.g. smectites; Higgins and Schrag, 2010). At ODP site 1241, on the north flank of Cocos Ridge, porewater magnesium concentrations were observed to remain constant with depth (Mix et al., 2003), reflecting a local balance between magnesium sources and sinks. The magnesium increase we observe at station 2 could be explained by a local net magnesium source, like weathering of igneous minerals and release of magnesium adsorbed to sediment surfaces (Higgins and Schrag, 2010). The fact that calcium concentrations remain constant with depth in the sediments while strontium concentrations increase reflects that, while net precipitation of calcium carbonate might not be changing, recrystallization of calcium carbonate in the sediments may enhance strontium release (Mottl, 1989). Iron becomes detectable at the depth of nitrate depletion for stations 3 and 4, which is expected and consistent with a scarcity of dissolved manganese at these stations. Our porewater profiles for iron and nitrate for all stations, and for manganese at station CR 02 are consistent with previously reported ones for the Eastern Equatorial Pacific (Emerson et al., 1980; Klinkhammer, 1980) and look similar to typical porewater profiles from pelagic oxygenated sediments (Froelich et al., 1979). About 95% of the organic C remineralized in sediments of the Eastern Equatorial Pacific is oxidized by oxygen, with secondary oxidants like MnO_2, NO_3^-, Fe_2O_3 and SO_4^{2-} together oxidizing less than 5% of organic carbon

with a rate comparable to the organic carbon burial rate (Bender and Heggie, 1984).

Sulfate stays above 27 mM throughout the length of the gravity cores, which is expected from a low organic matter flux at Cocos Ridge. The first 70 cm of the sulfate profiles do not change appreciably with depth, possibly due to bioirrigation and the use of other oxidants, after which they steadily decrease from ~28.5 mM to ~27.5 mM. In order to establish if this pattern could be consistent with sulfate reduction (Jørgensen, 1982), we measured the sulfur and oxygen isotopic compositions of porewater sulfate at two of the Cocos Ridge stations. The increase in both the $\delta^{34}S$ and $\delta^{18}O$ from their seawater values (21‰; Rees C. E. et al., 1978 and 9.3‰; Longinelli and Craig, 1967, respectively) with depth is consistent with a normal kinetic isotope effect from bacterial sulfate reduction (BSR) for both sulfur (Kaplan and Rittenberg, 1964) and oxygen (Fritz et al., 1989; Turchyn et al., 2006). The sulfur isotopic composition of porewater sulfate has been found to reach up to ~100‰ (Antler et al., 2013; Brüchert and Pratt, 1999; Jørgensen et al., 2004), and that of oxygen, up to 27‰ (Turchyn et al., 2006) at sites where sulfate is depleted to concentrations or 10 mM or below. These values are much higher than the heaviest values of 22.5‰ for sulfur and 11‰ for oxygen that we measured, which is a consequence of the small depletions in sulfate we observe for the ~2 m porewater columns at Cocos Ridge.

The sulfur and oxygen isotope profiles of porewater sulfate at Cocos Ridge exhibit regions at which the isotopic values remain constant with depth (Fig. 3). For station 2, they occur between 60 and 100 cm for both sulfur and oxygen, whereas for station 3, they correspond to 70 to 130 cm for sulfur, and 20 to 60 cm and 110 to 150 cm for oxygen. At both station 2 and station 3, the static regions in the sulfur isotope profiles coincide with increments in the concentrations of dissolved iron, which suggests that iron is preferentially utilized over sulfate as an electron acceptor at depths above ~1m. These also coincide with the last glacial maximum

(LGM) depth for the sediments of the Eastern Equatorial Pacific, which roughly encompasses between 60 and 90 cm near Cocos Ridge (Pedersen, 1983). We found an increase in TOC leading to the LGM (above 60 cm depth) at both station 2 and station 3, which coincides with a decrease in its carbon isotope composition from ~-20 to -24‰, peaking at 80-90 cm depth (Fig. 6). This period (14-19 Kya) is characterized by lower productivity and higher organic carbon burial rates (Pedersen, 1983), which is supported by our data. Throughout this time, it would make sense for the sulfur isotopic compositions to remain steady, as potentially there was lower organic matter respiration via sulfate reduction. However, the incorporation of a ~3% decrease in sulfate concentrations, as well as the surface (21‰) and deepest (~22.5‰) sulfur isotope compositions of sulfate we measured in an approximation to the Rayleigh distillation equation (Mariotti et al., 1981), allows us to predict a fractionation factor of about -40‰, which falls near the center of the range measured for the deep ocean (compiled by (Sim et al., 2011). This further supports the notion that sulfate reduction is operating at Cocos Ridge, even though our data suggests that the relevance of this process for the oxidation of organic matter changed across time, as evidenced by differences in sulfate concentrations and isotopes with depth within the sediment.

The magnitude of the oxygen fractionation factor from bacterial sulfate reduction is roughly 25% that of sulfur (Mizutani and Rafter, 1969), which implies that, if bacterial sulfate reduction was the only process affecting the isotopic compositions of oxygen and sulfur in porewater sulfate at Cocos Ridge, the slope of a linear $\delta^{18}O_{SO_4^{2-}}$ profile should be shallower than that of a linear $\delta^{34}S_{SO_4^{2-}}$ profile (Turchyn et al., 2006). However, pure culture experiments (Fritz et al., 1989) and porewater profiles around the world (Antler et al., 2013; Turchyn et al., 2006) have found a decoupling between $\delta^{18}O_{SO_4^{2-}}$ and $\delta^{34}S_{SO_4^{2-}}$, in which the magnitude of $\delta^{18}O_{SO_4^{2-}}$ increases until it reaches a constant value, whereas $\delta^{34}S_{SO_4^{2-}}$ may continue to increase (Antler

et al., 2013; Fritz et al., 1989; Turchyn et al., 2006). This decoupling indicates that a process other than BSR is impacting the oxygen isotope compositions of porewater sulfate, which has been suggested to occur via oxygen isotope exchange between water and sulfite during sulfate reduction (Fritz et al., 1989; Mizutani and Rafter, 1969), given that it would take over 3 million years for sulfate and water to isotopically equilibrate at pH above 3 (Lloyd, 1968). We did not observe such an apparent equilibration of $\delta^{18}O_{SO_4^{2-}}$ with depth, but instead a decoupling at the center of the profile at station CR 03, which produced a break in the slope of the tangent between $\delta^{18}O_{SO_4^{2-}}$ and $\delta^{34}S_{SO_4^{2-}}$ (slope of the apparent linear phase -SALP). SALP is related to the overall sulfate reduction rate (SRR), with steeper SALPs associated with lower SRR (Antler and Pellerin, 2018) due to higher reversibility of the sulfate reduction pathways (Brunner and Bernasconi, 2005; Fritz et al., 1989). SALP values below 0.5 were thought to be distinctive of sulfate reduction coupled to anaerobic oxidation of methane (AOM-SR) in cultures (Deusner et al., 2014; Sivan et al., 2014) and natural environments (Antler et al., 2015). However, low SALPs are now known not to be unique to AOM-SR dominated environments (Crémière et al., 2017), and a compilation of measurements of SALP for pure cultures and natural environments (Antler and Pellerin, 2018) has shown that sulfate reduction driven by organic matter oxidation (organoclastic sulfate reduction; OSR) may have overlapping SALP values with AOM-SR, in particular at enclosed or low oxygen water bodies. The SALP values we determined here at CR 02 (1.17) and the deepest part of CR 03 (1.07) fall within the lower end of the range measured for pelagic sediments not associated to sulfate-methane transition zones (Antler and Pellerin, 2018). However, the SALP value measured at the uppermost part of CR 03 (0.55) falls at the upper end of the seep range (Antler and Pellerin, 2018). The change in SALP might indicate a change in oxidants after 1.2 m depth, from organic matter (Fig. 6) to methane or other hydrocarbons. We cannot prove this hypothesis at the

moment, since we did not measure methane concentrations.

A potential oxygen isotope exchange between sulfur intermediates (e.g. S0, sulfite, thiosulfate) and water could explain the steady regions in the $\delta^{18}O_{SO_4^{2-}}$ profiles at Cocos Ridge. To explore this possibility, we measured the concentrations of thiosulfate, sulfite, and sulfide (Fig. 4). The concentrations of sulfur intermediates in porewaters have been measured previously at a variety of locations in marine sediments (Zopfi et al., 2004), but there are only a few studies that have measured them with a derivatization-HPLC method similar to the one utilized here at euxinic basins like the Black Sea (Zopfi et al., 2004) and Concepción Bay in Chile (Zopfi, 2000), marshes (Vetter et al., 1989), and shelves (Zopfi, 2000), at maximum depths of only 30 cm. To our knowledge, this is the first time that sulfur intermediates have been measured in the porewaters of pelagic sediments, probably because it has been assumed that they would be undetectable, given the low rates of sulfate reduction that characterize them (Canfield and Des Marais, 1991; Froelich et al., 1979). However, it has been demonstrated that microniches within oxygenated sediments support sulfate reduction (Jørgensen, 1977), and as a consequence, they would also keep sulfur intermediates from being oxidized by oxygen. In low-oxygen marine sediments, reported concentrations of thiosulfate range between 70 nM and 5.7 μM, those of sulfite (Zopfi et al., 2004), between 0 and 2.6 μM (Zopfi et al., 2004), and sulfide can reach up to 10 mM (Volkov and Neretin, 2008; Werne et al., 2003). We detected tens to low hundreds of nM concentrations of thiosulfate, sulfite, and sulfide both at SCB and CR. These low concentrations are not surprising, considering that our measurements indicate that there is little sulfate reduction occurring across the 1.2 to 2 m porewater profiles at Cocos Ridge, and that there is a high abundance of iron and manganese oxides both at San Clemente Basin and Cocos Ridge, as suggested by their dissolved profiles, which are known to be involved in the chemical oxidation of sulfide (Aller and Rude, 1988; Elsgaard

and Jørgensen, 1992). It has also been established that sulfur intermediates have rapid turnover rates in sediments, in particular thiosulfate, because they have higher redox potentials and/or more energetically favorable pathways compared to sulfate as electron acceptors (Wasmund et al., 2017). The fact that sulfur intermediates can be both oxidized and reduced (i.e. disproportionated) by most sulfate-reducing bacteria (Finster, 2008) would contribute to an explanarion of their low concentrations in pelagic sediments.

We were interested in identifying potential correlations between the behavior of porewater reduced sulfur species, which could help in understanding their dynamics better. By plotting their concentrations against each other (Supp. Fig. 4), we noticed that sulfite and sulfide seem to linearly covary, most notably at station CR 02. The crossplots suggest that sulfide must accumulate up to a certain threshold before sulfite and thiosulfate can be detected -excluding spikes-, which lies around ~30 nM. This is expected, considering that sulfide is the most reduced form of sulfur, and as such, the starting point from which microbial oxidation pathways allow for the formation of intermediates. The range of depths at which the $\delta^{18}O_{SO_4^{2-}}$ profile stays at the same values for CR 02 (60 to 100 cm) and CR 03 (0 to 60 cm) coincides with increases in the concentration of both sulfide and sulfite. We also compared the sulfur species quantified in porewater profiles with the measured $\delta^{18}O_{SO_4^{2-}}$ (Supp. Fig. 5) for stations CR 02 and CR 03. After sulfate, the species that shows a more linear relationship with $\delta^{18}O_{SO_4^{2-}}$ is sulfite. Our crossplots of reduced sulfur species also indicate that thiosulfate is characterized by large spikes and variable concentrations at single concentrations of sulfide and sulfite, mostly at CR 02 and CR 03. A correlation analysis between the geochemical parameters measured at all stations (Supp. Fig. 6 - 9) indicates that, while the only significant ($p<0.001$) correlation between S species at SCB was between sulfate and sulfite, at CR 02 and CR 04 sulfide and sulfite are significantly correlated, as well as sulfite and TOC

%, $\delta^{18}O_{SO_4^{2-}}$, and $\delta^{34}S_{SO_4^{2-}}$ at CR 02. In contrast, at CR 03 sulfate is significantly correlated with thiosulfate ($p<0.01$), and it is sulfate who is correlated with TOC %, $\delta^{18}O_{SO_4^{2-}}$, and $\delta^{34}S_{SO_4^{2-}}$. At CR 04, sulfate is also significantly correlated with thiosulfate, and with sulfite.

The correlations between sulfate and reduced sulfur species support the hypothesis that sulfite might be exchanging oxygen atoms with water, which could end up in sulfate after sulfite reoxidation, thus altering its $\delta^{18}O$ and generating an apparent equilibrium in its porewater profile. Many factors, including the potential abiotic oxidation of sulfide to sulfite and thiosulfate during sampling, as well as the fact that the concentrations of reduced sulfur species we measured approach the detection limits, complicate the interpretation of their profiles. However, the relative covariance between sulfite and sulfide at some depths, and a spiky behavior for thiosulfate, could also be due to differences in the metabolic pathways that microorganisms may be utilizing to degrade sulfur at different depths. The most common biological sulfur oxidation pathways are Sox, involved in the oxidation of sulfur intermediates to sulfate (Friedrich et al., 2000), and Sqr (Schütz et al., 1999) + rDsr (Grimm et al., 2011), involved in the oxidation of sulfide to sulfate going through elemental sulfur and sulfite as intermediates (Supp. Fig. 13). Depths at which the Sox pathway is more active or operating at larger rates would exhibit lower thiosulfate concentrations, whereas thiosulfate spikes could be an indication of a suppression of this pathway. Conversely, depths at which the Sqr and rDsr pathways are dominant would exhibit low concentrations of sulfide and sulfite, which would be able to accumulate at depths in which these pathways become downregulated.

To address if the porewater concentration profiles of redox sensitive elements and sulfur species could be traced to differences in the microbial community composition at SCB and CR, we performed 16S rRNA sequencing of sediment-extracted DNA (Supp. Fig. 5). Very few studies have explored the microbial community composi-

tion in marine sediments from oligotrophic, oxic regions of the ocean (Durbin and Teske, 2011; Morono et al., 2020). At these regions, as indicated by our geochemical profiles, high-energy electron acceptors such as manganese and iron oxides are available over several meters of the sediment, which would be expected to favor aerobic, nitrate-respiring microorganisms at the top 50 cm of the core, and metal oxide-respiring microbes at further depths (Durbin and Teske, 2011). Microorganisms capable of utilizing other, less energetically favorable electron acceptors, such as sulfate and methane, would not be able to outcompete those utilizing the most energetically favorable ones unless their reduction became limited by low concentrations (Lovley and Goodwin, 1988). Previous studies on Pacific abyssal sediment microbial communities found an increase in *Chloroflexi* and *Planctomycetes* with depth, and a high abundance of *Actinobacteria*, *Alpha-* and *Gammaproteobacteria*, *Gemmatimonadetes*, and *Nitrospina* at the top first meter of sediment cores in which nitrate was not fully exhausted until 2.5 m depth (Durbin and Teske, 2011). At Cocos Ridge, we observed a high abundance of *Actinobacteria* and Bacilli, and an increase in the abundance of potential sulfur-oxidizers *Hyphomicrobiales* (*Alphaproteobacteria*), *Thiomicrospirales* (*Gammaproteobacteria*), and *Bacteroidota*, *Planctomycetota* and *Thermoplasmatota* with depth. In the depth horizons of 60-100 and 101-130 cm, we observe an increase in the abundance of *Halobacterota*, an archaeal group capable of using elemental sulfur and polysulfides as electron acceptors (Sorokin et al., 2018). This would be consistent with thiosulfate spikes and a decrease in elemental sulfur below 70 cm. However, a similar increase in *Halobacterota* with depth was not observed in the sediments of CR 03 and CR 04. At these two stations, a higher abundance of sulfur-oxidizing *Proteobacteria* is observed at increasing depths, particularly of *Betaproteobacteria* at CR03, and *Alpha-* and *Gammaproteobacteria* at CR 04. We detected many clades of microorganisms that are putative chemoorganotrophs and fermenters, such as *Aerophob-*

ota, *Bacteroidota*, *Latescibacterota*, *Verrucomicrobiota*, *Firmicutes*, *Spirochaetota*, *Bathyarchaeia*, and *Calditrichota*, which may generate hydrogen and low molecular weight organic acids as byproducts of their metabolism (Flood et al., 2021). These may support sulfur oxidizers with mixotrophic metabolisms, and have been found to be associated with *Beggiatoaceae*, sulfur-oxidizing *Epsilonproteobacteria*, in shallow marine sediments (Flood et al., 2021).

The diversity of the communities found across the cores was generally high (Shannon median: 3.5-4.2), but did not correlate with depth or geochemistry (Supp. Fig. 10). These diversity estimates are larger than those reported for the water column (Shannon median: 3-3.5) and sediments (Shannon median: 2.5) of the Western Pacific (Wang et al., 2020). We hypothesize that sediments from Cocos Ridge could have a larger microbial diversity than other places due to the large spread of the redox gradients, which should favor succession of microbial guilds, as opposed to highly specialized communities. The clusters obtained by NMDS did not separate the samples by core or depth (Supp. Fig. 11). Although none of the geochemical parameters were significantly correlated with clustering (Table 1), the sulfide and sulfate arrows point in different directions primarily along the NMDS2 axis, and samples distributed across the space between the two are not fully separated, but form a gradient instead. This could be explained by the interdependency of substrates between sulfate reduction and sulfide oxidation. On the other hand, the nitrate arrow points directly towards a cluster, which seems to better separate samples spatially across the NMDS1 axis. To gain an idea of which taxonomic groups drive the clustering, we determined the diversity at the order level for the most abundant and relevant groups for nutrient cycling detected at the phylum level (Supp. Fig. 3), namely *Proteobacteria* (Supp. Fig. 14), *Actinobacteria* (Supp. Fig. 15), *Planctomycetes* (Supp. Fig. 16), *Chloroflexi* (Supp. Fig. 17), *Crenarchaeota* (Supp. Fig. 18), *Acidobacteriota* (Supp. Fig. 19), *Bacteroidota* (Supp. Fig. 20), and *Firmicutes*

(Supp. Fig. 21). We located the samples that clustered together with NMDS in each one of the order level histograms, and highlighted the taxonomic groups that seem to drive the clustering in the NMDS plot. This comparison allowed us to establish that intraphylum diversity is what drives the similarity between samples. The community composition thus seems to be mostly determined by unique local physicochemical characteristics, potentially at finer spatial scales than sampled here. The existence of local microniches would allow for colonization by microbial communities which preferentially associate together regardless of depth and location, pointing at potential ecological specializations and cooperations. The correlation analysis between phyla and geochemical parameters identified positive correlations between *Acidobacteriota* and porewater iron and manganese at CR02, which is consistent with the involvement of members of this group in dissimilatory iron reduction (Kulichevskaya et al., 2014). At SCB, we identified positive correlations between nitrate and the denitrifiying group *Halobacterota* (Tomlinson et al., 1986), as well as *Crenarchaeota* and *Plantomycetota*, which include ammonia-oxidizing members (Strous et al., 1999; Weidler et al., 2008). These three groups were also positively correlated with sulfate at SCB, which highlights their potential role in sulfate reduction at his locality. Specific groups of microorganisms were not strongly correlated with reduced sulfur species for the CR stations. At SCB, most groups showed negative correlations with sulfide and manganese, and *Proteobacteria* and *Chloroflexi*, and *Thermoplasmatota*, were negatively and positively correlated with thiosulfate, respectively.

The fact that no major differences in microbial abundances are observed between SCB and CR, as well as between shallow and deep samples, suggests that the microbial community composition is not primarily controlled by organic matter fluxes or the availability of other oxidants. Instead, metabolic flexibility among microorganisms is the most feasible explanation for the general similarities in microbial

abundances we observe across depths. It has been found that *Deltaproteobacteria* in marine sediments, which are capable of sulfate reduction, also harbor genes and constitutively express enzymes involved in thiosulfate and sulfite transformations (Krämer and Cypionka, 1989), and are capable of oxidizing elemental sulfur (Pjevac, 2014). The *Deltaproteobacteria Desulfuromonadales*, which are capable of sulfate reduction and elemental sulfur oxidation, can also reduce Fe(III) and Mn(IV) in environmental sediments (Lovley, 2006; Roden and Lovley, 1993. Enrichments of methane seep sediments amended with thiosulfate, sulfate or elemental sulfur did not show differences in their microbial community compositions over a period of observation of over 100 days, which supports the notion that sediment microbial communities have flexible and adaptable metabolisms to utilize different sulfur species (Eitel et al., in prep). In situ experiments with elemental sulfur additions showed that a few types of bacteria, namely the *Epsilonproteobacteria Sulfuromonas/Sulfurovum* at shallow depths, and the *Deltaproteobacteria Desulfobulbaceae* and *Desulfurimonadales* at further depths, dominate microbial elemental sulfur consumption (Pjevac, 2014). *Alpha-* and *Gammaproteobacteria* have been found to dominate sulfur oxidation in shallow marine sediments, whereas *Epsilonproteobacteria* dominate in sulfidic hydrothermal and cold-seep habitats and *Deltaproteobacteria* account for the majority of the microbial community at anoxic habitats (Pjevac, 2014). We identified an abundance of *Alpha-* and *Gammaproteobacteria* at all depths, less than 10% *Deltaproteobacteria* (*Desulfobacterota*) mostly towards the central part of the CR cores (20-100 cm), and no *Epsilonproteobacteria* in any of the cores, which is expected for oxic sediments. However, their actual involvement in sulfur oxidation in the sediments of Cocos Ridge remains to be investigated.

5. CONCLUSIONS

We characterized the redox ladder in the pelagic sediments near Cocos Ridge, in the oligotrophic Equatorial Pacific Ocean, at a high depth resolution (3-5 cm) and a tens-of-meters scale for the first time. We found porewater gradients consistent with nitrate reduction in the top 60 cm, as well as iron reduction below 60 cm, and manganese reduction at one of the 3 sampled stations starting at the sediment-water interface. We also characterized variations at nM concentrations of porewater thiosulfate, sulfite, thiosulfate, and solid-phase elemental sulfur, which varied with depth. Sulfate concentrations decreased slightly with depth, and the sulfur and oxygen isotopes of sulfate were consistent with sulfate reduction. The microbial community composition was consistent with the sulfur cycling organisms, with clades known to utilize sulfur like *Bacilli*, *Actinobacteria*, and *Crenarchaeota* being highly abundant across all depths and stations. We observed correlations of some taxa with nitrate, iron, manganese, and reduced and oxidized sulfur species. In particular, we identified a higher abundance and diversity of *Alpha-* and *Gammaproteobacteria* with depth at all the stations, as well as an abundance of *Betaproteobacteria* at shallow depths at Cocos Ridge. We also established an increase with depth in the abundance of other clades that include sulfur-oxidizing microbes, such as *Bacteroidota*, *Planctomycetota*, and *Thermoplasmatota*, and clades that include members with the potential capability of sulfate reduction, such as *Chloroflexi* and *Acidobacteria*. The observed taxonomic diversity and high variance across cores indicates that oxic deep-sea sediments support diverse populations of microorganisms capable of adapting their metabolisms to a wide variety of electron donors and acceptors (Vigneron et al., 2021). Altogether, the geochemical and biological evidence support the potential for multiple sulfur, iron, manganese, and other redox-sensitive element utilization pathways operating at the same time throughout different depths within these sediments.

6. ACKNOWLEDGEMENTS

We thank the science party and the crew on board the *R/V Sally Ride*, cruise SR2113, for assistance with sample collection. In particular, we thank William Gray for help with the gravity cores deployment and retrieval and Matthew Quinan for performing porewater silica measurements. We are indebted to Stephanie Connon for help with DNA sample preparation for sequencing, Fenfang Wu for help with the EA-IRMS operation, Nathan Dalleska for help with the IC, ICP-MS, Xevo-TOF-Q UPLC, and HPLC operations, and Dana Brenner for help with the oxygen isotope measurements. We also thank the Adkins, Berelson, and Orphan labs for fruitful discussions, particularly Jaclyn Pittman Cetiner, Aditi Narayanan, Rebecca Wipfler, and John Magyar. This work was funded by NSF grant N 1559215.

7. SUPPLEMENTARY MATERIALS

Supp. Table 1: Non-metric multidimensional scaling (NMDS) scores for the relationship between the sequences identified by 16S rRNA across all sites and depths and the geochemical parameters measured. None of the parameters were found to be significantly correlated with the microbial community composition (all p-values are above 0.05).

Parameter	NMDS1	NMDS2	p-value
Iron	0.07	-0.47	0.40
Manganese	0.10	-0.40	0.54
Nitrate	0.36	-0.004	0.62
Sulfate	0.15	-0.54	0.28
Sulfide	0.07	0.20	0.84
Sulfite	0.04	-0.42	0.48
Thiosulfate	-0.04	0.07	0.98
TOC %	-0.03	-0.44	0.38
$\delta^{13}C_{org}$	-0.11	-0.15	0.89
$\delta^{18}O_{SO_4^{2-}}$	-0.14	0.38	0.55
$\delta^{34}S_{SO_4^{2-}}$	0.03	0.05	0.99
Total ASVs	0.23	-0.19	0.71

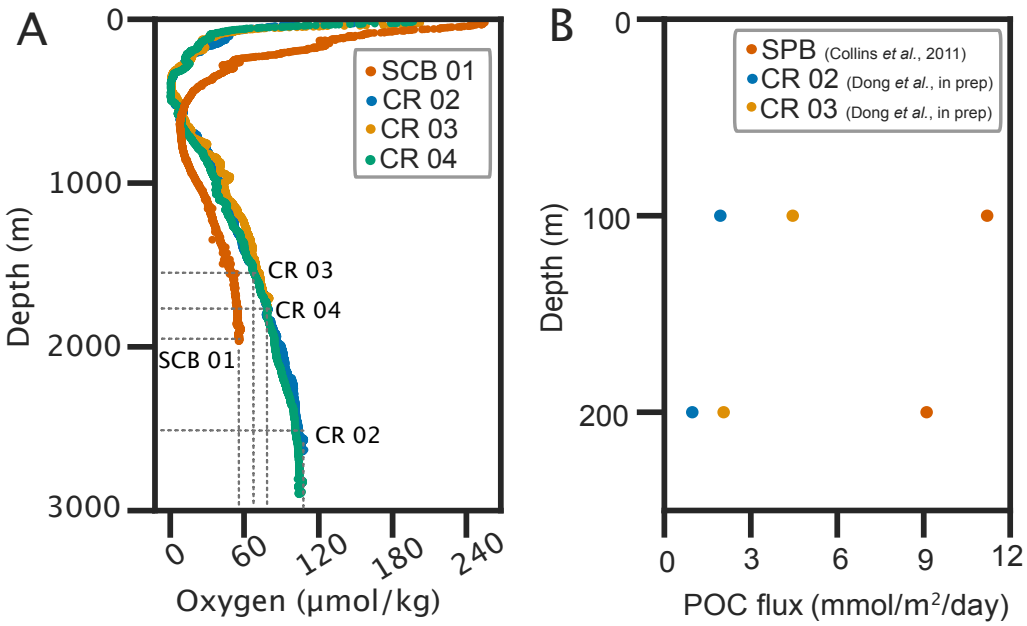

Supp. Fig. 1: Water column oxygen profiles (A) and particulate organic carbon (B) for the stations sampled in this study. SPB in (B) corresponds to the San Pedro Basin, which is located in the California Borderland and is assumed to have a similar POC flux as San Clemente Basin.

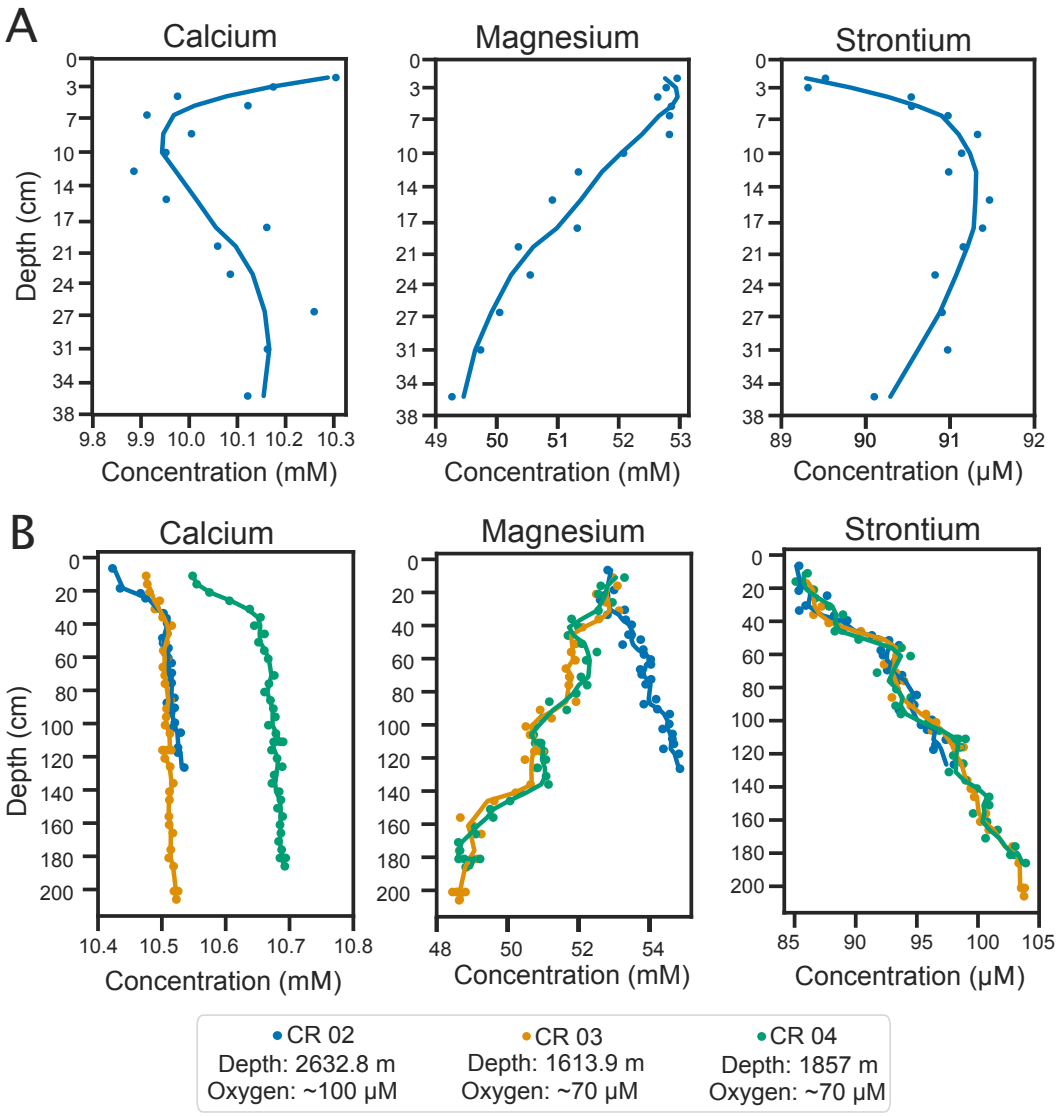

Supp. Fig. 2: Porewater profiles of calcium, magnesium, and strontium for (A) San Clemente Basin and (B) Cocos Ridge. The dots represent measured data, and the lines represent a Savitzky-Golay filter with a third-degree polynomial approximation to smoothening the data.

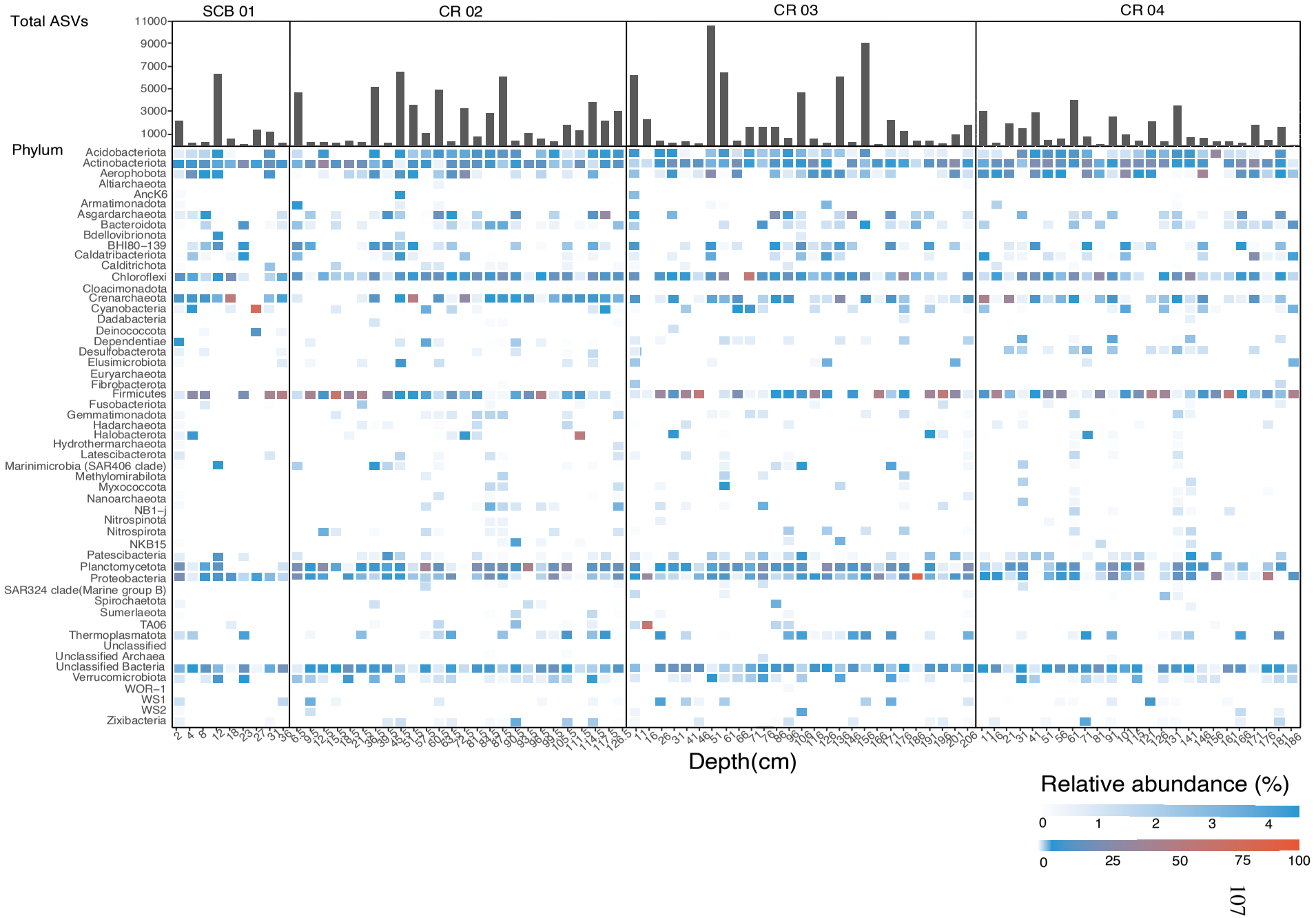

Supp. Fig. 3: Top: Total number of amplicon sequence variants (ASVs) from 16S rRNA sequencing. Bottom: Heatmap of the relative abundance of ASVs classified by phyla identified from 16S rRNA in the sediments of San Clemente Basin and Cocos Ridge. The x axis shows depth, increasing from left to right, and each vertical column corresponds to a core collected at a different station.

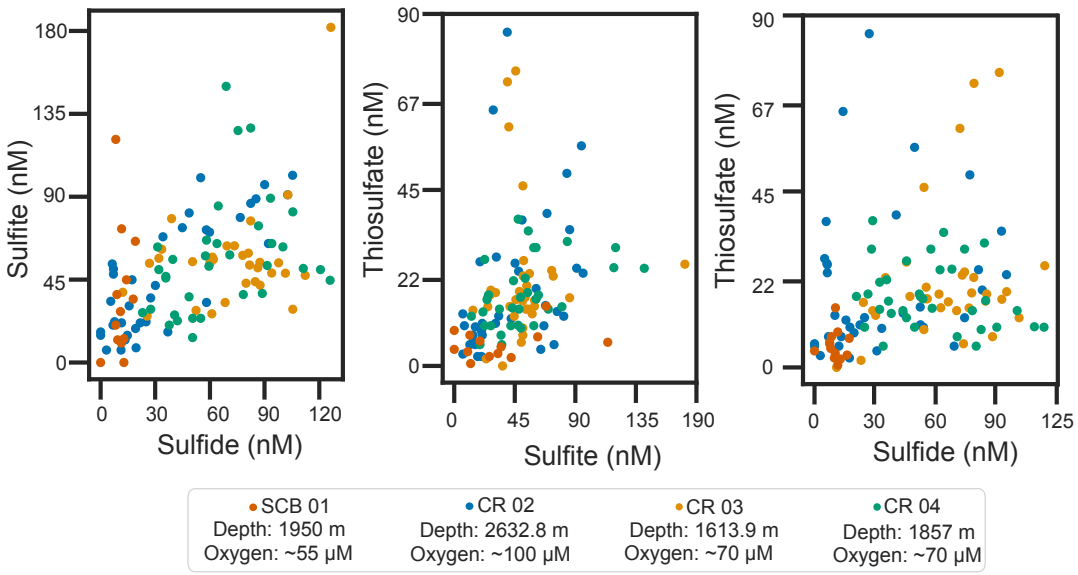

Supp. Fig. 4: Crossplots for the concentrations of reduced sulfur species measured in this study. SCB corresponds to the multicore sampled at San Clemente Basin, and CR 02, CR 03, and CR 04, to the Cocos Ridge stations.

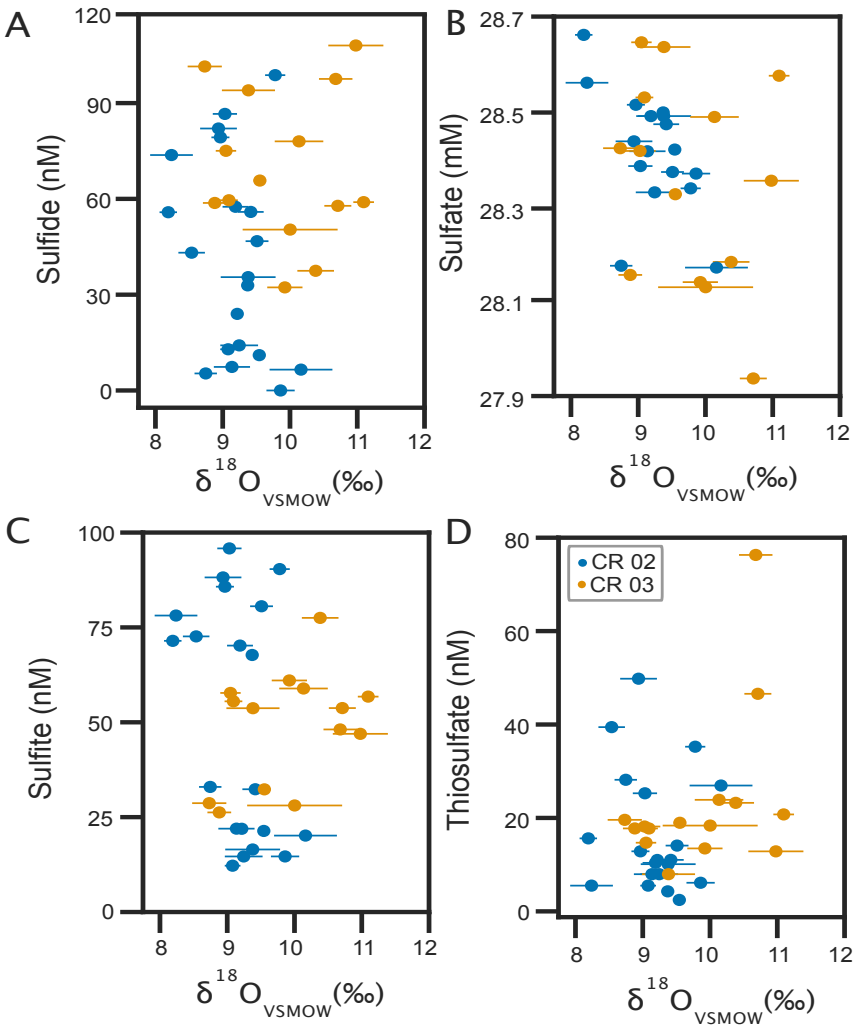

Supp. Fig. 5: Crossplots of the concentrations of porewater sulfur species vs. the oxygen isotope composition of porewater sulfate for (A) sulfide, (B) sulfate, (C) sulfite, and (D) thiosulfate. Horizontal lines represent the error of triplicate measurements.

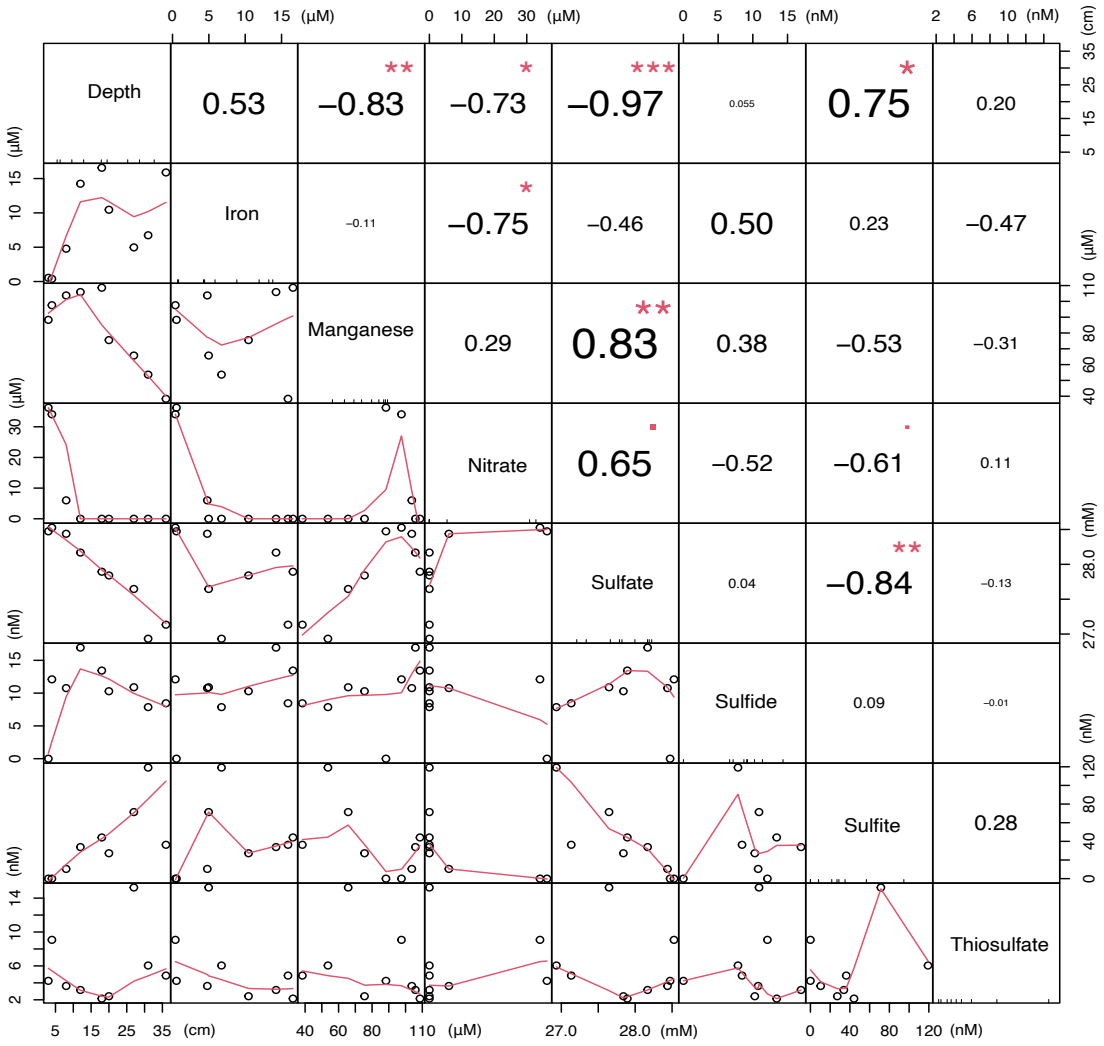

Supp. Fig. 6: Pearson correlation matrix between geochemical variables for the core collected at SCB 01. Each variable is shown on the diagonal. Bivariate scatter plots with a fitted line are displayed on the bottom of the diagonal, where numbers on the borders correspond to the x and y axis for the variable on the corresponding column and row, respectively. The value of the correlation (which ranges between -1 for strongly inverse and +1 for strongly direct) plus the significance level is displayed on the top of the diagonal, where larger magnitude correlations are shown in larger font sizes. Each significance level is associated to a symbol: p-values (0, 0.001, 0.01, 0.05, 0.1, 1) are equivalent to the symbols (“***”, “**”, “*”, “.”, “”).

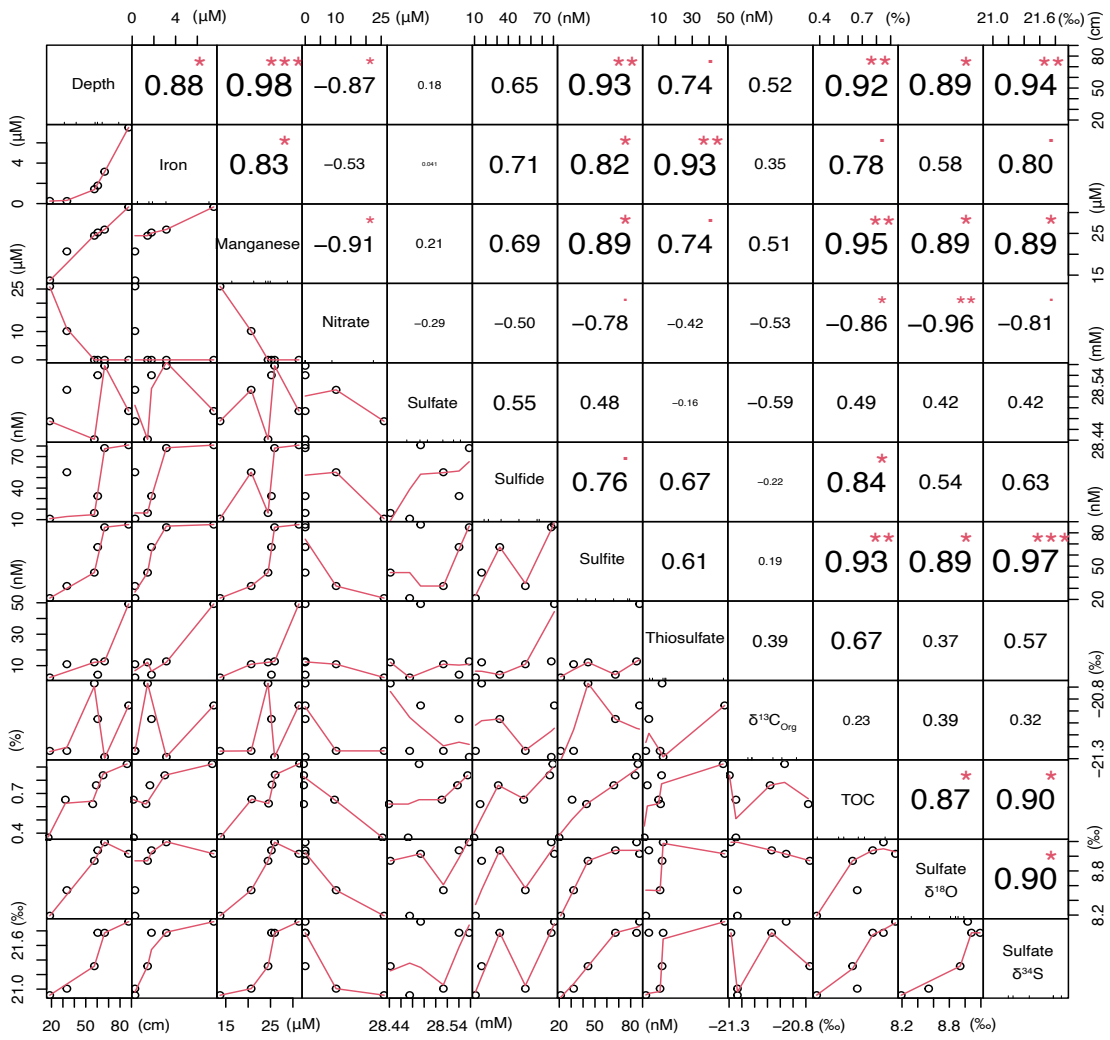

Supp. Fig. 7: Pearson correlation matrix between geochemical variables for the core collected at CR 02. Each variable is shown on the diagonal. Bivariate scatter plots with a fitted line are displayed on the bottom of the diagonal, where numbers on the borders correspond to the x and y axis for the variable on the corresponding column and row, respectively. The value of the correlation (which ranges between -1 for strongly inverse and +1 for strongly direct) plus the significance level is displayed on the top of the diagonal, where larger magnitude correlations are shown in larger font sizes. Each significance level is associated to a symbol: p-values (0, 0.001, 0.01, 0.05, 0.1, 1) are equivalent to the symbols (“***”, “**”, “*”, “.”, “”).

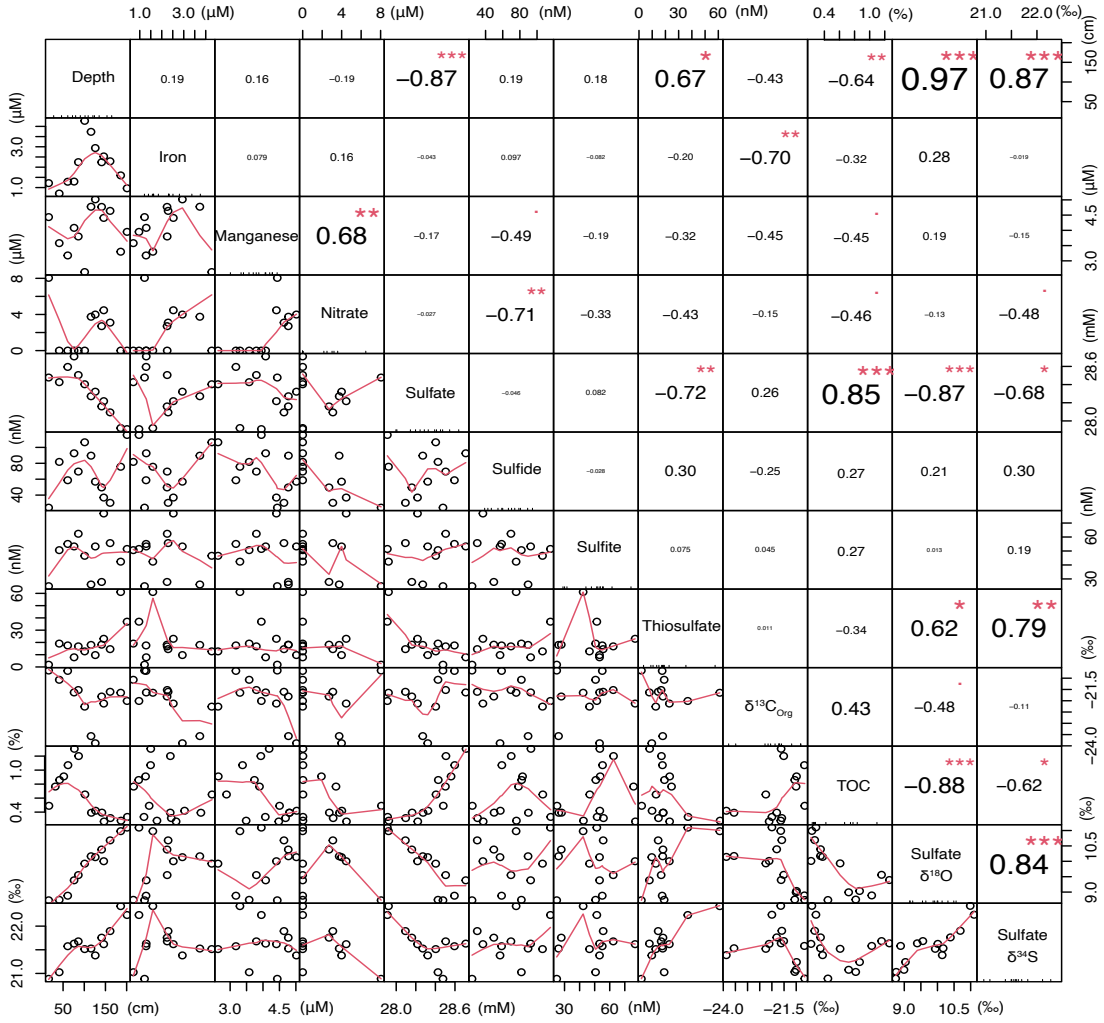

Supp. Fig. 8: Pearson correlation matrix between geochemical variables for the core collected at CR 03. Each variable is shown on the diagonal. Bivariate scatter plots with a fitted line are displayed on the bottom of the diagonal, where numbers on the borders correspond to the x and y axis for the variable on the corresponding column and row, respectively. The value of the correlation (which ranges between -1 for strongly inverse and +1 for strongly direct) plus the significance level is displayed on the top of the diagonal, where larger magnitude correlations are shown in larger font sizes. Each significance level is associated to a symbol: p-values (0, 0.001, 0.01, 0.05, 0.1, 1) are equivalent to the symbols (“***”, “**”, “*”, “.”, “”).

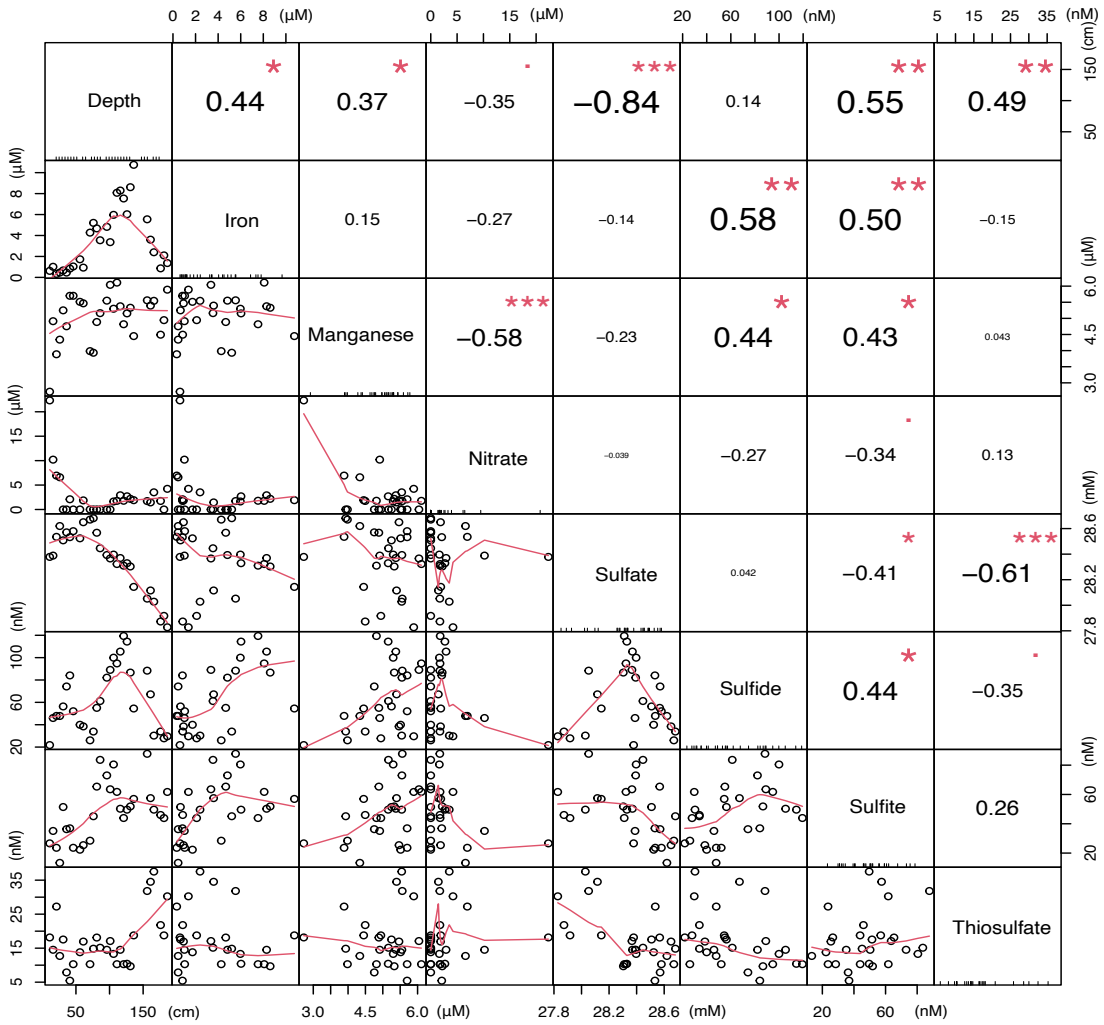

Supp. Fig. 9: Pearson correlation matrix between geochemical variables for the core collected at CR 04. Each variable is shown on the diagonal. Bivariate scatter plots with a fitted line are displayed on the bottom of the diagonal, where numbers on the borders correspond to the x and y axis for the variable on the corresponding column and row, respectively. The value of the correlation (which ranges between -1 for strongly inverse and +1 for strongly direct) plus the significance level is displayed on the top of the diagonal, where larger magnitude correlations are shown in larger font sizes. Each significance level is associated to a symbol: p-values (0, 0.001, 0.01, 0.05, 0.1, 1) are equivalent to the symbols (“***”, “**”, “*”, “.”, “”).

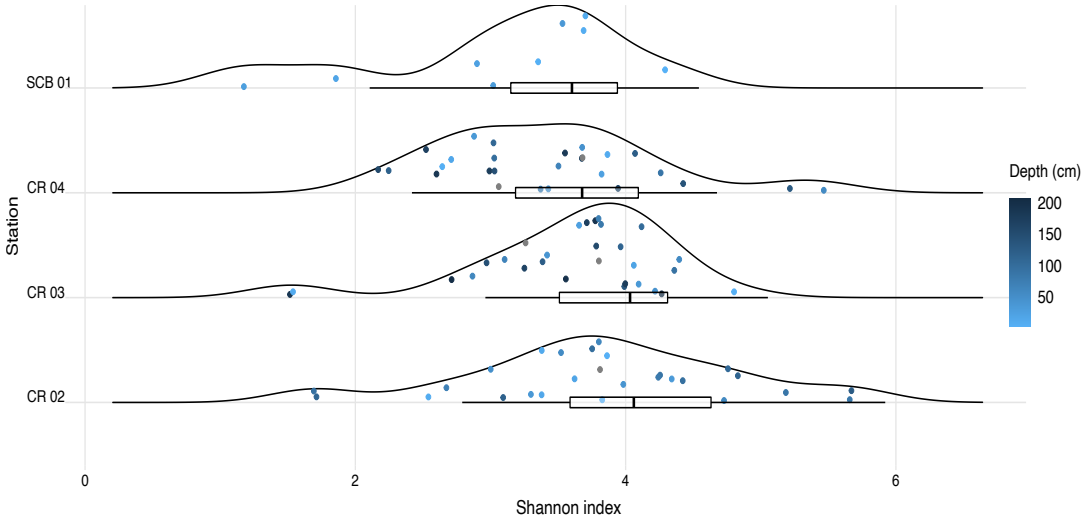

Supp. Fig. 10: Alpha diversity (from the Shannon index) of the sediment 16S sequences from the San Clemente Basin multicore and the Cocos Ridge gravity cores. The x axis corresponds to the Shannon index and the height of the ridges corresponds to sample frequency. The dots inside the ridges correspond to individual samples, which are colored by depth. The horizontal boxes at the bottom of each ridge plot represent the diversity distribution of each core.

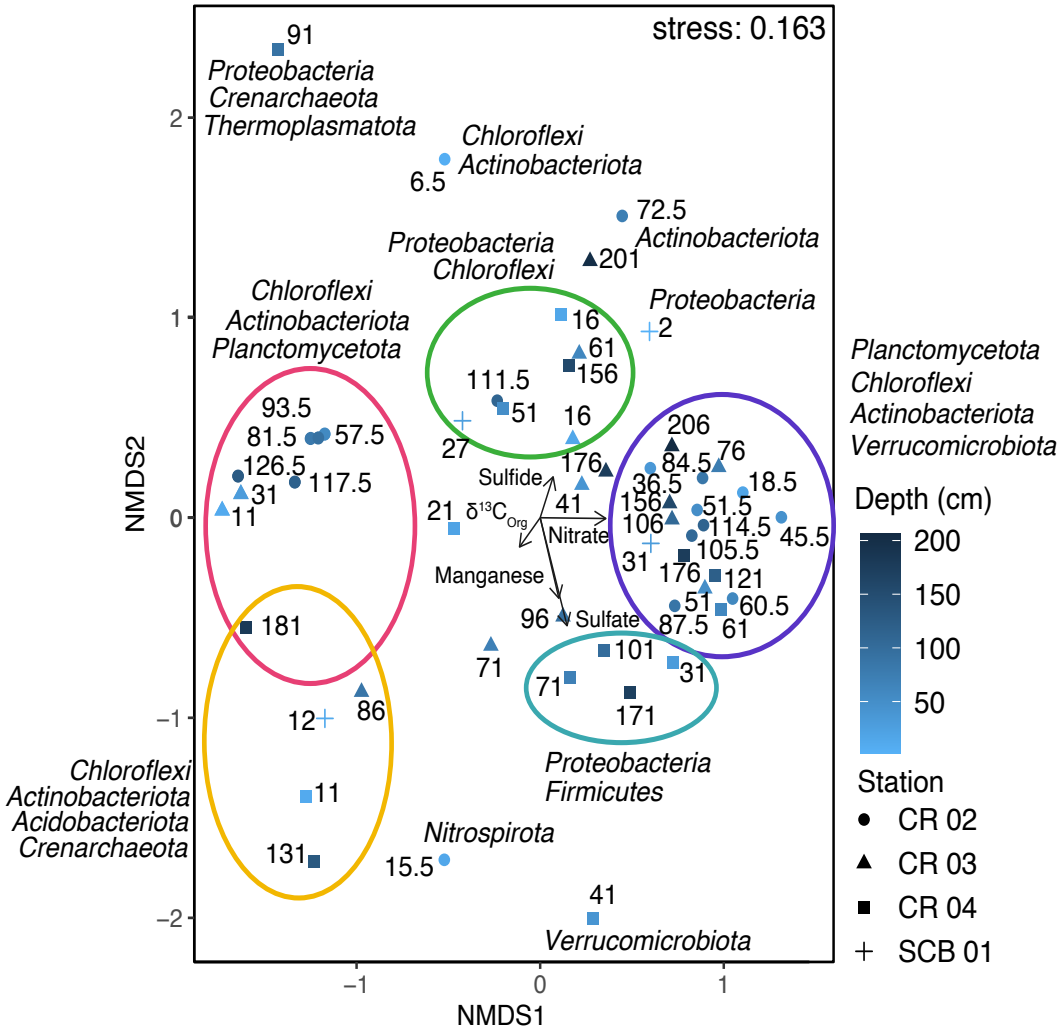

Supp. Fig. 11: Non-metric multidimensional scaling (NMDS) plot for the sediment 16S rRNA sequences from the San Clemente Basin multicore and the Cocos Ridge gravity cores. Each point corresponds to a sample taken at a different core (shape) and depth (color), with the numbers next to them indicating depth. Vectors for some of the geochemical parameters indicated in Table S1 are shown, as well as the stress value from the NMDS analysis. The circles indicate the clades that drive the clustering of samples.

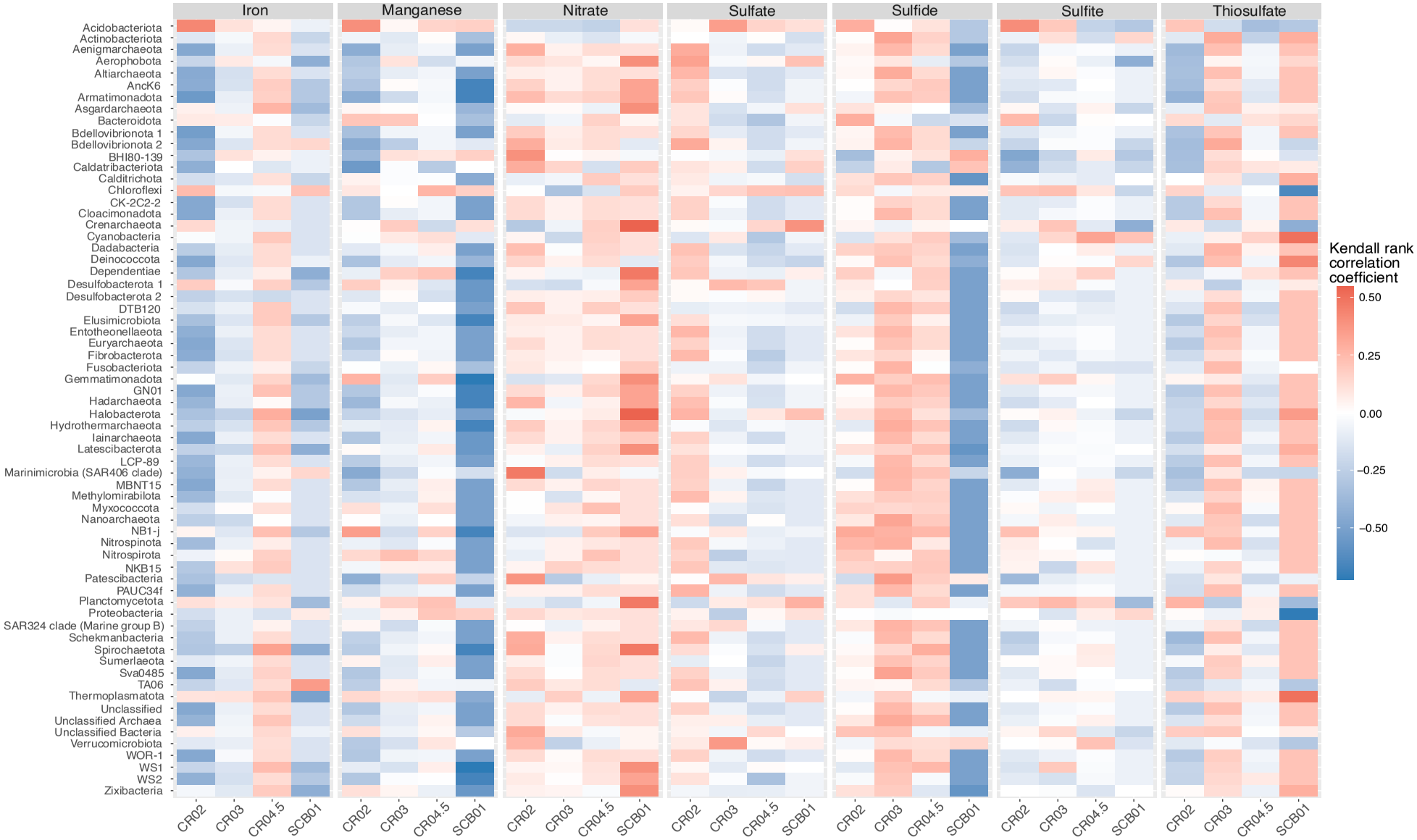

Supp. Fig. 12: Correlation plot between all the phyla detected from 16S rRNA in the sediments of San Clemente Basin and Cocos Ridge and redox-sensitive elements and sulfur intermediates in porewaters. Each column represents a different compound and each subcolumn represents a different core. Colors represent the score from the Kendall rank correlation coefficient, with positive associations in red and negative associations in blue. None of the correlations were found to be significant ($p < 0.05$).

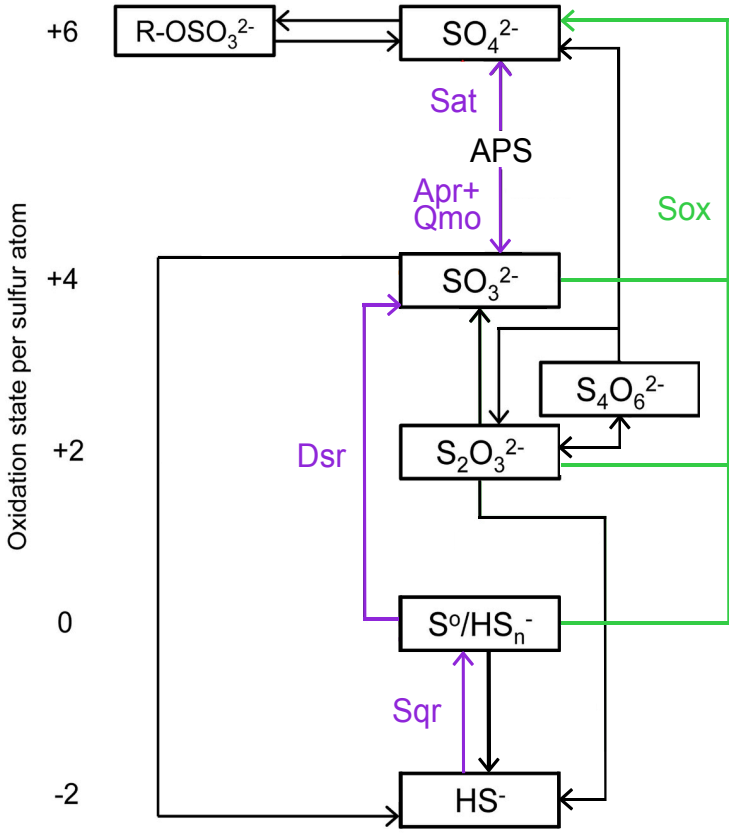

Supp. Fig. 13: Main metabolic pathways involved in the transformation of inorganic sulfur species. Modified from van Vliet et al., 2021.

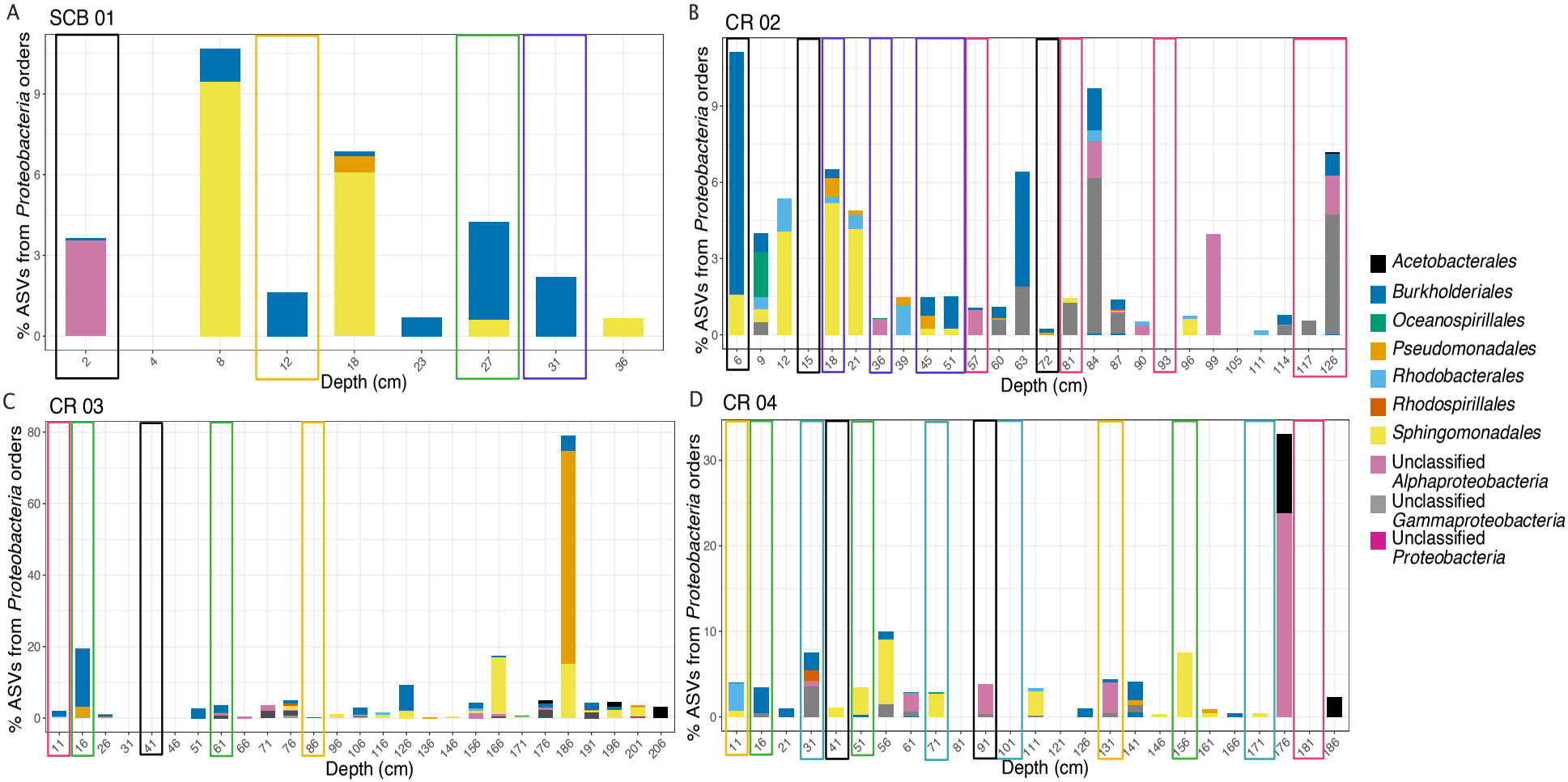

Supp. Fig. 14: Relative proportions of amplicon sequence variants (ASVs) detected through 16S rRNA of orders of *Proteobacteria* for A) SCB 01, B) CR 02, C) CR 03, and D) CR 04. Colored boxes around specific depths indicate clustering groups according to the NMDS analysis, where the colours of the clusters correspond to the same colors as in Supp. Fig. 11.

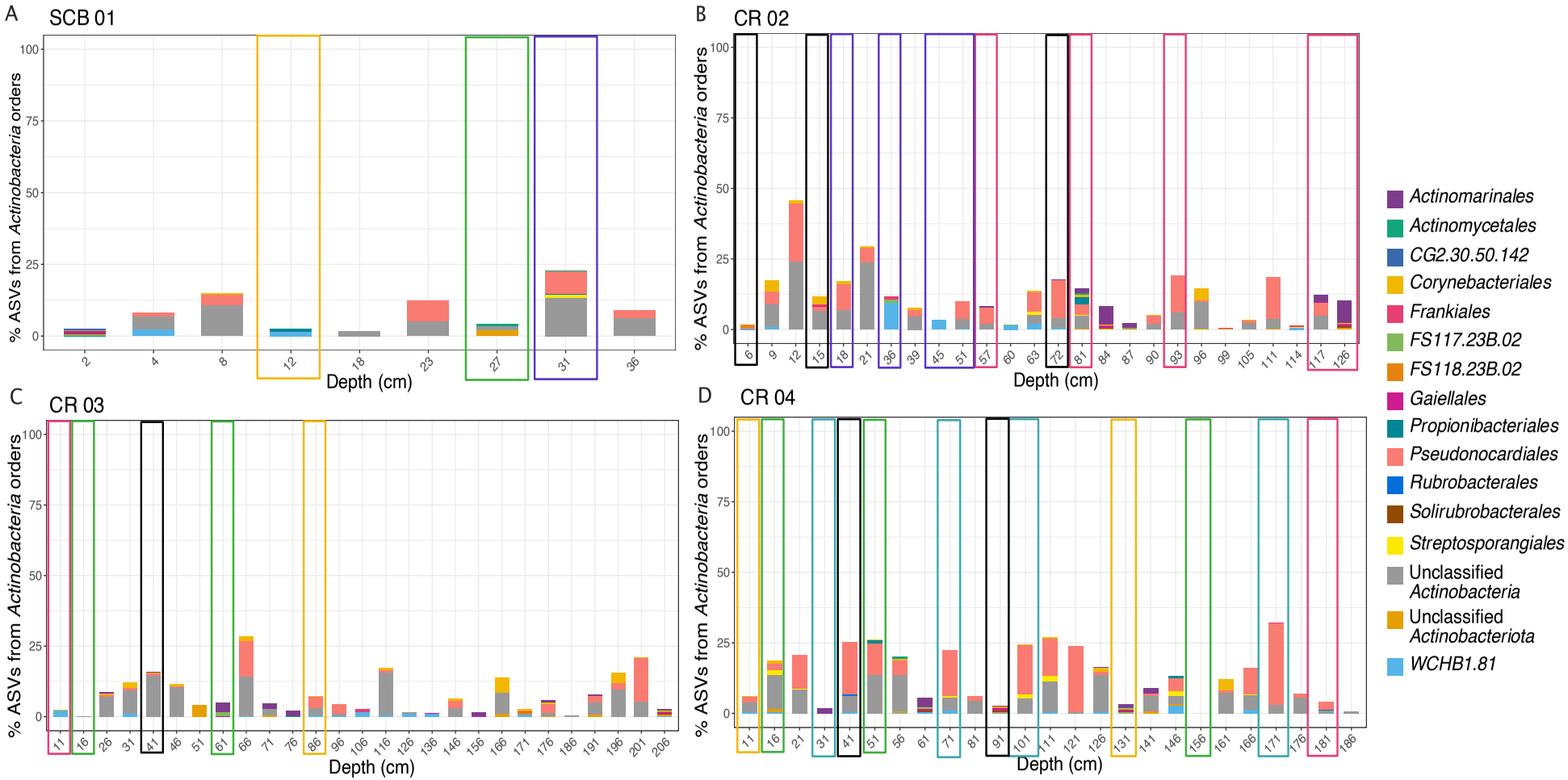

Supp. Fig. 15: Relative proportions of amplicon sequence variants (ASVs) detected through 16S rRNA of orders of *Actinobacteriota* for A) SCB 01, B) CR 02, C) CR 03, and D) CR 04. Colored boxes around specific depths indicate clustering groups according to the NMDS analysis, where the colours of the clusters correspond to the same colors as in Supp. Fig. 11.

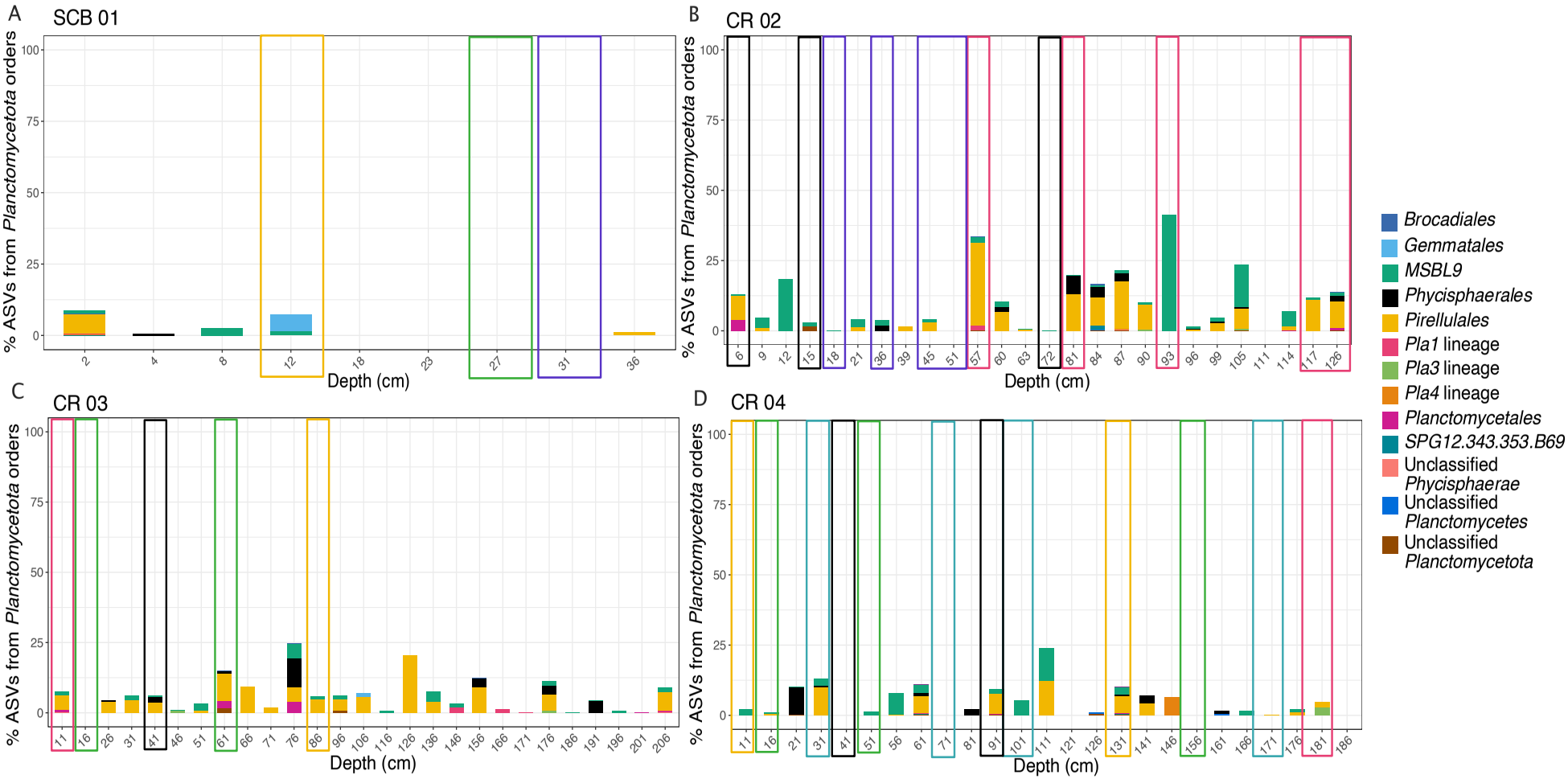

Supp. Fig. 16: Relative proportions of amplicon sequence variants (ASVs) detected through 16S rRNA of orders of *Planctomycetota* for A) SCB 01, B) CR 02, C) CR 03, and D) CR 04. Colored boxes around specific depths indicate clustering groups according to the NMDS analysis, where the colours of the clusters correspond to the same colors as in Supp. Fig. 11.

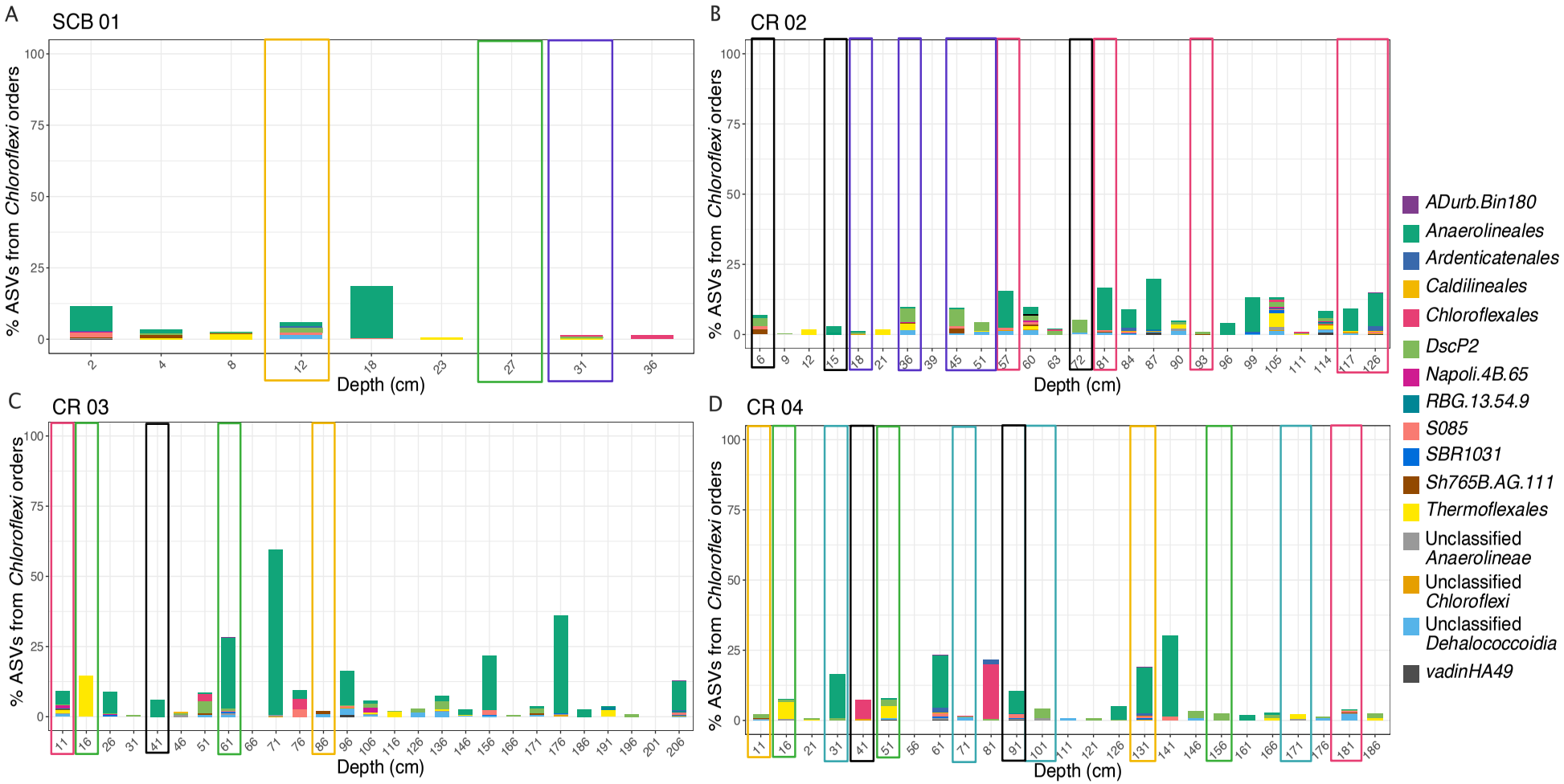

Supp. Fig. 17: Relative proportions of amplicon sequence variants (ASVs) detected through 16S rRNA of orders of *Chloroflexi* for A) SCB 01, B) CR 02, C) CR 03, and D) CR 04. Colored boxes around specific depths indicate clustering groups according to the NMDS analysis, where the colours of the clusters correspond to the same colors as in Supp. Fig. 11.

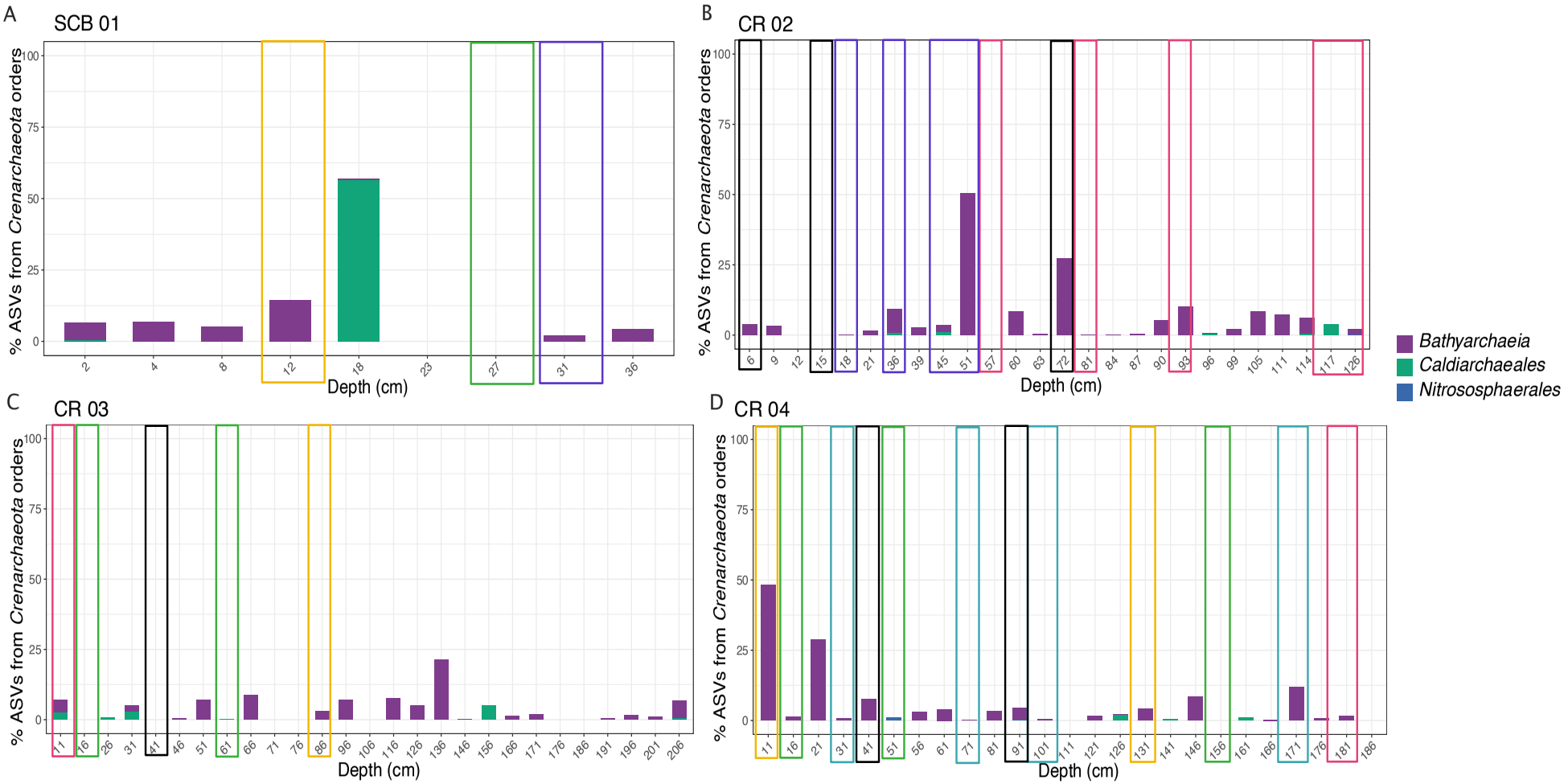

Supp. Fig. 18: Relative proportions of amplicon sequence variants (ASVs) detected through 16S rRNA of orders of *Crenarchaeota* for A) SCB 01, B) CR 02, C) CR 03, and D) CR 04. Colored boxes around specific depths indicate clustering groups according to the NMDS analysis, where the colours of the clusters correspond to the same colors as in Supp. Fig. 11.

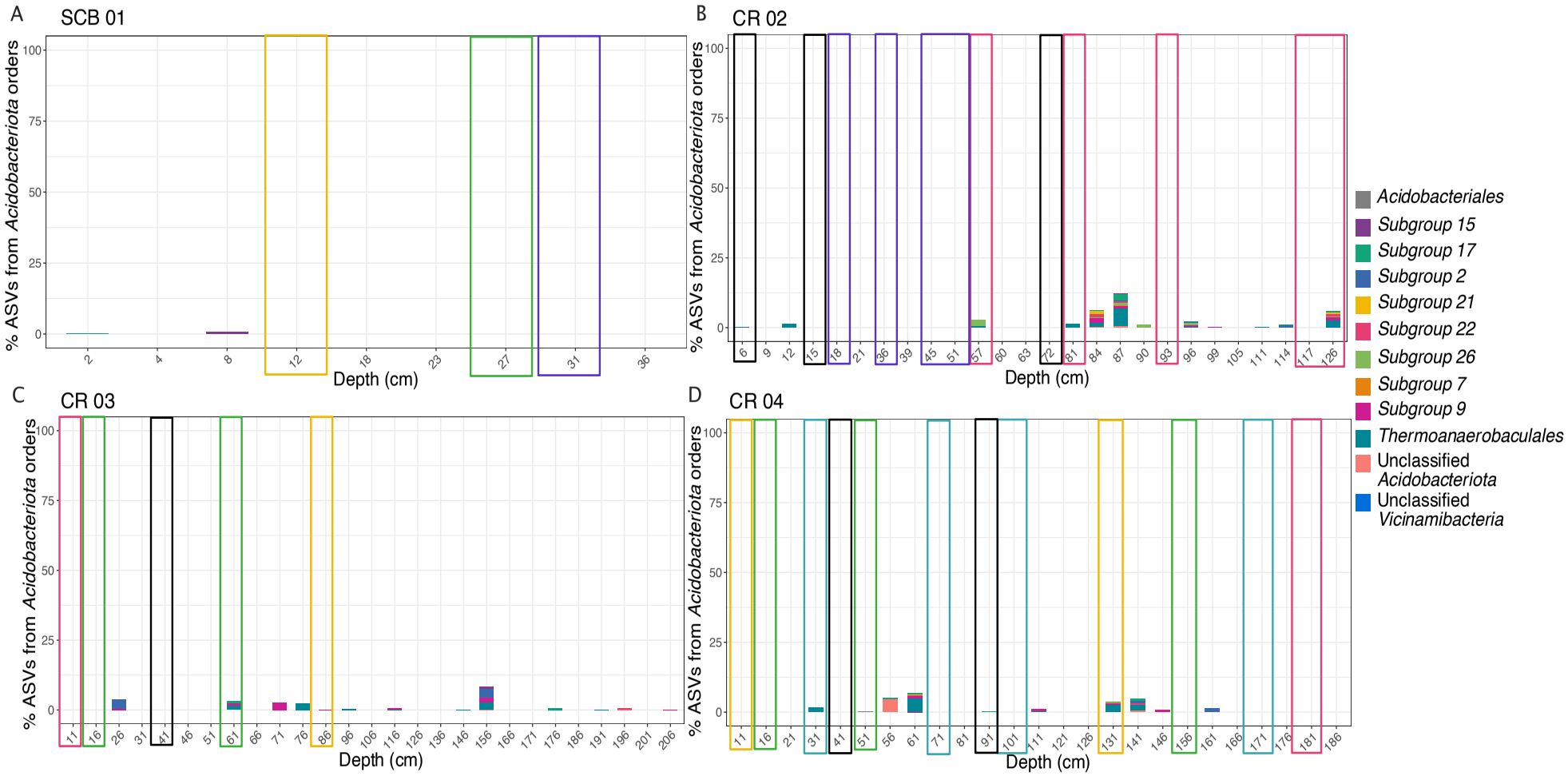

Supp. Fig. 19: Relative proportions of amplicon sequence variants (ASVs) detected through 16S rRNA of orders of *Acidobacteriota* for A) SCB 01, B) CR 02, C) CR 03, and D) CR 04. Colored boxes around specific depths indicate clustering groups according to the NMDS analysis, where the colours of the clusters correspond to the same colors as in Supp. Fig. 11.

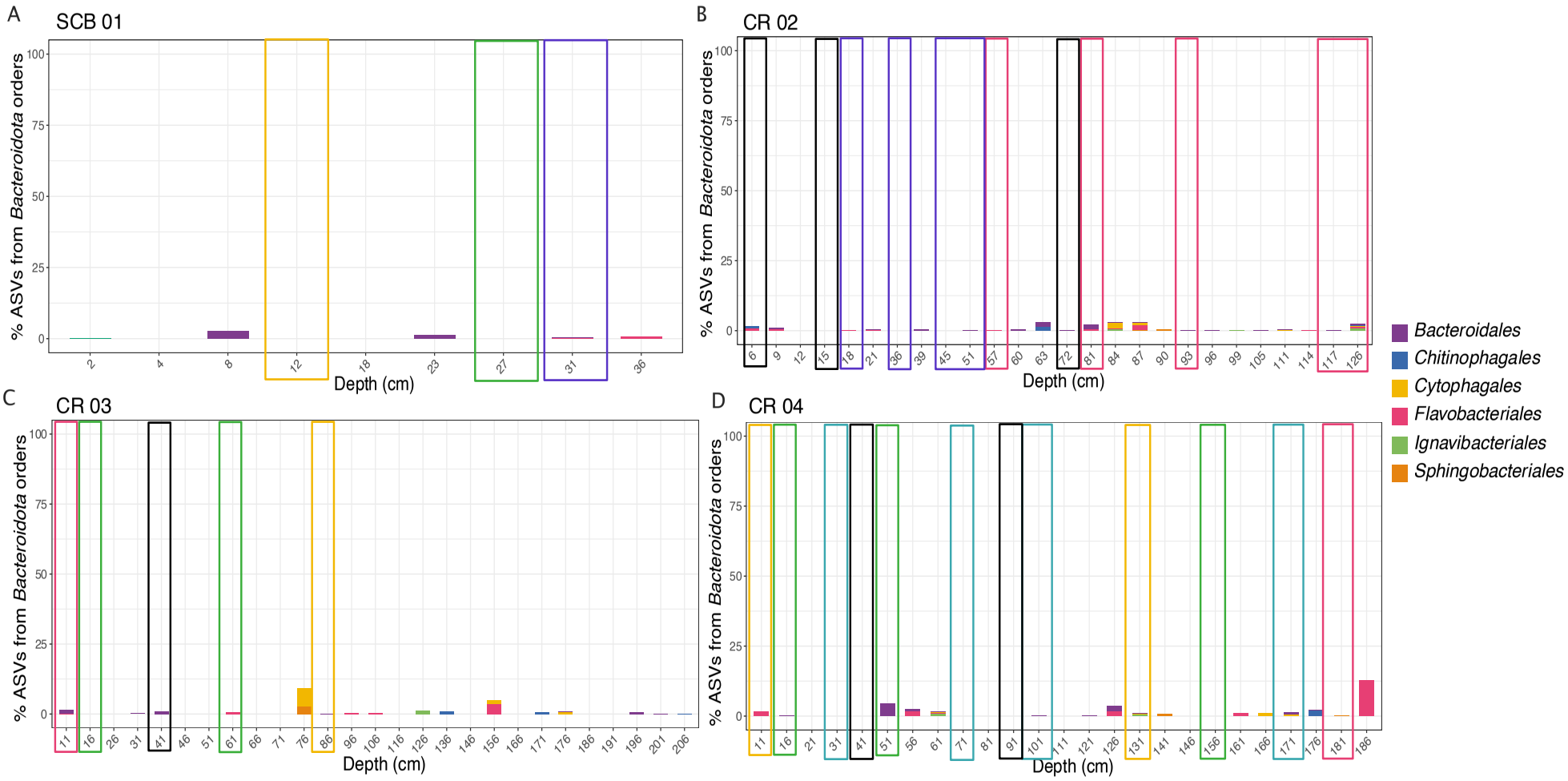

Supp. Fig. 20: Relative proportions of amplicon sequence variants (ASVs) detected through 16S rRNA of orders of *Bacteroidota* for A) SCB 01, B) CR 02, C) CR 03, and D) CR 04. Colored boxes around specific depths indicate clustering groups according to the NMDS analysis, where the colours of the clusters correspond to the same colors as in Supp. Fig. 11.

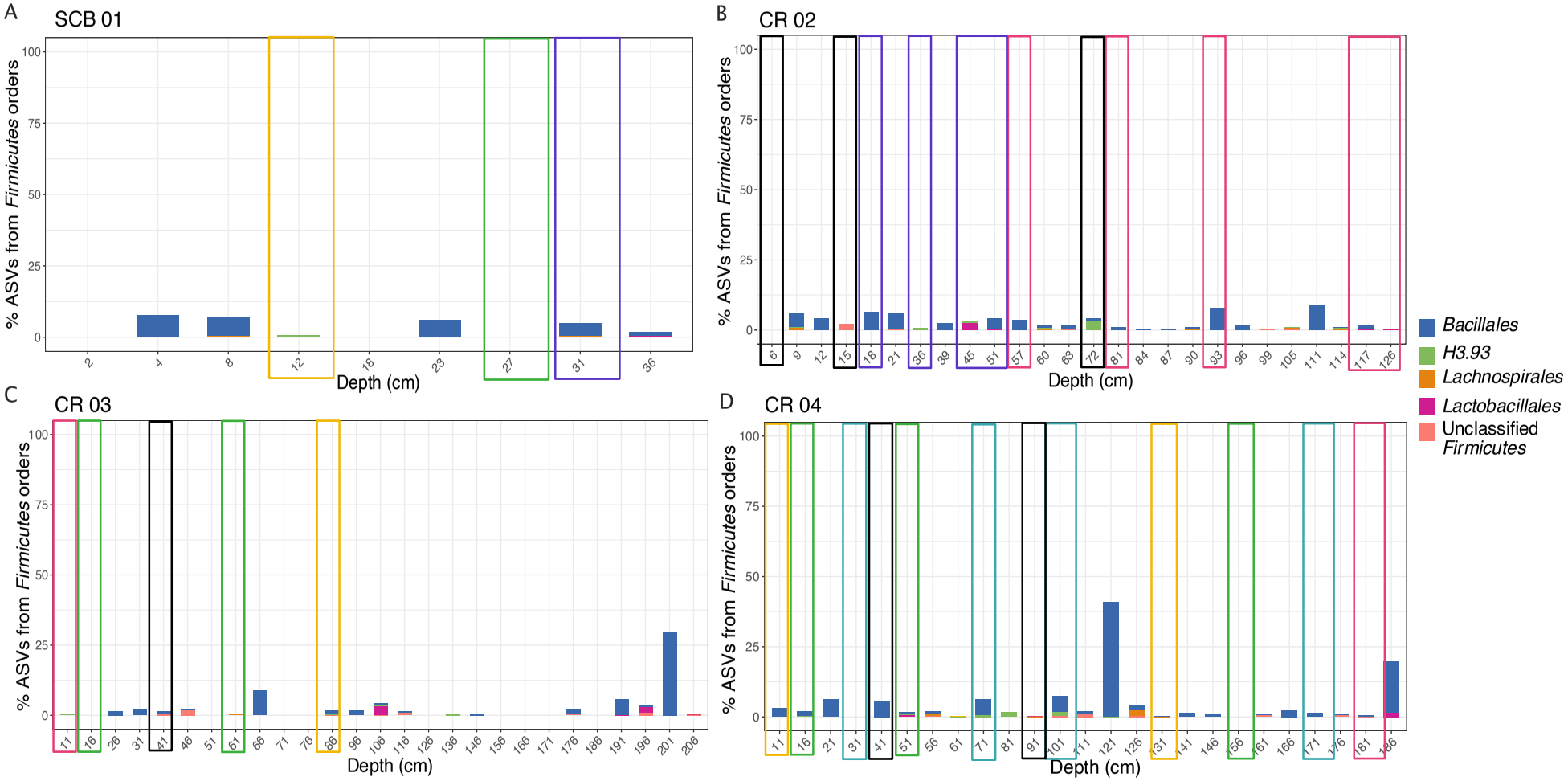

Supp. Fig. 21: Relative proportions of amplicon sequence variants (ASVs) detected through 16S rRNA of orders of *Firmicutes* for A) SCB 01, B) CR 02, C) CR 03, and D) CR 04. Colored boxes around specific depths indicate clustering groups according to the NMDS analysis, where the colours of the clusters correspond to the same colors as in Supp. Fig. 11.

References

Aller, R. C. (1990). Bioturbation and manganese cycling in hemipelagic sediments. *Philosophical Transactions of the Royal Society of London. Series A, Mathematical and Physical Sciences*, *331*(1616), 51–68.

Aller, R. C., & Rude, P. D. (1988). Complete oxidation of solid phase sulfides by manganese and bacteria in anoxic marine sediments. *Geochimica et Cosmochimica Acta*, *52*(3), 751–765.

Anantharaman, K., Hausmann, B., Jungbluth, S. P., Kantor, R. S., Lavy, A., Warren, L. A., Rappé, M. S., Pester, M., Loy, A., Thomas, B. C., & Banfield, J. F. (2018). Expanded diversity of microbial groups that shape the dissimilatory sulfur cycle. *ISME Journal*, *12*(7), 1715–1728. https://doi.org/10.1038/s41396-018-0078-0

Anderson, I. J., Dharmarajan, L., Rodriguez, J., Hooper, S., Porat, I., Ulrich, L. E., Elkins, J. G., Mavromatis, K., Sun, H., Land, M., Lapidus, A., Lucas, S., Barry, K., Huber, H., Zhulin, I. B., Whitman, W. B., Mukhopadhyay, B., Woese, C., Bristow, J., & Kyrpides, N. (2009). The complete genome sequence of Staphylothermus marinus reveals differences in sulfur metabolism among heterotrophic Crenarchaeota. *BMC Genomics*, *10*, 1–13. https://doi.org/10.1186/1471-2164-10-145

Antler, G., & Pellerin, A. (2018). A critical look at the combined use of sulfur and oxygen isotopes to study microbial metabolisms in methane-rich environments. *Frontiers in Microbiology*, *9*(APR), 1–7. https://doi.org/10.3389/fmicb.2018.00519

Antler, G., Turchyn, A. V., Herut, B., & Sivan, O. (2015). A unique isotopic fingerprint of sulfate-driven anaerobic oxidation of methane. *Geology*, *43*(7), 619–622. https://doi.org/10.1130/G36688.1

Antler, G., Turchyn, A. V., Rennie, V., Herut, B., & Sivan, O. (2013). Coupled sulfur and oxygen isotope insight into bacterial sulfate reduction in the natural environment. *Geochimica et Cosmochimica Acta*, *118*, 98–117. https://doi.org/10.1016/j.gca.2013.05.005

Aronson, H. S., Monteverde, D. R., Barnes, B. D., Johnson, B. R., Zawaski, M. J., Speth, D. R., Wang, X. T., Wu, F., Webb, S. M., & Trower, E. J. (2022). Sulfur cycling at natural hydrocarbon and sulfur seeps in Santa Paula Creek, CA. *Geobiology*, *20*(5), 707–725.

Bak, F., & Pfennig, N. (1987). Chemolithotrophic growth of Desulfovibrio sulfodismutans sp. nov. by disproportionation of inorganic sulfur compounds. *Archives of Microbiology*, *147*(2), 184–189.

Bak, F., & Cypionka, H. (1987). A novel type of energy metabolism involving fermentation of inorganic sulphur compounds. *Nature*, *326*(6116), 891–892.

Bender, M., Jahnke, R., Weiss, R., Martin, W., Heggie, D. T., Orchando, J., & Sowers, T. (1989). Organic carbon oxidation and benthic nitrogen and silica dynamics in San Clemente Basin, a continental borderland site. *Geochimica et Cosmochimica Acta*, *53*(January 1985), 685–697.

Bender, M. L., & Heggie, D. T. (1984). Fate of organic carbon reaching the deep sea floor: a status report. *Geochimica et Cosmochimica Acta*, *48*(5), 977–986. https://doi.org/10.1016/0016-7037(84)90189-3

Benjamini, Y., & Hochberg, Y. (1995). Controlling the False Discovery Rate: A Practical and Powerful Approach to Multiple Testing. *Journal of the Royal Statistical Society: Series B (Methodological)*, *57*(1), 289–300. https://doi.org/10.1111/j.2517-6161.1995.tb02031.x

Berner, R. A. (1978). Sulfate reduction and the rate of deposition of marine sediments. *Earth and Planetary Science Letters, 37*(3), 492–498.

Berner, R. A. (1964). Distribution and diagenesis of sulfur in some sediments from the Gulf of California. *Marine Geology*, *1*(2), 117–140. https://doi.org/10.1016/0025-3227(64)90011-8

Bowles, M. W., Mogollón, J. M., Kasten, S., Zabel, M., & Hinrichs, K.-U. (2014). Global rates of marine sulfate reduction and implications for sub–sea-floor metabolic activities. *Science*, *344*(6186), 889–891.

Brüchert, V., & Pratt, L. M. (1999). Stable Sulfur isotopic evidence for historical changes of sulfur cycling in estuarine sediments from northern Florida. *Aquatic Geochemistry*, *5*(3), 249–268. https://doi.org/10.1023/A:1009661812641

Brunner, B., & Bernasconi, S. M. (2005). A revised isotope fractionation model for dissimilatory sulfate reduction in sulfate reducing bacteria. *Geochimica et Cosmochimica Acta*, *69*(20), 4759–4771. https://doi.org/10.1016/j.gca.2005.04.015

Callahan, B. J., McMurdie, P. J., Rosen, M. J., Han, A. W., Johnson, A. J. A., & Holmes, S. P. (2016). DADA2: High-resolution sample inference from Illumina amplicon data. *Nature methods*, *13*(7), 581–583.

Canfield, D. E. (1991). Sulfate reduction in deep-sea sediments. https://doi.org/10.2475/ajs.291.2.177

Canfield, D. E. (2001). Biogeochemistry of sulfur isotopes. *Reviews in Mineralogy and Geochemistry*, *43*(1), 607–636.

Canfield, D. E. (1989). Sulfate reduction and oxic respiration in marine sediments: implications for organic carbon preservation in euxinic environments. *Deep Sea Research*, *36*(1), 121–138.

Canfield, D. E., & Des Marais, D. J. (1991). Aerobic sulfate reduction in microbial mats. *Science*, *251*(5000), 1471–1473.

Canfield, D. E., & Thamdrup, B. (2009). Towards a consistent classification scheme for geochemical environments , or , why we wish the term ' suboxic ' would go away. *Geobiology*, *7*, 385–392. https://doi.org/10.1111/j.1472-4669.2009.00214.x

Canfield, D. E., Thamdrup, E., & Hansen, J. W. (1993). The anaerobic degradation of organic matter in Danish coastal sediments: Iron reduction , manganese reduction, and sulfate reduction. *Geochimica et Cosmochimica Acta*, *57*, 3867–3883.

Canfield, D. E., Jørgensen, B. B., Fossing, H., Glud, R., Gundersen, J., Ramsing, N. B., Thamdrup, B., Hansen, J. W., Nielsen, L. P., & Hall, P. O. J. (1993). Pathways of organic carbon oxidation in three continental margin sediments. *Marine geology*, *113*(1-2), 27–40.

Chambers, L. A., & Trudinger, P. A. (1979). Microbiological fractionation of stable sulfur isotopes: A review and critique. *Geomicrobiology Journal*, *1*(3), 249–293. https://doi.org/10.1080/01490457909377735

Clarke, K. R. (1993). Non-parametric multivariate analyses of changes in community structure. *Australian journal of ecology*, *18*(1), 117–143.

Cline, J. D. (1969). Spectrophotometric Determination of Hydrogen Sulfide in Natural Waters. *Limnology and Oceanography*, *14*(3), 454–458. https://doi.org/10.4319/lo.1969.14.3.0454

Crémière, A., Strauss, H., Sebilo, M., Hong, W. L., Gros, O., Schmidt, S., Tocny, J., Henry, F., Gontharet, S., & Laverman, A. M. (2017). Sulfur diagenesis under rapid accumulation of organic-rich sediments in a marine mangrove from Guadeloupe (French West Indies). *Chemical Geology*, *454*, 67–79. https://doi.org/10.1016/j.chemgeo.2017.02.017

Detmers, J., Brüchert, V., Habicht, K. S., & Kuever, J. (2001). Diversity of sulfur isotope fractionations by sulfate-reducing prokaryotes. *Applied and Environmental Microbiology*, *67*(2), 888–894. https://doi.org/10.1128/AEM.67.2.888-894.2001

Deusner, C., Holler, T., Arnold, G. L., Bernasconi, S. M., Formolo, M. J., & Brunner, B. (2014). Sulfur and oxygen isotope fractionation during sulfate reduction coupled to anaerobic oxidation of methane is dependent on methane concentration. *Earth and Planetary Science Letters*, *399*, 61–73. https://doi.org/10.1016/j.epsl.2014.04.047

Durbin, A. M., & Teske, A. (2011). Microbial diversity and stratification of South Pacific abyssal marine sediments. *Environmental Microbiology*, *13*(12), 3219–3234. https://doi.org/10.1111/j.1462-2920.2011.02544.x

Elsgaard, L., & Jørgensen, B. B. (1992). Anoxic transformations of radiolabeled hydrogen sulfide in marine and freshwater sediments. *Geochimica et Cosmochimica Acta*, *56*(6), 2425–2435.

Emerson, S., Jahnke, R., Bender, M., Froelich, P., Klinkhammer, G., Bowser, C., & Setlock, G. (1980). Early diagenesis in sediments from the eastern equatorial Pacific, I. Pore water nutrient and carbonate results. *Earth and Planetary Science Letters*, *49*(1), 57–80. https://doi.org/10.1016/0012-821X(80)90150-8

Findlay, A. J., Bennett, A. J., Hanson, T. E., & Luther, G. W. (2015). Light-Dependent Sulfide Oxidation in the Anoxic Zone of the Chesapeake Bay Can Be Explained by Small Populations of Phototrophic Bacteria. *Applied and Environmental Microbiology*, *81*(21), 7560–7569. https://doi.org/10.1128/AEM.02062-15

Finster, K. (2008). Microbiological disproportionation of inorganic sulfur compounds. *Journal of Sulfur Chemistry*, *29*(3-4), 281–292.

Flood, B. E., Louw, D. C., Van der Plas, A. K., & Bailey, J. V. (2021). *Giant sulfur bacteria (Beggiatoaceae) from sediments underlying the Benguela upwelling system host diverse microbiomes* (Vol. 16). https://doi.org/10.1371/journal.pone.0258124

Friedrich, C. G., Quentmeier, A., Bardischewsky, F., Rother, D., Kraft, R., Kostka, S., & Prinz, H. (2000). Novel genes coding for lithotrophic sulfur oxidation of Paracoccus pantotrophus GB17. *Journal of Bacteriology*, *182*(17), 4677–4687. https://doi.org/10.1128/JB.182.17.4677-4687.2000

Fritz, P., Basharmal, G. M., Drimmie, R. J., Ibsen, J., & Qureshi, R. M. (1989). Oxygen isotope exchange between sulphate and water during bacterial reduction of sulphate. *Chemical Geology: Isotope Geoscience Section*, *79*(2), 99–105. https://doi.org/10.1016/0168-9622(89)90012-2

Froelich, P. N., Klinkhammer, G. P., Bender, M. L., Luedtke, N. A., Heath, G. R., Cullen, D., Dauphin, P., Hammond, D., Hartman, B., & Maynard, V. (1979). Early oxidation of organic matter in pelagic sediments of the eastern equatorial Atlantic: suboxic diagenesis. *Geochimica et Cosmochimica Acta*, *43*(7), 1075–1090. https://doi.org/10.1016/0016-7037(79)90095-4

Garcia, H. E., Weathers, K. W., Paver, C. R., Smolyar, I., Boyer, T. P., Locarnini, M. M., Zweng, M. M., Mishonov, A. V., Baranova, O. K., & Seidov, D. (2019). World Ocean Atlas 2018, Volume 3: Dissolved Oxygen, Apparent Oxygen Utilization, and Dissolved Oxygen Saturation.

Goldhaber, M. B., & Kaplan, I. R. (1975). Controls and consequences of sulfate reduction rates in recent marine sediments. *Soil Science*, *119*(1), 42–55.

Grimm, F., Franz, B., & Dahl, C. (2011). Regulation of dissimilatory sulfur oxidation in the purple sulfur bacterium Allochromatium vinosum. *Frontiers in Microbiology*, *2*(MAR), 1–11. https://doi.org/10.3389/fmicb.2011.00051

Habicht, K. S., & Canfield, D. E. (1997). Sulfur isotope fractionation during bacterial sulfate reduction in organic-rich sediments. *Geochimica et Cosmochimica Acta*, *61*(24), 5351–5361. https://doi.org/10.1016/S0016-7037(97)00311-6

Haegeman, B., Hamelin, J., Moriarty, J., Neal, P., Dushoff, J., & Weitz, J. S. (2013). Robust estimation of microbial diversity in theory and in practice. *ISME Journal*, *7*(6), 1092–1101. https://doi.org/10.1038/ismej.2013.10

Harrison, A. G., & Thode, H. G. (1958). Mechanism of the bacterial reduction of sulphate from isotope fractionation studies. *Transactions of the Faraday Society*, *54*, 84–92.

Hausmann, B., Pelikan, C., Herbold, C. W., Köstlbacher, S., Albertsen, M., Eichorst, S. A., Glavina Del Rio, T., Huemer, M., Nielsen, P. H., Rattei, T., Stingl, U., Tringe, S. G., Trojan, D., Wentrup, C., Woebken, D., Pester, M., & Loy, A. (2018). Peatland Acidobacteria with a dissimilatory sulfur metabolism. *ISME Journal*, *12*(7), 1729–1742. https://doi.org/10.1038/s41396-018-0077-1

Hayes, M. K., Taylor, G. T., Astor, Y., & Scranton, M. I. (2006). Vertical distributions of thiosulfate and sulfite in the Cariaco Basin. *Limnology and Oceanography*, *51*(1 I), 280–287. https://doi.org/10.4319/lo.2006.51.1.0280

Higgins, J. A., & Schrag, D. P. (2010). Constraining magnesium cycling in marine sediments using magnesium isotopes. *Geochimica et Cosmochimica Acta*, *74*(17), 5039–5053. https://doi.org/10.1016/j.gca.2010.05.019

Holmkvist, L., Ferdelman, T. G., & Barker, B. (2011). A cryptic sulfur cycle driven by iron in the methane zone of marine sediment (Aarhus Bay , Denmark). *Geochimica et Cosmochimica Acta*, *75*(12), 3581–3599. https://doi.org/10.1016/j.gca.2011.03.033

Holmkvist, L., Kamyshny Jr, A., Vogt, C., Vamvakopoulos, K., Ferdelman, T. G., & Jørgensen, B. B. (2011). Sulfate reduction below the sulfate–methane transition in Black Sea sediments. *Deep Sea Research Part I: Oceanographic Research Papers*, *58*(5), 493–504.

Jensen, M. M., Kuypers, M. M. M., Gaute, L., & Thamdrup, B. (2008). Rates and regulation of anaerobic ammonium oxidation and denitrification in the Black Sea. *Limnology and Oceanography*, *53*(1), 23–36.

Jones, G. E., & Starkey, R. L. (1957). Fractionation of stable isotopes of sulfur by microorganisms and their role in deposition of native sulfur. *Applied microbiology*, *5*(2), 111–118.

Jørgensen, B. B. (1977). Bacterial sulfate reduction within reduced microniches of oxidized marine sediments. *Marine Biology*, *41*(1), 7–17. https://doi.org/10.1007/BF00390576

Jorgensen, B. B., & Bak, F. (1991). Pathways and microbiology of thiosulfate transformations and sulfate reduction in a marine sediment (Kattegat, Denmark). *Applied and Environmental Microbiology*, *57*(3), 847–856. https://doi.org/10.1128/aem.57.3.847-856.1991

Jørgensen, B. B. (1990). A thiosulfate shunt in the sulfur cycle of marine sediments. *Science*, *249*(4965), 152–154. https://doi.org/10.1126/science.249.4965.152

Jørgensen, B. B. (1982). Mineralization of organic matter in the sea bed - the role of sulphate reduction. *Nature*, *296*(5858), 643–645.

Jørgensen, B. B., Böttcher, M. E., Lüschen, H., Neretin, L. N., & Volkov, I. I. (2004). Anaerobic methane oxidation and a deep H2 S sink generate isotopically heavy sulfides in Black Sea sediments. *Geochimica et Cosmochimica Acta*, *68*(9), 2095–2118. https://doi.org/10.1016/J.GCA.2003.07.017

Kaplan, I. R., Emery, K. O., & Rittenbebg, S. C. (1963). The distribution and isotopic abundance of sulphur in recent marine sediments off southern California. *Geochimica et Cosmochimica Acta*, *27*(4). https://doi.org/10.1016/0016-7037(63)90074-7

Kaplan, I. R., & Rittenberg, S. C. (1964). Microbiological Fractionation of Sulphur Isotopes. *Journal of General Microbiology*, *34*(2), 195–212. https://doi.org/10.1099/00221287-34-2-195

Kemp, A. L. W., & Thode, M. G. (1968). The mechanism of the baoterial reduction of sulphate and studi. *Geochimica et Cosmochimica Acta*, *32*, 71–91.

Klinkhammer, G. P. (1980). Early diagenesis in sediments from the eastern equatorial Pacific, II. Pore water metal results. *Earth and Planetary Science Letters*, *49*(1), 81–101. https://doi.org/10.1016/0012-821X(80)90151-X

Krämer, M., & Cypionka, H. (1989). Sulfate formation via ATP sulfurylase in thiosulfate-and sulfite-disproportionating bacteria. *Archives of microbiology*, *151*, 232–237.

Kulichevskaya, I. S., Suzina, N. E., Rijpstra, W. I. C., Damsté, J. S. S., & Dedysh, S. N. (2014). Paludibaculum fermentans gen. nov., sp. nov., a facultative anaerobe capable of dissimilatory iron reduction from subdivision 3 of the Acidobacteria. *International journal of systematic and evolutionary microbiology*, *64*(Pt 8), 2857–2864. https://doi.org/10.1099/ijs.0.066175-0

Liu, Y., Beer, L. L., & Whitman, W. B. (2012). Sulfur metabolism in archaea reveals novel processes. *Environmental Microbiology*, *14*(10), 2632–2644. https://doi.org/10.1111/j.1462-2920.2012.02783.x

Lloyd, R. (1968). Oxygen Isotope Behavior in Sulfate-Water System. *Journal of Geophysical Research*, *73*(18), 6099–6110. https://doi.org/10.1029/jb073i018p06099

Longinelli, A., & Craig, H. (1967). Oxygen-18 variations in sulfate ions in sea water and saline lakes. *Science*, *156*(3771), 56–59. https://doi.org/10.1126/science.156.3771.56

Lovley, D. R., & Goodwin, S. (1988). Hydrogen concentrations as an indicator of the predominant terminal electron-accepting reactions in aquatic sediments. *Geochimica et Cosmochimica Acta*, *52*(12), 2993–3003. https://doi.org/10.1016/0016-7037(88)90163-9

Lovley, D. (2006). Dissimilatory Fe(III)- and Mn(IV)-reducing prokaryotes. In M. Dworkin, S. Falkow, E. Rosenberg, K.-H. Schleifer, & E. Stackebrandt (Eds.), *Prokaryotes 2* (pp. 635–658).

Mariotti, A., Germon, J. C., Hubert, P., Kaiser, P., Letolle, R., Tardieux, A., & Tardieux, P. (1981). Experimental determination of nitrogen kinetic isotope fractionation: Some principles; illustration for the denitrification and nitrification processes. *Plant and Soil*, *62*(3), 413–430. https://doi.org/10.1007/BF02374138

Martin, M. (2011). Cutadapt removes adapter sequences from high-throughput sequencing reads. *EMBnet. journal*, *17*(1), 10–12.

McMurdie, P. J., & Holmes, S. (2013). phyloseq: an R package for reproducible interactive analysis and graphics of microbiome census data. *PloS one*, *8*(4), e61217.

Meyer, B., Imhoff, J. F., & Kuever, J. (2007). Molecular analysis of the distribution and phylogeny of the soxB gene among sulfur-oxidizing bacteria - Evolution of the Sox sulfur oxidation enzyme system. *Environmental Microbiology*, *9*(12), 2957–2977. https://doi.org/10.1111/j.1462-2920.2007.01407.x

Mix, A. C., Tiedemann, R., & Blum, P. (2003). *12. Site 1241* (Vol. 202). https://doi.org/10.2973/odp.proc.ir.202.112.2003

Mizutani, Y., & Rafter, T. A. (1969). Oxygen isotopic composition of sulphates. Part 4. Bacterial fracrtionation of oxygen isotopes in the reduction of sulphate and in the oxidation of sulphur. *New Zealand Journal of Science*, *12*, 60–68.

Mizutani, Y., & Rafter, T. A. (1973). Isotopic behaviour of sulphate oxygen in the bacterial reduction of sulphate. *Geochemical Journal*, *6*(4), 183–191.

Mo, S., Li, J., Li, B., Yu, R., Nie, S., Zhang, Z., Kashif, M., He, S., Liao, J., & Jiang, Q. (2020). Impacts of Crenarchaeota and Halobacterota on sulfate reduction in the subtropical mangrove ecosystem as revealed by SMDB analysis. *bioRxiv*, 2020–08.

Morono, Y., Ito, M., Hoshino, T., Terada, T., Hori, T., Ikehara, M., D'Hondt, S., & Inagaki, F. (2020). Aerobic microbial life persists in oxic marine sediment as old as 101.5 million years. *Nature Communications*, *11*(1), 3626.

Mottl, M. J. (1989). 17. Hydrothermal convection, reactions, and diffusion in sediments on the Costa Rica Rift flank: pore-water evidence from ODP Sites 677 and 678. In K. Becker & H. Sakai (Eds.), *Proceedings of the ocean drilling program, scientific results* (pp. 195–213). https://doi.org/10.2973/odp.proc.sr.111.125.1989

Oksanen, J., Blanchet, F. G., Friendly, M., Kindt, R., Legendre, P., McGlinn, D., Minchin, P. R., O'hara, R. B., Simpson, G. L., & Solymos, P. (2019). Vegan: community ecology package (version 2.5-6). *The Comprehensive R Archive Network*.

Parada, A. E., Needham, D. M., & Fuhrman, J. A. (2016). Every base matters: Assessing small subunit rRNA primers for marine microbiomes with mock communities, time series and global field samples. *Environmental Microbiology*, *18*(5), 1403–1414. https://doi.org/10.1111/1462-2920.13023

Parsons, T. R., Maita, Y., & Lalli, C. M. (1984). *A manual of chemical biological methods for seawater analysis*. Pergamon Press.

Pedersen, T. F. (1983). Increased productivity in the eastern equatorial Pacific during the last glacial maximum (19 000 to 14 000 yr BP). *Geology*, *11*(1), 16–19. https://doi.org/10.1130/0091-7613(1983)11<16:IPITEE>2.0.CO;2

Pjevac, P. (2014). *Co-existence and niche differentiation of sulfur oxidizing bacteria in marine environments* (Doctoral dissertation). University of Bremen, Bremen, Germany.

Quast, C., Pruesse, E., Yilmaz, P., Gerken, J., Schweer, T., Yarza, P., Peplies, J., & Glöckner, F. O. (2012). The SILVA ribosomal RNA gene database project: improved data processing and web-based tools. *Nucleic acids research*, *41*(D1), D590–D596.

R Core Team. (2019). R: a language and environment for statistical computing, version 3.0. 2. *Vienna, Austria: R Foundation for Statistical Computing, 2013*.

Raven, M. R., Adkins, J. F., Werne, J. P., Lyons, T. W., & Sessions, A. L. (2015). Sulfur isotopic composition of individual organic compounds from Cariaco Basin sediments. *Organic Geochemistry*, *80*, 53–59. https://doi.org/10.1016/j.orggeochem.2015.01.002

Raven, M. R., Sessions, A. L., Fischer, W. W., & Adkins, J. F. (2016). Sedimentary pyrite d34 S differs from porewater sulfide in Santa Barbara Basin: Proposed role of organic sulfur. *Geochimica et Cosmochimica Acta*, *186*, 120–134. https://doi.org/10.1016/j.gca.2016.04.037

Rees C. E., Jenkins, W. J., & Monster, J. (1978). The sulphur isotopic composition. *Geochimica et Cosmochimica Acta et Cosmochimica Acta*, *42*(65), 377–381.

Robertson, L. A., Dalsgaard, T., Revsbech, N.-P., & Kuenen, J. G. (1995). Confirmation of 'aerobic denitrification' in batch cultures, using gas chromatography and 15N mass spectrometry. *FEMS Microbiology Ecology*, *18*(2), 113–119.

Roden, E. E., & Lovley, D. R. (1993). Dissimilatory Fe (III) reduction by the marine microorganism Desulfuromonas acetoxidans. *Applied and Environmental Microbiology*, *59*(3), 734–742.

Savitzky, A., & Golay, M. J. E. (1964). Smoothing and differentiation of data by simplified least squares procedures. *Analytical chemistry*, *36*(8), 1627–1639.

Schütz, M., Maldener, I., Griesbeck, C., & Hauska, G. (1999). Sulfide-quinone reductase from Rhodobacter capsulatus: Requirement for growth, periplasmic localization, and extension of gene sequence analysis. *Journal of Bacteriology*, *181*(20), 6516–6523. https://doi.org/10.1128/jb.181.20.6516-6523.1999

Schwalbach, J. R., & Gorsline, D. S. (1985). Holocene sediment budgets for the basins of the California continental borderland. *Journal of Sedimentary Research*, *55*(6), 829–842.

Shannon, C. E. (1948). A mathematical theory of communication. *The Bell System Technical Journal*, *27*(3), 379–423. https://doi.org/10.1002/j.1538-7305.1948.tb01338.x

Shaw, M., Kes, J. G. I., & Nke, C. J. A. (1990). Early diagenesis in differing depositional environments : The response of transition metals in pore water. *Geochimica et Cosmochimica Acta*, *54*, 1233–1246.

Sim, M. S., Bosak, T., & Ono, S. (2011). Large Sulfur Isotope Fractionation Does Not Require Disproportionation. *Science*, *333*, 74–77. https://doi.org/10.1089/jmf.2016.3871

Sivan, O., Antler, G., Turchyn, A. V., Marlow, J. J., & Orphan, V. J. (2014). Iron oxides stimulate sulfate-driven anaerobic methane oxidation in seeps. *Proceedings of the National Academy of Sciences*, *111*(40), E4139–E4147. https://doi.org/10.1073/pnas.1412269111

Smith, D. A., Sessions, A. L., Dawson, K. S., Dalleska, N., & Orphan, V. J. (2017). Rapid quantification and isotopic analysis of dissolved sulfur specie. *Rapid Communications in Mass Spectrometry*, *31*(791-803).

Sorokin, D. Y., Messina, E., La Cono, V., Ferrer, M., Ciordia, S., Mena, M. C., Toshchakov, S. V., Golyshin, P. N., & Yakimov, M. M. (2018). Sulfur respiration in a Group of facultatively anaerobic natronoarchaea ubiquitous in hypersaline soda lakes. *Frontiers in Microbiology*, *9*(OCT). https://doi.org/10.3389/fmicb.2018.02359

Strous, M., Fuerst, J. A., Kramer, E. H. M., Logemann, S., Muyzer, G., van de Pas-Schoonen, K. T., Webb, R., Kuenen, J. G., & Jetten, M. S. M. (1999). Missing lithotroph identified as new planctomycete. *Nature*, *400*(6743), 446–449.

Stumm, W., & Morgan, J. J. (1970). *Aquatic chemistry*. Wiley-Interscience New York.

Thamdrup, B., Finster, K., Fossing, H., Hansen, J. W., & Jørgensen, B. B. (1994). Thiosulfate and sulfite distributions in porewater of marine sediments related to manganese, iron, and sulfur geochemistry. *Geochimica et Cosmochimica Acta*, *58*(1), 67–73. https://doi.org/10.1016/0016-7037(94)90446-4

Thode, H. G., Kleerekoper, H., & McElcheran, D. (1951). Isotope fractionation in the bacterial reduction of sulphate. *Research*, *4*(12), 581.

Tomlinson, G. A., Jahnke, L. L., & Hochstein, L. I. (1986). Halobacterium denitrificans sp. nov., an extremely halophilic denitrifying bacterium. *International journal of systematic bacteriology*, *36*(1), 66–70. https://doi.org/10.1099/00207713-36-1-66

Toth, D. J., & Lerman, A. (1977). Organic matter reactivity and sedimentation rates in the ocean. *American Journal of Science*, *277*(4), 465–485.

Troelsen, H., & Jørgensen, B. B. (1982). Seasonal dynamics of elemental sulfur in two coastal sediments. *Estuarine, Coastal and Shelf Science*, *15*(3), 255–266. https://doi.org/10.1016/0272-7714(82)90062-2

Turchyn, A. V., Sivan, O., & Schrag, D. P. (2006). Oxygen isotopic composition of sulfate in deep sea pore fluid: Evidence for rapid sulfur cycling. *Geobiology*, *4*(3), 191–201. https://doi.org/10.1111/j.1472-4669.2006.00079.x

Umezawa, K., Kojima, H., Kato, Y., & Fukui, M. (2020). Disproportionation of inorganic sulfur compounds by a novel autotrophic bacterium belonging to Nitrospirota. *Systematic and Applied Microbiology*, *43*(5), 126110.

van Vliet, D. M., von Meijenfeldt, F. A., Dutilh, B. E., Villanueva, L., Sinninghe Damsté, J. S., Stams, A. J., & Sánchez-Andrea, I. (2021). The bacterial sulfur cycle in expanding dysoxic and euxinic marine waters. *Environmental Microbiology*, *23*(6), 2834–2857. https://doi.org/10.1111/1462-2920.15265

Vetter, R., Matrai, P., Javor, B., & O'Brien, J. (1989). Reduced sulfur compounds in the marine environment. In E. Saltzman & W. Cooper (Eds.), *Biogenic sulfur in the environment* (pp. 243–261). American Chemical Society.

Vigneron, A., Cruaud, P., Culley, A. I., Couture, R. M., Lovejoy, C., & Vincent, W. F. (2021). Genomic evidence for sulfur intermediates as new biogeochemical hubs in a model aquatic microbial ecosystem. *Microbiome*, *9*(1), 1–14. https://doi.org/10.1186/s40168-021-00999-x

Volkov, I. I., & Neretin, L. N. (2008). Hydrogen sulfide in the black sea. *Handbook of Environmental Chemistry, Volume 5: Water Pollution*, *5*(Part Q), 309–331. https://doi.org/10.1007/698_5_083

Waite, D. W., Chuvochina, M., Pelikan, C., Parks, D. H., Yilmaz, P., Wagner, M., Loy, A., Naganuma, T., Nakai, R., Whitman, W. B., Hahn, M. W., Kuever, J., & Hugenholtz, P. (2020). Proposal to reclassify the proteobacterial classes deltaproteobacteria and oligoflexia, and the phylum thermodesulfobacteria into four phyla reflecting major functional capabilities. *International Journal of Systematic and Evolutionary Microbiology*, *70*(11), 5972–6016. https://doi.org/10.1099/ijsem.0.004213

Wang, M., Ma, Y., Feng, C., Cai, L., & Li, W. (2020). Diversity of Pelagic and Benthic Bacterial Assemblages in the Western Pacific Ocean. *Frontiers in Microbiology*, *11*(September), 1–12. https://doi.org/10.3389/fmicb.2020.01730

Wasmund, K., Mußmann, M., & Loy, A. (2017). The life sulfuric : microbial ecology of sulfur cycling in marine sediments. *Environmental microbiology Reports*, *9*, 323–344. https://doi.org/10.1111/1758-2229.12538

Weidler, G. W., Gerbl, F. W., & Stan-Lotter, H. (2008). Crenarchaeota and their role in the nitrogen cycle in a subsurface radioactive thermal spring in the Austrian Central Alps. *Applied and environmental microbiology*, *74*(19), 5934–5942. https://doi.org/10.1128/AEM.02602-07

Werne, J. P., Lyons, T. W., Hollander, D. J., Formolo, M. J., & Sinninghe Damsté, J. S. (2003). Reduced sulfur in euxinic sediments of the Cariaco Basin: Sulfur isotope constraints on organic sulfur formation. *Chemical Geology*, *195*(1-4), 159–179. https://doi.org/10.1016/S0009-2541(02)00393-5

Wickham, H., & Chang, W. (2016). Package 'ggplot2'. *Create elegant data visualisations using the grammar of graphics. Version 2.1*, 1–189.

Wright, E. S. (2016). Using DECIPHER v2. 0 to analyze big biological sequence data in R. *The R Journal*, *8*(1), 352–359.

Xia, Y., Lü, C., Hou, N., Xin, Y., Liu, J., Liu, H., & Xun, L. (2017). Sulfide production and oxidation by heterotrophic bacteria under aerobic conditions. *The ISME journal*, *11*(12), 2754–2766. https://doi.org/10.1038/ismej.2017.125

Yilmaz, P., Parfrey, L. W., Yarza, P., Gerken, J., Pruesse, E., Quast, C., Schweer, T., Peplies, J., Ludwig, W., & Glöckner, F. O. (2014). The SILVA and "all-species living tree project (LTP)" taxonomic frameworks. *Nucleic acids research*, *42*(D1), D643–D648.

Zawadzki, D., Maciag, Ł., Blasco, I., González, F. J., Wernette, B., Marino, E., Kozub-Budzyń, G. A., Piestrzyński, A., Wróbel, R. J., & McCartney, K. (2022). Geochemistry and Mineralogy of Ferromanganese Crusts from the Western Cocos-Nazca Spreading Centre, Pacific. *Minerals*, *12*(5), 1–30. https://doi.org/10.3390/min12050538

Zheng, P.-F., Wei, Z., Zhou, Y., Li, Q., Qi, Z., Diao, X., & Wang, Y. (2022). Genomic Evidence for the Recycling of Complex Organic Carbon by Novel Thermoplasmatota Clades in Deep-Sea Sediments. *mSystems*, *7*(3). https://doi.org/10.1128/msystems.00077-22

Zopfi, J. (2000). *Sulfide oxidation and speciation of sulfur intermediates in marine environments* (Doctoral Dissertation). University of Bremen.

Zopfi, J., Ferdelman, T. G., & Fossing, H. (2004). Distribution and fate of sulfur intermediates - Sulfite, tetrathionate, thiosulfate, and elemental sulfur - In marine sediments. *Special Paper of the Geological Society of America*, *379*, 97–116. https://doi.org/10.1130/0-8137-2379-5.97

Chapter 4

EFFECTS OF NUTRIENT LIMITATION ON SULFUR ISOTOPE FRACTIONATIONS DURING THE MICROBIAL OXIDATION OF SULFUR

Daniela Osorio-Rodriguez[1], Thomas E. Hanson[2,3], Victoria J. Orphan[1], Alex L. Sessions[1], Jess F. Adkins[1]

[1]Division of Geological and Planetary Sciences, California Institute of Technology, Pasadena, CA, 91125
[2]School of Marine Science and Policy, College of Earth, Ocean, and Environment, University of Delaware, Newark, DE, 19716
[3]Delaware Biotechnology Institute, University of Delaware, Newark, DE, 19716

Abstract

The microbial oxidation of sulfur (MSO) is an importance source of electrons for carbon fixation by autotrophic microbes in shallow aquatic environments. The sulfur isotope fractionations associated with this process have been found to lie between -5 and 4‰ for a variety of microbial sulfur oxidizers, which has led to the assumption that, unlike microbial sulfate reduction, which can have sulfur isotope fractionations in the range between -66 to 5‰ (Sim et al., 2011), fractionations during MSO are negligible. However, most studies have utilized culture conditions abundant in nutrients, which do not resemble those faced by microorganisms in the natural environments where these fractionations could be relevant and imparted to minerals that incorporate reduced sulfur. The recent discovery of a fractionation of 13‰ during the oxidation of sulfur by the *Deltaproteobacterium Desulfurivibrio alkaliphilus* (Pellerin et al., 2019) begs the question of whether specific metabolisms or growth conditions that have not been explored so far could produce large isotopic fractionations from MSO. In this study, we determined the sulfur isotope fraction-

ations from sulfide oxidation by *D. alkaliphilus*, a chemotrophic alkaliphile, and *Chlorobaculum tepidum*, a phototroph, under limited nutrients. We found that sulfur isotope fractionations by *D. alkaliphilus* only are sensitive to growth rates and cell specific sulfide oxidation rates. Albeit requiring further exploration, our results suggest that traditional sulfur oxidation pathways, which are present in the most abundant sulfur oxidizers in the environment, do not lead to large sulfur isotope fractionations during MSO under natural, oligotrophic conditions.

1. INTRODUCTION

About half of the organic matter in coastal sediments is remineralized via microbial sulfate reduction (MSR; Canfield, 1989; Jørgensen, 1982), and about 29% of marine organic matter gets remineralized through sulfate reduction on the seafloor globally, generating 11.3 teramoles of sulfide every year (Bowles et al., 2014). Sulfide serves as an electron donor for carbon fixation for a variety of aerobic chemolithotrophic (Friedrich et al., 2001) or anaerobic phototrophic microorganisms (Brune, 1989) that usually couple sulfur oxidation with the reduction of high redox potential electron acceptors, such as oxygen and nitrate, mainly in surface sediments where these electron acceptors are available (Wasmund et al., 2017). Among archaea, only members of the order *Sulfolobales* are known to be capable of sulfur oxidation (Brock et al., 1972), whereas *Alpha-*, *Beta-*, *Gamma-*, and *Epsilonproteobacteria*, *Aquificales*, *Campylobacterales*, and *Sulfobacillales* comprise aerobic sulfur-oxidizing bacteria (Dahl et al., 2008). Anaerobic sulfur-oxidizing bacteria (SOB) include *Alpha-* and *Gammaproteobacteria* ('purple sulfur bacteria'; Fowler et al., 1984) and *Chlorobiales* ('green sulfur bacteria'; Wahlund et al., 1991). The recent discovery of the capability of the *Deltaproteobacterium Desulfurivibrio alkaliphilus* to oxidize sulfur (Sorokin et al., 2008), potentially using the machinery for dissimilatory sulfate reduction in reverse (rDsr; Thorup et al., 2017), expanded the repertoire

of microbial phylogenetic clades and metabolic pathways known to be involved in sulfur oxidation. Despite the great diversity of microorganisms capable of oxidizing sulfur, the environmentally relevant sulfur oxidizers are probably only a few groups. Phototrophic bacteria dominate sulfur oxidation in stratified lakes (Rimmer et al., 2008) and basins (Findlay et al., 2015), and most of the dark carbon fixation is performed by sulfur-oxidizing *Epsilonproteobacteria* in sulfidic pelagic redoxclines (Grote et al., 2008) and *Gammaproteobacteria* in pelagic redoxclines (Glaubitz et al., 2013), coastal sediments (Dyksma et al., 2016; Lavik et al., 2009), and the oxygenated ocean (Swan et al., 2011).

The microbial fractionation of sulfur isotopes was first studied in the 1950s, where a fractionation of -10 to -12‰ was observed for MSR (Harrison and Thode, 1958; Thode et al., 1951). Since then, many studies have focused on isotopic fractionations by MSR, due to the fact that fractionations as low as -75‰ (Brunner and Bernasconi, 2005; Rees, 1973) and -66‰ (Kaplan and Rittenberg, 1964; Sim et al., 2011) for sulfur have been predicted and determined in culturing experiments for that process, respectively. In contrast, most of the reported sulfur isotope fractionations during microbial sulfide oxidation (MSO) lie between -5 and 4‰ (Pellerin et al., 2019; Fig. 1). Many of these studies were performed in the 1960s and '70s with an abundance of nutrients and electron donors (Chambers and Trudinger, 1979; Fry et al., 1984; Ivanov et al., 1976; Kaplan and Rafter, 1958; Kondrat'eva et al., 1966; Mekhtieva and Kondrat'eva, 1966), and led to the assumption that sulfur isotope fractionations during MSO are negligible. Their study drew research attention again in the late 2000s and 2010s (Böttcher et al., 2001; Brunner et al., 2008; Pisapia et al., 2007), mostly in the context of understanding them together with oxygen isotope fractionations (Balci et al., 2012; Balci et al., 2007; Böttcher et al., 2001; Brabec et al., 2012; Poser et al., 2014; Thurston et al., 2010; Zerkle et al., 2009). In 2019, S isotope fractionations of 13‰, and potentially up to 25‰ during MSO

were reported for the first time, by *D. alkaliphilus* (Pellerin et al., 2019). This finding suggests that sulfur isotope fractionations during MSO could be maximized under specific conditions. If the oxidation is fast enough to become transport limited, the only expressed fractionation is that associated with diffusion into the cell, which is reversible, and as such allows the expression of large fractionation factors (O'Leary, 1981). Similarly, as MSO slows down, the expressed fractionation would be expected to approach the equilibrium fractionation between sulfate and sulfide, which is close to 20‰ (Sakai and Dickson, 1978).

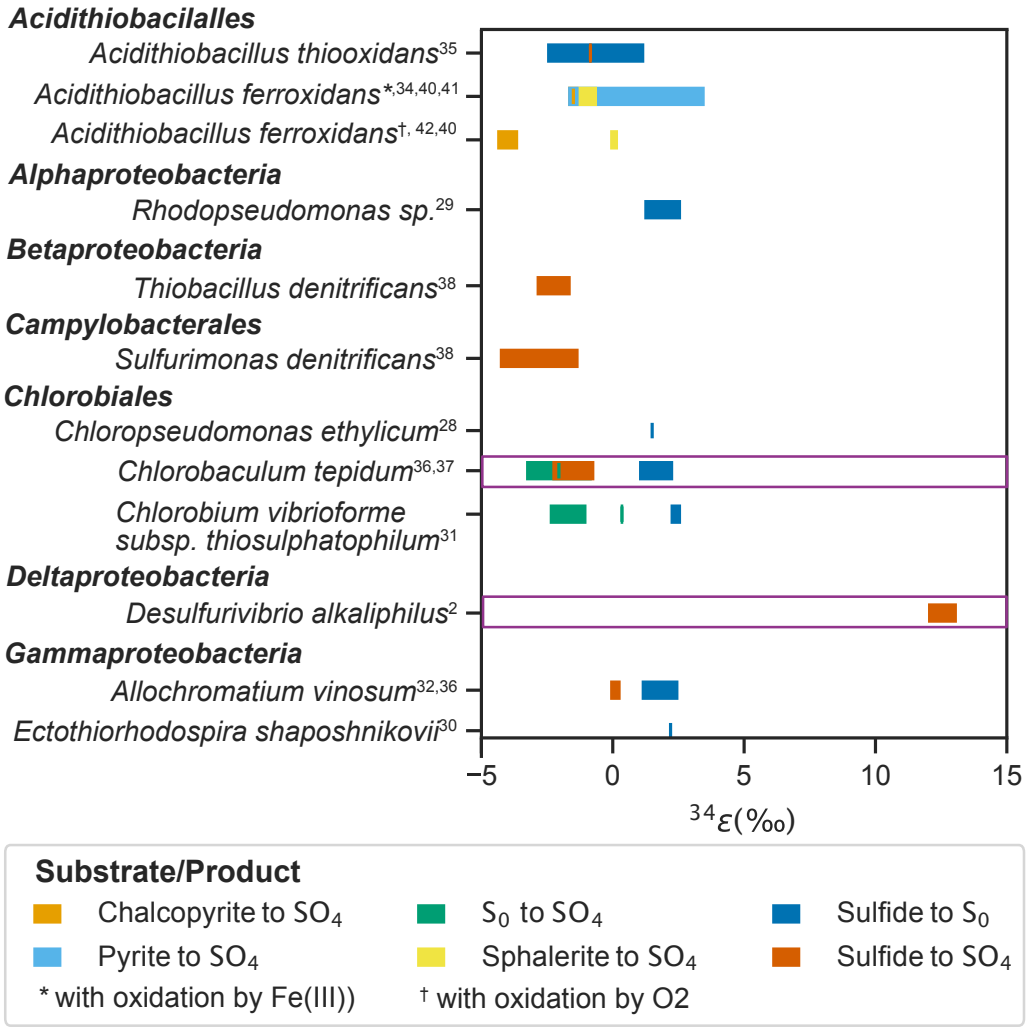

Figure 1: Compilation of reported isotopic fractionations for the microbial oxidation of different reduced sulfur forms, modified from (Pellerin et al., 2019). Purple boxes represent the microorganisms that were tested in this study.

90% of sulfide from sulfate reduction has been estimated to get reoxidized in sediments (Jørgensen, 1982), with the biotic oxidation rates being three orders of magnitude larger than the abiotic ones (Luther et al., 2011). The remainder becomes incorporated into pyrite and other reduced sulfur minerals, whose sulfur isotope compositions have been used to elucidate the carbon and sulfur cycles, oxygen budgets, and redox state of the ocean throughout Earth history (Berner and Raiswell, 1983; Garrels and Lerman, 1981; Holland, 1973). It has been hypothesized that anaerobic sulfur-oxidizing phototrophic bacteria might have been important players of the sulfur cycle in anoxic and euxinic basins during the Archaean (Brabec et al., 2012). Determining if sulfur isotope fractionations during MSO can be large and are expressed in natural environments, and under what circumstances, is thus fundamental towards deepening our understanding on the physiology of the process, as well as improving our interpretation of the geologic record of reduced sulfur minerals. It has been established that the magnitude of sulfur isotope fractionations from BSR correlates negatively with the concentration of electron donor (usually organic matter or methane; Harrison and Thode, 1958; Kaplan and Rittenberg, 1964) and the specific rate of sulfate reduction ($\mathrm{mass\,cell^{-1}time^{-1}}$; Chambers et al., 1975; Habicht and Canfield, 1997; Kaplan and Rittenberg, 1964), and positively with sulfate concentrations (Jones and Starkey, 1957). These factors could as well be relevant for isotopic fractionations during MSO, but they have been unexplored so far.

Here, we determined sulfur isotope fractionations during MSO for *D. alkaliphilus*, a chemotrophic alkaliphile, and *Chlorobaculum tepidum*, a phototroph, with under nutrient concentrations that resemble the ones encountered by these microorganisms in their natural environments. Both microorganisms oxidize sulfide to sulfate in a two-step process, with elemental sulfur ($\mathrm{S_0}$) as an intermediate. We found that the growth rates and specific sulfide oxidation rates (csSOR), which are correlated with

nutrient limitation, impact the S isotope fractionations by *D. alkaliphilus* only. This finding implies that unique traits of *D. alkaliphilus* may enhance large sulfur isotope fractionations by this microbe, which are otherwise small for most of the sulfur oxidizing microorganisms, even under oligotrophic conditions.

2. MATERIALS AND METHODS

Cultures and growth conditions

Desulfurivibrio alkaliphilus strain DMS 19089 was obtained from DSMZ. Cultures of *D. alkaliphilus* were grown anaerobically at 30°C in glass vials with 20 ml of a sodium carbonate/ bicarbonate–buffered liquid mineral media with pH adjusted to about 9.8, as described previously (Sorokin et al., 2008), with the exception of KH_2PO_4 and NH_4Cl. Trace metal SL-10 solution (1 ml $liter^1$), selenite-tungstate solution (1 ml $liter^1$), and vitamin solution (10 ml $liter^1$; Widdel and Bak, 1992) were added to the medium after sterilization. 2 mM sodium sulfide was added directly to the vials. For the sulfur tracking experiments, starter cultures were set by transferring twice an initial culture from a 10% glycerol stock kept at -80°C to anaerobic media with 2.9 mM K_2HPO_4 and 4 mM NH_4Cl. Triplicate treatments with low (20 μM K_2HPO_4, 50 μM NH_4Cl), medium (800 μM K_2HPO_4, 1 mM NH_4Cl), and high (2.9 μM K_2HPO_4, 4 mM NH_4Cl) nutrients were inoculated with cells from the starter culture centrifuged and washed three times with sulfide-, K_2HPO_4-, and NH_4Cl-free media.

Chlorobaculum tepidum WT2321, the plating strain derived from the original isolate TLS1 (Wahlund et al., 1991), was grown in medium Pf-7 with sodium sulfide as the sole electron donor prepared as previously described (L.-K. Chan et al., 2008) with the exception that sodium thiosulfate, dipotassium phosphate, and vitamin B12 were omitted. *C. tepidum* cultures were routinely grown in glass vials with 20 ml anaerobic Pf-7 and a 5% CO2/95% N_2 headspace, kept in a water bath at 40°C

with 6000 lux or with ~100 lux for the light limitation experiments. For all sulfur compound tracking experiments, starter cultures were set by transferring twice an initial culture from a 10% glycerol stock kept at -80°C to anaerobic Pf-7 with 4 mM sodium sulfide, 3.7 mM K_2HPO_4, and 13.8 nM vitamin B12. Cells from starter cultures were centrifugated and washed 3 times with sulfur-free Pf-7 medium, and inoculated in duplicate or triplicate vials to a density of 4 μg/ml protein. K_2HPO_4 was supplemented to a concentration of 5 μM to 3.7 mM, and vitamin B12 was supplemented in a range of 0.08 to 13.8 nM.

Sampling and quantifications

Sulfide concentrations in the cultures were monitored by quantification through Cline assay (Cline, 1969), and an appropriate volume of culture (between 500 μl and 5 ml) was retrieved at definite timepoints for cell and sulfur analyses. For *C. tepidum*, bacteriochlorophyll (bChl) c concentrations were determined by re-suspending cell pellets in cold methanol, incubating at -20°C for 10 minutes and reading the absorbance at 669 nm. Protein concentrations were determined through Bradford assay using the Pierce BCA Protein Assay KIT (Thermo Fisher Scientific). At definite timepoints, sulfate concentrations were measured through ion chromatography (Dionex 500, Sunnyvale, CA, USA). Data was processed using ThermoFisher Scientific Chromeleon software, version 7.2. To determine the sulfur isotopic compositions of sulfide and sulfate, an appropriate volume of culture was centrifuged to pellet the cells, and sulfide was precipitated as Ag_2S with 2X 0.5 M $AgNO_3$, followed by an addition of 1X 1M HNO_3 and 3 washes with MQ water. Sulfate was precipitated as $BaSO_4$ by adding 1X 1M $BaCl_2$.

Determination of growth and sulfur oxidation rates

The absorbance at 562 nm for protein was used to determine cell densities concentrations through a constant conversion factor of $2\text{x}10^6 \cdot \text{OD}_{562}^2 - 9.3\text{x}10^4 \cdot \text{OD}_{562} + 1$ for *C. tepidum*. For *D. alkaliphilus*, cell densities were monitored by measuring OD600 and a conversion factor of $8\text{x}10^8 \cdot \text{OD}_{600} - 9.6\text{x}10^5$ was used to determine cells/ml. The conversion factors were obtained by counting cells using a Petroff-Hausser chamber. Specific growth rates of exponentially growing cells (k day^{-1}) were calculated as

$$\text{k} = \frac{\ln(\text{C}_\text{t}/\text{C}_0)}{\Delta\text{t}}, \tag{4.1}$$

where C_t and C_0 are the concentrations of cells (in cells ml^{-1}) at the initial and end timepoints of the exponential phase and t is the time of the sampling (in days). Cell specific sulfide oxidation rates (csSOR) during exponential growth were calculated as

$$\text{csSOR} = \text{k}\frac{\Delta\text{m}_{(\text{HS}^-)}}{\Delta\text{C}} \cdot 10^{15}, \tag{4.2}$$

where $\Delta\text{m}_{\text{HS}^-}$ is the difference in the moles of sulfide, ΔC is the difference in the concentration of cells during exponential phase, and 10^{15} adjusts the units to femtomoles per cell per day.

Sulfur isotope analyses

0.1-1.3 mg of Ag_2S or BaSO_4 (plus 1 mg vanadium pentoxide) were weighed in tin capsules and measured as SO_2 by EA-IRMS (flash combustion elemental analyzer coupled to a Delta V Plus IRMS via a Conflo IV universal interface). We report sulfur isotope ratios using the conventional delta notation relative to the international standard Vienna-Canyon Diablo Troilite (VCDT)

$$\delta^{34}\text{S} = ({}^{34}\text{R}_{\text{sample}}/{}^{34}\text{R}_{\text{VCTD}}) - 1, \tag{4.3}$$

where $^{34}\mathrm{R}$ refers to the $^{34}\mathrm{S}/^{32}\mathrm{S}$ ratio. The values of each sample were corrected by subtracting the blank and using a linear interpolation between two in house working standards (sulfanilamide and seawater), with an analytical repeatability better than 0.19‰. The sulfur isotope fractionation factors for each microbe and condition ($^{34}\varepsilon$) were calculated from the slope of the linear regression analysis of the most accurate approximate solutions to the Rayleigh distillation equation (Mariotti et al., 1981; Scott et al., 2004):

$$1000 \cdot \ln(1 + \delta^{34}\mathrm{S}_{\mathrm{S}^{2-}}/1000) = 1000 \cdot \ln(1 + \delta^{34}\mathrm{S}_{\mathrm{S}^{2-},0}/1000) - {}^{34}\varepsilon_{\mathrm{S}^{2-}\,\mathrm{to}\,\mathrm{S}_0} \cdot \ln(\mathrm{f}_{\mathrm{S}^{2-}}), \tag{4.4}$$

$$1000 \cdot \ln(1 + \delta^{34}\mathrm{S}_{\mathrm{SO}_4^{2-}}/1000) = 1000 \cdot \ln(1 + \delta^{34}\mathrm{S}_{\mathrm{S}_0,0}/1000) + {}^{34}\varepsilon_{\mathrm{S}_0\,\mathrm{to}\,\mathrm{SO}_4^{2-}} \cdot \frac{(\mathrm{f}_{\mathrm{S}0} \cdot \ln \mathrm{f}_{\mathrm{S}0})}{(1 - \mathrm{f}_{\mathrm{S}0})}, \tag{4.5}$$

where $\mathrm{f}_{\mathrm{S}}^{2-}$ and $\mathrm{f}_{\mathrm{S}0}$ is the fraction of remaining sulfide and elemental sulfur in the cultures, respectively, $\delta^{34}\mathrm{S}_{\mathrm{S}^{2-},0}$ and $\delta^{34}\mathrm{S}_{\mathrm{S}^{2-}}$ are the sulfur isotopic compositions of the initial and remaining sulfide at the time of the measurement, respectively, $\delta^{34}\mathrm{S}_{\mathrm{S}_0,0}$ is the isotopic composition of initial elemental sulfur from the oxidation of sulfide, and $\delta^{34}\mathrm{S}_{\mathrm{SO}_4^{2-}}$ is the isotopic composition of sulfate oxidized from elemental sulfur. $\delta^{34}\mathrm{S}_{\mathrm{S}_0,0}$ was not measured, but inferred from $\delta^{34}\mathrm{S}_{\mathrm{S}^{2-}}$ at the last measured point and ${}^{34}\varepsilon_{\mathrm{S}^{2-}\,\mathrm{to}\,\mathrm{S}_0}$.

3. RESULTS

We cultured *D. alkaliphilus* under 3 different concentrations of phosphate and nitrate. As expected, the cells grew more rapidly in the high nutrient treatments, and a long lag-phase was observed for the low nutrient ones before any growth could be detected. Similarly, sulfide was consumed faster in the high nutrient treatments, followed by the medium and low ones. Sulfate production was detected earlier in the medium concentration treatments compared to the high and low ones. In all cases, cells reached a density of 10^8 and sulfate was close to 8 mM after 250h (Fig.

2). We also calculated growth rates and cell-specific sulfide oxidation rates for the 3 different nutrient regimes for *D. alkaliphilus* during exponential phase (Table 1).

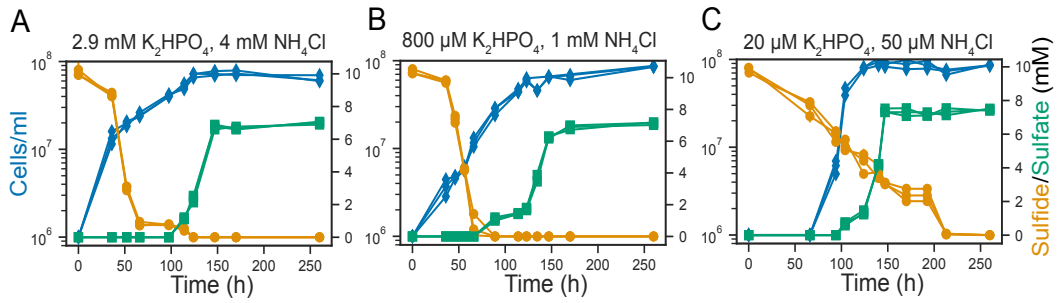

Figure 2: Growth of *Desulfurivibrio alkaliphilus* with sulfide as electron donor for A) high, B) medium, and C) low nutrient concentrations. The concentrations of sulfate and sulfide throughout the course of the experiment are shown in the right Y-axis.

Table 1: Growth rates and cell-specific sulfur oxidation rates for *Desulfurivibrio alkaliphilus* in exponential phase at different nutrient concentrations.

Treatment	**Time**	**Growth rate** (day^{-1})	**csSOR (fmol S/cell/day)**
2.9 mM KH_2PO_4, 4 mM NH_4Cl	0-36 h	1.73 ± 0.11	187.1 ± 47.3
800 µM KH_2PO_4, 1 mM NH_4Cl	0-36 h	0.85 ± 0.15	126.2 ± 55.9
20 µM KH_2PO_4, 50 µM NH_4Cl	66-94 h	1.61 ± 0.07	397.2 ± 121.8

We measured the S isotopic compositions of sulfide and sulfate at specific timepoints as they were consumed and produced by *D. alkaliphilus*, respectively. These $\delta^{34}S$ values were used to determine the fractionation factor ($^{34}\varepsilon$) for sulfide oxidation to elemental sulfur and elemental sulfur oxidation to sulfate (Fig. 3). All the fractionation factors were positive (i.e. inverse kinetic isotope effect), and their magnitudes increased with decreasing nutrient concentrations for the oxidation of sulfide step. In the case of elemental sulfur oxidation, a large fractionation factor (12‰) was only observed in the treatments grown under high nutrient concentrations.

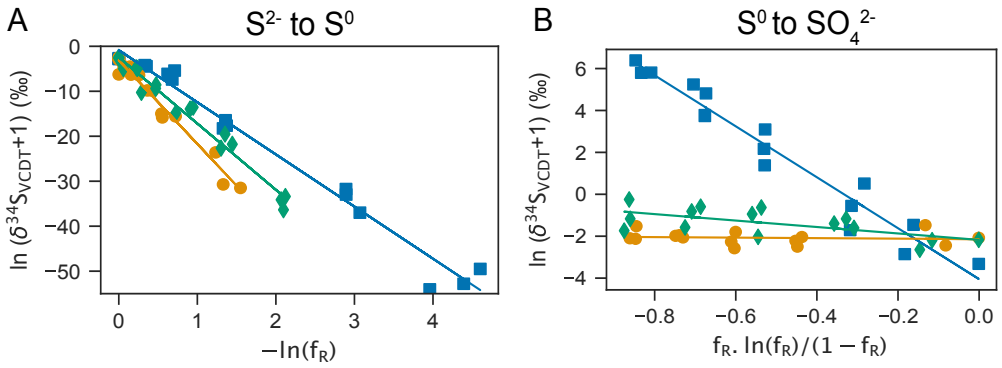

	[PO_4^{3-}] (μM)	[NH_4^+]	$^{34}\varepsilon_{S^{2-}\text{ to }S^0}$	$^{34}\varepsilon_{S^0\text{ to }SO_4^{2-}}$
■	2.9 mM	4 mM	11.59‰	12.16‰
◆	800 μM	1 mM	14.74‰	1.54‰
●	20 μM	50 μM	18.58‰	0.12‰

Figure 3: Fractionation of sulfur isotopes during A) sulfide and B) elemental sulfur oxidation by *Desulfurivibrio alkaliphilus*. Each color and symbol in the data points corresponds to a different nutrient condition. The lines represent a linear fit of the Rayleigh distillation equation, where the slope was taken as a measurement of the fractionation factor, $^{34}\varepsilon$.

We grew *C. tepidum* under two limitation conditions for phosphate and vitamin B12 (Supp. Fig. 1). We measured a minimum growth rate of 4.3 day^{-1} under 10 $\mu\mathrm{M}$ phosphate and 100 pM vitamin B12 (Supp. Table 1). We further limited nutrients in an attempt to obtain lower growth rates and csSOR, but we could not observe any growth below 100 pM vitamin B12. When determining the fractionation factors for the oxidation of sulfide and elemental sulfur from the $\delta^{34}\mathrm{S}$ of sulfide and sulfate, respectively, we found them to be between 1 and 2‰ for both oxidation steps, irrespective of differences in nutrient concentrations, growth rate and csSOR (Supp. Fig. 2). For this reason, we performed a second set of experiments with *C. tepidum* under light limitation and a range of phosphate and vitamin B12 concentrations (Supp. Fig. 3). The treatments with the highest and lowest nutrient concentrations showed visible differences in their growth curves, as well as in the times at which sulfide became exhausted and sulfate started to become detected (Fig. 4). The

growth rates and csSOR for all the intermediate nutrient concentration treatments were similar (Supp. Table 2), and growth rates below 0.5 day^{-1} were observed only in the most nutrient limited treatments (5 μM phosphate, 80 pM vitamin B12; Table 2).

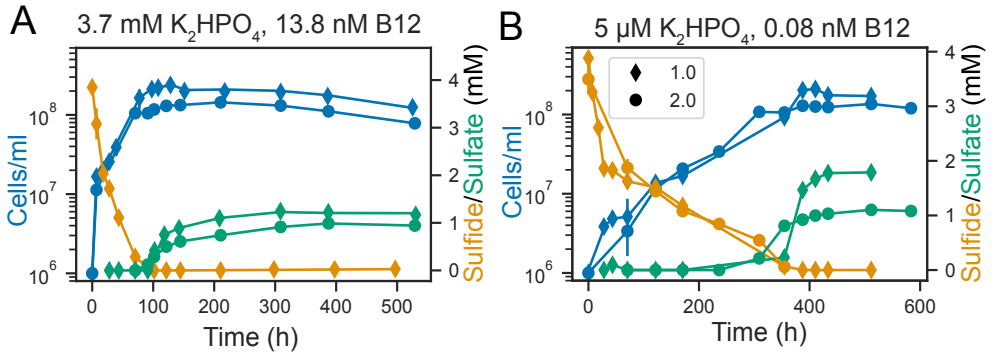

Figure 4: Growth of *Chlorobaculum tepidum* with sulfide as electron donor and with light stress under A) high nutrient and B) limited nutrient conditions. The concentrations of sulfate and sulfide throughout the course of the experiment are shown in the right Y-axis. Diamonds and circles correspond to independent replicates for each condition.

Table 2: Growth rates and cell-specific sulfur oxidation rates for nutrient (5 μM KH_2PO_4, 0.08 nM vitamin B12) and light limited (~100 lux) treatments of *C. tepidum*.

Replicate	Time	Phase	Growth rate (day^{-1})	csSOR (fmol S/cell/day)
1	0-387.5 h	All exponential	0.33	6.1
2	0-309 h	All exponential	0.36	9.7
1	0-121.5 h	Early exponential	0.52	95.7
2	0-121.5 h	Early exponential	0.48	110.9
1	121.5 - 387.5 h	Late exponential	0.24	2.4
2	121.5 - 309 h	Late exponential	0.28	2.9

The sulfur isotope fractionations for sulfide and elemental sulfur oxidation by *C. tepidum* under light limitation were measured for the high (3.7 mM phosphate, 13.8 nM vitamin B12) and low (5 μM phosphate, 80 pM vitamin B12) nutrient treatments. All the $^{34}\varepsilon$ were found to lie between 0.6 and 2.3‰ (Fig. 5).

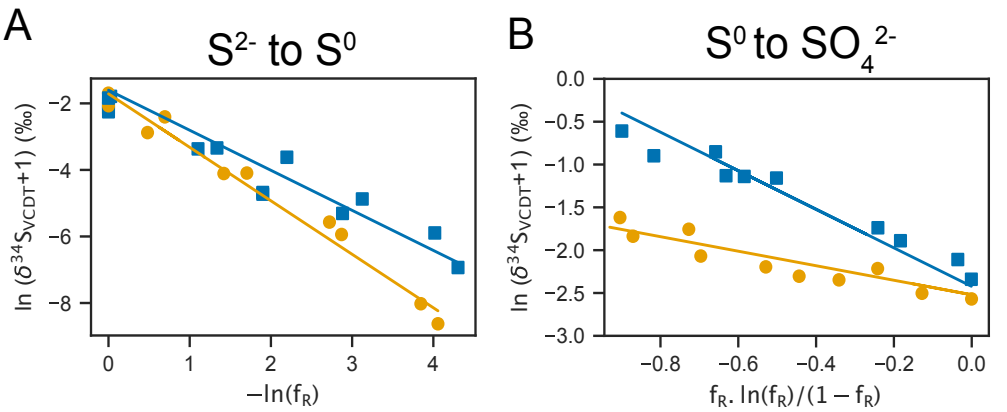

	[PO_4^{3-}]	[B12] (nM)	$^{34}\varepsilon_{S^{2-}\text{ to }S^0}$	$^{34}\varepsilon_{S^0\text{ to }SO_4^{2-}}$
■	3.7 mM	13.8	1.20‰	2.26‰
●	5 µM	0.8	1.61‰	0.63‰

Figure 5: Fractionation of sulfur isotopes during A) sulfide and B) elemental sulfur oxidation by *Chlorobaculum tepidum* under light stress. Each color and symbol in the data points corresponds to a different nutrient condition. The lines represent a linear fit of the Rayleigh distillation equation, where the slope was taken as a measurement of the fractionation factor, $^{34}\varepsilon$.

4. DISCUSSION

We tested the impact of different nutrient conditions on the fractionation factors associated with MSO for two different microorganisms, aiming at understanding if their impact on growth rates and csSOR could explain the magnitude of $^{34}\varepsilon$. For *D. alkaliphilus*, the growth rate (k) for the treatments with high and low nutrient concentrations were within experimental error from each other (1.6-1.7 day^{-1}). Besides, despite the exponential phase being significantly delayed in the low nutrient concentration treatments compared to the high and medium ones, the csSOR during exponential phase was largest for the low nutrient treatments (397.2 fmol $\text{cell}^{-1}\text{day}^{-1}$). We measured fractionation factors from 11.6 to 18.6‰ for *D. alkaliphilus*, observing an increase in the magnitude of $^{34}\varepsilon$ with decreasing nutrient concentrations. This finding suggests that, as expected, nutrient limitation is inversely

correlated with the sulfur isotope fractionations for sulfide oxidation. However, the size of the fractionation is independent of k and csSOR for *D. alkaliphilus*. A previous study reported an $^{34}\varepsilon$ of 12-13.1‰ for sulfide oxidation by this microbe (Pellerin et al., 2019), in cultures inoculated with cells growing in exponential phase, and grown under high nutrient conditions (2.9 mM phosphate, 4 mM ammonium). Our high nutrient treatment, which utilized the same phosphate and ammonium concentrations as that from Pellerin et al. (2019), yielded a comparable $^{34}\varepsilon$ of 11.6‰. The previously reported k and csSOR were 0.14-0.25 day^{-1} and 9-9.8 fmol $\mathrm{cell}^{-1}\mathrm{day}^{-1}$, respectively (Pellerin et al., 2019). We could not slow down microbial growth and sulfide consumption to values comparable to that previous report, despite limiting nutrients in our cultures. The fact that we utilized culture volumes of 20 ml as opposed to 2 L could be responsible for the difference. Additionally, the fractionation factors we measured were similar or larger, at higher growth rates and csSOR. This is surprising, considering that both studies utilized similar concentrations of sulfide as electron donor (8-10 mM). An even larger $^{34}\varepsilon$ of up to 26‰ was reported when *D. alkaliphilus* cultures were inoculated with cells from stationary phase, although k and csSOR were not reported for those conditions (Pellerin et al., 2019). Our findings support the idea that restricted growth conditions might lead to larger sulfur isotope fractionations during MSO by *D. alkaliphilus*.

It is surprising that it is only in *D. alkaliphilus* that large S isotope fractionations from MSO have been observed. Two particularities about this microorganism could explain this. The first one is that as an alkaliphile, this microorganism is unable to grow below pH 8. At this pH, most of the sulfide would be in the form of HS^-, which does not readily diffuse into cells, and allows for an equilibrium isotope effect of about 6‰ between $\mathrm{H_2S}$ and HS^- (Otake et al., 2008; Tudge and Thode, 1950). The second one is that *D. alkaliphilus* is a member of the class *Deltaproteobacteria*, which includes bacteria capable of sulfate reduction, yet it is capable of sulfur

oxidation and unable to grow with sulfate as sole electron acceptor (Thorup et al., 2017). The implication is that most likely *D. alkaliphilus* utilizes the machinery for sulfate reduction operating in reverse (rDsr; Thorup et al., 2017). Additionally, it could also disproportionate S0, for which an $^{34}\varepsilon$ of 5.6‰ has been reported (Poser et al., 2016). The addition of multiple equilibrium and kinetic isotope effects might be responsible for the large fractionation factors from MSO by *D. alkaliphilus*. The fact that the only other *Deltaproteobacteria* capable of sulfide oxidation and of growing at neutral pH are cable bacteria (Pfeffer et al., 2012), which are unculturable, difficults testing the aforementioned hypotheses.

In order to determine if other sulfide-oxidizing microorganisms can manifest large sulfur isotope fractionations during MSO, we tested *C. tepidum* under nutrient and light limitation, and found fractionation factors of 1.2 to 1.6‰ for sulfide oxidation and 0.6 to 2.3‰ for elemental sulfur oxidation. Despite achieving growth rates as low as 0.33 day^{-1} and 6.1 fmol $\mathrm{cell}^{-1}\mathrm{day}^{-1}$, which are comparable to the ones previously measured for *D. alkaliphilus* (Pellerin et al., 2019), the fractionation factors for sulfur oxidation by *C. tepidum* are small. Previous reports of $^{34}\varepsilon$ for *C. tepidum* of -2.3 (Brabec et al., 2012) to 1.8‰ (Zerkle et al., 2009) for the oxidation of sulfide, and -1.9 (Zerkle et al., 2009) to -0.7‰ (Brabec et al., 2012) for the oxidation of elemental sulfur, did not include k or csSOR, but were conducted under high nutrient conditions (3.7 mM phosphate, 13.8 nM vitamin B12). Although the $^{34}\varepsilon$ we measured for sulfide oxidation is similar to one of the previously measured one (Zerkle et al., 2009), the sign difference for the oxidation of elemental sulfur step could be accounted for by differences in k and csSOR. *C. tepidum* utilizes the sulfide-quinone oxidoreductase (SQR) pathway for the oxidation of sulfide to extracellular elemental sulfur globules (Shahak et al., 1992), possibly with a polysulfide as an intermediary (Eisen et al., 2002). It also possesses an alternative pathway, which utilizes a flavocytochrome c-sulfide dehydrogenase for the oxidation of sul-

fide and thiosulfate (Eddie and Hanson, 2013), and has been characterized in other anoxygenic phototrophs, like *Chlorobium thiosulfatophilum* (Kusai and Yamanaka, 1973) and *Chromatium vinosum* (Davidson et al., 1985). Many phototrophic bacteria contain genes that encode both enzymes (L. K. Chan et al., 2009). Sox is a third pathway utilized by bacteria to oxidize sulfide, sulfite, and thiosulfate. It is comprised of a 15 gene cluster, and it was first characterized in the *Alphaproteobacterium Paracoccus panthotrophus* (Friedrich et al., 2000). *C. tepidum* also possesses an incomplete Sox system that allows it to oxidize thiosulfate (Eisen et al., 2002). The dissimilatory sulfite reductase system operating in reverse (rDsr) is required in *C. tepidum* (Eisen et al., 2002), *C. vinosum* (Pott and Dahl, 1998), and potentially other sulfur-oxidizing phototrophs for the oxidation of elemental sulfur to sulfate.

A previous effort tried to establish if there are different fractionation factors associated with sulfide-oxidation through the SQR or the Sox pathways (Poser et al., 2014). That study utilized *Thiobacillus denitrificans* and *Sulfurimonas denitrificans* as purported representatives of microbes were only the SQR and the Sox pathway operates, respectively. A fractionation factor of -1.3 to -4.3‰ for *T. denitrificans*, and of -1.6 to -2.9‰ for *S. denitrificans*, was found for the oxidation of sulfide to sulfate (Poser et al., 2014). However, both organisms have genes that encode both pathways (Sievert et al., 2008), so their simultaneous operation, which would impact the fractionation factors measured, cannot be precluded. The high overlap between sulfur oxidation pathways among microorganisms (Pjevac, 2014) plain greatly difficults the endeavor of identifying the fractionation factors associated to each one of them. Ideally, these should be studied in mutants, which would need to have multigene knockouts to guarantee that none of the other pathways, usually involving many genes, is operational. To our knowledge, this has not been accomplished so far for any sulfur oxidizing microorganism. The fractionation factors for MSO we report here, as well as most of the previously reported ones (Fig. 1), are inverse (or

positive), which implies that the product is relatively enriched in $^{34}\mathrm{S}$. These inverse isotope effects have been interpreted as a combination between the equilibrium isotope effect of 6‰ for the exchange of S atoms between $\mathrm{HS^-}$ and $\mathrm{H_2S}$ at neutral pH (Fry et al., 1984; Otake et al., 2008; Thode et al., 1951), and metabolic effects (Zerkle et al., 2009).

To better understand what keeps the S isotope fractionations during MSO small despite low k and csSOR, we explored whether the sulfide oxidizers studied here could be limited by sulfide internalization. Considering a cell size of 3 $\mu\mathrm{m}$ for *D. alkaliphilus* (Sorokin et al., 2008) and 2 $\mu\mathrm{m}$ for *C. tepidum* (Wahlund et al., 1991), and a permeability coefficient of 11.9 $\mathrm{cm/s}$ for $\mathrm{H_2S}$ (Riahi and Rowley, 2014), we determined that the intracellular hydrogen sulfide concentrations needed to support the csSOR determined here are 8.18 nM and 0.59 nM, respectively. Considering that the ratio between the intracellular (nM) vs. ambient (mM) concentrations of sulfide in our experiments are in the order of at most 10^{-6}, sulfide supply to the cells must be transport limited (e.g. Brugnoli et al., 1988). During carbon dioxide incorporation by plants (O'Leary, 1981), and electron donor uptake for sulfate reduction (e.g. Bradley et al., 2016), it has been observed that transport limitation keeps S isotope fractionations small despite low k and csSOR. This leads us to hypothesize than large sulfur isotope fractionations from MSO by *D. alkaliphilus* must be caused by disproportionation as previously suggested (Pellerin et al., 2019), which is favored by low hydrogen sulfide concentrations under the alkaline conditions that this microbe requires for growth (Pellerin et al., 2019). Microorganisms that utilize more widespread sulfur oxidation pathways, like SQR, Sox, or flavocytochromes, and that operate at circumneutral pH, potentially do not express large sulfur isotope fractionations —even under low electron donor availability, growth rates, and specific sulfide oxidation rates—, because they are limited by sulfide diffusion into the cell. Since these are the most prevalent conditions

in natural environments were reduced sulfur species are present, the main implication of our findings is that sulfur isotope fractionations for MSO may have scarce utility as paleoenvironmental proxies.

5. CONCLUSIONS

We investigated the possibility that large sulfur isotope fractionations are expressed during nutrient-limited growth in the sulfide-oxidizing microorganisms *Desulfurivibrio alkaliphilus* and *Chlorobaculum tepidum*. Despite achieving comparable slow growth rates and cell-specific sulfide oxidation rates for both microorganisms, which in the case of *Chlorobaculum tepidum* required light limitation on top of nutrient limitation, S isotope fractionations in *C. tepidum* remained below 2.3‰, whereas *D. alkaliphilus* reached fractionations between 11.6 and 18.6‰. As the calculations based on the csSOR determined here show, the small sulfur isotope fractionations in *C. tepidum* could be fully explained by sulfide transport limitation despite low k and csSOR, which would make sulfide oxidation quantitative, and minimize isotopic fractionation due to mass balance. The large fractionations observed in *D. alkaliphilus* are probably related to the growth of this microbe at pH above 9.5, which leads to a combination of equilibrium isotope effects between HS^- (the most abundant sulfide form at high pH) and H_2S (the most cell membrane diffusible form of sulfide), and kinetic isotope effects during sulfide oxidation, which might be unique to the utilization of the rDsr pathway by this microorganism. We conclude that large sulfur isotope fractionations during microbial sulfide oxidation are probably not prevalent in nature, given that the most environmentally abundant or relevant sulfide oxidizers operate at neutral pH and utilize metabolic pathways similar to the ones used by *C. tepidum*. Resolving the isotopic record of reduced sulfur minerals might require inquiring further into the conditions that could induce large sulfur isotope fractionations by pathways or microorganisms different than the ones studied here.

6. ACKNOWLEDGEMENTS

We would like to thank Austin Grant for assistance with *C. tepidum* cultivation procedures, as well as Stephanie Connon for help with cell counting protocols, Nathan Dalleska for assistance with the IC, and Fenfang Wu for assistance with the EA-IRMS. We benefited from fruitful discussions with Tingting Yang, Kriti Sharma, and Robert Morris. This work was supported by the National Science Foundation Grant 1737404.

7. SUPPLEMENTARY MATERIALS

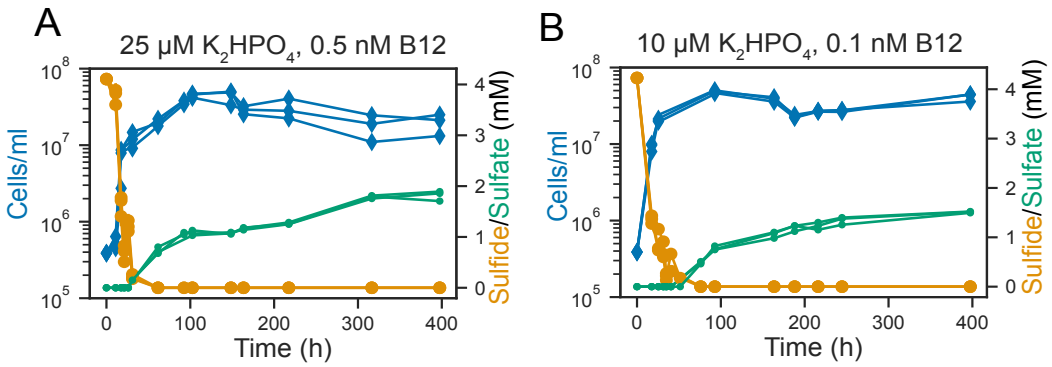

Supp. Fig. 1: Growth of *Chlorobaculum tepidum* with sulfide as electron donor, with no light stress, for A) medium, and B) low nutrient conditions. The concentrations of sulfate and sulfide throughout the course of the experiment are shown in the right Y-axis.

Supp. Table 1: Growth rates and cell-specific sulfur oxidation rates for *C. tepidum* grown without light limitation in exponential phase at different nutrient concentrations.

Treatment	Time	Growth rate (day^{-1})	csSOR (fmol S/cell/day)
25 µM KH_2PO_4, 0.5 nM B12	0-17.5 h	9.91 ± 0.4	3052.5 ± 401.8
10 µM KH_2PO_4, 0.1 nM B12	0-17.5 h	4.34 ± 0.17	1460.9 ± 185.5

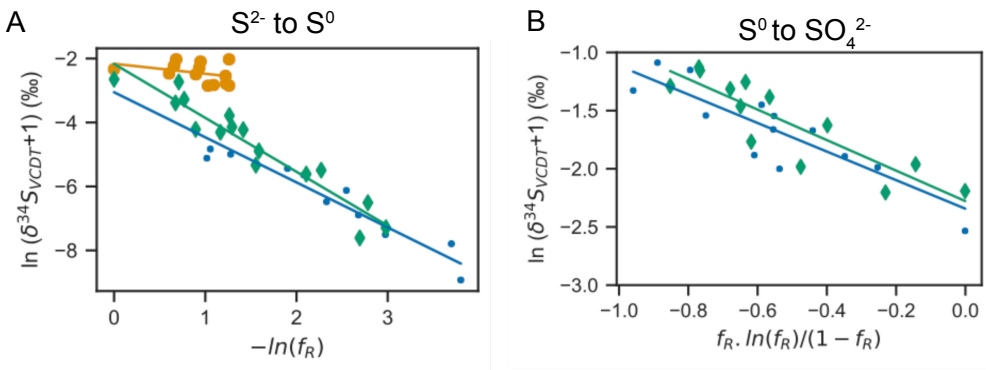

	[PO_4^{3-}] (μM)	[B12] (pM)	$^{34}\varepsilon_{S^{2-}\text{ to }S^0}$	$^{34}\varepsilon_{S^0\text{ to }SO_4^{2-}}$
●	25	500	1.41‰	1.31‰
◆	10	100	1.69‰	1.23‰
●	2,10	10	0‰	

Supp. Fig. 2: Fractionation of sulfur isotopes during A) sulfide and B) elemental sulfur oxidation by *Chlorobaculum tepidum* grown without light limitation. Each color and symbol in the data points corresponds to a different nutrient condition. At 10 pM vitamin B12, very little growth was observed, and no sulfate was produced. The lines represent a linear fit of the Rayleigh distillation equation, where the slope was taken as a measurement of the fractionation factor, $^{34}\varepsilon$.

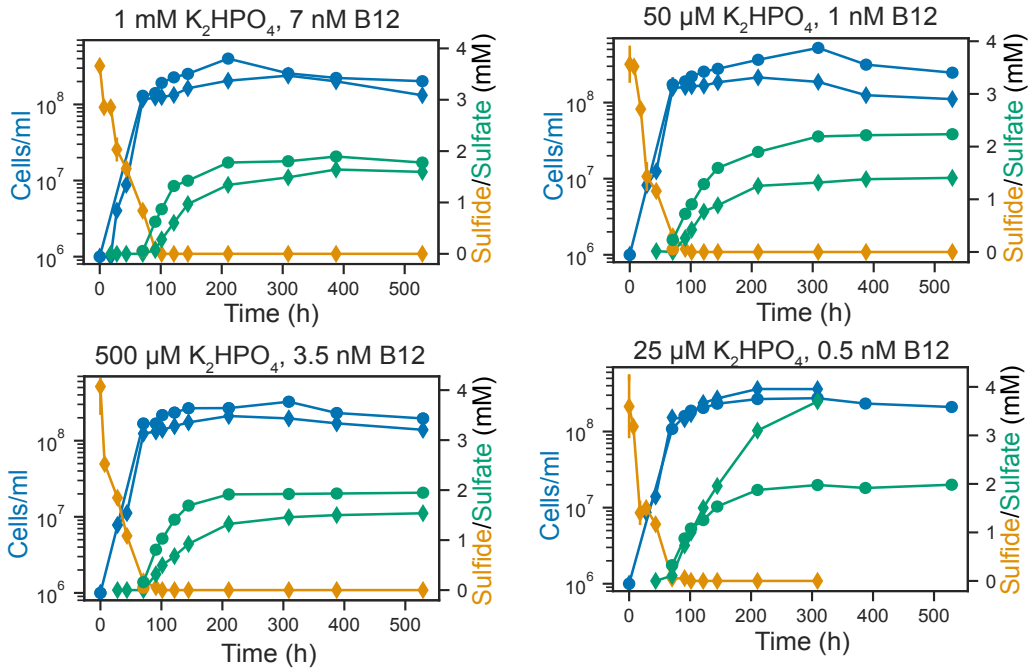

Supp. Fig. 3: Growth of *Chlorobaculum tepidum* with sulfide as electron donor and with light stress under different concentrations of KH2PO4 and vitamin B12. The concentrations of sulfate and sulfide throughout the course of the experiment are shown in the right Y-axis. Diamonds and circles correspond to independent replicates for each condition.

Supp. Table 2: Growth rates and cell-specific sulfur oxidation rates for light limited treatments of *C. tepidum* in exponential phase at different nutrient concentrations.

Treatment	Time	Growth rate (day^{-1})	csSOR (fmol S/cell/day)
3.7 mM KH_2PO_4, 13.8 nM B12	0-7 h	8.31 ± 0.75	1061.4 ± 287.8
1 mM KH_2PO_4, 7 nM B12	0-28 h	1.19 ± 0.34	642.4 ± 53.4
500 µM KH_2PO_4, 3.5 nM B12	0-28 h	1.76 ± 0.26	576.2 ± 40.6
50 µM KH_2PO_4, 1 nM B12	0-28 h	1.8 ± 0.14	533.5 ± 56.8
25 µM KH_2PO_4, 0.5 nM B12	0-28 h	1.84 ± 0.28	507.3 ± 65.9

References

Balci, N., Mayer, B., Shanks III, W. C., & Mandernack, K. W. (2012). Oxygen and sulfur isotope systematics of sulfate produced during abiotic and bacterial oxidation of sphalerite and elemental sulfur. *Geochimica et Cosmochimica Acta*, *77*, 335–351.

Balci, N., Shanks, W. C., Mayer, B., & Mandernack, K. W. (2007). Oxygen and sulfur isotope systematics of sulfate produced by bacterial and abiotic oxidation

of pyrite. *Geochimica et Cosmochimica Acta*, *71*(15), 3796–3811. https://doi.org/10.1016/j.gca.2007.04.017

Berner, R. A., & Raiswell, R. (1983). Burial of organic carbon and pyrite sulfur in sediments over phanerozoic time: a new theory. *Geochimica et Cosmochimica Acta*, *47*(5), 855–862. https://doi.org/10.1016/0016-7037(83)90151-5

Böttcher, M. E., Thamdrup, B., & Vennemann, T. W. (2001). Anaerobic sulfide oxidation and stable isotope fractionation associated with bacterial sulfur disproportionation in the presence of MnO2. *Geochimica et Cosmochimica Acta*, *65*(10), 1573–1581. https://doi.org/10.1016/S0016-7037(00)00622-0

Bowles, M. W., Mogollón, J. M., Kasten, S., Zabel, M., & Hinrichs, K.-U. (2014). Global rates of marine sulfate reduction and implications for sub–sea-floor metabolic activities. *Science*, *344*(6186), 889–891.

Brabec, M. Y., Lyons, T. W., & Mandernack, K. W. (2012). Oxygen and sulfur isotope fractionation during sulfide oxidation by anoxygenic phototrophic bacteria. *Geochimica et Cosmochimica Acta*, *83*, 234–251. https://doi.org/10.1016/j.gca.2011.12.008

Bradley, A. S., Leavitt, W. D., Schmidt, M., Knoll, A. H., Girguis, P. R., & Johnston, D. T. (2016). Patterns of sulfur isotope fractionation during microbial sulfate reduction. *Geobiology*, *14*(1), 91–101. https://doi.org/10.1111/gbi.12149

Brock, T. D., Brock, K. M., Belly, R. T., & Weiss, R. L. (1972). Sulfolobus: A new genus of sulfur-oxidizing bacteria living at low pH and high temperature. *Archiv für Mikrobiologie*, *84*(1), 54–68. https://doi.org/10.1007/BF00408082

Brugnoli, E., Hubick, K. T., Von Caemmerer, S., Wong, S. C., & Farquhar, G. D. (1988). Correlation between the carbon isotope discrimination in leaf starch and sugars of C3 plants and the ratio of intercellular and atmospheric partial pressures of carbon dioxide. *Plant Physiology*, *88*(4), 1418–1424. https://doi.org/10.1104/pp.88.4.1418

Brune, D. C. (1989). Sulfur oxidation by phototrophic bacteria. *BBA - Bioenergetics*, *975*(2), 189–221. https://doi.org/10.1016/S0005-2728(89)80251-8

Brunner, B., & Bernasconi, S. M. (2005). A revised isotope fractionation model for dissimilatory sulfate reduction in sulfate reducing bacteria. *Geochimica et Cosmochimica Acta*, *69*(20), 4759–4771. https://doi.org/10.1016/j.gca.2005.04.015

Brunner, B., Yu, J. Y., Mielke, R. E., MacAskill, J. A., Madzunkov, S., McGenity, T. J., & Coleman, M. (2008). Different isotope and chemical patterns of pyrite oxidation related to lag and exponential growth phases of Acidithiobacillus ferrooxidans reveal a microbial growth strategy. *Earth and Planetary Science Letters*, *270*(1-2), 63–72. https://doi.org/10.1016/j.epsl.2008.03.019

Canfield, D. E. (1989). Sulfate reduction and oxic respiration in marine sediments: implications for organic carbon preservation in euxinic environments. *Deep Sea Research*, *36*(1), 121–138.

Chambers, L. A., & Trudinger, P. A. (1979). Microbiological fractionation of stable sulfur isotopes: A review and critique. *Geomicrobiology Journal*, *1*(3), 249–293. https://doi.org/10.1080/01490457909377735

Chambers, L. A., Trudinger, P. A., Smith, J. W., & Burns, M. S. (1975). Fractionation of sulfur isotopes by continuous cultures of Desulfovibrio desulfuricans. *Canadian Journal of Microbiology*, *21*(10), 1602–1607.

Chan, L. K., Morgan-Kiss, R. M., & Hanson, T. E. (2009). Functional analysis of three sulfide:Quinone oxidoreductase homologs in Chlorobaculum tepidum. *Journal of Bacteriology*, *191*(3), 1026–1034. https://doi.org/10.1128/JB.01154-08

Chan, L.-K., Weber, T. S., Morgan-Kiss, R. M., & Hanson, T. E. (2008). A genomic region required for phototrophic thiosulfate oxidation in the green sulfur bacterium Chlorobium tepidum (syn . Chlorobaculum tepidum). *Microbiology*, *154*, 818–829. https://doi.org/10.1099/mic.0.2007/012583-0

Cline, J. D. (1969). Spectrophotometric Determination of Hydrogen Sulfide in Natural Waters. *Limnology and Oceanography*, *14*(3), 454–458. https://doi.org/10.4319/lo.1969.14.3.0454

Dahl, C., Friedrich, C., & Kletzin, A. (2008). Sulfur Oxidation in Prokaryotes. *Encyclopedia of Life Sciences*. https://doi.org/10.1002/9780470015902.a0021155

Davidson, M. W., Gray, G. O., & Knaff, D. B. (1985). Interaction of Chromatium vinosum flavocytochrome c-552 with cytochromes c studied by affinity chromatography. *FEBS letters*, *187*(1), 155–159.

Dyksma, S., Bischof, K., Fuchs, B. M., Hoffmann, K., Meier, D., Meyerdierks, A., Pjevac, P., Probandt, D., Richter, M., Stepanauskas, R., & Mußmann, M. (2016). Ubiquitous Gammaproteobacteria dominate dark carbon fixation in coastal sediments. *ISME Journal*, *10*(8), 1939–1953. https://doi.org/10.1038/ismej.2015.257

Eddie, B. J., & Hanson, T. E. (2013). Chlorobaculum tepidum TLS displays a complex transcriptional response to sulfide addition. *Journal of bacteriology*, *195*(2), 399–408. https://doi.org/10.1128/JB.01342-12

Eisen, J. A., Nelson, K. E., Paulsen, I. T., Heidelberg, J. F., Wu, M., Dodson, R. J., Deboy, R., Gwinn, M. L., Nelson, W. C., & Haft, D. H. (2002). The complete genome sequence of Chlorobium tepidum TLS, a photosynthetic, anaerobic, green-sulfur bacterium. *Proceedings of the National Academy of Sciences*, *99*(14), 9509–9514.

Findlay, A. J., Bennett, A. J., Hanson, T. E., & Luther, G. W. (2015). Light-Dependent Sulfide Oxidation in the Anoxic Zone of the Chesapeake Bay Can Be Explained by Small Populations of Phototrophic Bacteria. *Applied and Environmental Microbiology*, *81*(21), 7560–7569. https://doi.org/10.1128/AEM.02062-15

Fowler, V. J., Pfennig, N., Schubert, W., & Stackebrandt, E. (1984). Towards a phylogeny of phototrophic purple sulfur bacteria-16S rRNA oligonucleotide cataloguing of 11 species of Chromatiaceae. *Archives of Microbiology*, *139*(4), 382–387. https://doi.org/10.1007/BF00408384

Friedrich, C. G., Quentmeier, A., Bardischewsky, F., Rother, D., Kraft, R., Kostka, S., & Prinz, H. (2000). Novel genes coding for lithotrophic sulfur oxidation of Paracoccus pantotrophus GB17. *Journal of Bacteriology*, *182*(17), 4677–4687. https://doi.org/10.1128/JB.182.17.4677-4687.2000

Friedrich, C. G., Rother, D., Bardischewsky, F., Quentmeier, A., & Fischer, J. (2001). Oxidation of Reduced Inorganic Sulfur Compounds by Bacteria.pdf. *Applied and Environmental Microbiology*, *67*(7), 2873–2882. https://doi.org/10.1128/AEM.67.7.2873

Fry, B., Gest, H., & Hayes, J. M. (1984). Isotope effects associated with the anaerobic oxidation of sulfide by the purple photosynthetic bacterium, Chromatium vinosum. *FEMS Microbiology Letters*, *22*(3), 283–287. https://doi.org/10.1111/j.1574-6968.1984.tb00742.x

Garrels, R. M., & Lerman, A. (1981). Phanerozoic cycles of sedimentary carbon and sulfur. *Proceedings of the National Academy of Sciences*, *78*(8), 4652–4656. https://doi.org/10.1073/pnas.78.8.4652

Glaubitz, S., Kießlich, K., Meeske, C., Labrenz, M., & Jürgens, K. (2013). SUP05 Dominates the gammaproteobacterial sulfur oxidizer assemblages in pelagic redoxclines of the central baltic and black seas. *Applied and Environmental Microbiology*, *79*(8), 2767–2776. https://doi.org/10.1128/AEM.03777-12

Grote, J., Jost, G., Labrenz, M., Herndl, G. J., & Jürgens, K. (2008). Epsilonproteobacteria represent the major portion of chemoautotrophic bacteria in sulfidic waters of pelagic redoxclines of the baltic and black seas. *Applied and Environmental Microbiology*, *74*(24), 7546–7551. https://doi.org/10.1128/AEM.01186-08

Habicht, K. S., & Canfield, D. E. (1997). Sulfur isotope fractionation during bacterial sulfate reduction in organic-rich sediments. *Geochimica et Cosmochimica Acta*, *61*(24), 5351–5361. https://doi.org/10.1016/S0016-7037(97)00311-6

Harrison, A. G., & Thode, H. G. (1958). Mechanism of the bacterial reduction of sulphate from isotope fractionation studies. *Transactions of the Faraday Society*, *54*, 84–92.

Holland, H. D. (1973). Systematics of the isotopic composition of sulfur in the oceans during the Phanerozoic and its implications for atmospheric oxygen. *Geochimica et Cosmochimica Acta*, *37*(12), 2605–2616. https://doi.org/10.1016/0016-7037(73)90268-8

Ivanov, M. V., Gogotova, G. I., Matrosov, A. G., & Ziakun, A. M. (1976). Fractionation of sulfur isotopes by phototrophic sulfur bacterium Ectothiorhodospira shaposhnikovii. *Mikrobiologiia*, *45*(5), 757–762.

Jones, G. E., & Starkey, R. L. (1957). Fractionation of stable isotopes of sulfur by microorganisms and their role in deposition of native sulfur. *Applied microbiology*, *5*(2), 111–118.

Jørgensen, B. B. (1982). Mineralization of organic matter in the sea bed - the role of sulphate reduction. *Nature*, *296*(5858), 643–645.

Kaplan, I. R., & Rafter, T. A. (1958). Fractionation of stable isotopes of sulfur by Thiobacilli. *Science*, *127*(3297), 517–518.

Kaplan, I. R., & Rittenberg, S. C. (1964). Microbiological Fractionation of Sulphur Isotopes. *Journal of General Microbiology*, *34*(2), 195–212. https://doi.org/10.1099/00221287-34-2-195

Kondrat'eva, E. N., Mekhtieva, V. L., & Sumarokova, R. S. (1966). Concerning the directionality of the isotope effect in the first steps of sulphide oxidation by purple bacteria. *Vest. Mosk. Univ. Ser.*, *6*, 45–48.

Kusai, K., & Yamanaka, T. (1973). The oxidation mechanisms of thiosulphate and sulphide in Chlorobium thiosulphatophilum: roles of cytochrome c-551 and cytochrome c-553. *Biochimica et Biophysica Acta (BBA)-Bioenergetics*, *325*(2), 304–314.

Lavik, G., Stührmann, T., Brüchert, V., Van der Plas, A., Mohrholz, V., Lam, P., Mußmann, M., Fuchs, B. M., Amann, R., & Lass, U. (2009). Detoxification of sulphidic African shelf waters by blooming chemolithotrophs. *Nature*, *457*(7229), 581–584.

Luther, G. W., Findlay, A. J., MacDonald, D. J., Owings, S. M., Hanson, T. E., Beinart, R. A., & Girguis, P. R. (2011). Thermodynamics and kinetics of sulfide oxidation by oxygen: A look at inorganically controlled reactions and biologically mediated processes in the environment. *Frontiers in Microbiology*, *2*(APR), 1–9. https://doi.org/10.3389/fmicb.2011.00062

Mariotti, A., Germon, J. C., Hubert, P., Kaiser, P., Letolle, R., Tardieux, A., & Tardieux, P. (1981). Experimental determination of nitrogen kinetic isotope fractionation: Some principles; illustration for the denitrification and nitrification processes. *Plant and Soil*, *62*(3), 413–430. https://doi.org/10.1007/BF02374138

Mekhtieva, V. L., & Kondrat'eva, E. N. (1966). Fractionation of stable isotopes of sulfur by photosynthesizing purple sulfur bacteria Rhodopseudomonas sp. *Dokl. Akad. Nauk SSSR*, *166*, 465–468.

O'Leary, M. H. (1981). Carbon isotope fractionation in plants. *Phytochemistry*, *20*(4), 553–567.

Otake, T., Lasaga, A. C., & Ohmoto, H. (2008). Ab initio calculations for equilibrium fractionations in multiple sulfur isotope systems. *Chemical Geology*, *249*(3-4), 357–376.

Pellerin, A., Antler, G., Holm, S. A., Findlay, A. J., Crockford, P. W., Turchyn, A. V., Jørgensen, B. B., & Finster, K. (2019). Large sulfur isotope fractionation by bacterial sulfide oxidation. *Science Advances*, *5*, eaaw1480.

Pfeffer, C., Larsen, S., Song, J., Dong, M., Besenbacher, F., Meyer, R. L., Kjeldsen, K. U., Schreiber, L., Gorby, Y. A., & El-Naggar, M. Y. (2012). Filamentous bacteria transport electrons over centimetre distances. *Nature*, *491*(7423), 218–221.

Pisapia, C., Chaussidon, M., Mustin, C., & Humbert, B. (2007). O and S isotopic composition of dissolved and attached oxidation products of pyrite by Acidithiobacillus ferrooxidans: Comparison with abiotic oxidations. *Geochimica et Cosmochimica Acta*, *71*(10), 2474–2490. https://doi.org/10.1016/j.gca.2007.02.021

Pjevac, P. (2014). *Co-existence and niche differentiation of sulfur oxidizing bacteria in marine environments* (Doctoral dissertation). University of Bremen, Bremen, Germany.

Poser, A., Vogt, C., Knöller, K., Ahlheim, J., Weiss, H., Kleinsteuber, S., & Richnow, H. H. (2014). Stable sulfur and oxygen isotope fractionation of anoxic sulfide oxidation by two different enzymatic pathways. *Environmental Science and Technology*, *48*(16), 9094–9102. https://doi.org/10.1021/es404808r

Poser, A., Vogt, C., Knöller, K., Sorokin, D. Y., Finster, K. W., & Richnow, H.-H. (2016). Sulfur and oxygen isotope fractionation during bacterial sulfur disproportionation under anaerobic haloalkaline conditions. *Geomicrobiology Journal*, *33*(10), 934–941.

Pott, A. S., & Dahl, C. (1998). Sirohaem sulfite reductase and other proteins encoded by genes at the dsr locus of Chromatium vinosum are involved in the oxidation of intracellular sulfur. *Microbiology*, *144*(7), 1881–1894.

Rees, C. E. (1973). A steady-state model for sulphur isotope fractionation in bacterial reduction processes. *Geochimica et Cosmochimica Acta*, *37*(5), 1141–1162. https://doi.org/10.1016/0016-7037(73)90052-5

Riahi, S., & Rowley, C. N. (2014). Why can hydrogen sulfide permeate cell membranes? *Journal of the American Chemical Society*, *136*(43), 15111–15113. https://doi.org/10.1021/ja508063s

Rimmer, A., Ostrovsky, I., & Yacobi, Y. Z. (2008). Light availability for Chlorobium phaeobacteroides development in Lake Kinneret. *Journal of plankton research*, *30*(7), 765–776.

Sakai, H., & Dickson, F. W. (1978). Experimental determination of the rate and equilibrium fractionation factors of sulfur isotope exchange between sulfate and sulfide in slightly acid solutions at 300°C and 1000 bars. *Earth and Planetary Science Letters*, *39*(1), 151–161.

Scott, K. M., Lu, X., Cavanaugh, C. M., & Liu, J. S. (2004). Optimal methods for estimating kinetic isotope effects from different forms of the Rayleigh distillation equation. *Geochimica et Cosmochimica Acta*, *68*(3), 433–442. https://doi.org/10.1016/S0016-7037(03)00459-9

Shahak, Y., Hauska, G., Herrmann, I., Arieli, B., Taglicht, D., & Padan, E. (1992). Sulfide-quinone reductase (SQR) drives anoxygenic photosynthesis in prokaryotes. In M. N. (Ed.), *Research in photosynthesis* (Vol. II, pp. 483–486). Kluwer Academic Publisher.

Sievert, S. M., Scott, K. M., Klotz, M. G., Chain, P. S. G., Hauser, L. J., James, H., Michael, H., Miriam, L., Alla, L., Larimer, F. W., Susan, L., Malfatti, S. A., Folker, M., Paulsen, I. T., Qinghu, R., & Jörg, S. (2008). Genome of the Epsilonproteobacterial Chemolithoautotroph Sulfurimonas denitrificans. *Applied and Environmental Microbiology*, *74*(4), 1145–1156. https://doi.org/10.1128/AEM.01844-07

Sim, M. S., Bosak, T., & Ono, S. (2011). Large Sulfur Isotope Fractionation Does Not Require Disproportionation. *Science*, *333*, 74–77. https://doi.org/10.1089/jmf.2016.3871

Sorokin, D. Y., Tourova, T. P., Mußmann, M., & Muyzer, G. (2008). Dethiobacter alkaliphilus gen. nov. sp. nov., and Desulfurivibrio alkaliphilus gen. nov. sp. nov.: Two novel representatives of reductive sulfur cycle from soda lakes. *Extremophiles*, *12*(3), 431–439. https://doi.org/10.1007/s00792-008-0148-8

Swan, B. K., Martinez-Garcia, M., Preston, C. M., Sczyrba, A., Woyke, T., Lamy, D., Reinthaler, T., Poulton, N. J., Masland, E. D. P., Gomez, M. L., Sieracki, M. E., DeLong, E. F., Herndl, G. J., & Stepanauskas, R. (2011). Potential for Chemolithoautotrophy Among Ubiquitous Bacteria Lineages in the Dark Ocean. *Science*, *333*(September), 1296–9.

Thode, H. G., Kleerekoper, H., & McElcheran, D. (1951). Isotope fractionation in the bacterial reduction of sulphate. *Research*, *4*(12), 581.

Thorup, C., Schramm, A., Findlay, A. J., Finster, K. W., & Schreiber, L. (2017). Disguised as a sulfate reducer: Growth of the deltaproteobacterium Desulfurivibrio alkaliphilus by Sulfide Oxidation with Nitrate. *mBio*, *8*(4), 1–9. https://doi.org/10.1128/mBio.00671-17

Thurston, R. S., Mandernack, K. W., & Shanks, W. C. (2010). Laboratory chalcopyrite oxidation by Acidithiobacillus ferrooxidans: Oxygen and sulfur isotope fractionation. *Chemical Geology*, *269*(3-4), 252–261. https://doi.org/10.1016/j.chemgeo.2009.10.001

Tudge, A. P., & Thode, H. G. (1950). Thermodynamic properties of isotopic compounds of sulphur. *Canadian Journal of Research*, *28*(9), 567–578.

Wahlund, T. M., Woese, C. R., Castenholz, R. W., & Madigan, M. T. (1991). A thermophilic green sulfur bacterium from New Zealand hot springs, Chlorobium tepidum sp. nov. *Archives of Microbiology*, *156*(2), 81–90. https://doi.org/10.1007/BF00290978

Wasmund, K., Mußmann, M., & Loy, A. (2017). The life sulfuric : microbial ecology of sulfur cycling in marine sediments. *Environmental microbiology Reports*, *9*, 323–344. https://doi.org/10.1111/1758-2229.12538

Widdel, F., & Bak, F. (1992). Gram-Negative Mesophilic Sulfate-Reducing Bacteria. In A. Balows, H. Trüper, M. Dworkin, W. Harder, & K. H. Schleifer (Eds.), *The prokaryotes* (pp. 3352–3378). Springer, New York. https://doi.org/10.1007/978-1-4757-2191-1_21

Zerkle, A. L., Farquhar, J., Johnston, D. T., Cox, R. P., & Canfield, D. E. (2009). Fractionation of multiple sulfur isotopes during phototrophic oxidation of sulfide and elemental sulfur by a green sulfur bacterium. *Geochimica et Cosmochimica Acta*, *73*(2), 291–306. https://doi.org/10.1016/j.gca.2008.10.027

Part II: Insights on biomineralization and microbial preservation in rocks

Chapter 5

SILICATE BIOMINERALIZATION OF SEDIMENT- AND CARBONATE-HOSTED ANAEROBIC METHANE-OXIDIZING CONSORTIA AND IMPLICATIONS FOR MICROBIAL FOSSIL PRESERVATION

Daniela Osorio-Rodriguez[1,*], Kyle S. Metcalfe[1,*], Shawn Erin McGlynn[1,2], Hang Yu[1,3], Anne E. Dekas[1,4], Mark Ellisman[5,6], Tom Deerinck[5,6], John P. Grotzinger[1], Victoria J. Orphan[1]
[*]These authors contributed equally to this work

[1] Division of Geological and Planetary Sciences, California institute of Technology, Pasadena, CA, 91125, USA
[2] Earth-Life Science Institute, Tokyo Institute of Technology, Meguro, Tokyo, 152-8550, Japan
[3] College of Urban and Environmental Sciences, Peking University, Beijing, 100871, China
[4] Department of Earth System Science, Stanford University, Stanford, CA 94305, USA
[5] National Center for Microscopy and Imaging Research (NCMIR), Center for Research in Biological Systems (CRBS), University of California, San Diego (UCSD), School of Medicine, La Jolla, California, USA
[6] Department of Neurosciences, University of California, San Diego (UCSD), La Jolla, California, USA

Osorio-Rodriguez, D.*, Metcalfe K.S.*, McGlynn, S.E., Yu, H., Dekas, A.E., Ellisman, M. H., Deerink, T. J., Grotzinger, J. P. & Orphan, V. J. "Silicate biomineralization by anaerobic methane-oxidizing consortia and implications for microbial fossil preservation". In review at *Proceedings of the National Academy of Sciences.* * These authors contributed equally to this work.

Abstract

Authigenic carbonate minerals can preserve organic and isotopic biosignatures of anaerobic methane oxidation (AOM) in the rock record. It is not currently known if the microorganisms that mediate sulfate-coupled AOM—often occurring as consortia of anaerobic methanotrophic archaea (ANME) and sulfate-reducing bacteria

(SRB)—are directly preserved as microfossils. Electron microscopy of ANME-SRB consortia has shown that these microorganisms can be associated with silicate minerals (Chen et al., 2014; Dekas, 2013) but the biogenicity of these phases, their geochemical composition, and their potential presence in the rock record is poorly constrained. Here, we demonstrate that exceptionally Si-rich 200 nm diameter spherical minerals encrust surfaces of multi-celled methane-oxidizing ANME-2 and SRB consortia that were enriched from methane seeps in media that was undersaturated with respect to silica. We further show that putative ANME-SRB consortia preserved in methane seep carbonates are enveloped in silicates with similar composition to those encrusting active ANME-SRB consortia in sediment-free cultures. The Si-rich composition of this mineral phase is similar to the composition of silicates associated with cyanobacteria (Moore et al., 2020), suggesting a common but underexamined mode of biomineralization that may enhance the preservation of microfossils, with implications for the structural finding of microbial remains in rocks from Earth and other planetary bodies which formed in methane-rich environments.

1. INTRODUCTION

Anaerobic oxidation of methane (AOM) is a microbially-driven process in coastal sediments worldwide that modulates methane flux and mediates the precipitation of authigenic minerals. Multicellular ANME-SRB consortia couple methane oxidation to sulfate reduction (Boetius et al., 2000; Orphan, Hinrichs, et al., 2001; Orphan, House, et al., 2001, 2002):

$$\mathrm{CH_4(g) + SO_4^{2-}(aq) \longrightarrow HS^-(aq) + HCO_3^-(aq) + H_2O(l)} \tag{5.1}$$

The production of one mole each of bicarbonate and sulfide increases porewater alkalinity in two total units in zones of AOM activity per mole of oxidized methane, driving the precipitation of carbonate minerals (Aloisi et al., 2002; Luff and Wallmann, 2003; Naehr et al., 2007; Teichert et al., 2005). Geochemical modeling

(Luff and Wallmann, 2003) and isotope signatures (Loyd et al., 2016; Thiagarajan et al., 2020) in methane seep carbonates imply rapid precipitation rates during early diagenesis, suggesting that the ANME-SRB consortia inhabiting these rocks (Marlow et al., 2014; Mason et al., 2015) may mediate carbonate precipitation. Therefore, it is surprising that silicates —not carbonates— with compositions and platy morphologies similar to clay minerals, intimately associate with ANME-SRB consortia (Chen et al., 2014; Dekas, 2013) isolated from methane seep sediments. These silicates have been proposed to precipitate via microbially-mediated interactions between dissolved silicon (Si) and metal cations adsorbed to ANME-SRB consortia exteriors (Chen et al., 2014). Local acidic microenvironments in the cells exteriors may be enhanced by extracellular electron transfer from ANME to SRB (Franks et al., 2009), which would favor the precipitation of amorphous silica and inhibit carbonate precipitation in the immediate vicinity of the consortia. Silica-rich cements and clay mineral envelopes were proposed to play a role in adhesion within ANME-SRB consortia (Chen et al., 2014). However, as these phases have been observed on ANME-SRB consortia extracted from AOM enrichments of sediment samples, the extent to which ANME-SRB consortia mediated the precipitation of these phases, as opposed to a passive attachment, was unclear.

Authigenic silicate precipitation can occur in sediments due to interactions between porewater Si and clay-type aluminosilicates (Michalopoulos and Aller, 2004), potentially producing abiotic silicate precipitates that may adhere to ANME-SRB consortia and thus obscure the true biogenicity of these phases. Additionally, whether ANME-SRB consortia inhabiting seep carbonates (Marlow et al., 2021; Marlow et al., 2014; Mason et al., 2015; Michalopoulos and Aller, 2004; A. Pernthaler et al., 2008) may also associate with silicates had not been explored so far. AOM coupled to SR enhances the dissolution of silicon from quartz and other silicates in sediments by increasing the pH of the environment, which could redeposit on the surface of

ANME-SRB consortia (Chen et al., 2014). Microbial surface ligands could favor the nucleation of amorphous silica, as previously suggested for ANME-SRB consortia (Chen et al., 2014), and microorganisms in hot spring and geothermal systems (Konhauser et al., 2004). Authigenic silicates can entomb and preserve organic carbon (Channing and Edwards, 2003; Walter et al., 1996); if ANME-SRB consortia indeed mediate silicate precipitation, this process may enhance the preservation of microbial biomass in methane seep carbonates. Previous studies have revealed active ANME-SRB consortia living within modern seep carbonates (Marlow et al., 2021; Marlow et al., 2014; Mason et al., 2015) and have documented mineral precipitates with consortium-like morphology (Bailey et al., 2010), but have yet to identify ANME-SRB consortia in modern carbonates with high preservation potential such as that conferred by early silica precipitation (Newman et al., 2016).

Here we provide evidence for the active involvement of ANME-SRB consortia in silica precipitation from undersaturated solutions. We performed direct microscopy and analysis of the exteriors of ANME-SRB consortia separated from methane seep sediments and maintained in the laboratory in media with [Si] insufficient to produce abiotic silica precipitates or drive Si sorption to preexisting, consortium-attached silicates. We find the growth of abundant Si-rich phases embedded in EPS and attached to ANME-SRB consortium exteriors with compositions (1) significantly Si-enriched relative to the Si content of source sediment from the Santa Monica Basin, which is composed of ~40% smectite, 40% illite and 20% kaolinite+chlorite (Hein et al., 2003), and (2) similar to those of mineral phases found adhered to ANME-SRB consortia sourced directly from diverse seep sediment. These observations demonstrate de novo growth of a Si-rich phase from solutions undersaturated with respect to amorphous silica, and are suggestive of bona fide silicate precipitation mediated by ANME-SRB consortia, both in culture experiments, and in a diversity of methane seep sediments. We also identified ANME-SRB consortia in modern

seep carbonates associated with silica, either as rims or as precipitates adjacent to the consortia (Metcalfe, 2021). We posit that a silica incrustation of ANME-SRB consortia in seep carbonates might enhance their long-term preservation and is thus a key trait for identifying fossilized ANME-SRB consortia in the rock record.

2. MATERIALS AND METHODS

Sample Collection and Processing

Sediment samples analyzed in this study were collected by push coring using the submersible HOV Alvin and the *R/V Atlantis* from two seafloor methane seep sites, in the Eel River Basin (AT 15-11, October 2006) and off the coast of Costa Rica (AT 37-13, May 2017), and by the ROV Doc Ricketts of the *R/V Western Flyer* from a seafloor methane seep site in Santa Monica Basin (October 2013). Push core (PC) samples PC14 and PC15 from Alvin dive AD4254 (AT 15-11) were collected from a microbial mat proximal to an active methane seep site 520 m below sea level (mbsl) on the Northern Ridge of Eel River Basin (40.786533, -124.5951). Samples from the Costa Rica Margin (AT 37-13) were obtained during Alvin dive AD4912 from a microbial mat (PC 6) collected at 1811 mbsl in the Jaco Scar submarine landslide (9.1163, -84.8372). Samples from Santa Monica Basin were retrieved from a microbial mat at a seafloor methane seep site (33.788835, -118.668298) at 863 mbsl during DR 459 (PC 43). Samples were processed shipboard by extruding sediment from the push core liner and sectioning sediment at 3 cm intervals and either frozen at -80°C, PFA-fixed for microscopy, or sealed in Ar-sparged mylar bags at 4°C for laboratory-based microcosm experiments. Additionally, carbonate samples were collected in the Jaco Scar site using the submersible HOV Alvin and the *R/V Atlantis* (AT42-03, October-November 2018) for microscopy of endolithic AOM consortia.

Percoll Separation

Using a modified protocol (Orphan et al., 2002), separation of ANME-SRB consortia from bulk sediment for downstream microscopy or cultivation was performed using a Percoll (Sigma-P1644) density gradient on an aliquot of seep sediment. Briefly, cells were disaggregated from bulk sediment by sonication for 3 x 10-second intervals on ice using a Branson Sonifier 50 with a power output of 4 W. The 1 mL aliquot of sonicated sediment was then pipetted onto $500\ \mu L$ of a 100% Percoll density gradient and centrifuged at 18000 x G for 30 minutes at 10°C using a Beckman-Coulter Microfuge 18 centrifuge. The supernatant (~1 mL) was then pipetted into 250 mL 1X PBS in a filter tower and vacuumed through a 5 µm polyethersulfone (PES) filter until ~50 mL solution remained in the tower, which was then diluted by ~200 mL 1X PBS added to the tower. Repeated filtration and dilution by 1X PBS was performed 3 times. We calculated this dilution and filtration to remove 99.2% of the 500 μL Percoll (initially containing 0.43 μmol Si (G.E. Healthcare Life Sciences, 2018) present in the density separation supernatant, with the final filtration step yielding a 1 mL aliquot used for downstream microscopy. According to this calculation, final [Si] from Percoll should not exceed 3.4 μM. For microscopy, cells were initially fixed by incubating a 1mL aliquot of sediment with 4% glutaraldehyde overnight at 4°C. For cultivation, the procedures were done in an anaerobic chamber (Coy Laboratory Inc.) as previously described (Yu et al., 2022).

Sediment-free enrichment cultures of AOM consortia

To enrich for ANME-SRB consortia, seep sediments were homogenized with 0.2 μm filter-sterilized and Ar-sparged seawater sampled at the sampling site, and placed in N_2-sparged Pyrex bottles sealed with butyl rubber stoppers as previously described (Yu et al., 2022). Aliquots from anaerobic Percoll separation to enrich ANME-SRB consortia for sediment-free incubation (see above) were mixed with N_2-sparged

artificial seawater (media composition from (Scheller, Yu, Chadwick, McGlynn, 2016)) and placed in N_2-sparged serum vials with butyl rubber stoppers. Carbonate samples were also placed in Pyrex bottles together with filter-sterile N_2-sparged seawater. All incubations were supplied with a CH_4 headspace pressurized to ~2 atm. These anoxic incubations were maintained in the dark at 10°C with partial exchange of spent media with the addition of 0.2 μm filter-sterilized Ar-sparged seawater and CH_4 every 3 months. Sediment-free incubations were maintained in these conditions over ~5 years. Sulfate-reducing activity during the course of the incubations was measured using a modified Cline assay (Cline, 1969).

Fluorescence in situ hybridization and epifluorescence microscopy of ANME-SRB consortia in sediments

Conventional fluorescence in situ hybridization (FISH) with a single fluorophore on the 5' end was used to identify ANME-SRB consortia for analysis of consortium exteriors. In this study, cells fixed by glutaraldehyde and Percoll-separated were filtered down or dried onto 0.2 μm EMD Millipore white polycarbonate filters (Code GTTP) and incubated in 50 μL hybridization buffer for 24 hr at the appropriate formamide stringency, following published protocols (J. Pernthaler et al., 2001). Percoll separation was only performed on samples from sediment-bearing incubations. In this study, we used probes targeting general Archaea (Arch915; Stahl and Amann, 1991), ANME-2 (Eel932; Boetius et al., 2000), ANME-2a/b (Treude et al., 2005), and SRB (DSS658; Boetius et al., 2000). 4',6-diamino-2-phenylindole (DAPI) was subsequently applied as a counterstain, and filters were illuminated using an XCite Series 120Q fluorescence source and imaged with a Qimage QIClick camera attached to an Olympus BX51 epifluorescence microscope using 60x (Olympus PlanApo N Oil, N.A. 1.42) and 100x (Olympus UPlan FL N Oil, N.A. 1.30) objectives. cellSens Dimension imaging software was used to

acquire images. Epifluorescence image compositing was performed using the image processing software Q-Capture Pro 7.

NanoSIMS imaging of ANME-SRB consortia in sediments

Sample preparation for NanoSIMS, analytical conditions and image analysis were performed as previously described (McGlynn et al., 2018). Briefly, aggregates from the 3730 incubation were fixed in glutaraldehyde and prepared for TEM in Durcupan as described previously (McGlynn et al., 2018). The samples were cut at 500nm thickness and placed on an ITO square and gold coated. The primary ion beam during analysis was ~1.3pA. Images were acquired from 10 μm to 47 μm at 512x512, and the primary beam was at (D1=3, and either ES=2 or 3). Pre-sputtering was performed at D1=0 ES=2 until 12C- counts were over 150,000 ct/s.

Fluorescence in situ hybridization and epifluorescence microscopy of endolithic ANME-SRB consortia in carbonate rocks

The Jaco Scar (Costa Rica margin) rock sample was incubated for 1 year under the conditions described above for the sediment-free enrichment cultures. A fragment of this carbonate was fixed in 1% PFA, embedded in Epoxicure 2 (Buehler Ltd., Lake Bluff, IL), glued to a 1-inch round glass, sectioned by rock saw and polished with alumina polishing film of grits 60, 30, 12, 5 and 2 μm to get a rock section of about 50 μm thickness. For FISH, a dehydration series (50%, 75%, 100% ethanol, 1 min each) was performed on the thin section, followed by hybridization with probes targeting ANME-2 (ANME-2-712; Knittel et al., 2005) and SRB (DSS658; Boetius et al., 2000) in 40% formamide hybridization buffer, as previously described (J. Pernthaler et al., 2001). 5 μl/ml of a DAPI-Citifluor mounting medium was added prior to epifluorescence microscopy. Epifluorescence pictures were taken with a fluorescence microscope (Elyra S.1, Zeiss) at 10x (EC Plan-Neofluar 10x/0.30

M27 objective) and 63x magnification (Plan-Apochromat 63x/1.4 Oil DIC M27 objective). Images were acquired using the Zen black software (Zeiss) and the image compositing was performed using the software Fiji (Schindelin et al., 2012).

Scanning Electron Microscopy

Scanning electron microscopy (SEM) and energy-dispersive spectroscopy (EDS) of ANME-SRB consortia immobilized on white polycarbonate filters were performed and correlated with optical microscopy. Additionally, sediment from each of the source sediments was filtered onto 0.2 μm EMD Millipore white polycarbonate filters (Code GTTP). These sediment samples and the rock thin section hybridized with DAPI/FISH were Pd-coated (10 nm thickness) using a Cressington Sputter Coater 208HR and examined using a Zeiss 1550VP Field Emission SEM equipped with an Oxford INCA Energy 300 X-ray EDS system. After SEM image acquisition, EDS mapping of consortia was performed to characterize the spatial distribution of consortium-adhered phases, and EDS point spectra were collected to characterize the compositional range of consortium-adhered phases as well as sediment samples from which consortia were extracted, allowing a comparison between consortium-attached silicates and silicates not associated with consortia. SEM images were acquired using an electron beam energy of 10 eV and EDS mapping and spectra were acquired with an electron beam of 15 eV. Statistical analysis of EDS-acquired compositional data was performed in R.

TEM

ANME-SRB consortia from our sediment-free enrichments were embedded in hydrophilic resin following published protocols (McGlynn et al., 2018), and sectioned using a Leica Ultracut UCT ultramicrotome fitted with a diamond knife. Sections were stained using the contrasting agent osmium tetraoxide and subsequently im-

aged at UCSD using a FEI Spirit transmission electron microscope operated at 120 kV with a Tietz TemCam F224 2K by 2K CCD camera.

FIB-EDS

ANME-SRB consortium cross-sections recovered directly from seep sediments were prepared using a focused Ga+ ion beam (FEI Nova-600) at the Kavli Nanoscience Institute at Caltech followed by EDS analysis of FIB-sectioned consortia to acquire cross-sectional compositional variability of consortium-attached silicates and consortium interiors.

ICP-MS

Dissolved silicon was measured using an Agilent 8800 ICP-MS in oxygen mass-shift mode. Ions of 28 m/z were transmitted through the first quadrupole to a collision reaction cell where they interacted with oxygen gas. Silicon cations that reacted with oxygen to form 28Si16O+ were able to transmit the final quadrupole which was set at 44 m/z. Isobars at 32 m/z such as O2+ are unable to undergo this reaction to form a stable product, practically eliminating the interfering signal. Silica concentrations were quantified after calibration with orthosilicic acid standards (Sigma-Aldrich) in a range of 0.2-10 μM at 1:10 dilutions.

Data and code availability

All data and custom scripts were collected and stored using Git version control. Code for raw data processing, analysis, and figure generation is available in the GitHub repository (https://github.com/daniosro/Si_biomineralization_ANME_SRB).

3. RESULTS

ANME-SRB consortia in sediment-free cultures are associated with nanoscale spheres of amorphous silica

We investigated the hypothesis of ANME-SRB-mediated silicate precipitation (Chen et al., 2014) by examining methane-oxidizing ANME-SRB consortia obtained after 5 years of enrichment cultivation in the laboratory. These sediment-free cultures were initially prepared by gentle sonication and Percoll-based density separation performed under anoxic conditions, followed by size selection to enrich for multicellular ANME-SRB consortia (Yu et al., 2022). These consortia were maintained with a CH_4 headspace in 0.2 μm-filtered sterile defined seawater media, which was exchanged periodically to remove metabolic byproducts (i.e. bicarbonate, sulfide), while maintaining pH and replenishing sulfate (Yu et al., 2022). Using correlated fluorescence in situ hybridization (FISH), SEM, and EDS imaging (Fig. 1a-c), we identified clusters of enriched AOM consortia that were frequently covered with ~200 nm diameter spherical particles rich in Si (Fig. 1d). These were inferred to be amorphous silica based on EDS-derived compositional data and similarities with previously reported amorphous silica spheres associated with cyanobacteria in hot springs (Benning et al., 2004; Renaut et al., 1998). SEM imaging of consortium exteriors revealed the universal presence of Si-rich phases in these cultures, often embedded within C-rich extracellular polymeric material connecting clusters of multiple ANME-SRB consortia (Supp. Fig. 1). TEM imaging corroborated these findings, showing these Si phases formed a matrix within which many dozens of consortia were embedded (Fig. 1e). Image analysis of this TEM data estimated a fairly uniform particle size for these silica spheres (230±62 nm, n=6060) notably similar to the texture of authigenic silica precipitated during microbial respiration of iron-bearing clays (Zhang et al., 2007). FISH-SEM-EDS performed on FIB-sectioned consortia sampled directly from Santa Monica Basin methane seep

sediment (Supp. Fig. 1f-h) also demonstrated that the spatial distribution of silica spheres associated with ANME-SRB consortia from sediment was similar to that observed on consortia grown in sediment-free cultures (Supp. Fig. 1e), namely that silica spheres appear on the exterior of individual ANME-SRB consortia and are not present within consortia interiors. NanoSIMS imaging showed that silica forms rims around ANME-SRB consortia isolated from the Santa Monica Basin methane seep sediment (Fig. 2).

Compositional analysis of amorphous silica attached to ANME-SRB consortia grown in sediment-free cultures revealed it has silicates have a similar composition to Si-rich phases associated with consortia directly extracted from Santa Monica Basin methane seep sediments (Fig. 1f; Fig. 3a), suggesting that the Si-rich composition of this mineral phase is common to AOM consortia. Notably, the amorphous silica phase attached to AOM consortia in sediment-free cultures and from methane seep sediment has a distinct composition from the siliciclastic methane seep sediment particles from which the original inoculum of ANME-SRB consortia was sourced. Mineral phases attached to AOM consortia extracted from both native sediments and within our sediment-free cultures typically had lower Si, Al and Fe (5-20 atom % Si, ~0-5% Al, and ~0-3% Fe) than the sediment particles which hosted them (~15-25 atom % Si, ~5-10% Al, and ~3-10% Fe; Supp. Fig. 2). We note that raw atom % values calculated from EDS data may underrepresent Si, Al, and Fe in consortia given the high local C or O from proximal biomass. Thus, we characterized the composition of consortium-attached silica by ratios of elements typically found in octahedral sites of clays (Mg, Al, Fe) to Si, and found that AOM consortia had Al:Si ratios < 0.37 and (Mg+Al+Fe):Si ratios < 0.5, which are generally lower than those of the sediment from which they were drawn (Fig. 3). Based on these elemental ratios, we conclude that the phases attached to ANME-SRB consortia are predominantly amorphous silica, as opposed to clay minerals. Notably, the Si-rich

phases attached to ANME-SRB consortia from this work were significantly more Si-rich than cell-attached silicates previously used as a model for silica precipitation resulting from cation bridging by Fe or Al adsorbed on cell walls (Konhauser and Urrutia, 1999) (Supp. Fig. 3).

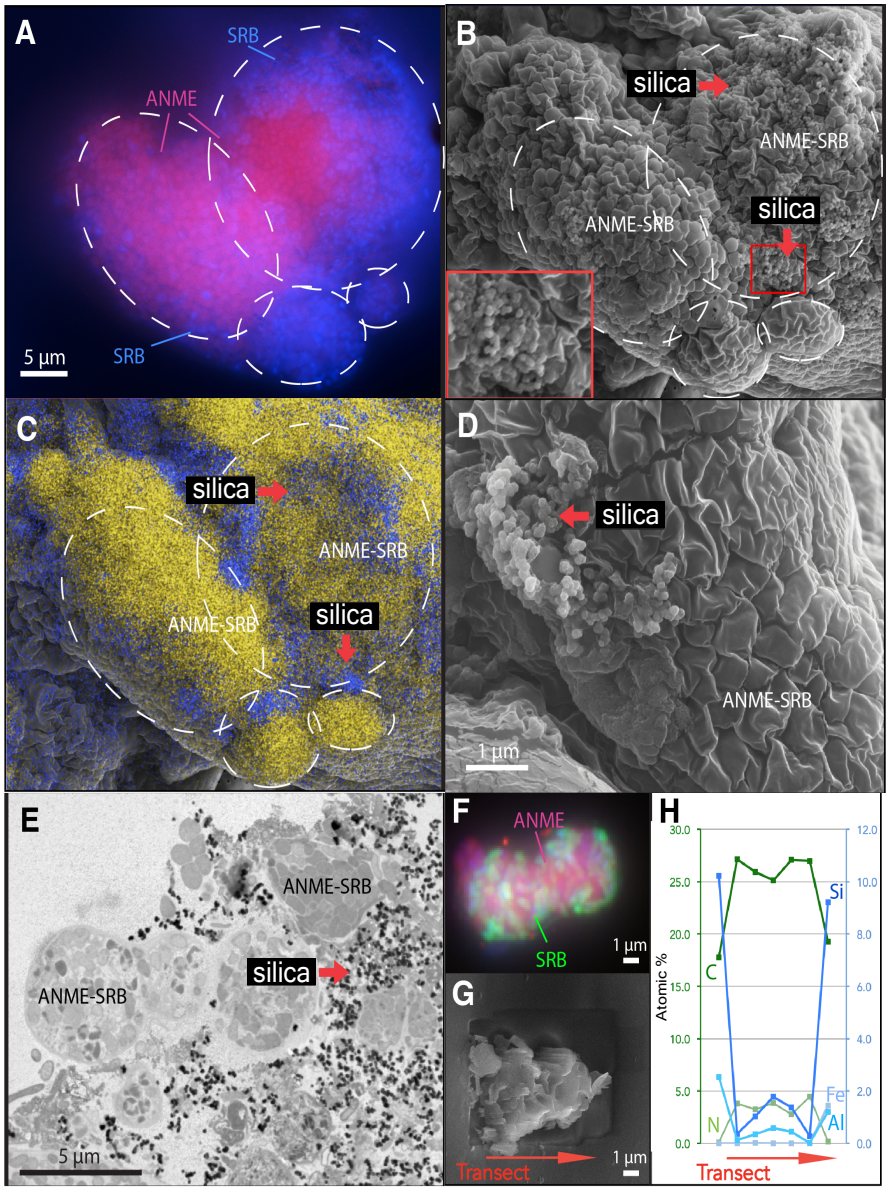

Figure 1: Epifluorescence and microscopy of ANME-2-SRB isolated from sediments. A-E) correspond to sediment-free ANME-2-SRB consortia in laboratory incubations, and F-H) correspond to ANME-2-SRB consortia isolated from sediments.

Figure 1: (cont.) A-C) Correlated FISH, SEM, and EDS imaging of ANME-2/SRB consortia and associated Si-rich phases. Dashed ovals outline individual AOM consortia within the cluster across all 3 panels. A) FISH image of a cluster of ANME- SRB consortia, with ANME-2 cells stained in pink and inferred SRB cells in blue. B) Paired SEM image of the same cluster of AOM consortia in A, where red arrows denote areas enriched in silica. Red inset box: 2X magnified view of ~200 nm amorphous silica spheres. C) EDS map showing elemental distribution, where yellow is carbon associated with ANME-SRB biomass, with silicon (blue) is concentrated in the extracellular matrix around individual AOM consortia. D) Higher magnification SEM image showing nanoscale silica spheres associated with AOM consortia. E) TEM cross-section of ANME-SRB consortia and closely associated Si-rich particles (red arrow). F) FISH of a sediment-associated ANME-SRB consortium, with ANME in pink and SRB in green. G) SEM of the consortium in F after FIB section. H) Elemental composition by EDS along a transect of the consortium in G, which shows higher C and N relative abundances in the interior and an enrichment in Si and Al at the edges of the consortia.

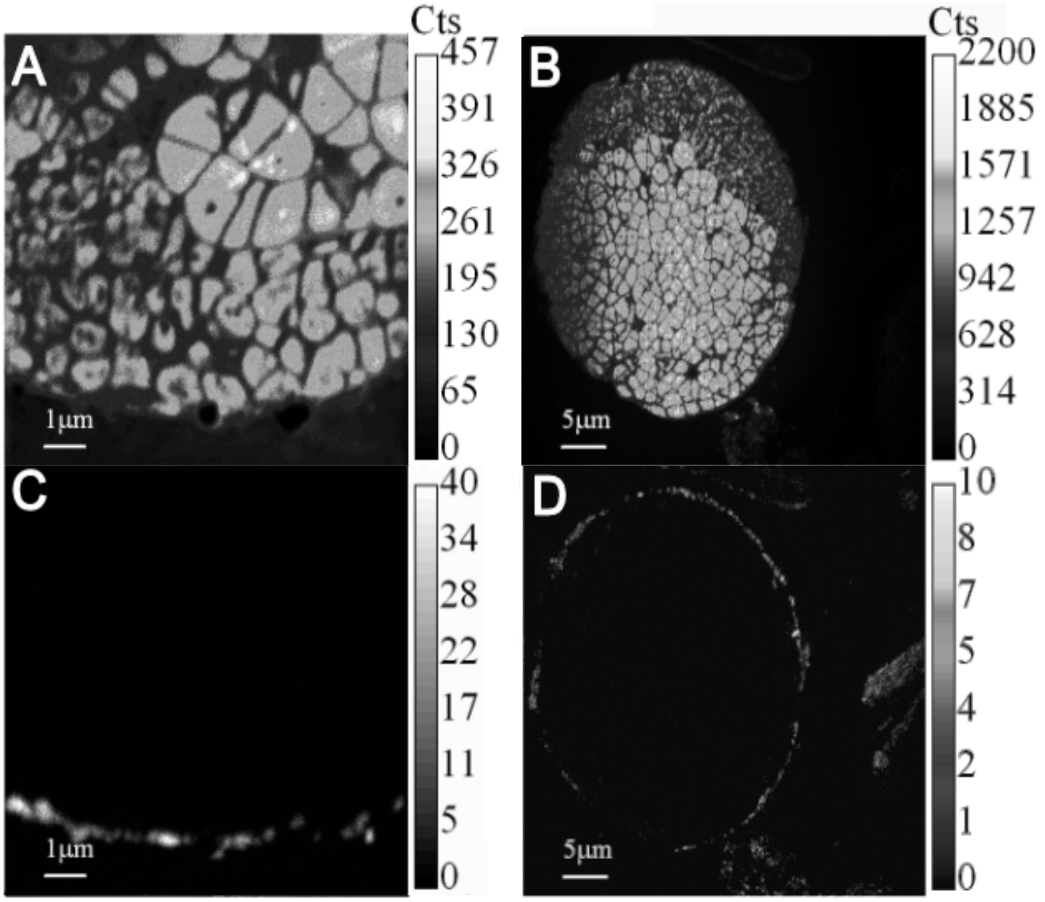

Figure 2: NanoSIMS images of ANME-SRB consortia from sediments. A-B) $^{12}C^{14}N$ maps C-D) ^{28}Si maps of the same ANME-SRB consortia shown in A and B, respectively, where silicon can be observed forming rims around the consortia. Lighter colors indicate higher counts, shown by the bars to the left of the images.

Si-rich phases attached to AOM consortia precipitated from undersaturated media

The long-term maintenance of our AOM enrichment cultures and the absence of a sediment matrix provided the opportunity to place additional constraints on the process by which amorphous silica associates with ANME-SRB consortia. We formulated a simple model of ANME-SRB growth, using estimates of consortium doubling time from the literature (3 to 7.5 months; Dekas et al., 2009; Girguis et al., 2005; Meulepas et al., 2009; Nauhaus et al., 2007; Orphan et al., 2009), to roughly estimate the maximum number of consortia that would have produced an aggregation of 55 ANME-SRB consortia (Supp. Fig. 3) after 5 years of growth in sediment-free anaerobic seawater media. For simplification purposes, the model makes the assumption that the clusters of aggregates were formed by consortia growth, since these clusters were not observed initially in the enrichment cultures. The results of this model (Fig. 3) implied that a 55-consortium cluster could have grown from no more than 2 consortia, assuming a doubling time of 7.5 months. Doubling times shorter than ~ 6 months in this model imply a 55-consortium cluster would have grown from < 1 consortium. Similarly, clusters smaller than ~ 32 consortia with a doubling time of 7.5 months are calculated to have grown from < 1 consortium, suggesting these smaller clusters grew from consortia subsequent to inoculation that were not part of the initial inoculum or possibly represent clusters that separated from larger aggregates during incubation or processing. Based on the observed and modeled consortia growth, we reason that the Si-rich phases detected in the extracellular matrix between clusters of AOM consortia must have developed over the 3-year cultivation period, as essentially all consortia associated with amorphous silica were predicted based on the modeled doubling times to have grown after inoculation.

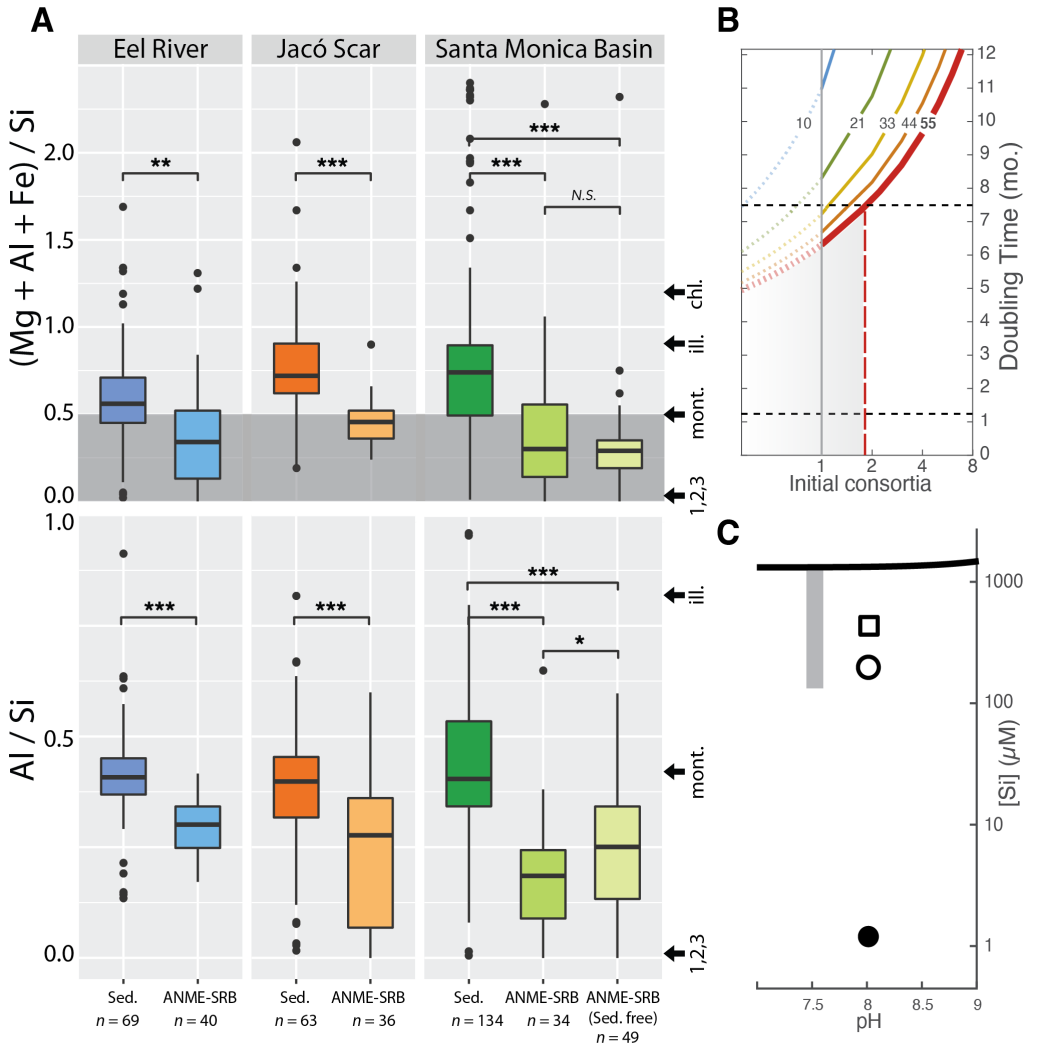

Figure 3: Composition of Si-rich phases associated with ANME-SRB consortia isolated from sediments and in sediment-free incubations. A) Elemental ratios of EDS-acquired compositional data of ANME-SRB consortium-attached Si-rich phases extracted directly from methane seep sediments ('ANME-SRB') or grown under sediment-free conditions ('sed. free') compared with the range of compositions of sediments from 3 different seep sediment locations from Northern and Southern California and the Costa Rican margin from which the AOM consortia were recovered ('sed.'). Sampling location details can be found in Methods. Reference clay mineral compositions are also noted (arrows on right; montmorillonite (mont), illite (ill), chlorite (chl)). Also shown is the composition of 3 different Si-rich rings surrounding carbon-rich cell aggregates in a seep carbonate (black arrow, numbered 1,2,3). B) A general model of AOM consortia growth showing the estimated final number of consortia (contours) within a cluster as a function of the initial consortia numbers within the enrichment, constrained by the range of reported values for ANME-SRB doubling times (dashed lines).

Figure 3: (cont.) C) ICP-MS measurement of [Si] in seawater media from the sediment-free AOM enrichments (filled circle) showing significant undersaturation compared to the equilibrium concentration for sorption of Si to illite (open circle), montmorillonite (open square), precipitation of amorphous silica at different pH regimes (black line), and the reported range of Si concentrations in which silicate precipitation on cyanobacterial cells occurs (grey bar).

The concentration of silica was measured in the sediment-free enrichments by ICP-MS and this value was compared with the [Si] equilibria of abiotic processes known to generate amorphous silica, including silica precipitation (Gunnarsson and Arnórsson, 2000) and sorption of Si to clay minerals (Siever and Woodford, 1973). Unlike in several previous experiments examining potential microbial silicate biomineralization, where precipitation on bacterial or archaeal cell surfaces was only observed under conditions supersaturated with respect to clay (Konhauser et al., 1993; Konhauser et al., 1994; Konhauser and Urrutia, 1999) or silica precipitation (Hugo et al., 2011; Lalonde et al., 2005; Phoenix et al., 2002; Phoenix et al., 2003; Yee et al., 2003), the silica concentration (21 to 64 μM) in the sediment-free enrichments (Table 1) was several orders of magnitude below [Si] for abiotic silicate precipitation (4.3 mM; Iler, 1979; Fig. 3c). Since neither silica or aluminum were directly added to the incubation media, we hypothesize that traces of these elements may have been washed out from the walls of the glass incubation vials, or were present as part of the original sediments where the aggregates were retrieved from. These results implied Si-rich phases attached to ANME-SRB consortia were precipitated by a yet unknown mechanism that is likely mediated by an aspect of the physiology of the methanotrophic ANME-2 and/or associated SRB partners, given the intimate physical association between silica and AOM consortia. It has been proven that monomers of silicic acid can condensate forming soluble polymeric silicic acid (PSA) particles which can aggregate at pH < 7 (Annenkov et al., 2017). Local low pH conditions around ANME-SRB consortia, conducive to PSA formation, may be enhanced by the

export of protons produced from methane oxidation outside of the cells (McGlynn, 2017), as well as protons produced by silica dissolution and carbonate precipitation (Chen et al., 2014). Organic polymers may enhance the condensation of monomeric silicic acid, leading to the formation of silica nanoparticles (Annenkov et al., 2017). Whether organic ligands are responsible for the precipitation of silica on the surfaces of ANME-SRB consortia grants further examination.

Table 1: Silica concentrations in sediment-free ANME-SRB incubations and sample locations

Location	Si (μM)	Reference
Santa Monica Basin porewater	110-300	Berelson et al. (2005)
Costa Rica cold seeps porewater	110-500	Söding and Wallmann (2003)
Eel River Basin porewater	700-1000	Lyle et al. (2000)
ANME-SRB sed-free enrichment 1	63.24	This study
ANME-SRB sed-free enrichment 2	21.08	This study

Amorphous silica surrounds putative ANME-SRB consortia in seep carbonates

The preservation of AOM signatures in paleo methane seeps primarily exist within authigenic carbonates, where mineral, isotopic, and lipid biosignatures provide evidence for past sulfate-coupled methane oxidation activity catalyzed by ANME and SRB that are analogous to those observed in modern methane seep ecosystems worldwide (Bailey et al., 2010; Naehr et al., 2007; Peckmann et al., 2002). As the greatest potential for Si-enhanced preservation of microfossils of AOM consortia is likely to be found within authigenic carbonates, we extended our investigation to active endolithic AOM consortia within modern methane seep carbonates and the possibility that these assemblages, similar to those in sediments and enrichment culture, also showed evidence of silica precipitation. To investigate this possibility, we examined an authigenic carbonate sample composed primarily of calcite collected from an active deep sea methane seep site off the coast of Costa Rica (~ 1800 m depth). This

seep carbonate was incubated in the laboratory under conditions supporting active sulfate-coupled AOM and showing enrichment in ANME-2c, ANME3, and SRB1 by 16S rRNA gene survey. Epifluorescence microscopy (Fig. 4a) and SEM imaging (Fig. 4b) of an embedded and sectioned sample of this seep carbonate revealed ~10-20 μm diameter consortia comprised of tightly packed cocci cells stained by the general DNA stain DAPI. Correlated SEM-EDS revealed these electron-dense domains were more C-rich than the carbonate matrix (Fig. 4c) and notably, were surrounded by Si-rich rings (Fig. 4d), in a similar way to the ANME-SRB consortia from sediment. FISH hybridization of these embedded endolithic aggregates in rock thin section confirmed that they were in fact composed of ANME-2/SRB (Fig. 5, Supp. Fig. 5), and correlated SEM (Supp. Fig. 6) and EDS (Fig. 5) allowed for confirmation of the presence of silica in close association with the aggregates. FISH labelling of ANME-SRB aggregates in carbonates in situ was only accomplished recently for the first time (Marlow et al., 2021), and ours is the first study to successfully achieve it in thin section and to correlate it with element composition and distribution around the aggregates. The morphology of the ANME-2/SRB aggregates in the carbonates is consistent with that of some of the ANME-2/SRB consortia in sediments identified by FISH (Orphan, Hinrichs, et al., 2001), where cell sizes appear bimodal, with larger cells located in the center of and smaller cells near aggregate margins. Compositional spectra from EDS (Dataset A1) documented low Al, Fe, and Mg content (< 0.6 % wt) in Si-rich rings, with (Mg+Al+Fe):Si and Al:Si ratios similar to those of Si-rich phases attached to ANME-SRB consortia recovered directly from seep sediments and in our sediment-free cultures (Fig. 3a; Dataset A2). Given the compositional and textural similarities between these Si-rich rings and the Si-rich phases associated with ANME-SRB consortia, we interpreted these Si-rich rings surrounding endolithic aggregates in seep carbonates to be analogous to those found encrusting ANME-SRB consortia originating from sediments.

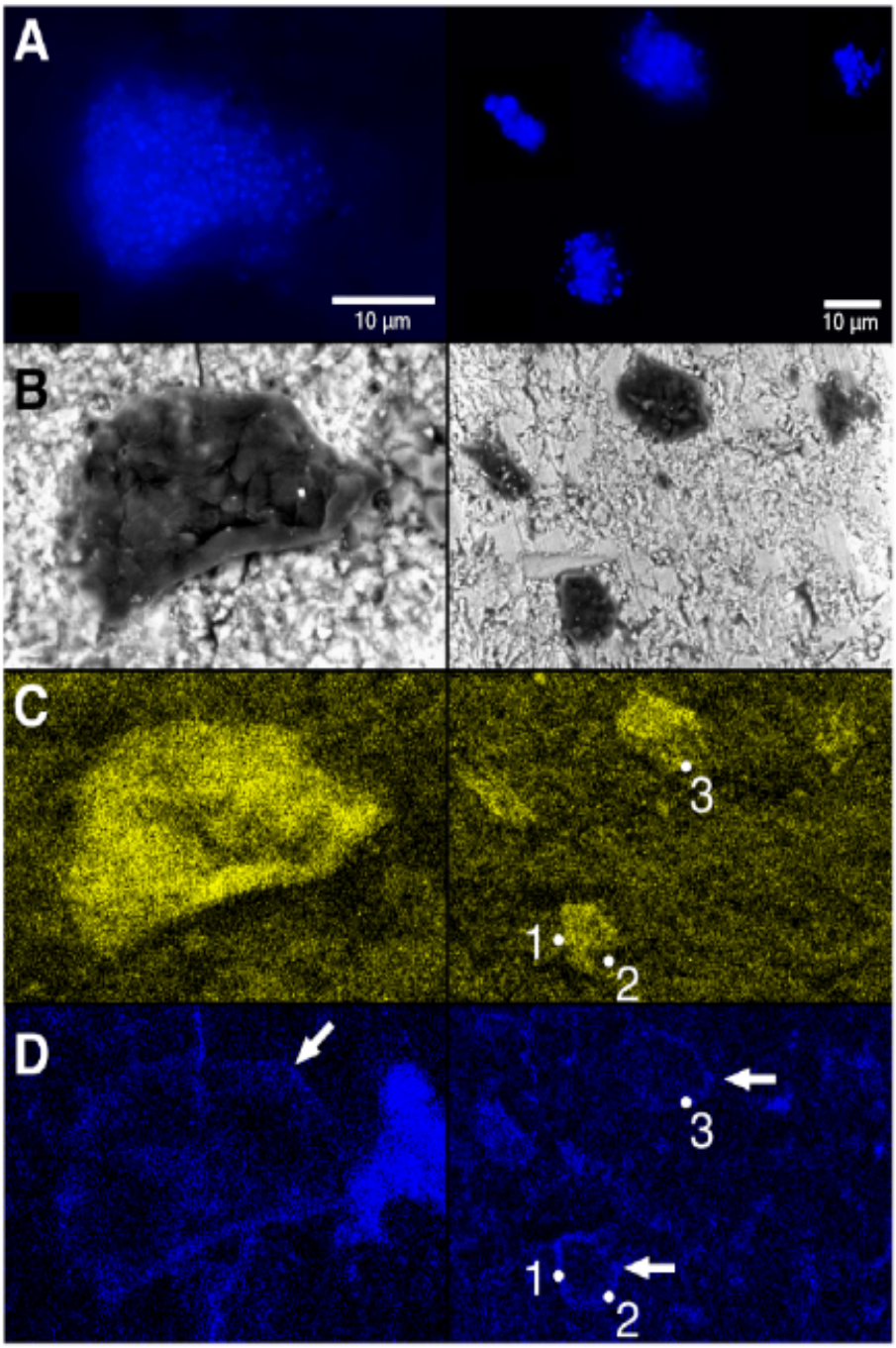

Figure 4: Correlated epifluorescence microscopy, SEM, and elemental analysis of endolithic microbial consortia and associated Si-rich phases in seep carbonate. A) DAPI-stained putative endolithic ANME-SRB consortia embedded within the seep carbonate matrix. B) Correlated SEM of the same microbial consortia shown in A). C-D) EDS analysis of the same consortia as in A) and B) showing carbon rich biomass (yellow, C) surrounded by Si-rich rings in blue (white arrows, D). Numbered points correspond to EDS point spectra (Dataset A1) taken to compare elemental composition of rings to amorphous silica spheres attached to ANME-SRB consortia shown in Fig. 3a.

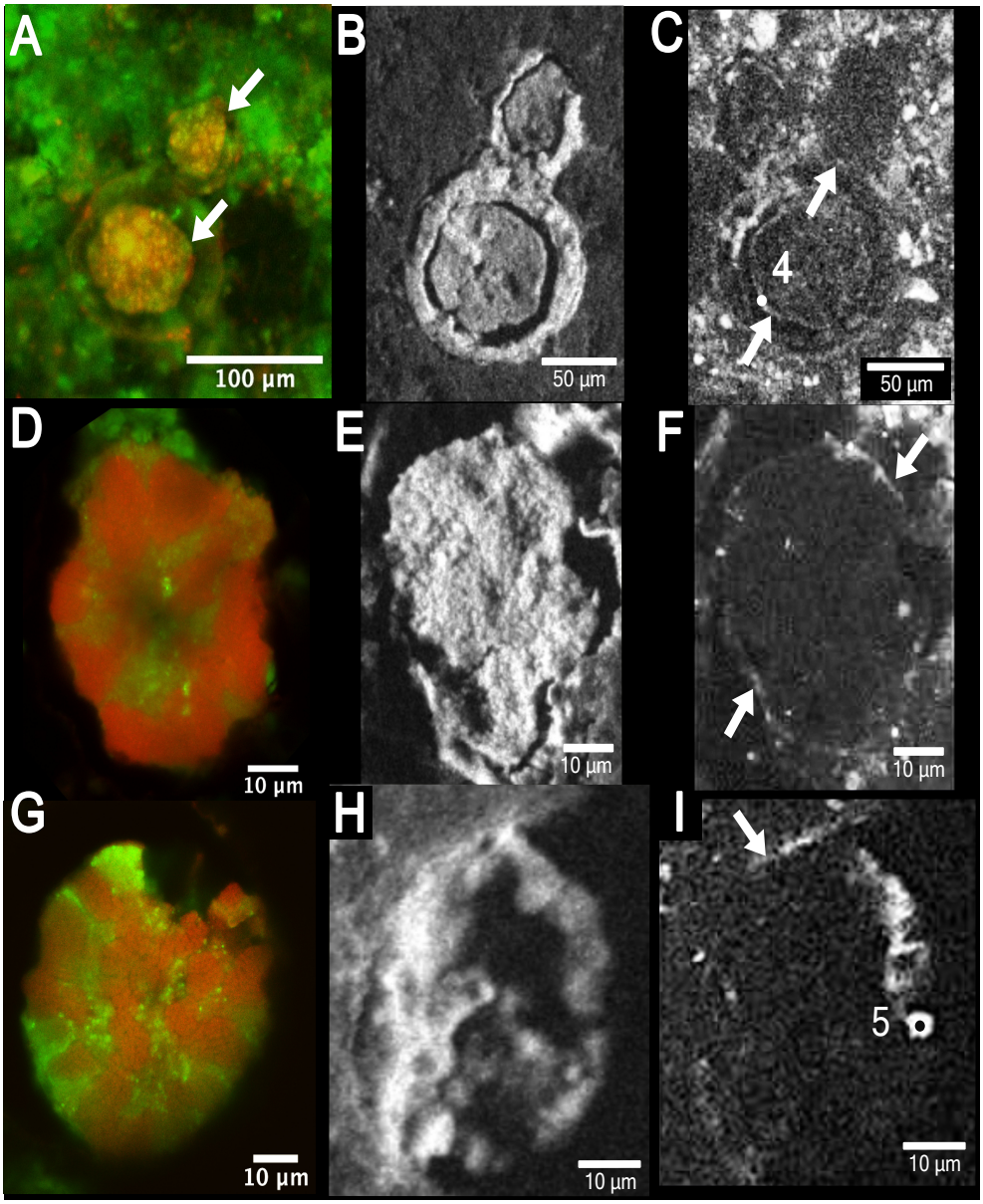

Figure 5: Correlated epifluorescence microscopy and elemental analysis of ANME-2-SRB consortia and associated Si-rich phases in seep carbonate. A, D, G) FISH-stained endolithic ANME-2-SRB consortia (white arrows) embedded within the seep carbonate matrix. Cells hybridized with the ANME-2 (ANME-2-712; Knittel et al., 2005) and SRB (DSS658; Boetius et al., 2000) specific FISH probes are stained in red and green, respectively. B, E, H) Carbon maps from EDS analysis of the consortia shown in A, D, and G, respectively. C, F, I) Silica maps from EDS analysis of the consortia shown in A, D, and G, respectively. White arrows point at Si-rims surrounding the consortia. Numbered points correspond to EDS point spectra (Dataset A1) taken to compare elemental composition of rings to amorphous silica spheres attached to ANME-SRB consortia shown in Fig. 3a.

4. DISCUSSION

We observed and identified Si-rich phases on ANME-SRB consortium exteriors incubated under sediment-free conditions in filtered seawater undersaturated with respect to silica. Measurement of [Si] in sediment-free incubation media via ICP-MS precluded abiotic mechanisms of Si enrichment of consortium-attached Si-rich phases, as [Si] was too low to drive either amorphous silica precipitation or Si sorption to pre-existing consortium-attached silicates. Additionally, most consortium-attached phases are enriched in silica with respect to detrital silicates in the sediments from which they were sourced, and also compared to known clay mineral compositions, suggesting these phases are not simply a product of the attachment of clay minerals in sediment. For example, in Si-rich endmember clay compositions such as montmorillonite [$(\mathrm{Na, Ca})_{0.33}(\mathrm{Al, Mg})_2(\mathrm{Si_4O_{10}})(\mathrm{OH})_2\mathrm{nH_2O}$)], with a 2:1 ratio of tetrahedral to octahedral sheets and where Si occupies all tetrahedral sites, the octahedral cation to Si ratio is 0.5 (Moore and Reynolds, 1989); however, consortium-attached Si-rich phases had octahedral cation: Si ratios generally < 0.5 (Fig. 3a). For comparison, methane seep sediment samples from which consortia were extracted had octahedral cation to Si ratios typically > 0.5, consistent with clay minerals (Fig. 3a). These results contrast with a previous report of incrustation of AOM consortia with clay minerals (Chen et al., 2014), however, the phases reported in that study also had cation: Si ratios generally < 0.5, implying they were as well more enriched in Si with respect to known clay minerals. One potential explanation for the Si-rich phases associated with AOM consortia is that clays become attached to the consortia and then lose cations by an unknown mechanism. However, the simplest explanation would be that there is a removal of Si from solution by ANME-SRB consortia and thus bona fide silicate biomineralization by ANME-SRB. Critically, the lines of evidence we provide would allow us to disprove the null hypothesis that consortium-attached silica exists either due to passive attachment of detrital phases

to consortium surfaces or by abiotic silicate precipitation.

Microbial precipitation of silica in undersaturated conditions has been previously proposed to be mediated by iron (Yee et al., 2003) and magnesium (Moore et al., 2021; Moore et al., 2020) in solution. Experimental studies in cyanobacteria have proven that sulfate-rich extracellular polymeric substances (EPS) and an increase in pH promoted by photosynthesis enhance the precipitation of magnesium-rich silica. It is thought that magnesium acts as a cation bridge between positively charged silicic acid and negative functional groups in the EPS (Moore et al., 2021). Although we did observe a carbon-rich rim around two ANME-SRB consortia in the carbonate rock (Fig. 5a, 4b), consistent with the presence of EPS, this mechanism is not congruent with our observation that the silicates attached to ANME-SRB consortia have low Al, Fe, and Mg content (<0.6 % wt). In this study, silica biomineralization was observed at the exteriors of ANME-SRB consortia, which is consistent with previous reports (Chen et al., 2014). This is surprising, since it has been observed that cell interiors might be more conducive to silicification in undersaturated conditions through intracellular Si-concentrating mechanisms in diatoms (Martin-Jézéquel et al., 2000), but it is consistent with observations in surfaces of cyanobacterial cells (Moore et al., 2020). The silicification at cell surfaces is thought to be mediated by EPS and magnesium in cyanobacteria (Moore et al., 2021), and during the reductive dissolution of Fe^{3+}-rich clay minerals by metal-reducing *Shewanella oneidensis* (O'Reilly et al., 2005; Zhang et al., 2007), which appear to share common textural characteristics with the amorphous silica phase reported here (Zhang et al., 2007). Silicate precipitation concomitant with microbial respiration of Fe in clay minerals (Furukawa and O'Reilly, 2007; O'Reilly et al., 2005) has been proposed to occur through interactions with polyamines (Furukawa and O'Reilly, 2007). Long-chain polyamines (> 7 aminopropyl units) have been shown to precipitate silica from silica oligomers in undersaturated conditions (Patwardhan et al., 2011), and in bacteria

under natural (Saw et al., 2008) and experimental (Furukawa and O'Reilly, 2007) saturated silica conditions. Microbially-mediated silicate precipitation has also been observed in the spore coat of *Bacillus subtilis*, in this case mediated by a serine- and arginine-rich protein (Motomura et al., 2016). The zwitterionic nature of this protein conferred by serine and arginine residues is similar to that of silacidins and silaffins, proteins that mediate silica precipitation in diatoms (Kröger et al., 2000; Wenzl et al., 2008).

To explore potential biochemical mechanisms of silicate precipitation in our ANME-SRB incubations, we screened the genomes of ANME and syntrophic SRB-associated metagenome-assembled genomes (MAGs; Chadwick et al., 2022; Skennerton et al., 2017; Yu et al., 2022). Following the approach of previous work targeting silaffin-like proteins in diatom genomes (Scheffel et al., 2011), we performed a search of our database to find candidate proteins in ANME MAGs in sediment-free cultures with serine- and arginine-rich domains. We also searched our genomic database for homologs of aminopropyl transferases. However, no definitive proteins responsible for silicate precipitation could be identified. The fact that there are currently several independent pathways for microbially mediated silica precipitation described suggests there are likely additional discoveries of biological mechanisms underlying this process. It has been established that different polyamines, such as co-polypeptides with high block ratio of lysine and phenylalanine, polyallylamine, polyethylenimine, poly(acrylamide-co-2-(dimethylamino)) ethyl methacrylate, or amine terminated dendrimers can act as templates for silica formation in vitro (Della Rosa et al., 2020). Additionally, a number of posttranslational modifications (PTMs) have been proven to be critical for the Si-precipitating property of silaffins, such as di- or trimethylation or alkylation of lysine residues with N-methylated oligo-propyleneimine chains, hydroxylation, and phosphorylation of all the trimethylated lysine residues at the δ-position, and phosphorylation of all serine hydroxyl groups. The PTMs introduce

a significant amount of both positive and negative charges, which render the peptide zwitterionic, a property critical for silica precipitation (Lechner and Becker, 2015). These characteristics could be used as targets for searching and identifying potential proteins involved in silica precipitation. While the genomic mechanism remains elusive at this time, our modeling results (Fig. 3b) and geochemical measurements (Fig. 3c) support biologically mediated Si-rich silicate precipitation by AOM consortia in undersaturated conditions that is inconsistent with abiotic precipitation conditions. Silicification relies on reactive cell surface ligands that can adsorb silica from solution, implying that cell surface charge may be critical for the initial silicification process (Konhauser et al., 2004). A neutral membrane, such as the one that enhances silica biomineralization in the cyanobacterium *Calothrix*, would be hydrophobic, thus enhancing the attachment of silica (Phoenix et al., 2002). For negatively-charged cells, metal cation bridges (e.g. $\mathrm{Fe}^{3+}, \mathrm{Al}^{3+}$) might be necessary for silicification, since the organic ligands at cell surfaces would be electrostatically repulsed to the negatively-charged silica species (Konhauser et al., 2004). We suggest that future research focuses on investigating cell or consortia surface charges (Nishino et al., 2020), and differences in the functional groups between the cell wall and EPS, to hint at the silica precipitation mechanisms used specifically by ANME-SRB.

The mode of ANME-SRB biologically-mediated silica precipitation described in this study may be important for the preservation of organic carbon in seep carbonates. Early diagenetic silica is observed in fossil seep carbonates spanning the Phanerozoic, where silica appears as fibrous and botryoidal cements replacing aragonite (Himmler et al., 2008; Kaim et al., 2008; Kuechler et al., 2012; Miyajima et al., 2016; Peckmann et al., 2002; Smrzka et al., 2015). Early silica precipitation in seep carbonates can entomb organics; in one striking example, preservation of Cretaceous chemosynthetic symbiotic tube worm chitin in early silica cements has

been documented (Hikida et al., 2003). The observations that ANME-SRB consortia precipitate Si-rich phases both in laboratory enrichments and what appears to be *in situ* within seep sediments and carbonates suggest early amorphous silica cementation in seep carbonates may also improve the preservation potential of body fossils and associated organics from ANME-SRB consortia in the rock record. We propose that future work could use Si-rich rings around carbonaceous domains in fossil seep carbonates as a search image to examine ANME-SRB consortia preserved in the rock record.

5. CONCLUSIONS

ANME-SRB consortia have been found to be associated with silicates, but a proof of their direct involvement in silicate biomineralization was missing. We provide evidence for the removal and precipitation of silica from undersaturated solutions by ANME-SRB consortia. Our results suggest a so far underexamined role for microorganisms in the precipitation of silicates from undersaturated solutions. The observation of a similar process of microbially-mediated silicate biomineralization in diverse microorganisms suggests a common but as yet poorly understood mechanism catalyzing the precipitation of silicates in undersaturated conditions. As the early precipitation of authigenic silicates is thought to improve the preservation potential of fossils generally (Callow and Brasier, 2009; Newman et al., 2016; Sallstedt et al., 2019) our results further support the possibility that massive chert precipitation as observed in classic microfossil localities such as the Gunflint (Barghoorn and Tyler, 1965) may not be critical for preserving microbial fossils in the rock record. Instead, microscale associations between microorganisms and amorphous silica may provide adequate preservation potential, offering a new search image in paleo-seep carbonates, and further serve as a geochemical trace fossil in the rock record.

6. ACKNOWLEDGEMENTS

The authors would like to acknowledge Jake Bailey, Tom Bristow, Ted Present, Paul Myrow, Kelsey Moore, and Jen Glass for contributing to discussions about this work. We would like to thank Chi Ma for assistance with SEM-EDS, Yunbin Guan for assistance with NanoSIMS, and Nathan Dalleska for help with ICP-MS. The authors are additionally grateful to Alice Michel for discussions regarding sample preparation for FISH-SEM. The authors further acknowledge the crews of R/V Atlantis and R/V Western Flyer for assistance in sample collection and processing. Funding for this work was provided by the US Department of Energy's Office of Science (DE-SC0020373), the National Science Foundation BIO-OCE grant (1634002), a Gordon and Betty Moore Foundation Marine Microbiology Investigator grant (3780), the Simons Collaboration for the Origin of Life, and a grant from the Center for Environmental Microbial Interactions (to VJO). KSM was supported in part by a National Science Foundation Graduate Research Fellowship and a Schlanger Ocean Drilling Fellowship. VJO is a CIFAR science fellow in the Earth 4D program. Portions of this work were developed from the doctoral dissertation of Kyle Metcalfe, Symbiotic Diversity and Mineral-Associated Microbial Ecology in Marine Microbiomes (Metcalfe, 2021).

7. SUPPLEMENTARY MATERIALS

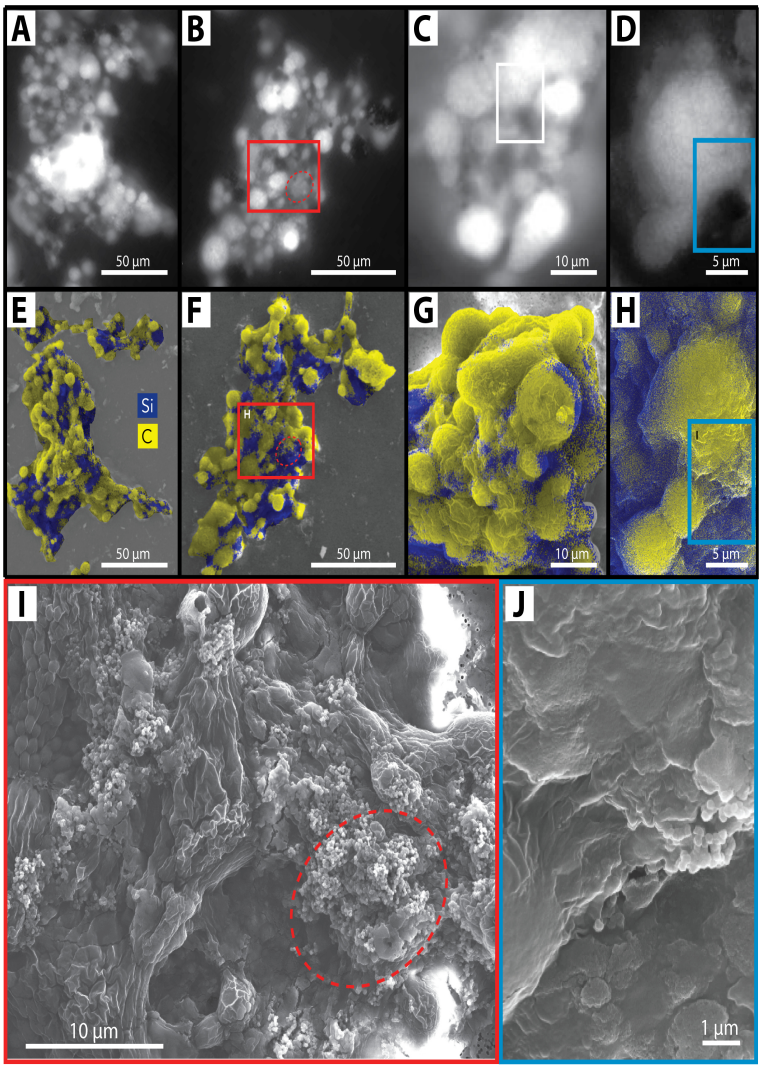

Supp. Fig. 1: Correlative epifluorescence microscopy and EDS analysis of ANME-SRB consortia clusters from sediment-free AOM enrichment cultures. A-D) DAPI-stained consortia clusters at different magnifications showing the gross morphology of the clusters. (E-H) Corresponding SEM-EDS data documenting the spatial proximity of Si-rich phases (blue) with carbon-rich AOM consortia (yellow). I-J) SEM images of silica rich spherules at 2 magnifications. I) Enlargement of the red box area in B and F, where a region enriched in silica nanoparticles is highlighted with dashed red oval. J) Enlargement of the blue box area in D and H, illustrating Si-rich silicates surrounding an ANME-SRB consortium.

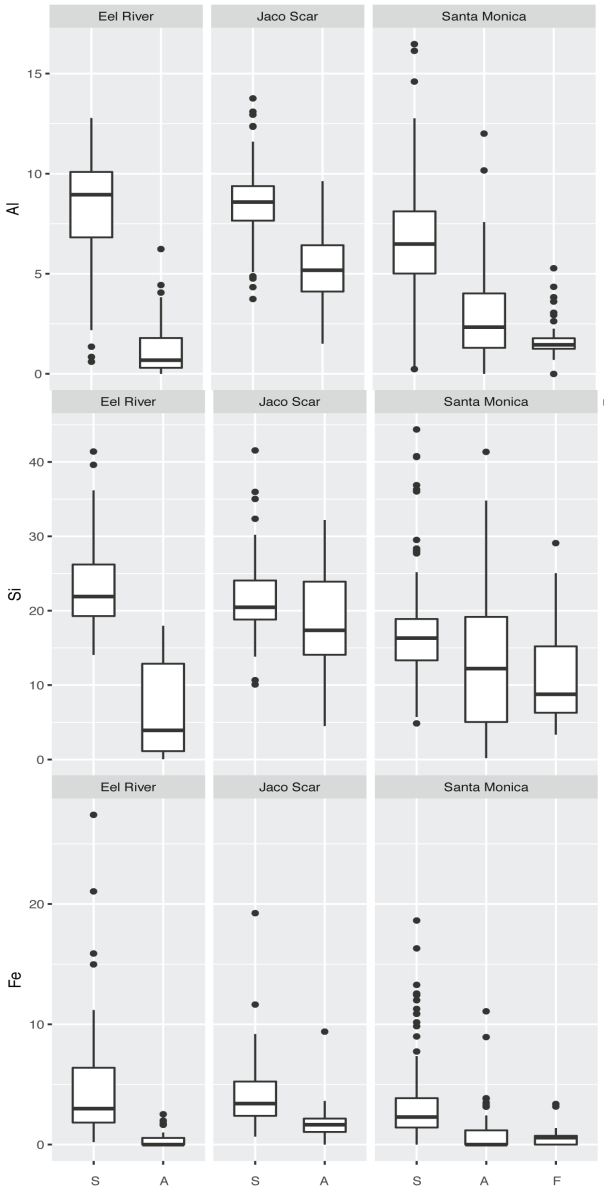

Supp. Fig. 2: EDS compositional data showing the difference in aluminum, silica, and iron in Si-rich phases attached to ANME-SRB consortia recovered directly from methane seep sediments (letter A) or grown under sediment-free conditions (letter F), compared with the composition of the source sediment (letter S). Details on sampling locations can be found in Methods.

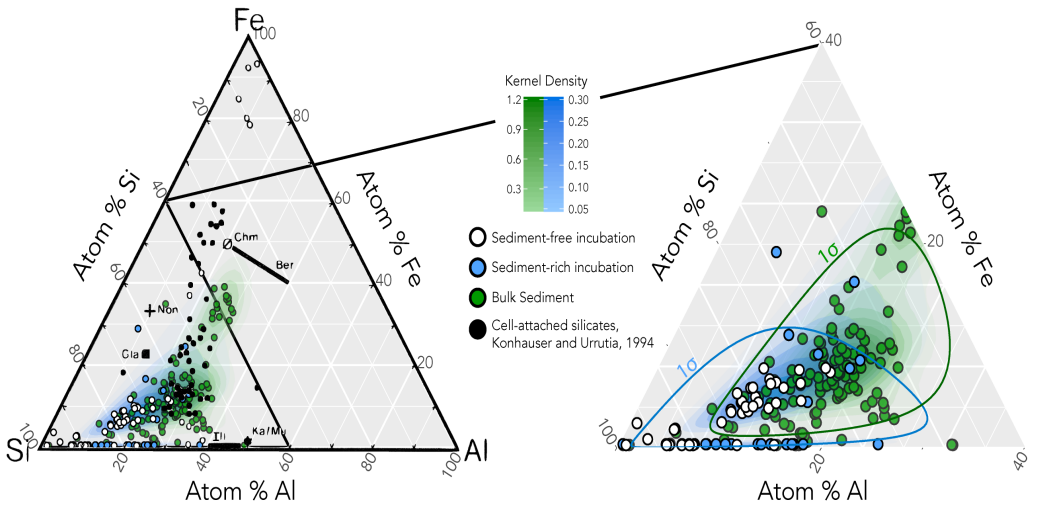

Supp. Fig. 3: Fe-Al-Si ternary plot of EDS compositional data for Si-rich phases attached to AOM consortia sourced directly from Santa Monica Basin methane seep sediments or from sediment-free AOM consortia enrichment cultures, plotted alongside reported compositions of silicates attached to bacterial cell walls.

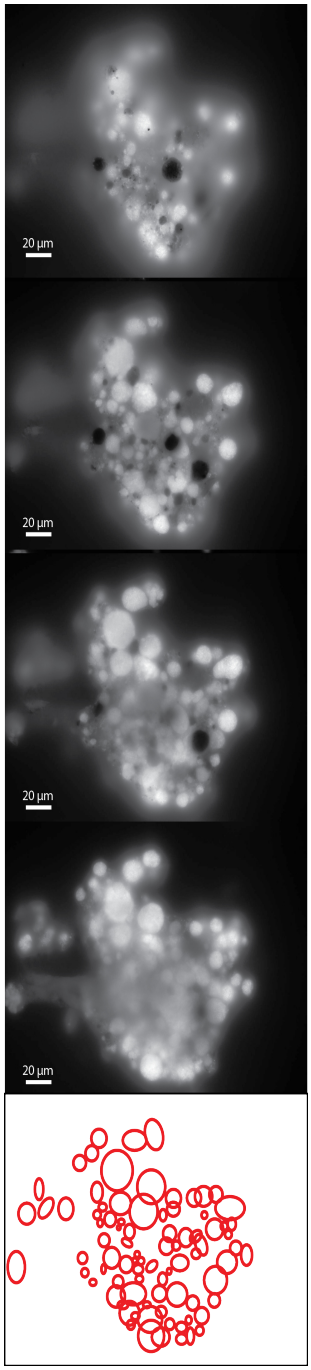

Supp. Fig. 4: Epifluorescence microscopy images of a DAPI-stained large cluster of multiple ANME-SRB consortia from a sediment-free AOM enrichment culture, and selected regions of interest (ROI) of consortia outlines (in red) shown in the lower panel. These ROIs illustrate the method used for estimating consortia numbers as an input for the growth model shown in Fig. 3b.

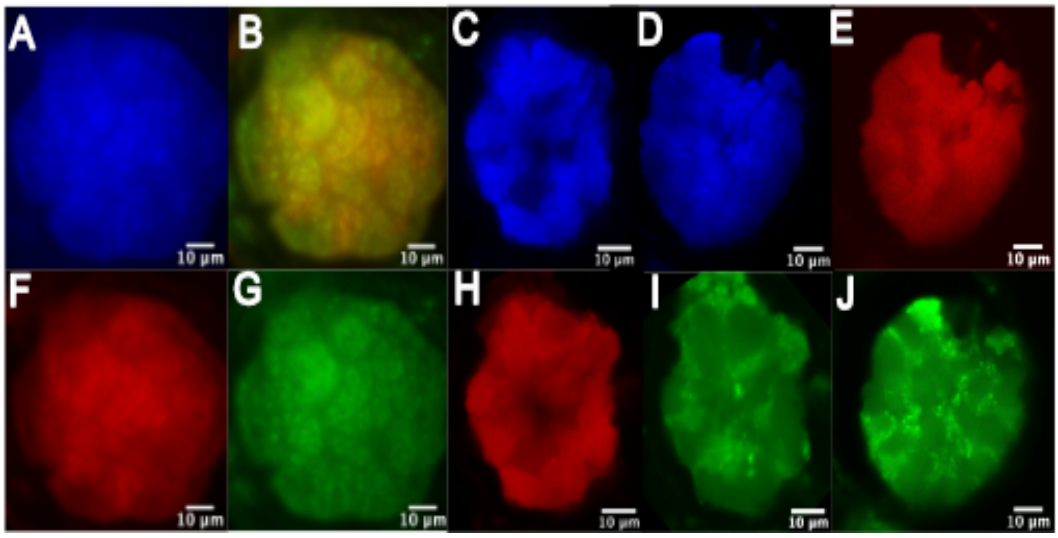

Supp. Fig. 5: Individual epifluorescence microscopy pictures of the ANME-2/SRB consortium in seep carbonate from Fig. 5, stained with A, C, D) DAPI for DNA, E, F, H) ANME-2 (ANME-2-712; Knittel et al., 2005) specific FISH probe, G, I, J) SRB (DSS658; Boetius et al., 2000) specific probe, and B) Both ANME-2 and SRB specific probes (enlargement of large consortia in Fig. 5a). A, B, F, and G correspond to the consortia in Fig 5a; C, H, and I correspond to the consortia in Fig. 5d; and D, E and J correspond to the consortia in Fig. 5g.

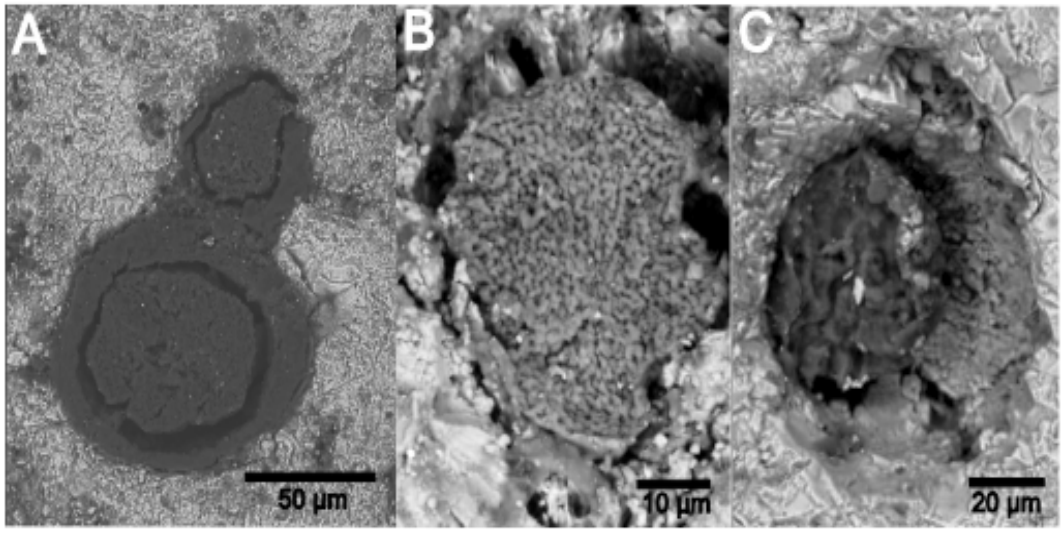

Supp. Fig. 6: Scanning electron microscopy (SEM) pictures of the ANME-2/SRB consortia shown in Fig.5. A) Consortia from Fig.5a, B) Consortia from Fig.5d, and C) Consortia from Fig.5g.

References

Aloisi, G., Bouloubassi, I., Heijs, S. K., Pancost, R. D., Pierre, C., Sinninghe Damsté, J. S., Gottschal, J. C., Forney, L. J., & Rouchy, J.-M. (2002). CH4-consuming microorganisms and the formation of carbonate crusts at cold seeps. *Earth and Planetary Science Letters*, *203*(1), 195–203. https://doi.org/10.1016/S0012-821X(02)00878-6

Annenkov, V. V., Danilovtseva, E. N., Pal'shin, V. A., Ol'ga, N. V., Zelinskiy, S. N., & Krishnan, U. M. (2017). Silicic acid condensation under the influence of water-soluble polymers: From biology to new materials. *Rsc Advances*, *7*(34), 20995–21027.

Bailey, J. V., Raub, T. D., Meckler, A. N., Harrison, B. K., Raub, T. M., Green, A. M., & Orphan, V. J. (2010). Pseudofossils in relict methane seep carbonates resemble endemic microbial consortia. *Palaeogeography, Palaeoclimatology, Palaeoecology*, *285*(1-2), 131–142. https://doi.org/10.1016/J.PALAEO.2009.11.002

Barghoorn, E. S., & Tyler, S. A. (1965). Microorganisms from the Gunflint Chert. *Science*, *147*(3658), 563–575. https://doi.org/10.1126/science.147.3658.563

Benning, L. G., Phoenix, V. R., Yee, N., & Konhauser, K. O. (2004). The dynamics of cyanobacterial silicification: an infrared micro-spectroscopic investigation. *Geochimica et Cosmochimica Acta*, *68*(4), 743–757.

Berelson, W. M., Prokopenko, M., Sansone, F. J., Graham, A. W., McManus, J., & Bernhard, J. M. (2005). Anaerobic diagenesis of silica and carbon in continental margin sediments: Discrete zones of TCO2 production. *Geochimica et Cosmochimica Acta*, *69*(19), 4611–4629. https://doi.org/10.1016/j.gca.2005.05.011

Boetius, A., Ravenschlag, K., Schubert, C. J., Rickert, D., Widdel, F., Gieseke, A., Amann, R., Jørgensen, B. B., Witte, U., & Pfannkuche, O. (2000). A marine microbial consortium apparently mediating anaerobic oxidation of methane. *Nature*, *407*, 623.

Callow, R. H. T., & Brasier, M. D. (2009). Remarkable preservation of microbial mats in Neoproterozoic siliciclastic settings: Implications for Ediacaran taphonomic models. *Earth-Science Reviews*, *96*(3), 207–219. https://doi.org/10.1016/j.earscirev.2009.07.002

Chadwick, G. L., Skennerton, C. T., Laso-Pérez, R., Leu, A. O., Speth, D. R., Yu, H., Morgan-Lang, C., Hatzenpichler, R., Goudeau, D., & Malmstrom, R. (2022). Comparative genomics reveals electron transfer and syntrophic mechanisms differentiating methanotrophic and methanogenic archaea. *PLoS biology*, *20*(1), e3001508.

Channing, A., & Edwards, D. (2003). Experimental taphonomy: silicification of plants in Yellowstone hot-spring environments. *Earth and Environmental Science Transactions of the Royal Society of Edinburgh*, *94*(4), 503–521.

Chen, Y., Li, Y. L., Zhou, G. T., Li, H., Lin, Y. T., Xiao, X., & Wang, F. P. (2014). Biomineralization mediated by anaerobic methane-consuming cell consortia. *Scientific Reports*, *4*, 1–9. https://doi.org/10.1038/srep05696

Cline, J. D. (1969). Spectrophotometric Determination of Hydrogen Sulfide in Natural Waters. *Limnology and Oceanography*, *14*(3), 454–458. https://doi.org/10.4319/lo.1969.14.3.0454

Dekas, A. E. (2013). *Diazotrophy in the deep: an analysis of the distribution, magnitude, geochemical controls, and biological mediators of deep-sea benthic nitrogen fixation* (Doctoral dissertation). California Institute of Technology.

Dekas, A. E., Poretsky, R. S., & Orphan, V. J. (2009). Deep-sea archaea fix and share nitrogen in methane-consuming microbial consortia. *Science*, *326*(5951), 422–426.

Della Rosa, G., Di Corato, R., Carpi, S., Polini, B., Taurino, A., Tedeschi, L., Nieri, P., Rinaldi, R., & Aloisi, A. (2020). Tailoring of silica-based nanoporous pod by spermidine multi-activity. *Scientific Reports*, *10*(1), 21142. https://doi.org/10.1038/s41598-020-77957-4

Franks, A. E., Nevin, K. P., Jia, H., Izallalen, M., Woodard, T. L., & Lovley, D. R. (2009). Novel strategy for three-dimensional real-time imaging of microbial fuel cell communities: Monitoring the inhibitory effects of proton accumulation within the anode biofilm. *Energy and Environmental Science*, *2*(1), 113–119. https://doi.org/10.1039/b816445b

Furukawa, Y., & O'Reilly, S. E. (2007). Rapid precipitation of amorphous silica in experimental systems with nontronite (NAu-1) and Shewanella oneidensis MR-1. *Geochimica et Cosmochimica Acta*, *71*(2), 363–377. https://doi.org/10.1016/j.gca.2006.09.006

Girguis, P. R., Cozen, A. E., & DeLong, E. F. (2005). Growth and population dynamics of anaerobic methane-oxidizing archaea and sulfate-reducing bacteria in a continuous-flow bioreactor. *Applied and Environmental Microbiology*, *71*(7), 3725–3733. https://doi.org/10.1128/aem.71.7.3725-3733.2005

Gunnarsson, I., & Arnórsson, S. (2000). Amorphous silica solubility and the thermodynamic properties of H4SiO4 in the range of 0 to 350C at Psat. *Geochimica et Cosmochimica Acta*, *64*(13), 2295–2307. https://doi.org/10.1016/S0016-7037(99)00426-3

Hein, J. R., Dowling, J. S., Schuetze, A., & Lee, H. J. (2003). Clay-mineral suites, sources, and inferred dispersal routes: Southern California continental shelf. *Marine Environmental Research*, *56*(1-2), 79–102. https://doi.org/10.1016/S0141-1136(02)00326-4

Hikida, Y., Suzuki, S., Togo, Y., & Ijiri, A. (2003). An exceptionally well-preserved fossil seep community from the Cretaceous Yezo Group in the Nakagawa area, Hokkaido, northern Japan. *Paleontological Research*, *7*(4), 329–342. https://doi.org/10.2517/prpsj.7.329

Himmler, T., Freiwald, A., Stollhofen, H., & Peckmann, J. (2008). Late Carboniferous hydrocarbon-seep carbonates from the glaciomarine Dwyka Group, southern Namibia. *Palaeogeography, Palaeoclimatology, Palaeoecology*, *257*(1-2), 185–197. https://doi.org/10.1016/j.palaeo.2007.09.018

Hugo, R. C., Cady, S. L., & Smythe, W. (2011). The Role of Extracellular Polymeric Substances in the Silicification of Calothrix: Evidence from Microbial Mat Communities in Hot Springs at Yellowstone National Park, USA. *Geomicrobiology Journal*, *28*(8), 667–675. https://doi.org/10.1080/01490451.2010.511983

Iler, R. K. (1979). *The Chemistry of Silica: Solubility, Polymerization, Colloid and Surface Properties, and Biochemistry*. Wiley-Interscience.

Kaim, A., Jenkins, R. G., & Waren, A. (2008). Provannid and provannid-like gastropods from the Late Cretaceous cold seeps of Hokkaido (Japan) and the fossil record of the Provannidae (Gastropoda: Abyssochrysoidea). *Zoological Journal of the Linnean Society*, *154*(3), 421–436. https://doi.org/10.1111/j.1096-3642.2008.00431.x

Knittel, K., Lösekann, T., Boetius, A., Kort, R., & Amann, R. (2005). Diversity and Distribution of Methanotrophic Archaea at Cold Seeps. *Applied and Environmental Microbiology*, *71*(1), 467–479. https://doi.org/10.1128/AEM.71.1.467-479.2005

Konhauser, K. O., Fyfe, W. S., Ferris, F. G., & Beveridge, T. J. (1993). Metal sorption and mineral precipitation by bacteria in two Amazonian river systems: Rio Solimoes and Rio Negro, Brazil. *Geology*, *21*, 1103–1106.

Konhauser, K. O., Schultze-Lam, S., Ferris, F. G., Fyfe, W. S., Longstaffe, F. J., & Beveridge, T. J. (1994). Mineral precipitation by epilithic biofilms in the speed river, ontario, Canada. *Appl Environ Microbiol*, *60*(2), 549–553.

Konhauser, K. O., Jones, B., Phoenix, V. R., Ferris, G., & Renaut, R. W. (2004). The microbial role in hot spring silicification. *AMBIO: A Journal of the Human Environment*, *33*(8), 552–558.

Konhauser, K. O., & Urrutia, M. M. (1999). Bacterial clay authigenesis: a common biogeochemical process. *Chemical Geology*, *161*(4), 399–413. https://doi.org/10.1016/S0009-2541(99)00118-7

Kröger, N., Deutzmann, R., Bergsdorf, C., & Sumper, M. (2000). Species-specific polyamines from diatoms control silica morphology. *Proceedings of the National Academy of Sciences*, *97*(26), 14133–14138. https://doi.org/10.1073/pnas.260496497

Kuechler, R. R., Birgel, D., Kiel, S., Freiwald, A., Goedert, J. L., Thiel, V., & Peckmann, J. (2012). Miocene methane-derived carbonates from southwestern Washington, USA and a model for silicification at seeps. *Lethaia*, *45*(2), 259–273. https://doi.org/10.1111/j.1502-3931.2011.00280.x

Lalonde, S. V., Konhauser, K. O., Reysenbach, A.-L., & Ferris, F. G. (2005). The experimental silicification of Aquificales and their role in hot spring sinter formation. *Geobiology*, *3*(1), 41–52. https://doi.org/10.1111/j.1472-4669.2005.00042.x

Lechner, C. C., & Becker, C. F. W. (2015). Silaffins in Silica Biomineralization and Biomimetic Silica Precipitation. https://doi.org/10.3390/md13085297

Loyd, S. J., Sample, J., Tripati, R. E., Defliese, W. F., Brooks, K., Hovland, M., Torres, M., Marlow, J., Hancock, L. G., Martin, R., Lyons, T., & Tripati, A. E. (2016). Methane seep carbonates yield clumped isotope signatures out of equilibrium with formation temperatures. *Nature Communications*, *7*, 1–12. https://doi.org/10.1038/ncomms12274

Luff, R., & Wallmann, K. (2003). Fluid flow, methane fluxes, carbonate precipitation and biogeochemical turnover in gas hydrate-bearing sediments at Hydrate Ridge, Cascadia Margin: numerical modeling and mass balances. *Geochimica et Cosmochimica Acta*, *67*(18), 3403–3421. https://doi.org/10.1016/S0016-7037(03)00127-3

Lyle, M., Koizumi, I., Delaney, M. L., & Barron, J. A. (2000). 32. SEDIMENTARY RECORD OF THE CALIFORNIA CURRENT SYSTEM, MIDDLE MIOCENE TO HOLOCENE: A SYNTHESIS OF LEG 167 RESULTS. In M. Lyle, I. Koizumi, C. Richter, & T. C. Moore (Eds.), *Proceedings of the ocean drilling program, scientific results, 167* (pp. 341–376).

Marlow, J. J., Hoer, D., Jungbluth, S. P., Reynard, L. M., Gartman, A., Chavez, M. S., El-Naggar, M. Y., Tuross, N., Orphan, V. J., & Girguis, P. R. (2021). Carbonate-hosted microbial communities are prolific and pervasive methane oxidizers at geologically diverse marine methane seep sites. *Proceedings of the National Academy of Sciences*, *118*(25), e2006857118.

Marlow, J. J., Steele, J. A., Ziebis, W., Thurber, A. R., Levin, L. A., Orphan, V. J., Ziebis, W., Marlow, J. J., Orphan, V. J., & Steele, J. A. (2014). Carbonate-hosted methanotrophy represents an unrecognized methane sink in the deep sea. *Nature Communications*, *5*(1), 1–12. https://doi.org/10.1038/ncomms6094

Martin-Jézéquel, V., Hildebrand, M., & Brzezinski, M. A. (2000). SILICON METABOLISM IN DIATOMS: IMPLICATIONS FOR GROWTH. *Journal of Phycology*, *36*(5), 821–840. https://doi.org/10.1046/j.1529-8817.2000.00019.x

Mason, O. U., Case, D. H., Naehr, T. H., Lee, R. W., Thomas, R. B., Bailey, J. V., & Orphan, V. J. (2015). Comparison of Archaeal and Bacterial Diversity in Methane Seep Carbonate Nodules and Host Sediments, Eel River Basin and

Hydrate Ridge, USA. *Microbial Ecology*, *70*(3), 766–784. https://doi.org/10.1007/s00248-015-0615-6

McGlynn, S. E. (2017). Energy metabolism during anaerobic methane oxidation in ANME archaea. *Microbes and environments*, *32*(1), 5–13.

McGlynn, S. E., Chadwick, G. L., O'Neill, A., Mackey, M., Thor, A., Deerinck, T. J., Ellisman, M. H., & Orphan, V. J. (2018). Subgroup Characteristics of Marine Methane-Oxidizing ANME-2 Archaea and Their Syntrophic Partners as Revealed by Integrated Multimodal Analytical Microscopy. *Applied and Environmental Microbiology*, *84*(11), e00399–18. https://doi.org/10.1128/AEM.00399-18

Metcalfe, K. S. (2021). *Symbiotic Diversity and Mineral-Associated Microbial Ecology in Marine Microbiomes* (Doctoral dissertation). California Institute of Technology.

Meulepas, R. J. W., Jagersma, C. G., Gieteling, J., Buisman, C. J. N., Stams, A. J. M., & Lens, P. N. L. (2009). Enrichment of anaerobic methanotrophs in sulfate-reducing membrane bioreactors. *Biotechnology and Bioengineering*, *104*(3), 458–470. https://doi.org/10.1002/bit.22412

Michalopoulos, P., & Aller, R. C. (2004). Early diagenesis of biogenic silica in the Amazon delta: alteration, authigenic clay formation, and storage. *Geochimica et Cosmochimica Acta*, *68*(5), 1061–1085. https://doi.org/10.1016/j.gca.2003.07.018

Miyajima, Y., Watanabe, Y., Yanagisawa, Y., Amano, K., Hasegawa, T., & Shimobayashi, N. (2016). A late Miocene methane-seep deposit bearing methane-trapping silica minerals at Joetsu, central Japan. *Palaeogeography, Palaeoclimatology, Palaeoecology*, *455*, 1–15.

Moore, D. M., & Reynolds, R. C. (1989). *X-Ray Diffraction and the Identification and Analysis of Clay Minerals*. Oxford University Press (OUP).

Moore, K. R., Gong, J., Pajusalu, M., Skoog, E. J., Xu, M., Feliz Soto, T., Sojo, V., Matreux, T., Baldes, M. J., Braun, D., Williford, K., & Bosak, T. (2021). A new model for silicification of cyanobacteria in Proterozoic tidal flats. *Geobiology*, *19*(5), 438–449. https://doi.org/10.1111/gbi.12447

Moore, K. R., Pajusalu, M., Gong, J., Sojo, V., Matreux, T., Braun, D., & Bosak, T. (2020). Biologically mediated silicification of marine cyanobacteria and implications for the Proterozoic fossil record. *Geology*, *48*(9), 862–866. https://doi.org/10.1130/G47394.1

Motomura, K., Ikeda, T., Matsuyama, S., Abdelhamid, M. A. A., Tanaka, T., Ishida, T., Hirota, R., & Kuroda, A. (2016). The C-Terminal Zwitterionic Sequence of CotB1 Is Essential for Biosilicification of the Bacillus cereus Spore Coat. *Journal of Bacteriology*, *198*(2), 276–282. https://doi.org/10.1128/jb.00447-15

Naehr, T. H., Eichhubl, P., Orphan, V. J., Hovland, M., Paull, C. K., Ussler, W., Lorenson, T. D., & Greene, H. G. (2007). Authigenic carbonate formation at hydrocarbon seeps in continental margin sediments : A comparative study. *Deep Sea Research Part II: Topical Studies in Oceanography*, *54*, 1268–1291. https://doi.org/10.1016/j.dsr2.2007.04.010

Nauhaus, K., Albrecht, M., Elvert, M., Boetius, A., & Widdel, F. (2007). In vitro cell growth of marine archaeal-bacterial consortia during anaerobic oxidation of methane with sulfate. *Environmental Microbiology*, *9*(1), 187–196.

Newman, S. A., Mariotti, G., Pruss, S., & Bosak, T. (2016). Insights into cyanobacterial fossilization in Ediacaran siliciclastic environments. *Geology*, *44*(7), 579–582. https://doi.org/10.1130/G37791.1

Nishino, M., Matsuzaki, I., Musangile, F. Y., Takahashi, Y., Iwahashi, Y., Warigaya, K., Kinoshita, Y., Kojima, F., & Murata, S.-i. (2020). Measurement and visualization of cell membrane surface charge in fixed cultured cells related with cell morphology. *PLoS One*, *15*(7), e0236373.

O'Reilly, S. E., Watkins, J., & Furukawa, Y. (2005). Secondary mineral formation associated with respiration of nontronite, NAu-1 by iron reducing bacteria. *Geochemical Transactions*, *6*(4), 1–10. https://doi.org/10.1186/1467-4866-6-67

Orphan, V. J., Hinrichs, K.-U., Ussler, W., Paull, C. K., Taylor, L. T., Sylva, S. P., Hayes, J. M., & DeLong, E. F. (2001). Comparative analysis of methane-oxidizing archaea and sulfate-reducing bacteria in anoxic marine sediments. *Applied and Environmental Microbiology*, *67*(4), 1922–1934.

Orphan, V. J., House, C. H., Hinrichs, K.-U., McKeegan, K. D., & DeLong, E. F. (2001). Methane-Consuming Archaea Revealed by Directly Coupled Isotopic and Phylogenetic Analysis. *Science*, *293*(5529), 484–487. https://doi.org/10.1126/science.1061338

Orphan, V. J., House, C. H., Hinrichs, K.-U., McKeegan, K. D., & DeLong, E. F. (2002). Multiple archaeal groups mediate methane oxidation in anoxic cold seep sediments. *Proceedings of the National Academy of Sciences*, *99*(11), 7663–7668. https://doi.org/10.1073/pnas.072210299

Orphan, V. J., Turk, K. A., Green, A. M., & House, C. H. (2009). Patterns of 15N assimilation and growth of methanotrophic ANME-2 archaea and sulfate-reducing bacteria within structured syntrophic consortia revealed by FISH-SIMS. *Environmental Microbiology*, *11*(7), 1777–1791. https://doi.org/10.1111/j.1462-2920.2009.01903.x

Patwardhan, S. V., Tilburey, G. E., & Perry, C. C. (2011). Interactions of Amines with Silicon Species in Undersaturated Solutions Leads to Dissolution and/or Precipitation of Silica. *Langmuir*, *27*(24), 15135–15145. https://doi.org/10.1021/la204180r

Peckmann, J., Goedert, J. L., Thiel, V., Michaelis, W., & Reitner, J. (2002). A comprehensive approach to the study of methane-seep deposits from the Lincoln Creek Formation, western Washington State, USA. *Sedimentology*, *49*(4), 855–873. https://doi.org/10.1046/j.1365-3091.2002.00474.x

Pernthaler, A., Dekas, A. E., Brown, C. T., Goffredi, S. K., Embaye, T., & Orphan, V. J. (2008). Diverse syntrophic partnerships from deep-sea methane vents revealed by direct cell capture and metagenomics. *Proceedings of the National Academy of Sciences*, *105*(19), 7052–7057. https://doi.org/10.1073/pnas.0711303105

Pernthaler, J., Glöckner, F.-O., Schönhuber, W., & Amann, R. (2001). Fluorescence in situ hybridization (FISH) with rRNA-targeted oligonucleotide probes. *Methods in microbiology*, *30*, 207–226.

Phoenix, V. R., Martinez, R. E., Konhauser, K. O., & Ferris, F. G. (2002). Characterization and Implications of the Cell Surface Reactivity of Calothrix sp. Strain KC97. *Applied and Environmental Microbiology*, *68*(10), 4827–4834. https://doi.org/10.1128/aem.68.10.4827-4834.2002

Phoenix, V. R., Konhauser, K. O., & Ferris, F. G. (2003). Experimental study of iron and silica immobilization by bacteria in mixed Fe-Si systems: implications for microbial silicification in hot springs. *Canadian Journal of Earth Sciences*, *40*(11), 1669–1678. https://doi.org/10.1139/e03-044

Renaut, R. W., Jones, B., & Tiercelin, J. J. (1998). Rapid in situ silicification of microbes at Loburu hot springs, Lake Bogoria, Kenya rift valley. *Sedimentology*, *45*(6), 1083–1103. https://doi.org/10.1046/j.1365-3091.1998.00194.x

Sallstedt, T., Ivarsson, M., Drake, H., & Skogby, H. (2019). Instant attraction: Clay authigenesis in fossil fungal biofilms. *Geosciences (Switzerland)*, *9*(9), 32–39. https://doi.org/10.3390/geosciences9090369

Saw, J. H., Mountain, B. W., Feng, L., Omelchenko, M. V., Hou, S., Saito, J. A., Stott, M. B., Li, D., Zhao, G., & Wu, J. (2008). Encapsulated in silica: genome, proteome and physiology of the thermophilic bacterium Anoxybacillus flavithermus WK1. *Genome biology*, *9*(11), 1–16.

Scheffel, A., Poulsen, N., Shian, S., & Kröger, N. (2011). Nanopatterned protein microrings from a diatom that direct silica morphogenesis. *Proceedings of the National Academy of Sciences*, *108*(8), 3175–3180. https://doi.org/10.1073/pnas.1012842108

Schindelin, J., Arganda-Carreras, I., Frise, E., Kaynig, V., Longair, M., Pietzsch, T., Preibisch, S., Rueden, C., Saalfeld, S., Schmid, B., Tinevez, J.-Y., White, D. J., Hartenstein, V., Eliceiri, K., Tomancak, P., & Cardona, A. (2012). Fiji: an open-source platform for biological-image analysis. *Nature Methods*, *9*(7), 676–682. https://doi.org/10.1038/nmeth.2019

Siever, R., & Woodford, N. (1973). Sorption of silica by clay minerals. *Geochimica et Cosmochimica Acta*, *37*(8), 1851–1880. https://doi.org/10.1016/0016-7037(73)90146-4

Skennerton, C. T., Chourey, K., Iyer, R., Hettich, R. L., Tyson, G. W., & Orphan, V. J. (2017). Methane-Fueled Syntrophy through Extracellular Electron Transfer: Uncovering the Genomic Traits Conserved within Diverse Bacterial Partners of Anaerobic Methanotrophic Archaea. *mBio*, *8*(4), e00530–17. https://doi.org/10.1128/mBio.00530-17

Smrzka, D., Kraemer, S. M., Zwicker, J., Birgel, D., Fischer, D., Kasten, S., Goedert, J. L., & Peckmann, J. (2015). Constraining silica diagenesis in methane-seep deposits. *Palaeogeography, Palaeoclimatology, Palaeoecology*, *420*, 13–26. https://doi.org/10.1016/j.palaeo.2014.12.007

Söding, E., & Wallmann, K. (2003). *RV Meteor Cruise Report M54/2+3: Fluids and Subduction Costa Rica 2002 ; M54/2 Caldera - Caldera, August 13 - September 7,2002, M54/3A Caldera - Caldera, September 10 - September 28, 2002, M 54/3B Caldera - Curaçao, October 1 - October 11,2002 ; Investigations in the Frame of SFB574 "Volatiles and Fluids in Subduction Zones: Climate Feedback and Tigger Mechanisms for Natural Disasters" ; Contribution Nr. 30 of SFB574*. GEOMAR.

Stahl, D. A., & Amann, R. (1991). Development and Application of Nucleic Acid Probes in Bacterial Systematics. In E. Stackebrandt & M. Goodfellow (Eds.), *Nucleic acid techniques in bacterial systematics* (pp. 205–248). John Wiley & Sons Ltd.

Teichert, B. M. A., Bohrmann, G., & Suess, E. (2005). Chemoherms on Hydrate Ridge—Unique microbially-mediated carbonate build-ups growing into the water column. *Palaeogeography, Palaeoclimatology, Palaeoecology*, *227*(1-3), 67–85.

Thiagarajan, N., Crémière, A., Blättler, C., Lepland, A., Kirsimäe, K., Higgins, J., Brunstad, H., & Eiler, J. (2020). Stable and clumped isotope characterization of authigenic carbonates in methane cold seep environments. *Geochimica et Cosmochimica Acta*, *279*, 204–219.

Treude, T., Knittel, K., Blumenberg, M., Seifert, R., & Boetius, A. (2005). Subsurface Microbial Methanotrophic Mats in the Black Sea. *Applied and Environmental Microbiology*, *71*(10), 6375–6378. https://doi.org/10.1128/aem.71.10.6375-6378.2005

Walter, M. R., Desmarais, D., Farmer, J. D., & Hinman, N. W. (1996). Lithofacies and biofacies of mid-Paleozoic thermal spring deposits in the Drummond Basin, Queensland, Australia. *Palaios*, 497–518.

Wenzl, S., Hett, R., Richthammer, P., & Sumper, M. (2008). Silacidins: Highly Acidic Phosphopeptides from Diatom Shells Assist in Silica Precipitation In

Vitro. *Angewandte Chemie International Edition*, *47*(9), 1729–1732. https://doi.org/10.1002/anie.200704994

Yee, N., Phoenix, V. R., Konhauser, K. O., Benning, L. G., & Ferris, F. G. (2003). The effect of cyanobacteria on silica precipitation at neutral pH: implications for bacterial silicification in geothermal hot springs. *Chemical Geology*, *199*(1), 83–90. https://doi.org/10.1016/S0009-2541(03)00120-7

Yu, H., Speth, D. R., Connon, S. A., Goudeau, D., Malmstrom, R. R., Woyke, T., & Orphan, V. J. (2022). Community Structure and Microbial Associations in Sediment-Free Methanotrophic Enrichment Cultures from a Marine Methane Seep. *Applied and Environmental Microbiology*, *88*(11), e02109–21. https://doi.org/10.1128/aem.02109-21

Zhang, G., Dong, H., Kim, J., & Eberl, D. D. (2007). Microbial reduction of structural Fe3+ in nontronite by a thermophilic bacterium and its role in promoting the smectite to illite reaction. *American Mineralogist*, *92*(8-9), 1411–1419. https://doi.org/10.2138/am.2007.2498

Chapter 6

ROLE OF EARLY SILICA CEMENTATION FOR MICROBIAL PRESERVATION IN CARBONATES: INSIGHTS FROM ANAEROBIC METHANOTROPHIC ARCHAEA AND SULFATE REDUCING BACTERIA (ANME-SRB) CONSORTIA IN MODERN METHANE-SEEP CARBONATES

Daniela Osorio-Rodriguez[1], Kyle S. Metcalfe[1], Victoria J. Orphan[1], John P. Grotzinger[1]

[1] Division of Geological and Planetary Sciences, California institute of Technology, Pasadena, CA, 91125, USA

Abstract

Anaerobic methane-oxidizing archaea (ANME) and sulfate reducing bacteria (SRB) influence the formation of methane-derived authigenic carbonates in deep ocean hydrocarbon seeps. Both microbial partners associate in syntrophy forming tens-of micrometer consortia named aggregates. Silica biomineralization by ANME-SRB aggregates has been reported recently and has been suggested as a potential mechanism for their preservation as fossils. Here, we used a combination of microscopy and analytical techniques to characterize modern ANME-SRB aggregates in carbonates from an active methane seep (Jaco Scar, Costa Rica). We specifically identified ANME2-SRB aggregates with fluorescence in-situ hybridization and observed silica precipitates associated with them, as well as Raman spectra, $\delta^{13}C$ signatures, and lipid biomarkers that together provide a search image for ANME-SRB aggregates in the rock record. We examined methane seep carbonates of the Tepee Buttes (CO, 75 Mya) and identified potential fossilized ANME-SRB aggregates based on these proxies. We recommend silica biomineralization by ANME-SRB aggregates

together with morphological, compositional, and isotopic criteria as a proxy for the identification of ANME-SRB microbial fossils in Earth and other planetary bodies where hydrocarbon seepage may occur.

1. INTRODUCTION

The anaerobic oxidation of methane (AOM) by anaerobic methanotrophic archaea (ANME) is a common energy yielding metabolism in marine methane seeps (Hinrichs et al., 1999; Wegener et al., 2008), usually coupled to sulfate reduction (SR) by sulfate-reducing bacteria (SRB; Hoehler et al., 1994; Michaelis et al., 2002). AOM-SR is a key component of the carbon cycle today, consuming >90% of the methane produced in the oceans (Hinrichs and Boetius, 2013; Reeburgh, 2007), and supporting communities of chemosynthetic bivalves, gastropods, tubeworms, and bacterial mats (Sibuet and Olu, 1998). The metabolism of AOM-SRB modifies the chemistry of their environment, by means of an increase in alkalinity by two units per mole of bicarbonate and sulfide produced. For this reason, it influences the formation of methane-derived authigenic carbonates (Aloisi et al., 2002; Ritger et al., 1987), and the precipitation of iron sulfides (Jørgensen et al., 2004; Neretin et al., 2004).

ANME and SRB represent more than 90% of the total microbial community in methane seeps (Boetius et al., 2000; Michaelis et al., 2002; Orphan, Hinrichs, et al., 2001) and form consortia that group themselves in spherical structures defined as aggregates (Boetius et al., 2000). Usually, they have a diameter between 3 and 20 μm in sediments (Knittel et al., 2005) and up to ~100 μm in carbonates (Marlow et al., 2021, Osorio-Rodriguez et al., in prep.), and are enclosed by a thick organic matrix (Boetius et al., 2000; Nauhaus et al., 2007) that has been shown to facilitate the nucleation of clay minerals (Y. Chen et al., 2014). These aggregates have been described from modern sediments (Hinrichs et al., 1999; Orphan, House, et al.,

2001, 2002) and carbonate rocks (Himmler et al., 2022; Marlow et al., 2014). Recently, silica biomineralization by ANME-2-SRB from undersaturated solutions in sediment-free incubations was demonstrated and supported by the presence of silica precipitates and rims associated with ANME-2-SRB aggregates in carbonate rocks (Osorio-Rodriguez et al., in prep.). Most of the putative microfossils reported so far have been found in cherts (e.g., Walsh and Lowe, 1985), however, early silica entombment enhances the preservation of organic matter (e.g., Alleon et al., 2016), and as such might be key for the preservation of microbial fossils (e.g., Moore et al., 2021; Moore et al., 2020) in rocks where amorphous silica is not the primary phase. Here, we perform a comparative study of ANME-SRB aggregates in modern and ancient seep carbonates that host a suite of morphological fabrics and chemical signatures. We characterize confirmed ANME-SRB aggregates with specific DNA probes in modern carbonates to provide a solid framework to identify them in seep carbonates where DNA traces have been lost. Utilizing this tool, report fossilized ANME-SRB aggregates in ancient methane seep carbonates whereby silica precipitation might have enhanced structural preservation.

2. MATERIALS AND METHODS

Tepee Buttes geologic setting and sample collection

The Tepee Buttes (Gilbert and Gulliver, 1894) are a series of conical carbonate deposits aligned in a northeast-southwest direction along the eastern front of the Rocky Mountains, from the northern Dark Hills in South Dakota to the Texas-Mexico border (Metz, 2000). The cones are up to 60 m wide and 10 m tall (Kauffman et al., 1996), and occur within the Upper portion of the Pierre Shale Formation (Campanian-Lower Maastrichtian; 75 Mya), which accumulated in the Western Interior Seaway, a foreland basin formed during the Laramide Orogeny (Howe and Kauffman, 1986). The Tepee Buttes have been interpreted as methane

seep deposits with vent cores associated with east-dipping normal faults. From core to vent, the following lithofacies have been described: spring core, Nymphalucina (bivalve) coquina, pelletoid micrite, flank breccias in shale, and concretionary Pierre Shale with stromatolites (Howe, 1987).

Our study suite includes samples from Tepee Buttes, which were collected slightly east of Boone, Colorado, in June 2019, where they comprise all of the seep carbonate facies that have been previously identified, as well as samples from the Panoche Hills (CA; ~62 Mya; Schwartz et al., 2003), and Bear Creek (CA; ~140 Mya; Campbell et al., 1993). Representative samples were shipped to Spectrum Petrographics (Vancouver, WA, USA) for thin sections. Attenuated total reflectance – Fourier transform infrared spectroscopy (ATR-FTIR) was used to determine the mineral composition.

Sample collection and preparation of thin sections

Samples of modern seep carbonates were collected using the submersible HOV Alvin and the *R/V Atlantis* at Jaco Scar (AT42-03, October-November 2018), a "hydrothermal seep" Levin et al., 2012 first described by Bohrmann et al., 2002, located at a convergent plate margin to the south of Costa Rica (~1800 m depth). Carbonates were placed in Pyrex bottles together with filter-sterile N_2-sparged seawater. All incubations were supplied with a CH_4 headspace pressurized to ~2 atm. These anoxic incubations were maintained in the dark for 1 year at 10 °C with partial exchange of spent media with the addition of 0.2 μm filter-sterilized Ar-sparged seawater and CH_4 every 3 months. All samples were kept at ambient bottom water temperatures (6 °C) during recovery. A fragment of this carbonate was fixed in 1% paraformaldehyde, embedded in Epoxicure 2 (Buehler Ltd., Lake Bluff, IL), glued to a 1-inch round glass, sectioned by rock saw, and polished with alumina polishing film of grits 60, 30, 12, 5 and 2 μm to get a rock section of about 50 μm thickness.

Tepee Buttes samples were collected slightly east of Boone, Colorado, on June 2019, where they comprise all of the facies that have been previously identified. Representative samples were shipped to Spectrum Petrographics (Vancouver, WA, USA) for thin sections. Attenuated total reflectance – Fourier transform infrared spectroscopy (ATR-FTIR) was used to determine the mineral composition.

Extraction of aggregates from Jaco Scar carbonate

A piece of rock previously fixed in 1% paraformaldehyde was placed in a plastic vial with acetic acid buffer (1.9 M sodium acetate), pH 4.2. After overnight dissolution, the sample was centrifuged for 3 min at max speed. The supernatant was removed, and 2 washes with 3X and 1X PBS (phosphate-buffered saline) buffer were performed. Finally, the sample was resuspended in a 1:1 mixture of 1XPBS:ethanol and sonicated 3 times (10 seconds). In order to separate ANME-SRB aggregates from sample debris, 700 μl of a 70% Nycodenz solution in 1X PBS were added to the sample, followed by centrifugation at 4 °C for 20 minutes. The upper layer was transferred to a 3μm polycarbonate filter in a vacuum tower, followed by several washes with 1X PBS. The filter was placed upside down against an aluminum wafer to transfer the extracted aggregates.

Identification of ANME2-SRB aggregates and elemental characterization

Fluorescence in-situ hybridization (FISH) was used to specifically identify ANME2-SRB aggregates in the carbonate thin sections from Jaco Scar and extracted from them. We focused on the identification of ANME-2 as opposed to ANME in general given that, from the three described groups of ANME (ANME-1, ANME-2, and ANME-3), ANME-2 is the one that has been found to associate with SRB forming aggregates (Boetius et al., 2000; Orphan, House, et al., 2001). A dehydration series (50%, 75%, 100% ethanol, 1 min each) was first applied, followed by hybridiza-

tion with probes targeting ANME-2 (ANME-2-712; Knittel et al., 2005) and SRB (DSS658; Boetius et al., 2000) in 40% formamide hybridization buffer, as previously described (Pernthaler et al., 2001). 5 μg/ml of a 46-diamidino-2-phenylindole (DAPI)-Citifluor mounting medium was added prior to epifluorescence microscopy. Epifluorescence pictures were taken with a fluorescence microscope (Elyra S.1, Zeiss) at 10x (EC Plan-Neofluar 10x/0.30 M27 objective) and 63x magnification (Plan-Apochromat 63x/1.4 Oil DIC M27 objective), or with a confocal microscope (LSM 880, Zeiss) at 63x magnification (Plan-Apochromat 63x/1.4 Oil DIC objective). Images were acquired using the Zen black software (Zeiss) and the image compositing was performed using the software Fiji (Schindelin et al., 2012).

Aggregates identified with FISH in the modern carbonates and purported aggregates in ancient carbonates were observed under plain-light petrographic microscopes for the characterization of mineralogy and textures. Scanning electron microscopy (SEM) pictures and electron diffraction X-ray spectroscopy (EDS) elemental spectra were collected using a Zeiss 1550 VP with an angle selective Backscattered detector (AsB) with variable pressure and an electron beam of 15 eV.

Raman spectroscopy

Raman spectroscopic data were obtained with a Renishaw inVia Raman microprobe equipped with a Leica DM 2500 M microscope at the Caltech Mineral Spectroscopy Laboratory. Before each measurement session, the system was calibrated to maximize scattering from a silica calibration standard. The Raman scattering from the targets was generated with a 1800 lines mm^{-1} grating, and a 532 nm diode-pumped solid-state (DPSS) laser (Renishaw RL532C50) as the excitation source with a 23.5 mW output power. The spectra were collected with 50 accumulations of 2 s each and 5% laser power, covering a range of ~500 to 2000 cm^{-1}.

Carbon Isotope Analyses

Secondary Ion Mass Spectrometry: SIMS measurements on FISH-confirmed ANME-2-SRB aggregates in situ in the Jaco scar carbonate, and purported ANME-SRB aggregates in the ancient seep carbonates, were performed using a SIMS Cameca IMS 7f-GEO at the Caltech Microanalysis Center using the working standard for organic carbon UWLA-1 (LCNN Anthracite from the Pennsylvania State University collection; Williford et al., 2016). The $\delta^{13}C$ of the standard was measured in triplicates at the beginning and the end of the day on each analytical session to calibrate the instrumental mass fractionation (IMF). All mounts were cleaned with ethanol and gold-coated before analyses. SIMS data were collected in two analytical sessions (Session-1, 11/12/2020 to 11/14/2020; and Session-2, 5/21/2021 to 5/23/2021). The SIMS acquisitions were performed using a 10 keV $^{133}Cs^{+}$ primary ion beam, with a $10\mu m$ spot size and a primary beam current of 0.4-0.4 nA, with a pre-sputtering time of 120s at 3 nA. Secondary ions of -9 keV were collected in peak jumping mode. In order to guarantee that the carbon measured was mostly coming from the organic matter and not from the carbonate matrix, $^{12}C^{-}$ and $^{13}C^{-}$ were measured with an electron multiplier (EM) with the mass resolving power set at 3000, enough to resolve the interference of $^{12}CH^{-}$ to $^{13}C^{-}$. The secondary energy bandwidth was 45 eV. Collecting times were 1 sec for ^{12}C, 10 sec for ^{13}C, and the total analysis time for each spot (including pre-sputtering, beam centering, mass calibration, and data collection) was about 35 minutes. Data were corrected for the deadtime of the EM. Only C-rich values ($> 10^5$ counts) were accepted. The analytical repeatability of ^{13}C counts was between and 0.8 and 1.1 ‰, including the errors from repeated measurements of standards and the internal counting statistic errors or each spot.

NanoSIMS: NanoSIMS measurements on FISH-confirmed ANME-2-SRB aggregates extracted from the Jaco scar carbonate were made with a Cameca NanoSIMS 50L at the Caltech Microanalysis Center using an in-house working standard (*Clostridia* spores) to determine the instrumental mass fractionation (IMF). A +8 kV Cs^+ primary beam was used to sputter the sample surface to generate secondary ions. Areas of interest were first identified with the secondary electron image (SEI) generated by a tiny (1-3 pA) Cs^+ beam rastering over large sample surface areas. Then, a large Cs^+ beam (about 300 pA) was used to pre-sputter the areas of interest for a few minutes to obtain a steady C^- signal. After the pre-sputtering, a 3pA beam, rastering over an area of 5x5 μm, was used for data collection. To avoid a possible edge effect, an electronic gate was applied so that only the secondary ions from the center 3.8 x3.8 μm were collected. The primary Cs^+ beam was running in the scanning mode of 64 x 64 pixels over the 5x5 μm area, with a dwelling time of 244 microseconds per pixel for a total 1 sec per scanning frame. Secondary $^{12}C^-$ and $^{13}C^-$ ions of -8 kV were simultaneously measured with two electron multipliers (EM) for 500 frames, with a total collection time of about 9 minutes. The setup of the mass spectrometer ensured that the $^{13}C^-$ is fully resolved from the interference peak of ^{12}CH. The centering of the secondary ion signals (E0S and SIBC) and mass peak calibration (HMR) were performed automatically during each measurement. The carbon isotopic results of the samples were processed with EM deadtime and IMF corrections.

Carbon isotope ratios are reported here using the conventional delta notation:

$$\delta^{13}C = {}^{13}R_{sample}/{}^{13}R_{VPDB} - 1 \cdot 1000, \tag{6.1}$$

where $^{13}R_{sample}$ and $^{13}R_{VPDB}$ are the $^{13}C/^{12}C$ ratios of sample and Vienna Peedee Belemnite (VPDB; reference material), respectively.

Data and code availability

All data and custom scripts were collected and stored using Git version control. Code for raw data processing, analysis, and figure generation is available in the GitHub repository (https://github.com/daniosro/Si_biomineralization_ANME_SRB).

3. RESULTS

The carbonates from modern (Jaco Scar, Costa Rica) and ancient (Tepee Buttes, Colorado) methane seeps analyzed here are mostly comprised of micrite, sometimes with a peloidal fabric, and spar cement (Fig. 1a, 1b). In the micritic phases of the modern seep carbonate, we identified 50-100 μm spheres with thick coatings, which resemble in shape and size ANME-SRB aggregates isolated from sediments (Boetius et al., 2000; Marlow et al., 2014; Fig. 1c, 1d).

We performed fluorescence *in situ* hybridization on the Jaco Scar carbonate sample, utilizing probes specific for ANME-2 and SRB. This allowed us to confirm the identity of the round shapes we observed in the petrographic microscope as ANME-2-SRB aggregates (Fig. 2). We further examined the round shapes under the scanning electron microscope (SEM) and energy dispersive X-ray spectroscopy (EDS) to find evidence of silica rims or attached silica/silicates (Fig. 3 and Supp. Fig. 1), as previous observations of ANME-SRB aggregates in sediments have found that they can attach clay minerals (Y. Chen et al., 2014) and precipitate silica (Supp. Fig. 2; Metcalfe, 2021, Osorio-Rodriguez et al. in prep).

We extracted aggregates from the Jaco scar carbonate by dissolving the rock, and we performed FISH, SEM, and EDS in a similar workflow as that performed for the aggregates in situ in the carbonate, in order to confirm their identity as ANME-2-SRB consortia, and identify associations with silica (Fig. 4, Supp. Figs. 3 and 4).

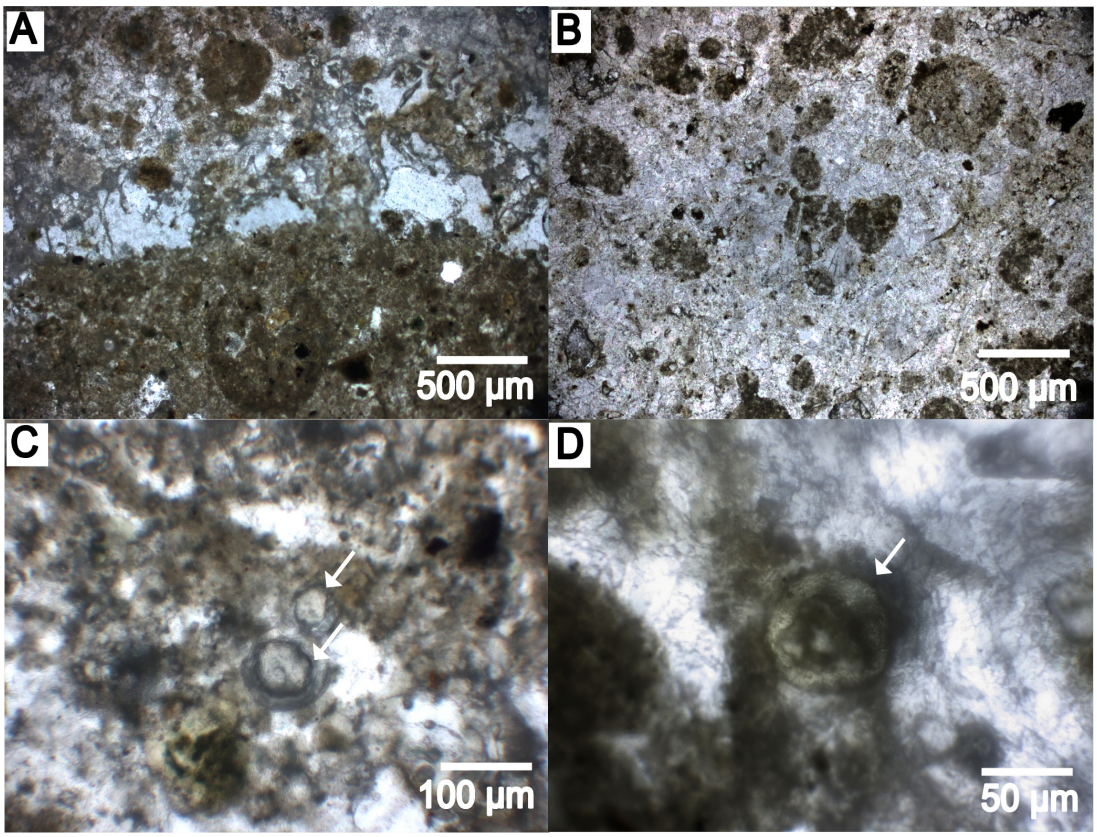

Figure 1: Transmitted light photomicrographs of peloidal micrite in spar matrix in seep carbonates from A) Jaco Scar (Costa Rica, modern) and B) Tepee Buttes (Colorado, ~75 Mya). C) and D) Purported ANME-SRB aggregates in the Jaco Scar sample, shown with white arrows.

The EDS analysis of ANME-2-SRB aggregates in situ and extracted from the carbonate revealed peaks corresponding to carbon and silica with similar intensities, suggestive of similar compositions as well, and smaller peaks for cations present in clay minerals like aluminum, magnesium, and calcium (Fig. 5).

We examined thin sections of seep carbonates from different ages and localities (Tepee Buttes, CO, 75 Mya; Moreno Fm, Panoche Hills, CA, ~62 Mya; Bear Creek, CA, ~140 Mya) to identify potential ANME-SRB aggregates based on morphology and silica association. In samples from the Tepee Buttes, we identified a few carbon-rich structures of less than 50 μm, that were embedded in the carbonate matrix and showed colocalization of carbon with silica (Fig. 6, Supp. Fig. 5).

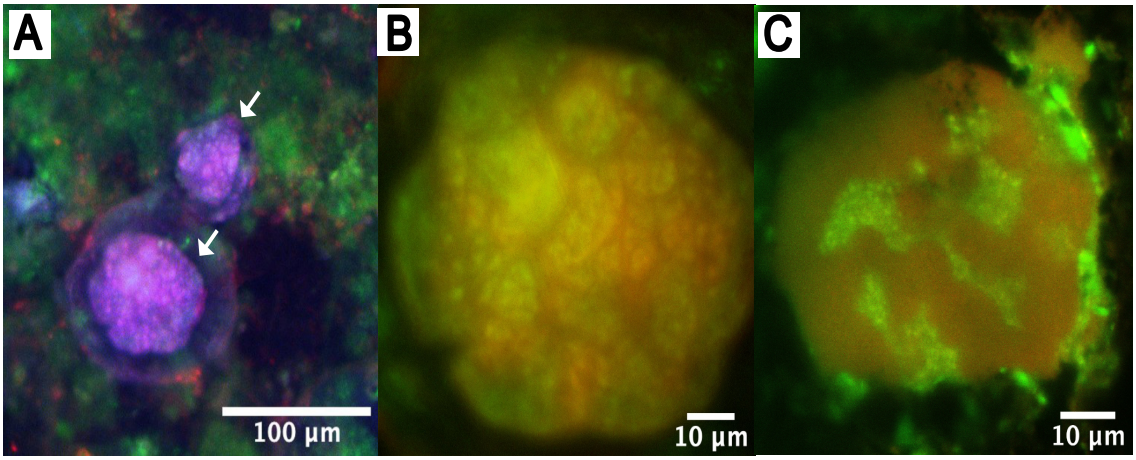

Figure 2: Fluorescence microscopy images of ANME2-SRB aggregates in carbonate rock from Jaco Scar shown in Fig. 1c (a and b) and 1d (c). A) FISH-hybridized ANME2-SRB aggregates shown in Fig. 1c (pointed at with white arrows). B) Enlarged image of the large aggregate shown in A. C) FISH-hybridized ANME2-SRB aggregate shown in Figure 1d. The red signal is from the hybridized ANME2-712 FISH probe, and the green signal is from the hybridized DSS-658 (SRB) FISH probe. The additional blue signal in a is from DAPI (DNA staining).

We further examined samples with Raman spectroscopy (Fig. 7.), in order to compare the spectra from extracted and in situ aggregates confirmed with FISH in the Jaco Scar modern carbonate with that of the purported aggregates from Tepee Buttes, and that of a black carbon precipitate that has been experimentally proven to be produced by ANME in culture (Allen et al., 2021). In all of them we identified similar carbon peaks (D (disorder/defect) band; 1350 cm^{-1} and G (graphite) band; 1580 cm^{-1}).

Additionally, since AOM produces a strong carbon isotope fractionation, whereby the produced bicarbonate (and the biomass that incorporates it) is depleted in $^{13}\mathrm{C}$ relative to the residual methane (Orphan, Hinrichs, et al., 2001; Orphan et al., 2002), we were interested in comparing the C isotopic composition of the FISH-confirmed ANME-2-SRB aggregates and the purported aggregates in the Tepee Buttes carbonate. SIMS/NanoSIMS analyses determined the relative abundances of $^{12}\mathrm{C}$ and $^{13}\mathrm{C}$ in of the ANME-2-SRB aggregates in situ and extracted from the Jaco

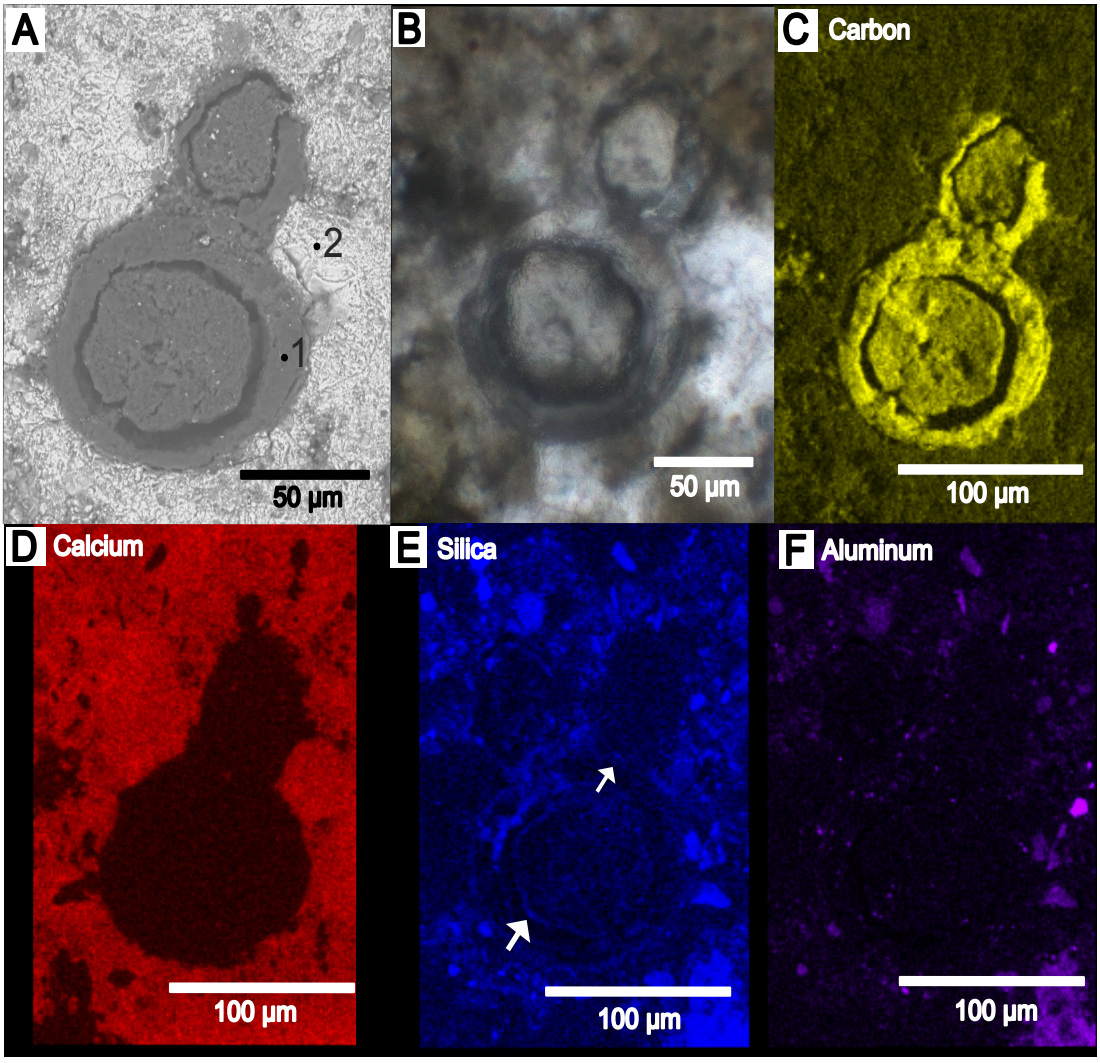

Figure 3: Correlated A) SEM, B) photomicrographs, and EDS maps for C) Carbon, D) Calcium, E) Silica and F) Aluminum of the aggregate shown in Fig. 1c (also in Fig. 2a and 2b). Points 1 and 2 in A correspond to spots where the EDS spectra shown in Fig. 5 were taken.

Scar carbonate, as well as putative aggregates in the Tepee Buttes carbonate (Fig. 8). We found similar $\delta^{13}C$ values for in situ and extracted ANME-2-SRB aggregates in the modern Jaco Scar carbonate, and slightly more positive $\delta^{13}C$ values in purported aggregates in the ancient seep carbonates.

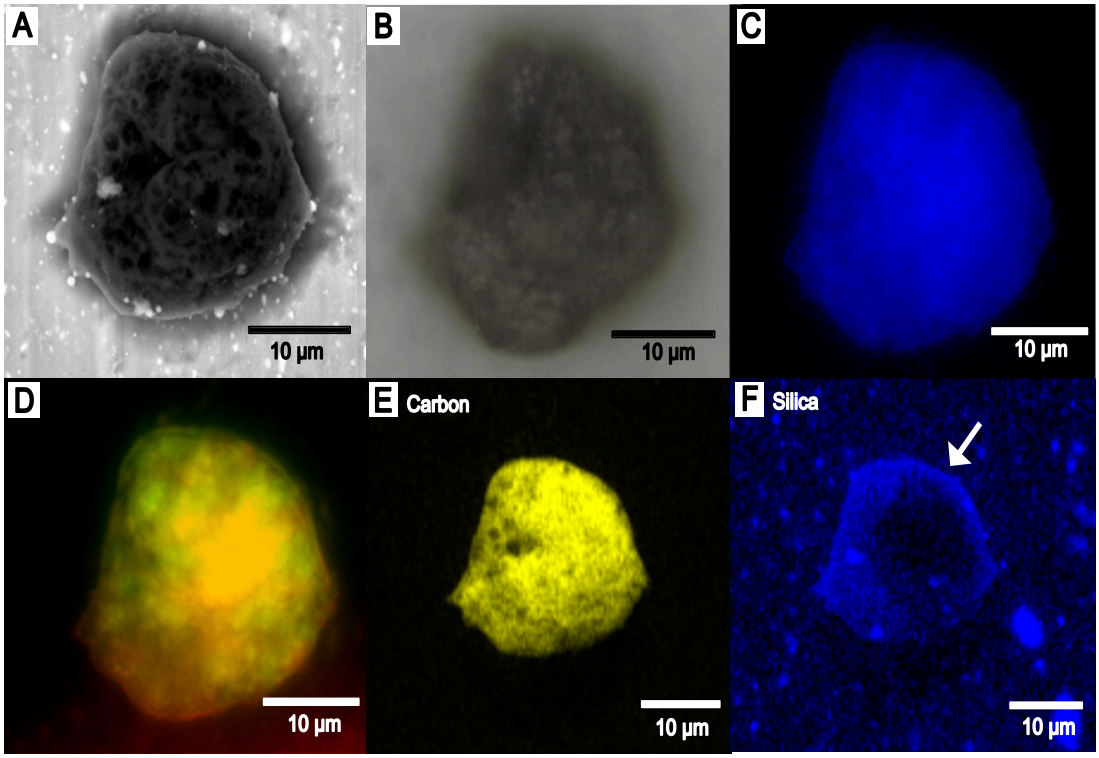

Figure 4: Correlated pictures of an aggregate extracted from a Jaco Scar carbonate from A) SEM, B) reflected light microscopy, fluorescence microscopy for C) DAPI staining (for DNA) and D) FISH with ANME2-712 (red) and DSS-658 (SRB; green) probes, and EDS maps for E) carbon and F) silica. The arrow in F points at a silica rim around the aggregate.

4. DISCUSSION

Some microbial fossils, particularly the oldest ones, are often highly disputed (e.g., Allwood et al., 2006; Dodd et al., 2017; Schopf et al., 2017) because biogenicity may be assessed only via textural, elemental, and mineralogical criteria. Texture-based criteria alone are particularly ambiguous, especially since it has been established that organic biomorphs, which resemble but do not constitute microbial fossils, can easily form abiotically, for instance, when RNA is exposed to diagenetic conditions (200°C, 15 bars) in the presence of quartz (Criouet et al., 2021), or when organics in sulfide-rich environments become silicified (Nims et al., 2021). Studies that experimentally simulate conditions of burial and diagenesis of microorganisms or try to determine whether they could be preserved by early silicification or pyritization (e.g. Moore

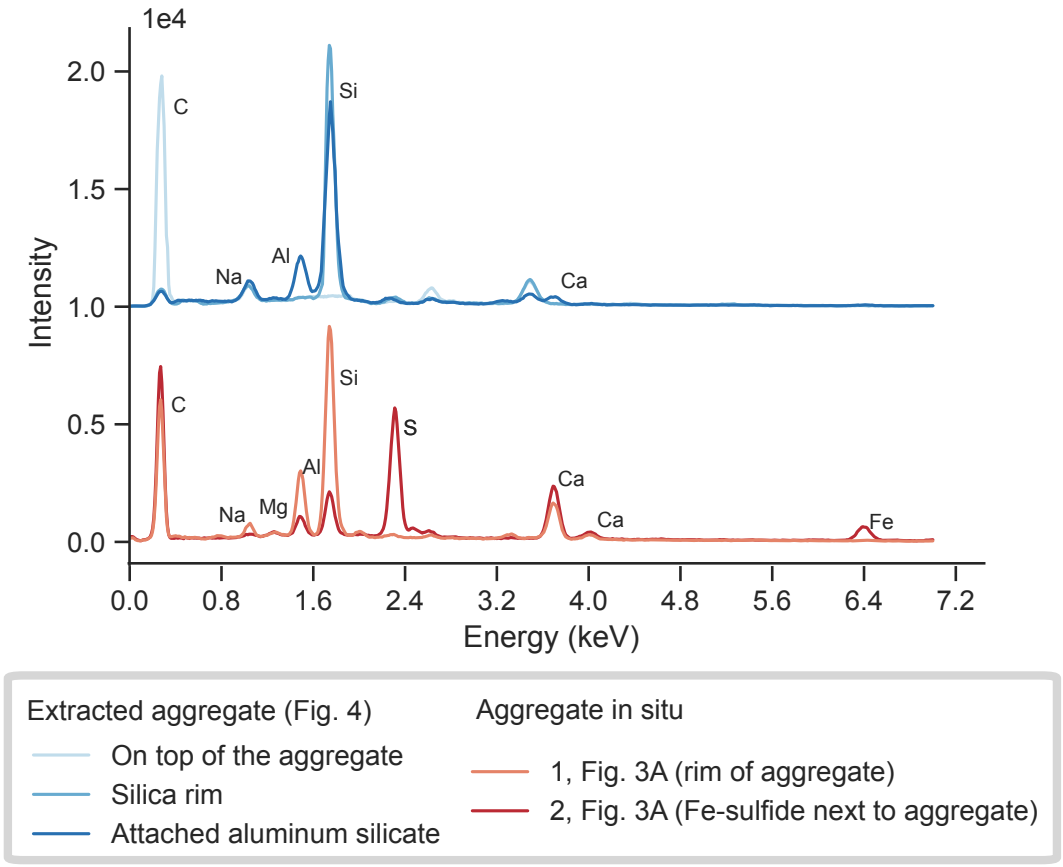

Figure 5: EDS spectra of elemental composition of ANME2-SRB aggregates in situ and extracted from a Jaco scar rock and their attached phases. Spectra on top correspond to extracted aggregates and the spectra at the bottom correspond to aggregates analyzed in situ in the carbonate rock matrix.

et al., 2021; Nims et al., 2021), help bridge the gap between observations of modern organisms and remnants of microbes preserved in the rock record. Our study attempts to compare textural, chemical, and isotopic signatures between purported microbial fossils in carbonates and similar modern microorganisms whose identity we can confirm by hybridization with specific DNA probes.

Isotopic compositions of organic matter and lipid biomarkers have been used to strengthen traditional interpretations of microbial fossils and are particularly useful for identifying molecular fossils of AOM coupled to SRB (reviewed by Niemann and Elvert, 2008). Methane seep carbonates are severely depleted in ^{13}C, with

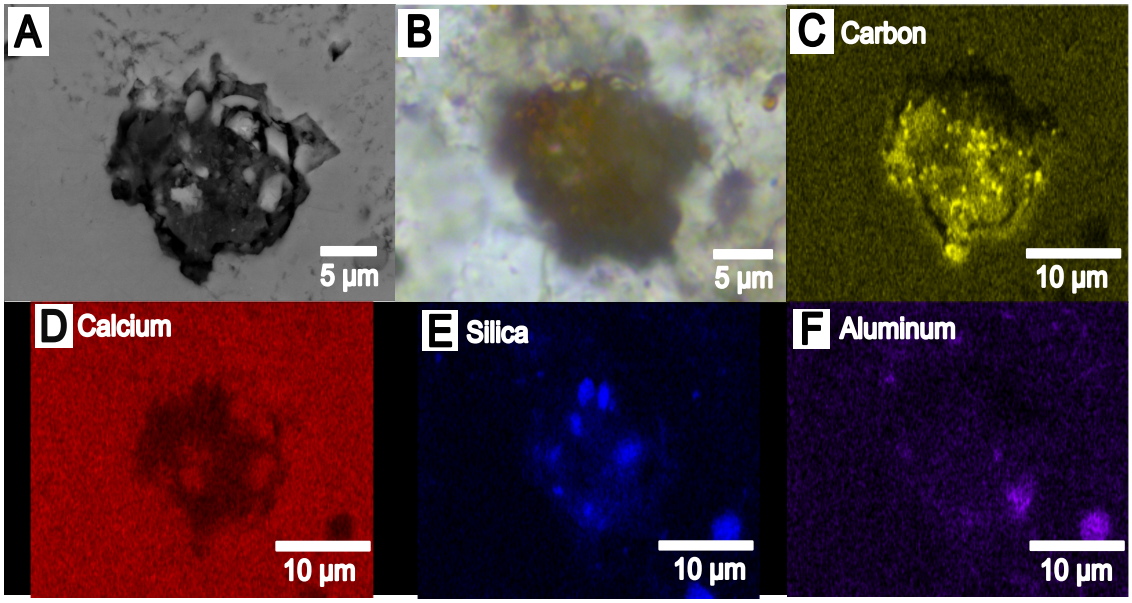

Figure 6: Purported ANME-SRB aggregate in a carbonate sample from the Tepee Buttes, Colorado (~75 Mya). Pictures correspond to correlated A) SEM, B) light microscopy, and EDS maps for C) Carbon, D) Calcium, E) Silica, and F) Aluminum. Organic carbon (identified with Raman spectroscopy) is embedded in the carbonate matrix, which follows its outline, and silica can be observed colocalizing with carbon and surrounding the aggregate.

values of $\delta^{13}C$ that are commonly in the -25 to -45‰ (VPDB) range (e.g., Birgel et al., 2006; Loyd et al., 2016) and as low as -69‰ in ancient methane seeps (Campbell et al., 2002). Methane that originates at hydrocarbon seeps is already very depleted in ^{13}C, with values as low as -50‰ for thermogenic methane and from 60 to 110‰ for biogenic methane (Whiticar, 1999); as AOM proceeds, the microorganisms incorporate preferentially the light (^{12}C) carbon isotope into their biomass, leaving the residual methane enriched in ^{13}C and the product (HCO_3^-) relatively depleted (Orphan, Hinrichs, et al., 2001). This fingerprint has been identified in lipid biomarkers from modern (e.g., Eel River Basin; Orphan, Hinrichs, et al., 2001) and ancient (e.g., Tepee Buttes; Birgel et al., 2006) methane seeps, with $\delta^{13}C$ values as low as -73.2‰ and -117.8‰ for SRB and archaea, respectively. Secondary-ion mass spectrometry (SIMS) has identified a range of -15 to -100‰ for ANME-2-SRB aggregates from modern sediments (Orphan, Hinrichs, et al.,

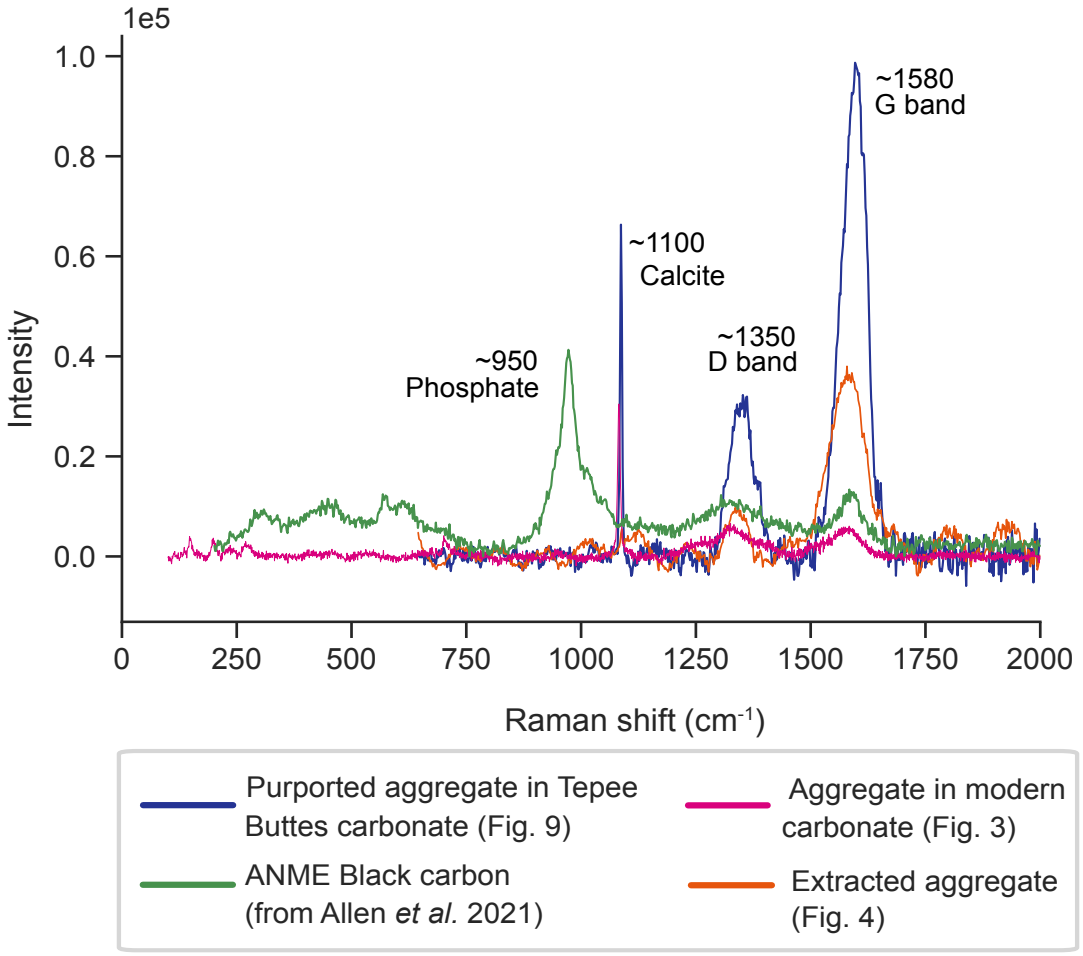

Figure 7: Raman spectra of ANME2-SRB aggregates in situ and extracted from a carbonate rock from Jaco scar, putative aggregates in a Tepee Buttes (~ 75 Mya) seep carbonate, and black carbon detected as a biomineralization product in ANME incubations (Allen et al., 2021). The D (disorder/defect) and G (graphite) bands characteristic of carbon are labelled, as well as the calcite peak from the matrix in which the aggregates are embedded in both the modern and ancient seep carbonates.

2001; Orphan et al., 2002). Recently, putative fossils of ANME-SRB aggregates were reported in Pleistocene seep carbonates off Svalbard, Norway (Himmler et al., 2022). These were described as round shapes of Mg-calcite with concentric rims of ~10 μm engulfed in aragonite cements. ^{13}C-depleted archaeal (including the diagnostic AOM biomarker crocetane; down to -113‰) and bacterial (down to -75‰) lipid biomarkers, and values as low as -42‰ for the Mg-calcite microstructures from NanoSIMS were used as complementary evidence for the identification of the

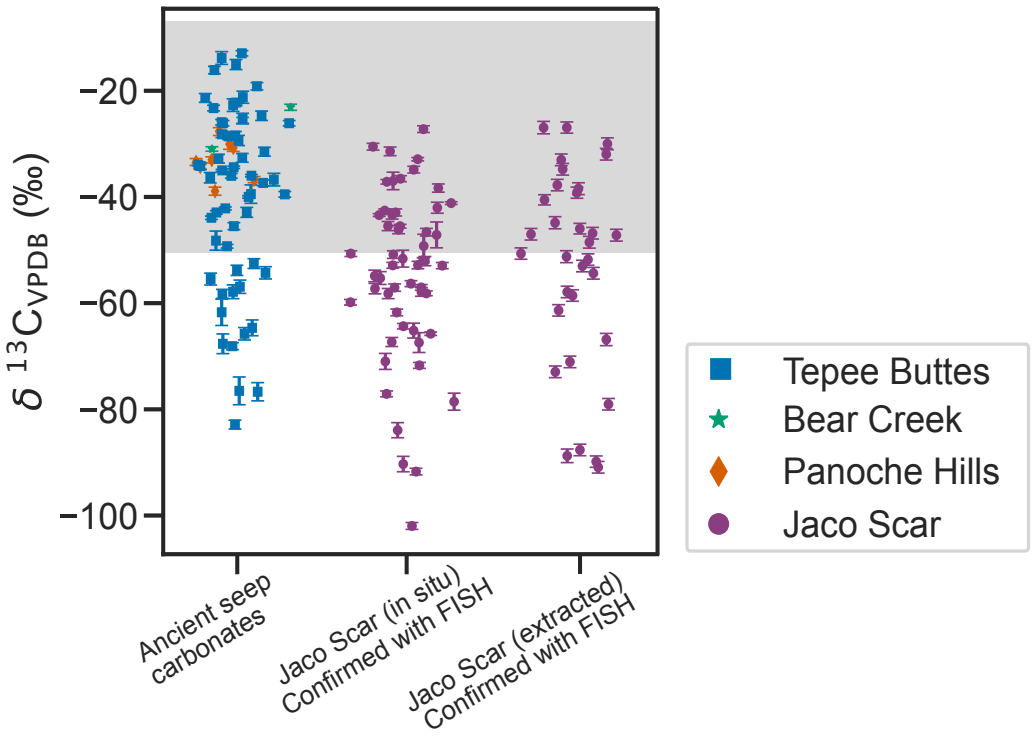

Figure 8: SIMS/NanoSIMS C isotopic composition of ANME2-SRB aggregates confirmed by FISH. In situ aggregates were analyzed with SIMS inside the native carbonate, and extracted aggregates were isolated from the rock matrix and analyzed with NanoSIMS. The shaded area corresponds to the range of $\delta^{13}C$ of the carbonate from Tepee Buttes samples.

putative microfossils. A previous report from modern carbonates from the seafloor in the Northeastern South China identified putative ANME-SRB fossils based on texture and morphology alone (D. F. Chen et al., 2005).

The putative ANME-SRB aggregates we observed in the Tepee Buttes carbonates are Cretaceous in age, substantially older than those reported by Himmler et al. (2022) and D. F. Chen et al. (2005); they were identified by comparison to modern ANME-2-SRB aggregates confirmed with FISH. We have observed silica enrichment in ANME-2-SRB aggregates identified by FISH in a Jaco Scar carbonate (Osorio-Rodriguez et al., in prep). Here, we supplement that earlier work through usage of correlative transmitted light, fluorescence, and electron microscopy coupled to EDS to identify ANME-SRB aggregates and their association with silica in seep

carbonates. Since the confirmed modern and purported ancient ANME-2-SRB aggregates had preserved organic carbon, they could be inspected with Raman spectroscopy for a direct comparison with black carbon precipitates from ANME in cultures (Allen et al., 2021). We identified similar carbon peaks in modern and purported ancient ANME-2-SRB aggregates as those for black carbon, providing further support for the purported ancient ANME-SRB aggregates. We also used SIMS/NanoSIMS to examine the $\delta^{13}C$ signature of the organic matter from modern ANME-2-SRB aggregates, both in situ and extracted from the Jaco Scar carbonate, and purported ANME-SRB aggregates in the Tepee buttes carbonate. We found a similar range of $\delta^{13}C$ values for modern ANME-2-SRB aggregates extracted from and in situ in the Jaco Scar carbonate rocks of ~-25 and -95‰, which falls within the range of aggregates isolated from sediments (Orphan, Hinrichs, et al., 2001; Orphan et al., 2002). However, the $\delta^{13}C$ values we obtained for purported ANME-SRB aggregates from ancient carbonates have a small ~10‰ offset towards heavier values (~-15 to -85‰). We do not believe that this offset can be attributed to the fact that the targets were inside a carbonate matrix, since both modern confirmed and ancient purported aggregates were analyzed with SIMS, and high carbon counts ($< 10^6$) were utilized as a threshold to guarantee that the measurements were performed in organic matter. An alternative explanation would involve displacement of light carbon atoms from organic matter into methane and carbon dioxide in the ancient carbonates, which occurs at the gas formation temperature (115-120°C for methane (Rooney et al., 1995), and 80-120°C for CO_2 (Hunt, 1979)). The bacterial biomarkers identified in the Tepee Buttes indicate a low thermal maturity (Birgel et al., 2006), which would be favorable for the decarboxylation of organic matter to CO_2. However, in spite of extensive decarboxylation, marine kerogen does not get 10‰ heavier in $\delta^{13}C$ (**Andresen1994**). We believe that the most feasible explanation is that, since the targets we analyzed with SIMS in ancient carbonates

could not be confirmed with FISH, it is likely that some of them do not actually constitute microbial fossils of ANME-SRB aggregates or are composed of a variety of microorganisms with a wider range of $\delta^{13}C$ values. Alternatively, the shift could be due to an unidentified systematic measurement bias, or different original $\delta^{13}C$ values for the methane sources between the analyzed modern and ancient carbonates. For these reasons, we suggest the use of a joint approach, in which the presence of co-localized carbon and silica and/or silica rims surrounding carbon, the black carbon signal from Raman spectroscopy, and SIMS $\delta^{13}C$ values in the range of ~-25 to <-100‰ can all be used as complementary proxies to identify ANME-SRB aggregates in ancient carbonates.

Microbial silica precipitation from undersaturated solutions has been experimentally proven for ANME-2-SRB aggregates (Osorio-Rodriguez et al., in prep), cyanobacteria (Moore et al., 2021; Moore et al., 2020), and *Bacillus subtilis* (Fein et al., 2002). Magnesium (Moore et al., 2021), and iron and aluminum (Fein et al., 2002; Konhauser et al., 1993; Konhauser and Urrutia, 1999), have been proposed to serve as bridges for the adsorption or precipitation of silica onto bacterial surfaces. Clay mineral encrustations around AOM consortia in sediments have been identified and invoked as a potential mechanism to preserve them as microbial fossils (Y. Chen et al., 2014). However, ANME-2-SRB aggregates precipitate amorphous silica that is depleted in cations relative to the compositions of common clay minerals (Osorio-Rodriguez et al., in prep). This is consistent with our EDS analysis of modern ANME-2-SRB aggregates, and most of the putative aggregates in the Tepee Buttes carbonates. We identified aluminum and iron surrounding silica and carbon in the inferred aggregates in the Tepee Buttes carbonate (Fig. 5). Even though we did not identify a close association with iron in modern ANME-2-SRB aggregates confirmed with FISH, pyritization has been deemed critical for the preservation of microbial fossils in environments as diverse as hydrothermal vents (Dodd et al.,

2017) and the deep ocean (Oehler, 1977), and its role aiding to the preservation of ANME-SRB microfossils remains to be established.

Unlike Tepee Buttes and other ancient seep carbonates, where multiple diagenetic carbonate phases such as yellow calcite, pseudospar, and banded and botryoidal cements have been identified (Birgel et al., 2006), our observation of modern carbonates allowed us to identify only micrite ± pellets and spar cements. We successfully observed ANME-2-SRB aggregates with transmitted light microscopy in a petrographic thin section from Jaco Scar, a modern seep carbonate with active methane seepage, mostly located in the micritic phases. This is expected considering that micrite is a primary carbonate precipitate, but because of its dark color, it makes it difficult the identification of ANME-SRB aggregates in ancient methane seep carbonates where a primary survey with FISH is not possible. Even with the possibility of using FISH as a tool to locate and confirm ANME-2-SRB aggregates in the modern Jaco Scar carbonate, their identification was challenging. Cell abundances in modern active methane seep carbonates that were powdered and processed through a Percoll density gradient to separate aggregates were found to be in the order of $10^8/\mathrm{cm}^3$ of rock (Marlow et al., 2021). Assuming an average size of 20 $\mu\mathrm{m}$ for endolithic ANME-2-SRB aggregates from our survey of the Jaco Scar carbonate, this would be equivalent to ~5000 aggregates in an area of 1 cm^2 for a 50 $\mu\mathrm{m}$ thin section. Even though these aggregates can be easily identified with a fluorescence microscope after FISH, if they are not exposed on the surface of the section, they cannot be observed with light microscopy or SEM. Furthermore, most of them are found lining rock pore spaces (Marlow et al., 2021), which makes them invisible under transmitted light microscopy and complicates the observation of microbe-mineral interactions. To maximize the probabilities of finding ANME-2-SRB aggregates and other microfossils in ancient methane seep carbonates, we suggest the use of complementary approaches to SEM and EDS,

such as near-infrared imaging spectroscopy (Greenberger et al., 2015) to better characterize spatial relationships between mineral phases, and synchrotron-based ptychographic X-ray computed tomography (PXCT; Maldanis et al., 2020), which allows for constraint of the 3D-location of organic matter within a mineral matrix.

5. CONCLUSIONS

Utilizing carbonates from Jaco Scar, Costa Rica, as a modern analog of ancient seep carbonates, we characterized ANME-2-SRB aggregates with FISH hybridization for DNA. This approach identified ANME-2-SRB aggregates associated with silica in carbonates, which often occurs in the form of rims, and has distinctive black carbon Raman spectra and $\delta^{13}C$ values between ~-25 and <-100‰. The fact that ANME-2-SRB aggregates are capable of mobilizing and reprecipitating silica from their environments constitutes an important mechanism for their potential preservation as microfossils. A combination of proxies is thus suggested for the search of fossilized ANME-2-SRB aggregates. Our findings are relevant for the identification of microfossils of ANME-2-SRB aggregates in rocks from Earth and extraterrestrial bodies where current or past methane emissions in aquatic environments may have occurred.

6. ACKNOWLEDGEMENTS

We would like to acknowledge Paul Myrow and Eliza Carter for help with Tepee Buttes sample collection, and the crews of *R/V Atlantis* and *R/V Western Flyer* for assistance in Jaco Scar sample collection and processing. We would also like to acknowledge the 2019 International Geobiology course for help with collection of the Panoche Hills samples. We thank Ken Williford and Adam Hoffmann from the NASA Jet Propulsion Laboratory for providing the carbon standard for SIMS, and training and assistance in the preparation of SIMS mounts. We further acknowledge Chi Ma, Yunbin Guan, George Rossman, and Giada Spigolon for technical assistance

with SEM/EDS, SIMS/NanoSIMS, the Raman spectrometer, and the confocal microscope, respectively. Confocal microscopy imaging was performed in the Caltech Biological Imaging Facility, with the support of the Caltech Beckman Institute and the Arnold and Mabel Beckman Foundation. We thank Russell Shapiro for valuable input and providing the Bear Creek samples, as well as Magdalena Mayr, Sergio Parra, Kelsey Moore, Ken Williford, Ted Present, Antoine Crémière, Stephanie Connon, John Magyar, and Kriti Sharma for useful discussions about this work. Funding for this work was provided by the Simons Collaboration for the Origin of Life (to DOR and JPG), and a grant from the Center for Environmental Microbial Interactions (to VJO). VJO is a CIFAR science fellow in the Earth 4D program.

7. SUPPLEMENTARY MATERIALS

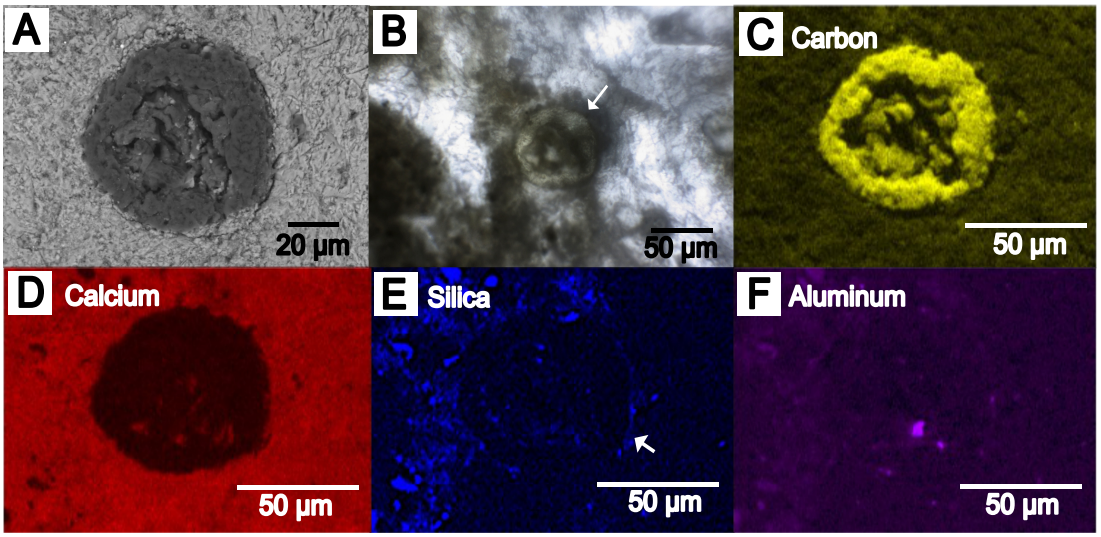

Supp. Fig. 1: Correlated A) SEM, B) photomicrographs, and EDS maps for C) Carbon, D) Calcium, E) Silica, and F) Aluminum of the aggregate shown in Fig. 1D (also in Fig. 2C).

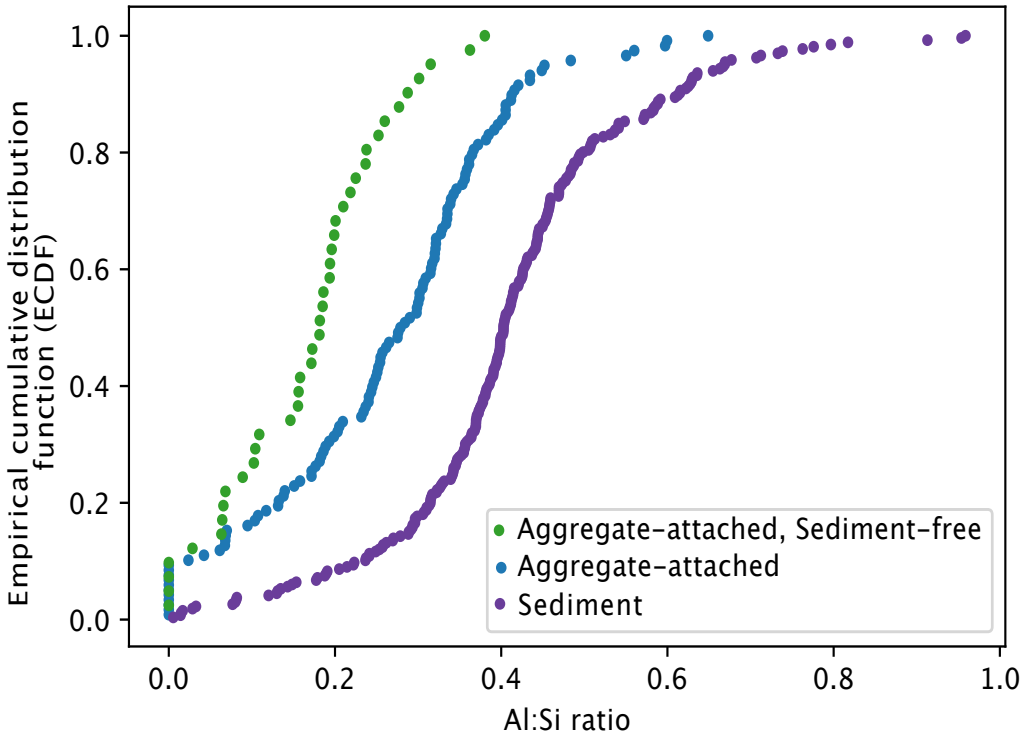

Supp. Fig. 2: Distribution of Al: Si ratios in samples of sediment (purple), ANME-SRB aggregates incubated with sediment (blue), and ANME-SRB aggregates in sediment-free incubations (green). Each point represents a different sample analyzed with EDS. Sediment samples have consistently larger Al:Si ratios than ANME-SRB aggregates in sediment-free incubations.

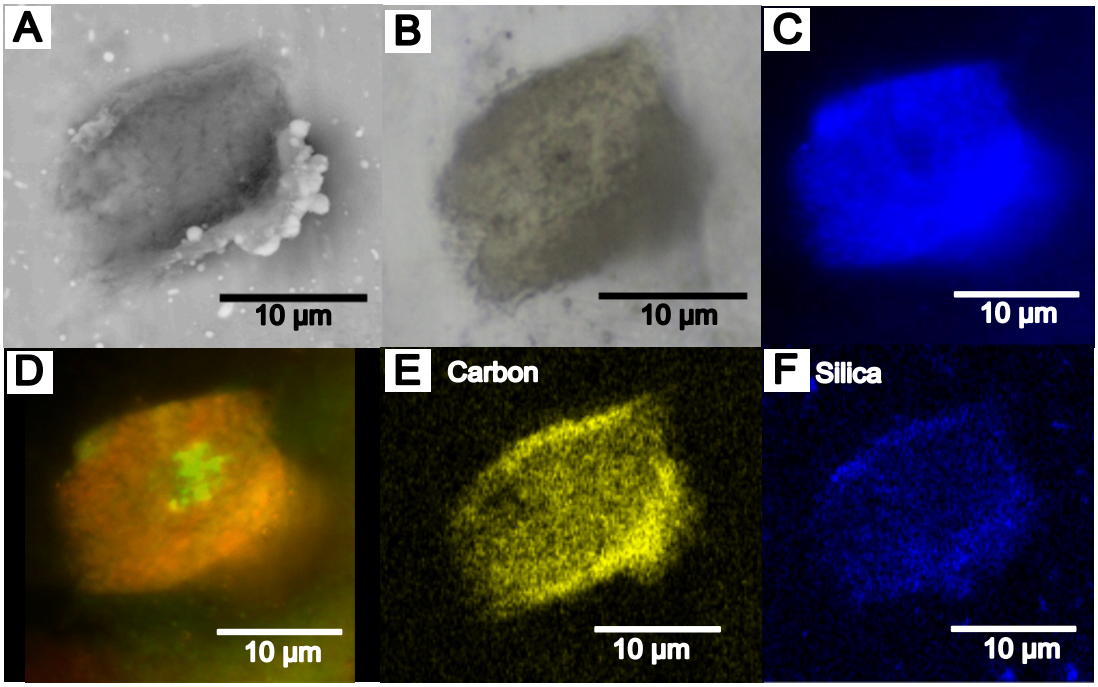

Supp. Fig. 3: Correlated pictures of an aggregate extracted from a Jaco Scar carbonate from A) SEM, B) reflected light microscopy, fluorescence microscopy for C) DAPI staining (for DNA) and D) FISH with ANME-2-712 (red) and DSS-658 (SRB; green) probes, and EDS maps for E) Carbon and F) Silica.

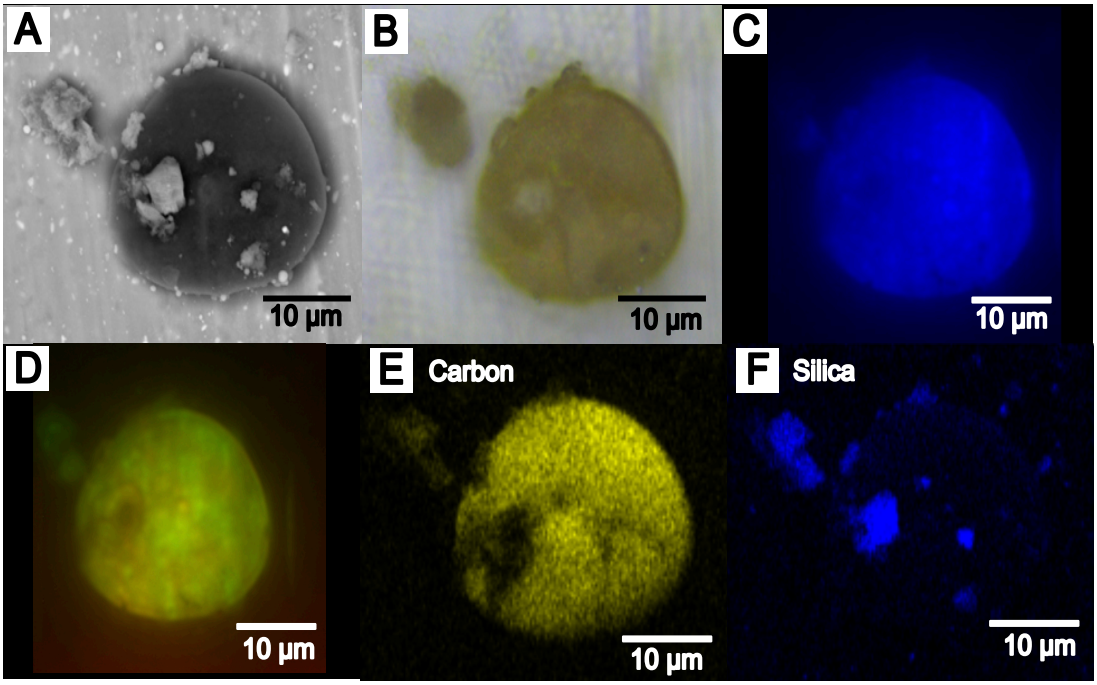

Supp. Fig. 4: Correlated pictures of an aggregate extracted from a Jaco Scar carbonate from A) SEM, B) reflected light microscopy, fluorescence microscopy for C) DAPI staining (for DNA) and D) FISH with ANME-2-712 (red) and DSS-658 (SRB; green) probes, and EDS maps for E) Carbon and F) Silica.

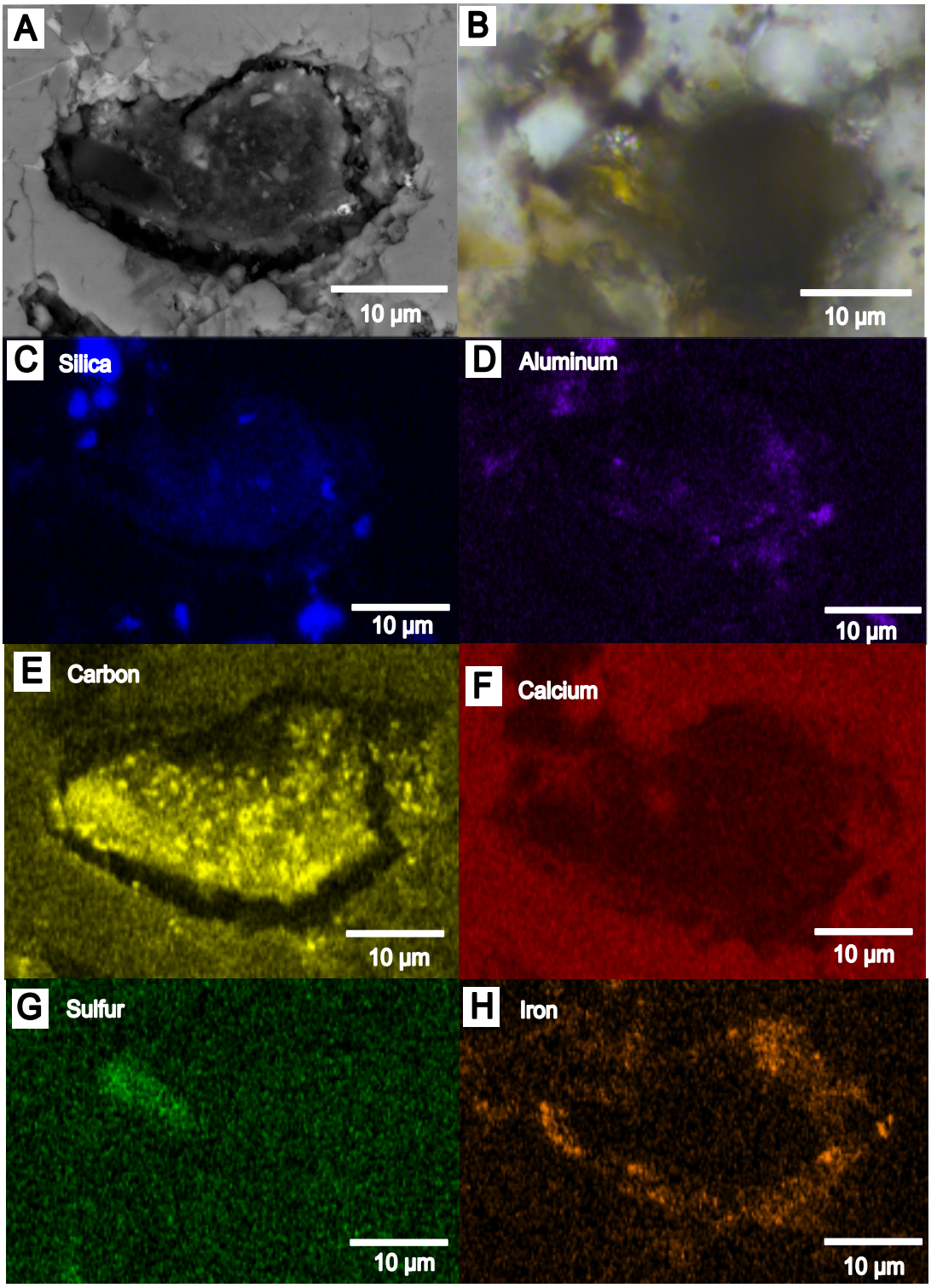

Supp. Fig. 5: Purported ANME-SRB aggregate in a carbonate sample from the Tepee Buttes, Colorado ($\sim$ 75 Mya). Pictures correspond to correlated A) SEM, B) light microscopy, and EDS maps for C) Carbon, D) Calcium, E) Silica, F) Aluminum, G) Sulfur, and H) Iron.

References

Allen, K. D., Wegener, G., Jr, D. M. S., Bodnar, R. J., Feng, X., Wendt, J., & White, R. H. (2021). Biogenic formation of amorphous carbon by anaerobic methanotrophs and select methanogens. *Science Advances*, *7*(October), eabg9739.

Alleon, J., Bernard, S., Le Guillou, C., Daval, D., Skouri-Panet, F., Pont, S., Delbes, L., & Robert, F. (2016). Early entombment within silica minimizes the molecular degradation of microorganisms during advanced diagenesis. *Chemical Geology*, *437*, 98–108. https://doi.org/10.1016/j.chemgeo.2016.05.034

Allwood, A. C., Walter, M. R., Kamber, B. S., Marshall, C. P., & Burch, I. W. (2006). Stromatolite reef from the Early Archaean era of Australia. *Nature*, *441*(7094), 714–718.

Aloisi, G., Bouloubassi, I., Heijs, S. K., Pancost, R. D., Pierre, C., Sinninghe Damsté, J. S., Gottschal, J. C., Forney, L. J., & Rouchy, J.-M. (2002). CH4-consuming microorganisms and the formation of carbonate crusts at cold seeps. *Earth and Planetary Science Letters*, *203*(1), 195–203. https://doi.org/10.1016/S0012-821X(02)00878-6

Birgel, D., Klautzsch, S., Thiel, V., & Reitner, J. (2006). Anaerobic and Aerobic Oxidation of Methane at Late Cretaceous Seeps in the Western Interior Seaway , USA. *Geomicrobiology Journal*, *23*(7), 565–577. https://doi.org/10.1080/01490450600897369

Boetius, A., Ravenschlag, K., Schubert, C. J., Rickert, D., Widdel, F., Gieseke, A., Amann, R., Jørgensen, B. B., Witte, U., & Pfannkuche, O. (2000). A marine microbial consortium apparently mediating anaerobic oxidation of methane. *Nature*, *407*, 623.

Bohrmann, G., Heeschen, K., Jung, C., Weinrebe, W., Baranov, B., Cailleau, B., Heath, R., Hühnerbach, V., Hort, M., Masson, D., & Trummer, I. (2002). Widespread fluid expulsion along the seafloor of the Costa Rica convergent margin. *Terra Nova*, *14*(2), 69–79. https://doi.org/10.1046/j.1365-3121.2002.00400.x

Campbell, K. A., Farmer, J. D., & Des Marais, D. (2002). Ancient hydrocarbon seeps from the Mesozoic convergent margin of California.pdf. *Geofluids*, *2*, 63–94.

Campbell, K. A., Carlson, C., & Bottjer, D. J. (1993). Fossil cold seep limestones and associated chemosymbiotic macroinvertebrate faunas, Jurassic-Cretaceous Great Valley Group, California. *In: Graham, S.A., Lowe, D.R. (Eds.), Advances in the Sedimentary Geology of the Great Valley Group, Sacramento Valley, California: Pacific Section of the Society of Economic Paleontologists and Mineralogists*, *73*, 37–50.

Chen, D. F., Huang, Y. Y., Yuan, X. L., & Cathles, L. M. (2005). Seep carbonates and preserved methane oxidizing archaea and sulfate reducing bacteria fossils suggest recent gas venting on the seafloor in the Northeastern South China Sea. *Marine and Petroleum Geology*, *22*(5), 613–621. https://doi.org/10.1016/j.marpetgeo.2005.05.002

Chen, Y., Li, Y. L., Zhou, G. T., Li, H., Lin, Y. T., Xiao, X., & Wang, F. P. (2014). Biomineralization mediated by anaerobic methane-consuming cell consortia. *Scientific Reports*, *4*, 1–9. https://doi.org/10.1038/srep05696

Criouet, I., Viennet, J. C., Jacquemot, P., Jaber, M., & Bernard, S. (2021). Abiotic formation of organic biomorphs under diagenetic conditions. *Geochemical Perspectives Letters*, *16*, 40–46. https://doi.org/10.7185/GEOCHEMLET.2102

Dodd, M. S., Papineau, D., Grenne, T., Slack, J. F., Rittner, M., Pirajno, F., O'Neil, J., & Little, C. T. (2017). Evidence for early life in Earth's oldest hydrothermal vent precipitates. *Nature*, *543*(7643), 60–64. https://doi.org/10.1038/nature21377

Fein, J. B., Scott, S., & Rivera, N. (2002). The effect of Fe on Si adsorption by Bacillus subtilis cell walls: insights into non-metabolic bacterial precipitation of silicate minerals. *Chemical Geology*, *182*(2), 265–273. https://doi.org/10.1016/S0009-2541(01)00294-7

Gilbert, G. K., & Gulliver, F. P. (1894). Tepee Buttes. *GSA Bulletin*, *6*(1), 333–342.

Greenberger, R. N., Mustard, J. F., Ehlmann, B. L., Blaney, D. L., Cloutis, E. A., Wilson, J. H., Green, R. O., & Fraeman, A. A. (2015). Imaging spectroscopy of geological samples and outcrops: Novel insights from microns to meters. *GSA Today*, *25*(12), 4–10. https://doi.org/10.1130/GSATG252A.1

Himmler, T., Crémière, A., Birgel, D., Wirth, R., Orphan, V. J., Kirsimäe, K., Knies, J., Peckmann, J., & Lepland, A. (2022). Putative fossils of chemotrophic microbes preserved in seep carbonates from Vestnesa Ridge, off northwest Svalbard, Norway. *Geology*, *50*(2), 169–173. https://doi.org/10.1130/g49620.1

Hinrichs, K.-U., Hayes, J. M., Sylva, S. P., Brewer, P. W., & Delong, E. (1999). Methane-consuming archaebacteria in marine sediments. *Nature*, *398*, 802–805.

Hinrichs, K.-U., & Boetius, A. (2013). The Anaerobic Oxidation of Methane: New Insights in Microbial Ecology and Biogeochemistry. *Ocean Margin Systems*, 457–477. https://doi.org/10.1007/978-3-662-05127-6_28

Hoehler, T. M., Alperin, M. J., Albert, D. B., & Martens, C. S. (1994). Field and laboratory, evidence for a methane-sulfate reducer consortium.pdf. *Global Biogeochemical Cycles*, *8*(4), 451–463.

Howe, B., & Kauffman, E. G. (1986). The lithofacies, biofacies, and depositional setting of Tepee Buttes, Cretaceous submarine springs, between Colorado Springs and Boone, Colorado. *Cretaceous biofacies of the central part of the Western Interior Seaway: A field guidebook: Fourth North American Paleontological Convention, Boulder, Colorado*, 155–175.

Howe, B. (1987). *Tepee Buttes: a petrological, paleontological, paleoenvironmental study of Cretaceous submarine spring deposits* (Doctoral dissertation). University of Colorado, Boulder.

Hunt, J. M. (1979). *Petroleum Geochemistry and Geology*. W. H. Freeman Company.

Jørgensen, B. B., Böttcher, M. E., Lüschen, H., Neretin, L. N., & Volkov, I. I. (2004). Anaerobic methane oxidation and a deep H2 S sink generate isotopically heavy sulfides in Black Sea sediments. *Geochimica et Cosmochimica Acta*, *68*(9), 2095–2118. https://doi.org/10.1016/J.GCA.2003.07.017

Kauffman, E. G., Arthur, M. A., Howe, B., & Scholle, P. A. (1996). Widespread venting of methane-rich fluids in Late Cretaceous (Campanian) submarine springs (Tepee Buttes), Western Interior seaway, U.S.A. *Geology*, *24*(9), 799–802. https://doi.org/10.1130/0091-7613(1996)024<0799:WVOMRF>2.3.CO;2

Knittel, K., Lösekann, T., Boetius, A., Kort, R., & Amann, R. (2005). Diversity and Distribution of Methanotrophic Archaea at Cold Seeps. *Applied and Environmental Microbiology*, *71*(1), 467–479. https://doi.org/10.1128/AEM.71.1.467-479.2005

Konhauser, K. O., Fyfe, W. S., Ferris, F. G., & Beveridge, T. J. (1993). Metal sorption and mineral precipitation by bacteria in two Amazonian river systems: Rio Solimoes and Rio Negro, Brazil. *Geology*, *21*, 1103–1106.

Konhauser, K. O., & Urrutia, M. M. (1999). Bacterial clay authigenesis: a common biogeochemical process. *Chemical Geology*, *161*(4), 399–413. https://doi.org/10.1016/S0009-2541(99)00118-7

Levin, L. A., Orphan, V. J., Rouse, G. W., Rathburn, A. E., Ussler, W., Cook, G. S., Goffredi, S. K., Perez, E. M., Waren, A., Grupe, B. M., Chadwick, G., & Strickrott, B. (2012). A hydrothermal seep on the Costa Rica margin: Middle ground in a continuum of reducing ecosystems. *Proceedings of the Royal Society B: Biological Sciences*, *279*(1738), 2580–2588. https://doi.org/10.1098/rspb.2012.0205

Loyd, S. J., Sample, J., Tripati, R. E., Defliese, W. F., Brooks, K., Hovland, M., Torres, M., Marlow, J., Hancock, L. G., Martin, R., Lyons, T., & Tripati, A. E. (2016). Methane seep carbonates yield clumped isotope signatures out of equilibrium with formation temperatures. *Nature Communications*, *7*, 1–12. https://doi.org/10.1038/ncomms12274

Maldanis, L., Hickman-Lewis, K., Verezhak, M., Gueriau, P., Guizar-Sicairos, M., Jaqueto, P., Trindade, R. I., Rossi, A. L., Berenguer, F., Westall, F., Bertrand, L., & Galante, D. (2020). Nanoscale 3D quantitative imaging of 1.88 Ga Gunflint microfossils reveals novel insights into taphonomic and biogenic characters. *Scientific Reports*, *10*(1), 1–9. https://doi.org/10.1038/s41598-020-65176-w

Marlow, J. J., Hoer, D., Jungbluth, S. P., Reynard, L. M., Gartman, A., Chavez, M. S., El-Naggar, M. Y., Tuross, N., Orphan, V. J., & Girguis, P. R. (2021). Carbonate-hosted microbial communities are prolific and pervasive methane oxidizers at geologically diverse marine methane seep sites. *Proceedings of the National Academy of Sciences*, *118*(25), e2006857118.

Marlow, J. J., Steele, J. A., Ziebis, W., Thurber, A. R., Levin, L. A., Orphan, V. J., Ziebis, W., Marlow, J. J., Orphan, V. J., & Steele, J. A. (2014). Carbonate-hosted methanotrophy represents an unrecognized methane sink in the deep sea. *Nature Communications*, *5*(1), 1–12. https://doi.org/10.1038/ncomms6094

Metcalfe, K. S. (2021). *Symbiotic Diversity and Mineral-Associated Microbial Ecology in Marine Microbiomes* (Doctoral dissertation). California Institute of Technology.

Metz, C. L. (2000). *Upper Cretaceous(Campanian) sequence-and biostratigraphy, West Texas to East-Central Utah: and development of cold-seep mounds in the Western Interior Cretaceous Basin* (Doctoral dissertation). Texas A&M University.

Michaelis, W., Seifert, R., Nauhaus, K., Treude, T., Thiel, V., Blumenberg, M., Knittel, K., Gieseke, A., Peterknecht, K., Pape, T., Boetius, A., Amann, R., Jørgensen, B. B., Widdel, F., Peckmann, J., Pimenov, N. V., & Gulin, M. B. (2002). Microbial Reefs in the Black Sea Fueled by Anaerobic Oxidation of Methane. *Science*, *297*(5583), 1013 LP –1015. https://doi.org/10.1126/science.1072502

Moore, K. R., Gong, J., Pajusalu, M., Skoog, E. J., Xu, M., Feliz Soto, T., Sojo, V., Matreux, T., Baldes, M. J., Braun, D., Williford, K., & Bosak, T. (2021). A new model for silicification of cyanobacteria in Proterozoic tidal flats. *Geobiology*, *19*(5), 438–449. https://doi.org/10.1111/gbi.12447

Moore, K. R., Pajusalu, M., Gong, J., Sojo, V., Matreux, T., Braun, D., & Bosak, T. (2020). Biologically mediated silicification of marine cyanobacteria and implications for the Proterozoic fossil record. *Geology*, *48*(9), 862–866. https://doi.org/10.1130/G47394.1

Nauhaus, K., Albrecht, M., Elvert, M., Boetius, A., & Widdel, F. (2007). In vitro cell growth of marine archaeal-bacterial consortia during anaerobic oxidation of methane with sulfate. *Environmental Microbiology*, *9*(1), 187–196.

Neretin, L. N., Böttcher, M. E., Jørgensen, B. B., Volkov, I. I., Lüschen, H., & Hilgenfeldt, K. (2004). Pyritization processes and greigite formation in the advancing sulfidization front in the upper Pleistocene sediments of the Black Sea. *Geochimica et Cosmochimica Acta*, *68*(9), 2081–2093. https://doi.org/10.1016/S0016-7037(03)00450-2

Niemann, H., & Elvert, M. (2008). Diagnostic lipid biomarker and stable carbon isotope signatures of microbial communities mediating the anaerobic oxidation of methane with sulphate. *Organic Geochemistry*, *39*(12), 1668–1677. https://doi.org/10.1016/j.orggeochem.2007.11.003

Nims, C., Lafond, J., Alleon, J., Templeton, A. S., & Cosmidis, J. (2021). Organic biomorphs may be better preserved than microorganisms in early Earth sediments. *Geology*, *49*(6), 629–634. https://doi.org/10.1130/G48152.1

Oehler, J. H. (1977). Microflora of the H.Y.C. Pyritic Shale Member of the Barney Creek Formation (McArthur Group), middle Proterozoic of northern Australia. *Alcheringa: An Australasian Journal of Palaeontology*, *1*(3), 315–349. https://doi.org/10.1080/03115517708527768

Orphan, V. J., Hinrichs, K.-U., Ussler, W., Paull, C. K., Taylor, L. T., Sylva, S. P., Hayes, J. M., & DeLong, E. F. (2001). Comparative analysis of methane-oxidizing archaea and sulfate-reducing bacteria in anoxic marine sediments. *Applied and Environmental Microbiology*, *67*(4), 1922–1934.

Orphan, V. J., House, C. H., Hinrichs, K.-U., McKeegan, K. D., & DeLong, E. F. (2001). Methane-Consuming Archaea Revealed by Directly Coupled Isotopic and Phylogenetic Analysis. *Science*, *293*(5529), 484–487. https://doi.org/10.1126/science.1061338

Orphan, V. J., House, C. H., Hinrichs, K.-U., McKeegan, K. D., & DeLong, E. F. (2002). Multiple archaeal groups mediate methane oxidation in anoxic cold seep sediments. *Proceedings of the National Academy of Sciences*, *99*(11), 7663–7668. https://doi.org/10.1073/pnas.072210299

Pernthaler, J., Glöckner, F.-O., Schönhuber, W., & Amann, R. (2001). Fluorescence in situ hybridization (FISH) with rRNA-targeted oligonucleotide probes. *Methods in microbiology*, *30*, 207–226.

Reeburgh, W. S. (2007). Oceanic Methane Biogeochemistry. *Chemical Reviews*, *107*(2), 486–513. https://doi.org/10.1021/cr050362v

Ritger, S., Carson, B., & Suess, E. (1987). Methane-derived authigenic carbonates formed by subduction-induced pore-water expulsion along the Oregon/Washington margin. *GSA Bulletin*, *98*(2), 147–156.

Rooney, M. A., Claypool, G. E., & Moses Chung, H. (1995). Modeling thermogenic gas generation using carbon isotope ratios of natural gas hydrocarbons. *Chemical Geology*, *126*(3), 219–232. https://doi.org/10.1016/0009-2541(95)00119-0

Schindelin, J., Arganda-Carreras, I., Frise, E., Kaynig, V., Longair, M., Pietzsch, T., Preibisch, S., Rueden, C., Saalfeld, S., Schmid, B., Tinevez, J.-Y., White, D. J., Hartenstein, V., Eliceiri, K., Tomancak, P., & Cardona, A. (2012). Fiji: an open-source platform for biological-image analysis. *Nature Methods*, *9*(7), 676–682. https://doi.org/10.1038/nmeth.2019

Schopf, J. W., Kitajima, K., Spicuzza, M. J., Kudryavtsev, A. B., & Valley, J. W. (2017). SIMS analyses of the oldest known assemblage of microfossils document their taxon-correlated carbon isotope compositions. *Proceedings of the National Academy of Sciences*, *115*(1), 53–58. https://doi.org/10.1073/pnas.1718063115

Schwartz, H., Sample, J., Weberling, K. D., Minisini, D., & Moore, J. C. (2003). An ancient linked fluid migration system : cold-seep deposits and sandstone intrusions in the Panoche Hills , California , USA. *Geo-Marine Letters*, *23*, 340–350. https://doi.org/10.1007/s00367-003-0142-1

Sibuet, M., & Olu, K. (1998). Biogeography, biodiversity and fluid dependence of deep-sea cold-seep communities at active and passive margins. *Deep-Sea Research Part II: Topical Studies in Oceanography*, *45*(1-3), 517–567. https://doi.org/10.1016/S0967-0645(97)00074-X

Walsh, M. M., & Lowe, D. R. (1985). Filamentous microfossils from the 3,500-Myr-old Onverwacht Group, Barberton Mountain Land, South Africa. *Nature*, *314*, 530–532.

Wegener, G., Niemann, H., Elvert, M., Hinrichs, K. U., & Boetius, A. (2008). Assimilation of methane and inorganic carbon by microbial communities mediating the anaerobic oxidation of methane. *Environmental Microbiology*, *10*(9), 2287–2298. https://doi.org/10.1111/j.1462-2920.2008.01653.x

Whiticar, M. J. (1999). Carbon and hydrogen isotope systematics of bacterial formation and oxidation of methane. *Chemical Geology*, *161*(1), 291–314. https://doi.org/10.1016/S0009-2541(99)00092-3

Williford, K. H., Ushikubo, T., Lepot, K., Kitajima, K., Hallmann, C., Spicuzza, M. J., Kozdon, R., Eigenbrode, J. L., Summons, R. E., & Valley, J. W. (2016). Carbon and sulfur isotopic signatures of ancient life and environment at the microbial scale: Neoarchean shales and carbonates. *Geobiology*, *14*(2), 105–128. https://doi.org/10.1111/gbi.12163

Appendices

Appendix A

DATASETS FROM CHAPTER V

Dataset A1: Elemental composition of Si-rich rings surrounding ANME2-SRB aggregates. The different spectra correspond to the points shown in Figs. 4 and 5.

Spectrum 1.

Element	Apparent Concentration	Wt%	Wt% Sigma
C	30.26	54.92	0.46
N	1.54	1.54	1.54
O	21.57	21.57	0.28
Mg	0.25	0.17	0.02
Al	0.10	0.07	0.02
Si	17.16	11.18	0.11
S	0.44	0.31	0.03
Ca	9.76	6.84	0.09
Fe	0.00	0.00	0.00
Sr	0.00	0.00	0.00
Ba	0.00	0.00	0.00

Spectrum 2.

Element	Apparent Concentration	Wt%	Wt% Sigma
C	42.61	61.48	0.19
N	0.00	0.00	0.00
O	12.42	13.94	0.18
Mg	0.32	0.17	0.02
Al	0.00	0.00	0.00
Si	22.33	11.79	0.07
S	0.09	0.05	0.02
Ca	21.88	12.56	0.09
Fe	0.00	0.00	0.00
Sr	0.00	0.00	0.00
Ba	0.00	0.00	0.00

Spectrum 3.

Element	Apparent Concentration	Wt%	Wt% Sigma
C	35.06	44.08	0.35
N	3.78	3.44	0.65
O	29.55	28.33	0.27
Mg	0.58	0.32	0.02
Al	0.16	0.08	0.02
Si	14.71	7.65	0.08
S	0.36	0.20	0.02
Ca	29.34	15.91	0.14
Fe	0.00	0.00	0.00
Sr	0.00	0.00	0.00
Ba	0.00	0.00	0.00

Spectrum 4.

Element	Apparent Concentration	Wt%	Wt% Sigma
C	8.95	51.05	0.21
Mg	0.73	0.80	0.03
Al	1.64	1.77	0.03
Si	24.09	26.60	0.13
S	0.20	0.26	0.03
Ca	15.18	18.55	0.11
Fe	0.63	0.96	0.07

Spectrum 5.

Element	Apparent Concentration	Wt%	Wt% Sigma
C	7.15	51.75	0.23
Mg	0.52	0.58	0.02
Al	8.07	9.00	0.06
Si	22.39	27.76	0.14
S	0.05	0.07	0.03
Ca	8.10	10.75	0.08
Fe	0.06	0.10	0.06

Dataset A2: Al:Si ratios for different basins and treatments, utilized to make the plots in Fig. 3.

Al: Si	Source	Basin	Source order	Basin order
0.000	Aggregate-attached, Sediment-free	Santa Monica	3	3
0.196	Aggregate-attached, Sediment-free	Santa Monica	3	3
0.181	Aggregate-attached, Sediment-free	Santa Monica	3	3
0.182	Aggregate-attached, Sediment-free	Santa Monica	3	3
0.029	Aggregate-attached, Sediment-free	Santa Monica	3	3
0.315	Aggregate-attached, Sediment-free	Santa Monica	3	3
0.238	Aggregate-attached, Sediment-free	Santa Monica	3	3
0.066	Aggregate-attached, Sediment-free	Santa Monica	3	3

Al: Si	Source	Basin	Source order	Basin order
0.1936	Aggregate-attached, Sediment-free	Santa Monica	3	3
0.1464	Aggregate-attached, Sediment-free	Santa Monica	3	3
0.1716	Aggregate-attached, Sediment-free	Santa Monica	3	3
0.2186	Aggregate-attached, Sediment-free	Santa Monica	3	3
0.199	Aggregate-attached, Sediment-free	Santa Monica	3	3
0.21	Aggregate-attached, Sediment-free	Santa Monica	3	3
0.1727	Aggregate-attached, Sediment-free	Santa Monica	3	3
0.2523	Aggregate-attached, Sediment-free	Santa Monica	3	3
0.277	Aggregate-attached, Sediment-free	Santa Monica	3	3
0.1861	Aggregate-attached, Sediment-free	Santa Monica	3	3
0.0643	Aggregate-attached, Sediment-free	Santa Monica	3	3
0.1555	Aggregate-attached, Sediment-free	Santa Monica	3	3
0.2368	Aggregate-attached, Sediment-free	Santa Monica	3	3
0.2599	Aggregate-attached, Sediment-free	Santa Monica	3	3
0.3802	Aggregate-attached, Sediment-free	Santa Monica	3	3
0.3624	Aggregate-attached, Sediment-free	Santa Monica	3	3
0.158	Aggregate-attached, Sediment-free	Santa Monica	3	3
0.225	Aggregate-attached, Sediment-free	Santa Monica	3	3
0.194	Aggregate-attached, Sediment-free	Santa Monica	3	3
0.1851	Aggregate-attached, Sediment-free	Santa Monica	3	3
0.2006	Aggregate-attached, Sediment-free	Santa Monica	3	3
0.2874	Aggregate-attached, Sediment-free	Santa Monica	3	3
0.3012	Aggregate-attached, Sediment-free	Santa Monica	3	3
0.0681	Aggregate-attached, Sediment-free	Santa Monica	3	3
0.0889	Aggregate-attached, Sediment-free	Santa Monica	3	3
0.1041	Aggregate-attached, Sediment-free	Santa Monica	3	3
0.1089	Aggregate-attached, Sediment-free	Santa Monica	3	3
0	Aggregate-attached, Sediment-free	Santa Monica	3	3
0.0632	Aggregate-attached, Sediment-free	Santa Monica	3	3
0.1023	Aggregate-attached, Sediment-free	Santa Monica	3	3
0	Aggregate-attached, Sediment-free	Santa Monica	3	3
0.1562	Aggregate-attached, Sediment-free	Santa Monica	3	3
0	Aggregate-attached, Sediment-free	Santa Monica	3	3
0	Aggregate-attached	Santa Monica	3	3
0	Aggregate-attached	Santa Monica	3	3
0.3533	Aggregate-attached	Santa Monica	3	3
0.649	Aggregate-attached	Santa Monica	3	3
0.2752	Aggregate-attached	Santa Monica	3	3
0.2435	Aggregate-attached	Santa Monica	3	3
0.3649	Aggregate-attached	Santa Monica	3	3
0	Aggregate-attached	Santa Monica	3	3
0	Aggregate-attached	Santa Monica	2	3
0.2982	Aggregate-attached	Santa Monica	2	3
0.4125	Aggregate-attached	Santa Monica	2	3
0.5601	Aggregate-attached	Santa Monica	2	3
0	Aggregate-attached	Santa Monica	2	3
0.3215	Aggregate-attached	Santa Monica	2	3
0.3561	Aggregate-attached	Santa Monica	2	3
0.2052	Aggregate-attached	Santa Monica	2	3
0	Aggregate-attached	Santa Monica	2	3
0.452	Aggregate-attached	Santa Monica	2	3
0.3157	Aggregate-attached	Santa Monica	2	3

Al: Si	Source	Basin	Source order	Basin order
0.189	Aggregate-attached	Santa Monica	2	3
0.484	Aggregate-attached	Santa Monica	2	3
0.095	Aggregate-attached	Santa Monica	2	3
0.140	Aggregate-attached	Santa Monica	2	3
0.068	Aggregate-attached	Santa Monica	2	3
0.334	Aggregate-attached	Santa Monica	2	3
0.177	Aggregate-attached	Santa Monica	2	3
0.132	Aggregate-attached	Santa Monica	2	3
0.329	Aggregate-attached	Santa Monica	2	3
0.240	Aggregate-attached	Santa Monica	2	3
0.343	Aggregate-attached	Santa Monica	2	3
0.247	Aggregate-attached	Santa Monica	2	3
0.254	Aggregate-attached	Santa Monica	2	3
0.405	Aggregate-attached	Santa Monica	2	3
0.070	Aggregate-attached	Santa Monica	2	3
0.276	Aggregate-attached	Santa Monica	2	3
0.597	Aggregate-attached	Santa Monica	2	3
0.138	Aggregate-attached	Santa Monica	2	3
0.117	Aggregate-attached	Santa Monica	2	3
0.107	Aggregate-attached	Santa Monica	2	3
0.158	Aggregate-attached	Santa Monica	2	3
0.359	Aggregate-attached	Santa Monica	2	3
0.340	Aggregate-attached	Santa Monica	2	3
0.763	Sediment	Santa Monica	1	3
0.797	Sediment	Santa Monica	1	3
0.776	Sediment	Santa Monica	1	3
0.738	Sediment	Santa Monica	1	3
0.712	Sediment	Santa Monica	1	3
0.591	Sediment	Santa Monica	1	3
0.655	Sediment	Santa Monica	1	3
0.707	Sediment	Santa Monica	1	3
0.677	Sediment	Santa Monica	1	3
0.625	Sediment	Santa Monica	1	3
0.572	Sediment	Santa Monica	1	3
0.615	Sediment	Santa Monica	1	3
0.733	Sediment	Santa Monica	1	3
0.014	Sediment	Santa Monica	1	3
0.306	Sediment	Santa Monica	1	3
0.370	Sediment	Santa Monica	1	3
0.541	Sediment	Santa Monica	1	3
0.403	Sediment	Santa Monica	1	3
0.541	Sediment	Santa Monica	1	3
0.403	Sediment	Santa Monica	1	3
0.370	Sediment	Santa Monica	1	3
0.541	Sediment	Santa Monica	1	3
0.403	Sediment	Santa Monica	1	3
0.249	Sediment	Santa Monica	1	3
0.322	Sediment	Santa Monica	1	3
0.388	Sediment	Santa Monica	1	3
0.444	Sediment	Santa Monica	1	3
0.262	Sediment	Santa Monica	1	3
0.179	Sediment	Santa Monica	1	3

Al: Si	Source	Basin	Source order	Basin order
0.188	Sediment	Santa Monica	1	3
0.080	Sediment	Santa Monica	1	3
0.270	Sediment	Santa Monica	1	3
0.177	Sediment	Santa Monica	1	3
0.425	Sediment	Santa Monica	1	3
0.387	Sediment	Santa Monica	1	3
0.352	Sediment	Santa Monica	1	3
0.629	Sediment	Santa Monica	1	3
0.588	Sediment	Santa Monica	1	3
0.414	Sediment	Santa Monica	1	3
0.513	Sediment	Santa Monica	1	3
0.589	Sediment	Santa Monica	1	3
0.364	Sediment	Santa Monica	1	3
0.455	Sediment	Santa Monica	1	3
0.505	Sediment	Santa Monica	1	3
0.613	Sediment	Santa Monica	1	3
0.629	Sediment	Santa Monica	1	3
0.663	Sediment	Santa Monica	1	3
0.954	Sediment	Santa Monica	1	3
0.959	Sediment	Santa Monica	1	3
0.015	Sediment	Santa Monica	1	3
0.404	Sediment	Santa Monica	1	3
0.390	Sediment	Santa Monica	1	3
0.296	Sediment	Santa Monica	1	3
0.310	Sediment	Santa Monica	1	3
0.237	Sediment	Santa Monica	1	3
0.082	Sediment	Santa Monica	1	3
0.583	Sediment	Santa Monica	1	3
0.257	Sediment	Santa Monica	1	3
0.428	Sediment	Santa Monica	1	3
0.381	Sediment	Santa Monica	1	3
0.457	Sediment	Santa Monica	1	3
0.486	Sediment	Santa Monica	1	3
0.131	Sediment	Santa Monica	1	3
0.223	Sediment	Santa Monica	1	3
0.381	Sediment	Santa Monica	1	3
0.005	Sediment	Santa Monica	1	3
0.444	Sediment	Santa Monica	1	3
0.404	Sediment	Santa Monica	1	3
0.478	Sediment	Santa Monica	1	3
0.478	Sediment	Santa Monica	1	3
0.622	Sediment	Santa Monica	1	3
0.378	Sediment	Santa Monica	1	3
0.293	Sediment	Santa Monica	1	3
0.507	Sediment	Santa Monica	1	3
0.364	Sediment	Santa Monica	1	3
0.377	Sediment	Santa Monica	1	3
0.315	Sediment	Santa Monica	1	3
0.315	Sediment	Santa Monica	1	3
0.452	Sediment	Santa Monica	1	3
0.253	Sediment	Santa Monica	1	3
0.571	Sediment	Santa Monica	1	3

Al: Si	Source	Basin	Source order	Basin order
0.509	Sediment	Santa Monica	1	3
0.484	Sediment	Santa Monica	1	3
0.345	Sediment	Santa Monica	1	3
0.339	Sediment	Santa Monica	1	3
0.189	Sediment	Santa Monica	1	3
0.289	Sediment	Santa Monica	1	3
0.426	Sediment	Santa Monica	1	3
0.222	Sediment	Santa Monica	1	3
0.323	Sediment	Santa Monica	1	3
0.386	Sediment	Santa Monica	1	3
0.356	Sediment	Santa Monica	1	3
0.347	Sediment	Santa Monica	1	3
0.346	Sediment	Santa Monica	1	3
0.369	Sediment	Santa Monica	1	3
0.365	Sediment	Santa Monica	1	3
0.349	Sediment	Santa Monica	1	3
0.299	Sediment	Santa Monica	1	3
0.279	Sediment	Santa Monica	1	3
0.458	Sediment	Santa Monica	1	3
0.549	Sediment	Santa Monica	1	3
0.431	Sediment	Santa Monica	1	3
0.499	Sediment	Santa Monica	1	3
0.413	Sediment	Santa Monica	1	3
0.343	Sediment	Santa Monica	1	3
0.399	Sediment	Santa Monica	1	3
0.237	Sediment	Santa Monica	1	3
0.580	Sediment	Santa Monica	1	3
0.342	Sediment	Santa Monica	1	3
0.424	Sediment	Santa Monica	1	3
0.494	Sediment	Santa Monica	1	3
0.395	Sediment	Santa Monica	1	3
0.288	Sediment	Santa Monica	1	3
0.355	Sediment	Santa Monica	1	3
0.384	Sediment	Santa Monica	1	3
0.616	Sediment	Santa Monica	1	3
0.396	Sediment	Santa Monica	1	3
0.586	Sediment	Santa Monica	1	3
0.669	Sediment	Santa Monica	1	3
0.583	Sediment	Santa Monica	1	3
0.627	Sediment	Santa Monica	1	3
0.410	Sediment	Santa Monica	1	3
0.472	Sediment	Santa Monica	1	3
0.488	Sediment	Santa Monica	1	3
0.445	Sediment	Santa Monica	1	3
0.361	Sediment	Santa Monica	1	3
0.444	Sediment	Santa Monica	1	3
0.457	Sediment	Santa Monica	1	3
0.370	Sediment	Santa Monica	1	3
0.437	Sediment	Santa Monica	1	3
0.444	Sediment	Santa Monica	1	3
0.296	Sediment	Santa Monica	1	3
0.509	Sediment	Santa Monica	1	3

Al: Si	Source	Basin	Source order	Basin order
0.379	Sediment	Santa Monica	1	3
0.401	Aggregate-attached	Eel River	6	2
0.600	Aggregate-attached	Eel River	6	2
0.412	Aggregate-attached	Eel River	6	2
0.449	Aggregate-attached	Eel River	6	2
0.339	Aggregate-attached	Eel River	6	2
0.151	Aggregate-attached	Eel River	6	2
0.024	Aggregate-attached	Eel River	6	2
0.042	Aggregate-attached	Eel River	6	2
0.299	Aggregate-attached	Eel River	6	2
0.186	Aggregate-attached	Eel River	6	2
0.183	Aggregate-attached	Eel River	6	2
0.104	Aggregate-attached	Eel River	6	2
0.435	Aggregate-attached	Eel River	6	2
0.172	Aggregate-attached	Eel River	6	2
0.421	Aggregate-attached	Eel River	6	2
0.061	Aggregate-attached	Eel River	6	2
0.435	Aggregate-attached	Eel River	6	2
0.000	Aggregate-attached	Eel River	6	2
0.357	Aggregate-attached	Eel River	6	2
0.315	Aggregate-attached	Eel River	6	2
0.000	Aggregate-attached	Eel River	6	2
0.321	Aggregate-attached	Eel River	6	2
0.000	Aggregate-attached	Eel River	6	2
0.000	Aggregate-attached	Eel River	6	2
0.550	Aggregate-attached	Eel River	6	2
0.255	Aggregate-attached	Eel River	6	2
0.346	Aggregate-attached	Eel River	6	2
0.322	Aggregate-attached	Eel River	6	2
0.335	Aggregate-attached	Eel River	6	2
0.327	Aggregate-attached	Eel River	6	2
0.000	Aggregate-attached	Eel River	6	2
0.132	Aggregate-attached	Eel River	6	2
0.069	Aggregate-attached	Eel River	6	2
0.068	Aggregate-attached	Eel River	6	2
0.232	Aggregate-attached	Eel River	6	2
0.372	Aggregate-attached	Eel River	6	2
0.412	Sediment	Jaco Scar	4	1
0.368	Sediment	Jaco Scar	4	1
0.469	Sediment	Jaco Scar	4	1
0.293	Sediment	Jaco Scar	4	1
0.143	Sediment	Jaco Scar	4	1
0.341	Sediment	Jaco Scar	4	1
0.426	Sediment	Jaco Scar	4	1
0.426	Sediment	Jaco Scar	4	1
0.399	Sediment	Jaco Scar	4	1
0.214	Sediment	Jaco Scar	4	1
0.507	Sediment	Jaco Scar	4	1
0.409	Sediment	Jaco Scar	4	1
0.382	Sediment	Jaco Scar	4	1
0.413	Sediment	Jaco Scar	4	1
0.331	Sediment	Jaco Scar	4	1

Al: Si	Source	Basin	Source order	Basin order
0.438	Sediment	Jaco Scar	4	1
0.343	Sediment	Jaco Scar	4	1
0.395	Sediment	Jaco Scar	4	1
0.441	Sediment	Jaco Scar	4	1
0.573	Sediment	Jaco Scar	4	1
0.636	Sediment	Jaco Scar	4	1
0.446	Sediment	Jaco Scar	4	1
0.408	Sediment	Jaco Scar	4	1
0.414	Sediment	Jaco Scar	4	1
0.328	Sediment	Jaco Scar	4	1
0.402	Sediment	Jaco Scar	4	1
0.395	Sediment	Jaco Scar	4	1
0.398	Sediment	Jaco Scar	4	1
0.474	Sediment	Jaco Scar	4	1
0.458	Sediment	Jaco Scar	4	1
0.399	Sediment	Jaco Scar	4	1
0.393	Sediment	Jaco Scar	4	1
0.411	Sediment	Jaco Scar	4	1
0.421	Sediment	Jaco Scar	4	1
0.456	Sediment	Jaco Scar	4	1
0.391	Sediment	Jaco Scar	4	1
0.913	Sediment	Jaco Scar	4	1
0.609	Sediment	Jaco Scar	4	1
0.459	Sediment	Jaco Scar	4	1
0.148	Sediment	Jaco Scar	4	1
0.631	Sediment	Jaco Scar	4	1
0.469	Sediment	Jaco Scar	4	1
0.469	Sediment	Jaco Scar	4	1
0.469	Sediment	Jaco Scar	4	1
0.469	Sediment	Jaco Scar	4	1
0.296	Sediment	Jaco Scar	4	1
0.370	Sediment	Jaco Scar	4	1
0.191	Sediment	Jaco Scar	4	1
0.439	Sediment	Jaco Scar	4	1
0.313	Sediment	Jaco Scar	4	1
0.483	Sediment	Jaco Scar	4	1
0.374	Sediment	Jaco Scar	4	1
0.357	Sediment	Jaco Scar	4	1
0.357	Sediment	Jaco Scar	4	1
0.399	Sediment	Jaco Scar	4	1
0.135	Sediment	Jaco Scar	4	1
0.291	Sediment	Jaco Scar	4	1
0.430	Sediment	Jaco Scar	4	1
0.415	Sediment	Jaco Scar	4	1
0.416	Sediment	Jaco Scar	4	1
0.378	Sediment	Jaco Scar	4	1
0.403	Sediment	Jaco Scar	4	1
0.393	Sediment	Jaco Scar	4	1
0.405	Aggregate-attached	Jaco Scar	5	1
0.405	Aggregate-attached	Jaco Scar	5	1
0.335	Aggregate-attached	Jaco Scar	5	1
0.396	Aggregate-attached	Jaco Scar	5	1

Al: Si	Source	Basin	Source order	Basin order
0.335	Aggregate-attached	Jaco Scar	5	1
0.251	Aggregate-attached	Jaco Scar	5	1
0.237	Aggregate-attached	Jaco Scar	5	1
0.392	Aggregate-attached	Jaco Scar	5	1
0.320	Aggregate-attached	Jaco Scar	5	1
0.193	Aggregate-attached	Jaco Scar	5	1
0.182	Aggregate-attached	Jaco Scar	5	1
0.382	Aggregate-attached	Jaco Scar	5	1
0.416	Aggregate-attached	Jaco Scar	5	1
0.361	Aggregate-attached	Jaco Scar	5	1
0.300	Aggregate-attached	Jaco Scar	5	1
0.249	Aggregate-attached	Jaco Scar	5	1
0.234	Aggregate-attached	Jaco Scar	5	1
0.252	Aggregate-attached	Jaco Scar	5	1
0.302	Aggregate-attached	Jaco Scar	5	1
0.245	Aggregate-attached	Jaco Scar	5	1
0.284	Aggregate-attached	Jaco Scar	5	1
0.209	Aggregate-attached	Jaco Scar	5	1
0.290	Aggregate-attached	Jaco Scar	5	1
0.361	Aggregate-attached	Jaco Scar	5	1
0.317	Aggregate-attached	Jaco Scar	5	1
0.172	Aggregate-attached	Jaco Scar	5	1
0.203	Aggregate-attached	Jaco Scar	5	1
0.385	Aggregate-attached	Jaco Scar	5	1
0.320	Aggregate-attached	Jaco Scar	5	1
0.309	Aggregate-attached	Jaco Scar	5	1
0.305	Aggregate-attached	Jaco Scar	5	1
0.199	Aggregate-attached	Jaco Scar	5	1
0.279	Aggregate-attached	Jaco Scar	5	1
0.265	Aggregate-attached	Jaco Scar	5	1
0.257	Aggregate-attached	Jaco Scar	5	1
0.367	Aggregate-attached	Jaco Scar	5	1
0.306	Aggregate-attached	Jaco Scar	5	1
0.262	Aggregate-attached	Jaco Scar	5	1
0.302	Aggregate-attached	Jaco Scar	5	1
0.241	Aggregate-attached	Jaco Scar	5	1
0.373	Sediment	Eel River	1	1
0.346	Sediment	Eel River	1	1
0.017	Sediment	Eel River	1	1
0.454	Sediment	Eel River	1	1
0.371	Sediment	Eel River	1	1
0.427	Sediment	Eel River	1	1
0.431	Sediment	Eel River	1	1
0.029	Sediment	Eel River	1	1
0.391	Sediment	Eel River	1	1
0.531	Sediment	Eel River	1	1
0.495	Sediment	Eel River	1	1
0.442	Sediment	Eel River	1	1
0.667	Sediment	Eel River	1	1
0.432	Sediment	Eel River	1	1
0.370	Sediment	Eel River	1	1
0.400	Sediment	Eel River	1	1

Al: Si	Source	Basin	Source order	Basin order
0.454	Sediment	Eel River	1	1
0.153	Sediment	Eel River	1	1
0.405	Sediment	Eel River	1	1
0.537	Sediment	Eel River	1	1
0.481	Sediment	Eel River	1	1
0.488	Sediment	Eel River	1	1
0.459	Sediment	Eel River	1	1
0.241	Sediment	Eel River	1	1
0.403	Sediment	Eel River	1	1
0.399	Sediment	Eel River	1	1
0.120	Sediment	Eel River	1	1
0.536	Sediment	Eel River	1	1
0.081	Sediment	Eel River	1	1
0.307	Sediment	Eel River	1	1
0.258	Sediment	Eel River	1	1
0.398	Sediment	Eel River	1	1
0.492	Sediment	Eel River	1	1
0.205	Sediment	Eel River	1	1
0.033	Sediment	Eel River	1	1
0.269	Sediment	Eel River	1	1
0.397	Sediment	Eel River	1	1
0.130	Sediment	Eel River	1	1
0.317	Sediment	Eel River	1	1
0.359	Sediment	Eel River	1	1
0.382	Sediment	Eel River	1	1
0.406	Sediment	Eel River	1	1
0.412	Sediment	Eel River	1	1
0.310	Sediment	Eel River	1	1
0.493	Sediment	Eel River	1	1
0.421	Sediment	Eel River	1	1
0.443	Sediment	Eel River	1	1
0.375	Sediment	Eel River	1	1
0.420	Sediment	Eel River	1	1
0.355	Sediment	Eel River	1	1
0.386	Sediment	Eel River	1	1
0.523	Sediment	Eel River	1	1
0.373	Sediment	Eel River	1	1
0.669	Sediment	Eel River	1	1
0.077	Sediment	Eel River	1	1
0.340	Sediment	Eel River	1	1
0.329	Sediment	Eel River	1	1
0.316	Sediment	Eel River	1	1
0.442	Sediment	Eel River	1	1
0.326	Sediment	Eel River	1	1
0.241	Sediment	Eel River	1	1
0.459	Sediment	Eel River	1	1
0.636	Sediment	Eel River	1	1
0.450	Sediment	Eel River	1	1
0.450	Sediment	Eel River	1	1
0.484	Sediment	Eel River	1	1
0.817	Sediment	Eel River	1	1
0.315	Sediment	Eel River	1	1
0.391	Sediment	Eel River	1	1

Appendix B

DATASETS FROM CHAPTER VI

Dataset B1: Carbon and oxygen isotope compositions of the Tepee Buttes carbonates.

ID	Phase	Replicate	δ13C DIC	δ18O DIC	δ13C DIC s.d.	δ18O DIC s.d.	Source
100-110	Micrite		-34.93	-10.31			Loyd *et al.* (2016)
130-140	Micrite		-37.75	-10			Loyd *et al.* (2016)
190-200	Micrite		-35.03	-10.64			Loyd *et al.* (2016)
20-30	Micrite		-36.4	-10.39			Loyd *et al.* (2016)
230-240	Micrite		-36.47	-7.97			Loyd *et al.* (2016)
250-260	Micrite		-35.41	-11.16			Loyd *et al.* (2016)
310-320	Micrite		-41.35	-11.07			Loyd *et al.* (2016)
320-2h	Micrite		-41.05	-0.89			Loyd *et al.* (2016)
360-370	Micrite		-43.28	-11.09			Loyd *et al.* (2016)
40-50	Micrite		-38.01	-9.6			Loyd *et al.* (2016)
65-70	Micrite		-38.16	-11.33			Loyd *et al.* (2016)
star 230-240	Micrite		-27.37	-11.1			Loyd *et al.* (2016)
teepee hrm 210-220	Micrite		-40.35	-9.8			Loyd *et al.* (2016)
teepee hrm 400-40	Micrite		-30.52	-11.17			Loyd *et al.* (2016)
100-110fc	Fibrous cement		-41.22	-8.6			Loyd *et al.* (2016)
190-200fc	Fibrous cement		-45.21	-7.57			Loyd *et al.* (2016)
210-220fc	Fibrous cement		-45.21	-6.28			Loyd *et al.* (2016)
460-470fc	Fibrous cement		-43.29	-8.09			Loyd *et al.* (2016)
711.5 VI S 2	Equant cement		-14.31	-12.09			Loyd *et al.* (2016)
320-2 PS	Biopelmicrite		-44.75	-0.3			Loyd *et al.* (2016)
704.5 1 PS	Biopelmicrite		-44.11	-1.5			Loyd *et al.* (2016)
711 WI PS	Biopelmicrite		-37.01	-4.12			Loyd *et al.* (2016)
711.5 VI PS 2	Biopelmicrite		-44.76	-1.04			Loyd *et al.* (2016)
711.5 VI PS1	Biopelmicrite		-45.16	-1.55			Loyd *et al.* (2016)
HRS 674.6 PS	Biopelmicrite		-35.16	-3.58			Loyd *et al.* (2016)
a_1	Micrite		-49.65	-1.05			Birgel *et al.* (2006)
a_2	Micrite		-49.66	-1.12			Birgel *et al.* (2006)
a_3	Micrite		-48.49	-1.09			Birgel *et al.* (2006)
a_4	Micrite		-48.57	-1.12			Birgel *et al.* (2006)
a_5	Micrite		-46.61	-1.19			Birgel *et al.* (2006)
a_6	Micrite		-46.57	-1.26			Birgel *et al.* (2006)

ID	Phase	Replicate	δ13C DIC	δ18O DIC	δ13C DIC s.d.	δ18O DIC s.d.	Source
a_7	Micrite		-43.11	-0.35			Birgel *et al.* (2006)
a_8	Micrite		-45.34	-0.68			Birgel *et al.* (2006)
b_1	Botryoidal cement		-40.46	-3.57			Birgel *et al.* (2006)
b_2	Botryoidal cement		-45.45	-1.78			Birgel *et al.* (2006)
b_3	Botryoidal cement		-42.32	-3.45			Birgel *et al.* (2006)
b_4	Botryoidal cement		-40.40	-3.67			Birgel *et al.* (2006)
b_5	Botryoidal cement		-22.08	-7.42			Birgel *et al.* (2006)
b_6	Botryoidal cement		-38.62	-3.91			Birgel *et al.* (2006)
b_7	Botryoidal cement		-13.24	-6.67			Birgel *et al.* (2006)
b_8	Botryoidal cement		-35.69	-5.46			Birgel *et al.* (2006)
b_9	Botryoidal cement		-36.48	-4.76			Birgel *et al.* (2006)
b_10	Botryoidal cement		-25.33	-6.01			Birgel *et al.* (2006)
b_11	Botryoidal cement		-40.30	-3.08			Birgel *et al.* (2006)
b_12	Botryoidal cement		-44.31	-2.60			Birgel *et al.* (2006)
b_13	Botryoidal cement		-44.25	-2.54			Birgel *et al.* (2006)
c_1	Ferroan equant cement		-28.98	-9.88			Birgel *et al.* (2006)
c_2	Ferroan equant cement		-17.53	-9.89			Birgel *et al.* (2006)
c_3	Ferroan equant cement		-20.21	-11.35			Birgel *et al.* (2006)
d_1	Yellow calcite		-36.07	-3.41			Birgel *et al.* (2006)
d_2	Yellow calcite		-35.59	-3.18			Birgel *et al.* (2006)
d_3	Yellow calcite		-39.70	-2.04			Birgel *et al.* (2006)
d_4	Yellow calcite		-31.73	-6.68			Birgel *et al.* (2006)
d_5	Yellow calcite		-45.86	-2.51			Birgel *et al.* (2006)
d_6	Yellow calcite		-42.68	-3.89			Birgel *et al.* (2006)
d_7	Yellow calcite		-40.19	-4.02			Birgel *et al.* (2006)
d_8	Yellow calcite		-41.99	-2.26			Birgel *et al.* (2006)
d_9	Yellow calcite		-35.72	-3.55			Birgel *et al.* (2006)
d_10	Yellow calcite		-37.57	-2.33			Birgel *et al.* (2006)
d_11	Yellow calcite		-33.51	-4.98			Birgel *et al.* (2006)
d_12	Yellow calcite		-43.21	-0.74			Birgel *et al.* (2006)
e_1	Microspar recrystallization		-19.09	-0.70			Birgel *et al.* (2006)
e_2	Microspar recrystallization		-18.00	-0.52			Birgel *et al.* (2006)

ID	Phase	Replicate	δ13C DIC	δ18O DIC	δ13C DIC s.d.	δ18O DIC s.d.	Source
e_3	Microspar recrystallization		-20.90	-0.55			Birgel *et al.* (2006)
e_4	Microspar recrystallization		-18.28	-0.30			Birgel *et al.* (2006)
e_5	Microspar recrystallization		-18.69	-0.02			Birgel *et al.* (2006)
e_6	Microspar recrystallization		-25.22	-0.16			Birgel *et al.* (2006)
e_7	Microspar recrystallization		-23.32	-0.20			Birgel *et al.* (2006)
a_1	Ferroan equant cement		-14.50	-13.00			Kauffman *et al.* (1996)
a_2	Ferroan equant cement		-12.00	-12.00			Kauffman *et al.* (1996)
a_3	Ferroan equant cement		-18.50	-11.80			Kauffman *et al.* (1996)
a_4	Ferroan equant cement		-19.00	-11.50			Kauffman *et al.* (1996)
a_5	Ferroan equant cement		-14.00	-11.50			Kauffman *et al.* (1996)
a_6	Ferroan equant cement		-23.00	-8.50			Kauffman *et al.* (1996)
a_7	Ferroan equant cement		-18.50	-9.00			Kauffman *et al.* (1996)
b_1	Fibrous cement		-35.50	-5.10			Kauffman *et al.* (1996)
b_2	Fibrous cement		-40.00	-4.20			Kauffman *et al.* (1996)
b_3	Fibrous cement		-41.00	-4.30			Kauffman *et al.* (1996)
b_4	Botryoidal cement		-45.70	0.20			Kauffman *et al.* (1996)
b_5	Botryoidal cement		-42.00	-1.20			Kauffman *et al.* (1996)
b_6	Botryoidal cement		-40.50	-2.00			Kauffman *et al.* (1996)
b_7	Botryoidal cement		-42.00	-2.00			Kauffman *et al.* (1996)
BR4_1	Biopelmicrite	a	-37.51	-9.29	0.03	0.05	This study
BR4_1	Pseudospar	b	-17.69	-11.86	0.04	0.04	This study
BR4_1	Biopelmicrite	c	-37.03	-9.73	0.04	0.05	This study
BR4_1	Pseudospar	a	-9.79	-11.64	0.06	0.09	This study
BR4_1	Pseudospar	b	-18.38	-12.23	0.04	0.08	This study
BR4_1	Botryoidal cement	a	-42.95	-6.46	0.02	0.04	This study
BR4_1	Botryoidal cement	b	-41.86	-6.24	0.04	0.06	This study
BR4_1	Botryoidal cement	c	-38.60	-9.83	0.03	0.08	This study
BR4_1	Yellow calcite	a	-34.96	-10.55	0.03	0.06	This study
BR4_1	Yellow calcite	b	-33.20	-10.07	0.02	0.08	This study
BR4_1	Yellow calcite	c	-39.30	-10.56	0.05	0.07	This study
BR4_1	Massive	a	-11.57	-12.38	0.05	0.06	This study
BR4_1	Massive	b	-12.19	-11.99	0.11	0.16	This study
BR4_1	Massive	c	-13.74	-13.13	0.04	0.05	This study
BR1_8	Biopelmicrite	a	-39.80	-1.69	0.02	0.05	This study
BR1_8	Biopelmicrite	b	-37.73	-2.69	0.06	0.06	This study

ID	Phase	Replicate	δ13C DIC	δ18O DIC	δ13C DIC s.d.	δ18O DIC s.d.	Source
BR1_8	Biopelmicrite	c	-40.52	-2.70	0.05	0.08	This study
BR1_8	Pseudospar	a	-16.59	-12.30	0.05	0.05	This study
BR1_8	Pseudospar	b	-15.53	-12.38	0.04	0.06	This study
BR1_8	Pseudospar	c	-15.79	-12.01	0.01	0.03	This study
BR1_8	Massive	a	-36.51	-4.03	0.09	0.19	This study
BR1_8	Massive	b	-37.63	-4.72	0.05	0.10	This study
BR1_8	Massive	c	-19.09	-13.94	0.04	0.08	This study
BR1_8	Micrite	a	-36.37	-1.81	0.04	0.10	This study
BR1_8	Micrite	b	-40.89	-2.77	0.04	0.09	This study
BR1_8	Micrite	c	-38.86	-2.21	0.06	0.08	This study
BR2_3	Biopelmicrite	a	-34.39	-11.47	0.05	0.09	This study
BR2_3	Biopelmicrite	b	-34.82	-11.41	0.03	0.07	This study
BR2_3	Biopelmicrite	c	-34.47	-11.27	0.05	0.06	This study
BR2_3	Pseudospar	d	-10.50	-12.31	0.05	0.07	This study
BR2_3	Equant cement	a	-36.54	-10.82	0.03	0.08	This study
BR2_3	Equant cement	b	-40.88	-4.77	0.05	0.06	This study
BR2_3	Equant cement	c	-42.04	-5.12	0.04	0.08	This study
BR2_3	Yellow calcite	a	-38.56	-6.04	0.06	0.10	This study
BR2_3	Yellow calcite	b	-40.53	-5.75	0.03	0.08	This study
BR2_3	Yellow calcite	c	-39.19	-8.65	0.10	0.11	This study
BR2_3	Yellow calcite	d	-41.58	-4.14	0.03	0.04	This study
BR2_1	Biopelmicrite	a	-38.41	-7.16	0.05	0.03	This study
BR2_1	Biopelmicrite	b	-31.71	-10.21	0.07	0.10	This study
BR2_1	Biopelmicrite	c	-29.47	-9.48	0.04	0.07	This study
BR2_1	Pseudospar	a	-15.54	-11.55	0.06	0.08	This study
BR2_1	Pseudospar	b	-19.32	-10.95	0.04	0.06	This study
BR2_1	Micrite	a	-41.77	-4.44	0.04	0.06	This study
BR2_1	Micrite	b	-40.27	-6.54	0.02	0.05	This study
BR2_1	Micrite	c	-36.40	-7.70	0.03	0.06	This study
BR2_1	Massive	a	-22.12	-11.34	0.04	0.08	This study
BR2_1	Massive	b	-30.41	-8.94	0.08	0.06	This study
BR2_1	Botryoidal cement	a	-43.68	-3.73	0.04	0.07	This study
BR2_1	Botryoidal cement	b	-41.99	-4.31	0.06	0.09	This study
BR1_1	Micrite	a	-43.26	-0.73	0.04	0.07	This study
BR1_1	Micrite	b	-43.30	-1.42	0.06	0.07	This study
BR1_1	Micrite	c	-42.00	-1.44	0.03	0.05	This study
BR1_1	Pseudospar	a	-25.84	-8.53	0.04	0.08	This study
BR1_1	Pseudospar	b	-16.72	-11.41	0.03	0.08	This study
BR1_1	Botryoidal cement	a	-44.01	-3.35	0.02	0.06	This study
BR1_1	Botryoidal cement	b	-40.10	-4.36	0.04	0.06	This study
BR1_1	Botryoidal cement	c	-29.34	-8.22	0.04	0.08	This study
BR1_1	Yellow calcite	a	-44.46	-0.93	0.04	0.06	This study
BR1_1	Yellow calcite	b	-45.00	-1.08	0.04	0.05	This study
BR1_1	Yellow calcite	c	-37.28	-4.62	0.05	0.06	This study
BR1_1	Equant cement	a	-39.77	-5.43	0.04	0.08	This study
BR1_1	Equant cement	b	-44.73	-3.15	0.05	0.10	This study
BR1_1	Equant cement	c	-45.74	-2.64	0.05	0.06	This study